



THE HONG KONG
POLYTECHNIC UNIVERSITY

香港理工大學

Pao Yue-kong Library

包玉剛圖書館

Copyright Undertaking

This thesis is protected by copyright, with all rights reserved.

By reading and using the thesis, the reader understands and agrees to the following terms:

1. The reader will abide by the rules and legal ordinances governing copyright regarding the use of the thesis.
2. The reader will use the thesis for the purpose of research or private study only and not for distribution or further reproduction or any other purpose.
3. The reader agrees to indemnify and hold the University harmless from and against any loss, damage, cost, liability or expenses arising from copyright infringement or unauthorized usage.

IMPORTANT

If you have reasons to believe that any materials in this thesis are deemed not suitable to be distributed in this form, or a copyright owner having difficulty with the material being included in our database, please contact lbsys@polyu.edu.hk providing details. The Library will look into your claim and consider taking remedial action upon receipt of the written requests.

FLOW CONTROL OF BLUFF BODY

ZENG LINGWEI

PhD

The Hong Kong Polytechnic University

2024

The Hong Kong Polytechnic University
Department of Mechanical Engineering

Flow Control of Bluff Body

Zeng Lingwei

**A thesis submitted in partial fulfilment of the requirements for
the degree of Doctor of Philosophy**

December 2023

Certificate of Originality

I hereby declare that this thesis is my own work and that, to the best of my knowledge and belief, it reproduces no material previously published or written, nor material that has been accepted for the award of any other degree or diploma, except where due acknowledgement has been made in the text.

- _____(Signed)

ZENG Lingwei (Name of Student)

Abstract

Bluff bodies are ubiquitous in nature and engineering applications, such as bridges, buildings, and marine structures, to name a few. Fluid flow around these bluff bodies can usually lead to various phenomena such as vortex shedding, flow separation, and flow-induced vibration (FIV). These phenomena may have detrimental effects on engineering structures, significantly compromising their safety and reliability. Historical incidents, such as the collapse of Tacoma Bridge and Ferrybridge Power Station and the very large vibration of structures like the Humen Bridge and SEG Building, have emphasized the importance of effective control mechanisms for these bluff bodies.

For decades, various technologies have been applied to control the flow around bluff bodies. These technologies can be classified into passive control, such as surface modifications by spiral wire, splitter plate, and attached fins et al., and active control, such as body motion, blowing/suction, and synthetic jets et al. However, some unsolved issues still need to be addressed. For example, passive control of FIV of bluff bodies with high mass ratios has seldom been studied. In addition, the implementation of nature-inspired shapes like cactus structures can be a novel approach for the control. These research gaps motivated us to conduct the present research.

This study aims to address several important issues in passive and active flow control of bluff bodies. These issues are related to the use of trailing-edge splitter plate, attached fins, biomimetic surface, and oscillatory morphing surface and its variants. Here, we mainly demonstrate the control ideas by using a circular cylinder, which is the most representative and

simplified shape to stand for bluff bodies. First, a cylinder attached by a trailing edge splitter plate was evaluated to assess its impact on the resulting FIV. Five different vibration modes have been found with the increase of splitter length (L), i.e., typical vortex-induced-vibration (VIV when $L/D = 0, 0.125$, where D is the diameter of the cylinder), Transition I ($L/D = 0.25$), Galloping ($L/D = 0.5, 0.75$), Transition II ($L/D = 1.0$) and Suppression regions ($L/D = 1.5 \sim 3.5$). These observations supplement the research gap at high mass ratio cases and may offer guidelines for engineering applications.

Next, a cylinder attached with fins was investigated on its FIV and energy harvesting performance. A new innovative device for harvesting bi-directional flow energy has been created by attaching four fins on both the windward and leeward sides of a cylinder. This device surpasses the performance of a plain cylinder by producing greater vibration amplitudes and functioning efficiently over a broader range of velocities. This new bi-directional flow-energy harvester is an appropriate candidate to work at sites where the flow periodically changes its directions, for example, in tidal flows.

Then, we examined the FIV performance of a nature-inspired cylinder equipped with three or four ribs. The findings revealed that the three ribs suppress the cylinder's oscillation at lower angles of attack (AOAs at $0^\circ \sim 30^\circ$) while promoting galloping at higher AOAs ($45^\circ \sim 60^\circ$) compared to the normal cylinder. In comparison, the four-rib cases at lower AOAs ($0^\circ \sim 15^\circ$) exhibit a typical VIV response, accompanied by a symmetry break, while remarkably mitigating the cylinder's oscillation at higher AOAs ($30^\circ \sim 45^\circ$). This offers new potential avenues for FIV control of bluff bodies.

Last, the wake of a cylinder was actively controlled by the cylinder's oscillatory morphing surface. It was found that, compared to a normal cylinder, oscillatory morphing surface results

in a smaller vortex formation length L_f , especially at intermediate frequency perturbations. Beyond this, L_f for the smaller or higher frequency perturbations will increase. For these intermediate frequency oscillatory morphing cases, the shear layers transition and roll up earlier due to the significantly enhanced flow instability. For higher perturbation case, small vortices will form regularly along and superimpose upon the separated shear layers. To further explore the feasibility of using morphing surface for drag reduction, CFD simulation has been conducted based on the variants of the morphing surface, namely oscillating surface, and anti-phase jets. It was found that, for Reynolds number $Re = 1,000$, using an oscillating surface can effectively manipulate the wake of the cylinder and reduce the drag. Anti-phase jets can also achieve similar control performance (drag reduction of about 16.6%). A similar control effect has also been achieved in a three-dimensional control case; through lock-on, the jet can stabilize the spanwise flow and delay the occurrence of three-dimensional flow, forming a quasi-two-dimensional one.

The findings from this study can provide more physical insights into the flow control of bluff bodies, which may be useful in the realm of engineering applications, including civil engineering, aerospace engineering, mechanical engineering, and marine engineering.

List of Publications

Journal Papers

1. **Lingwei Zeng**, Fuwang Zhao, Hanfeng Wang, Zhaokun Wang, Waikin Yeung, Yang Liu, Hui Tang. A bi-directional flow-energy harvester. *Applied Physics Letters*, 2023, 122, 153901.
2. **Lingwei Zeng**, Fuwang Zhao, Hanfeng Wang, Yang Liu, Hui Tang. Control of flow-induced vibration of a circular cylinder using a splitter plate. *Physics of Fluids*, 2023, 35(8).
3. **Lingwei Zeng**, T. H. New, Hui Tang. Control of cylinder wake using oscillatory morphing surface. *Physics of Fluids*, 2024, 36(5).

Conference papers

1. **Lingwei Zeng**, Fuwang Zhao, Yang Liu, Hui Tang. Flow induced vibration of a circular cylinder with an attached splitter plate. The 25th Annual Conference of HKSTAM 2022, the 17th Jiangsu–Hong Kong Forum on Mechanics and Its Application. 4, April, 2022. Hong Kong, China.

List of Publications

2. **Lingwei Zeng**, Wei Wang, Yang Liu, Hui Tang. Flow induced vibration of a cactus-shaped cylinder with three/four ribs. The 26th Annual Conference of HKSTAM 2023, the 18th Shanghai–Hong Kong Forum on Mechanics and Its Application. 15, April, 2023. Hong Kong, China. **(Best presentation award)**.

3. **Lingwei Zeng**, T.H. New, Yang Liu, Hui Tang. Wake control by a cylinder with oscillatory morphing surface. The 20th International Symposium on Flow Visualization (ISFV-20). 10-13, July, 2023. Delft, the Netherlands.

4. **Lingwei Zeng**, T.H. New, Chenglei Wang, Hui Tang. Wake control by a cylinder with oscillatory morphing surface: An experimental and numerical study. 16th International Conference on Fluid Control, Measurements, and Visualization. Beijing, China, November 26-30, 2023.

List of Publications

Acknowledgements

Firstly, I would like to express my deepest gratitude towards my supervisor, Dr. Tang Hui, who always gives me patient guidance and timely help. As a distinguished authority in the field of fluid mechanics, Dr. Tang's unfailing commitment to rigorous scientific inquiry and his unparalleled expertise have left an indelible mark on my research life. Not only did he meticulously outline my limitations, but he also furnished them with crucial direction, guidance, and support, employing incredible patience, and exceptional insight, which enabled me to surmount challenges and barriers encountered during my Ph.D. study period. Without his help, I cannot finish this thesis.

Secondly, I want to express my profound gratitude to my co-supervisor, Dr. Liu Yang, for providing unwavering support and encouragement throughout my Ph.D. period. The invaluable suggestions and guidance provided by Dr. Liu have been instrumental in helping me overcome various obstacles and challenges. In addition, I want to extend my heartfelt appreciation to my former supervisor, Prof. Wang Hanfeng, for demonstrating exceptional guidance, attentiveness, and assistance in my academic pursuits.

Thirdly, I wish to express sincere thanks to Dr. T.H. New Daniel for his kind hosting and patient guidance during my attachment at Nanyang Technological University. Dr. Daniel demonstrated a friendly disposition and effectively imparted numerous invaluable experimental skills centered around fluid mechanics to me. Special thanks to Dr. Chen

Acknowledgements

Songlin, Dr. Li Xuefeng, Xu Bowen, Se Wenxuan, and Li Jingfeng when I studied in Singapore.

Fourthly, I want to express my extreme thanks to my friends and colleagues at PolyU for their kind help, encouragement, and friendship, particularly Dr. Wang Chenglei, Dr. Zhao Fuwang, Dr. Wang Zhaokun, Dr. AI Chunhui, Dr. Wang Wei, Dr. Li Ying, Dr. Ma Yuan, Dr. Zhang Hongfu, Dr. Cui Jingyu, Dr. Deng Fuquan, Dr. Cui Jianzhong, Dr. Bi Xiaobo, Peng Si, Piao Jinli, Jiang Qian, Deng Fang, Waikin Yeung, Hou Zhao, Cao Xu, Liu Ze, Zhou Zengcheng. I also extend special appreciation towards the administrative supporting staff of the general office, particularly Ms. Lily Tam, Ms. Merlin Wong, and Ms. Yan Wong, for their support.

Finally, I would like to thank my parents and my beloved spouse, Zhang Liquan, for their love, encouragement, and support. Without their unconditional support, it is impossible for me to go this far.

Table of Contents

Abstract.....	III
List of Publications	IX
Acknowledgements	XIII
Table of Contents	XVI
List of Figures.....	XX
List of Tables	XXIX
List of Symbols	XXIX
Chapter 1 Introduction	1
1.1 Background.....	1
1.2 Research aim and objectives	4
1.3 Organization of the thesis	7
Chapter 2 Literature review	10
2.1 FIV of bluff body.....	10
2.2 Passive control of bluff body	18
2.2.1 FIV control using trailing-edge splitter plate.....	19
2.2.2 FIV control using fins	23
2.2.3 FIV control using biomimetic surfaces.....	25
2.3 Active flow control via oscillatory morphing surface.....	29
Chapter 3 FIV control with an attached splitter plate	33

3.1 Experimental setup and measurements	33
3.2 CFD setup and validation.....	35
3.3 Hydrodynamic forces.....	42
3.4 Flow dynamics	52
3.5 Vibration modes.....	61
3.6 Remarks	63
Chapter 4 FIV control and flow energy harvesting using fins	68
4.1 Experimental setup and measurements	68
4.2 CFD setup and validation.....	70
4.3 System dynamics	73
4.4 Power extraction performance	80
4.5 Remarks	83
Chapter 5 FIV of a cactus-shaped cylinder	87
5.1 Experimental setup and measurements	87
5.2 CFD setup and validation.....	89
5.3 Hydrodynamic performance	92
5.4 Flow dynamics	98
5.5 Remarks	106
Chapter 6 Wake and force control with oscillatory morphing surface	109
6.1 Experimental setup and measurements	109
6.2 Evolution of oscillatory morphing surface.....	113
6.3 Effects on vortex shedding.....	115
6.4 Effects on mean flow field.....	122
6.5 POD analysis.....	128
6.6 Wake and force control using oscillating surface/anti-phase jets	134
6.6.1 CFD setup and validation.....	135
6.6.2 Oscillating surface vs. anti-phase jets.....	141
6.6.3 Effects of Reynolds number.....	147

Table of Contents

6.6.4 Control in three-dimensional space.....	156
6.7 Remarks	162
Chapter 7 Conclusions and future work.....	166
7.1 Conclusions.....	166
7.1.1 FIV control with an attached splitter plate	166
7.1.2 FIV control and flow energy harvesting using fins.....	167
7.1.3 FIV of a cactus-shaped cylinder.....	168
7.1.4 Wake and force control with oscillatory morphing surface	169
7.2 Future work.....	170
References	174

List of Figures

Figure 1.1 Summary of flow control techniques for a bluff body^[1].....4

Figure 1.2 Summary of flow control techniques used in the present report: (a) trailing edge splitter plate^[14], (b) attached fins^[15], (c)&(d) biomimetic surface features treatment^[16,17], (e) oscillatory morphing surface^[18], (f) anti-phase jets^[19].....7

Figure 2.1 Amplitude ($A^* = \frac{1}{4\pi^3} \frac{C_y \sin \varphi}{(m^* + C_A)\zeta} (\frac{U^*}{f^*})^2 f^*$) and frequency response ($f^* = \sqrt{\frac{m^* + C_A}{m^* + C_{EA}}}$) versus reduced velocity U^* (a) at high $m^*\zeta$ ($m^*=320$, $(m^* + C_A)\zeta = 0.251$) and (b) at low $m^*\zeta$ ($m^*= 8.63$, $\zeta = 0.00151$); ● data from ^[2], □ data from ^[3], and ···wake mode map from^[27]. C_A denotes the potential flow added-mass coefficient, and $C_A = 1.0$ for a circular cylinder. C_{EA} is the effective added mass coefficient, and $C_{EA} = \frac{1}{2\pi^3 A^*} (\frac{U^*}{f^*}) C_y \cos \varphi$ 12

Figure 2.2 Force and phase difference versus reduced velocity (a) at high $m^*\zeta$ ($m^*=320$, $(m^* + C_A)\zeta = 0.251$) and (b) at low $m^*\zeta$ ($m^*= 8.63$, $\zeta = 0.00151$)^[2].....13

Figure 2.3 Galloping response of cylinder attached with splitter^[20]: (a) vibration amplitude, (b) frequency, and (c) mean drag coefficient vs. U_r . ◇ normal cylinder, ○ solid plate with $L/D = 1$, △ slotted plate with $L/D = 1$14

Figure 2.4 The sketch drawing of force decomposition of a cylinder.....15

Figure 2.5 Schematic graph of the typical relationship of no-interaction and interaction between VIV and galloping^[4].....17

Figure 2.6 Some commonly used flow control techniques for a bluff body^[1]: (a) spiral wires, (b) segmented trailing edge, (c) wavy trailing edge, (d) wavy stagnation surface, (e) sinusoidal axis, (f) hemispherical bulge, (g,h) tiny tabs.....19

Figure 2.7 Succulent plants with three and four of ribs in nature^[17]: (a) Euphorbia Trigona and (b) Euphorbia Abyssinica.....29

Figure 3.1 (a) Test rig installed in a closed-loop water channel; (b) schematic of the force and displacement measurements.....35

Figure 3.2 Numerical simulation model and boundary condition (a) and calculation mesh (b&c).....38

Figure 3.3 The validation of (a) rms of the oscillation amplitude y_{rms} ; (b) dimensionless frequency f^* of the lift force; (c) mean drag coefficient $\overline{C_d}$ and (d) rms of lift coefficient $C_{l,rms}$41

Figure 3.4 Response comparison of (a) y_{rms} versus U_r and (b) $C_{l,rms}$ versus U_r43

Figure 3.5 (a) y_{rms} and (b) $C_{l,rms}$ of a cylinder attached with a splitter plate vs. U_r46

Figure 3.6 Time-history amplitude curves for selected cases: (a) $L/D = 0$, $U_r = 5.2$, (b) $L/D = 0.125$, $U_r = 7.4$, (c) $L/D = 0.25$, $U_r = 10.6$, (d) $L/D = 0.25$, $U_r = 10.6$, (d) $L/D = 0.5$, $U_r = 23.5$, (e) $L/D = 2.0$, $U_r = 5.6$46

Figure 3.7 Dimensionless frequency f^* of the lift force on the cylinders versus U_r47

Figure 3.8 (a) mean drag coefficient $\overline{C_d}$ vs. U_r ; (b) rms drag coefficient $C_{d,rms}$ vs. U_r49

Figure 3.9 The lift-displacement phase angle φ for a circular cylinder attached with splitters vs. U_r50

Figure 3.10 (a) lift force term synchronizes with structure’s acceleration; (b) energy transmitted from fluid to the FIV system in one period.....51

Figure 3.11 Simulated instant vortex evolution in one oscillation cycle53

Figure 3.12 Simulated instant shear layer variation in one oscillation cycle.....54

Figure 3.13 Simulated instantaneous pressure fields in one vibrating period.....55

Figure 3.14 Calculated time-history of amplitude and lift coefficient for (a) $L/D = 0$, $U_r = 5.2$, (b) $L/D = 0$, $U_r = 10.6$ and (c) power spectral density (PSD) functions of C_l57

Figure 3.15 Calculated time-history of amplitude and lift coefficient for (a) $L/D = 0.125$, $U_r = 7.4$ & (b) $L/D = 0.25$, $U_r = 10.6$ and time-history of U and C_{l_sp} for (c) $L/D = 0.25$, $U_r = 10.6$, (d) $L/D = 0.5$, $U_r = 16.4$, (e) $L/D = 1.0$, $U_r = 16.4$ and (f) PSD of C_l57

Figure 3.16 The time-history of the actual lift coefficient $C_l(t)$ vs. the actual angles of attack $\alpha(t)$: (a) $L/D = 0.25$, $U_r = 10.97$; (b) $L/D = 0.5$, $U_r = 10.97$; (c) $L/D = 0.25$, $U_r = 16.89$; (d) $L/D = 0.5$, $U_r = 16.89$. The data is coming from the experiment, and the results are presented based on several vibration periods.....60

Figure 3.17 (a) Simulated instantaneous vortex patterns and (b) shear layers in an oscillating cycle for the case of $L/D = 0.25$, $U_r = 16.4$61

Figure 3.18 Vibration mode for a cylinder attached with splitter at $m^* = 50$. The legend bar given at the top of the figure denotes the y_{rms} values.....63

Figure 4.1 Sketches of (a) the four cylinders used in the experiments and (b) the test rig. Where the displacement was recorded by a high-speed camera, and the force was measured by a load cell.....70

Figure 4.2 Numerical simulation model and calculation mesh.....72

Figure 4.3 Dynamic response comparison: (a) y_{rms} of the four typical cases, ■ plain-cylinder case, ■ four-fin case, ■ two-windward-fin case, ■ two-leeward-fin case; (b), (c) & (d) y_{rms} , dimensionless frequency f^* and phase angle ϕ of the four-fin case with different α and L/D , ■ $0^\circ-0.25$, ■ $2.5^\circ-0.25$, ■ $5^\circ-0.25$, ■ $8^\circ-0.25$, ■ $0^\circ-0.5$, ■ $2.5^\circ-0.5$, ■ $5^\circ-0.5$, ■ $8^\circ-0.5$75

Figure 4.4 Instantaneous vortex patterns around (a) plain cylinder, $U_r = 5.3$; (b) two-windward-fin cylinder, $U_r = 10.0$; (c) two-leeward-fin cylinder, $U_r = 10.0$; (d) four-fin cylinder, $U_r = 10.0$. $0T/8$, $2T/8$ and $4T/8$ represent the instants when the cylinder is at the highest position, moving downward through the equilibrium position, and at the lowest position, respectively. ω_z^* is the spanwise vorticity normalized by D and U_∞78

Figure 4.5 The instantaneous pressure field at typical cases: (a) plain-cylinder case, $U_r = 5.3$; (b) two-windward-fin case, $U_r = 10.0$; (c) two-leeward-fin case, $U_r = 10.0$; (d) four-fin case, $U_r = 10.0$79

Figure 4.6 Comparison of the y_{rms} of four-fin case at $L/D = 0.5$: ■ rotate the cylinder by 2.5° and ■ rotate the air-bearing systems by 2.5° . Where ■ denotes the y_{rms} of four-fin case at $\alpha = 0^\circ$80

Figure 4.7 (a) variation of the rms voltage output V_{rms} of four-fin case with load resistance R ; (b), (c) & (d) variation of V_{rms} , P_{avg} , and the performance enhancement percentages of P_V for

the four-fin case with different α and L/D . The symbols are identical to Figure 4.3.....83

Figure 5.1 (a) the sketch of the typical tested cases; (b) test rig installed in a closed-loop water channel.....89

Figure 5.2 Numerical simulation model and calculation mesh.....90

Figure 5.3 Comparison of the time-history displacement between experimental and numerical results at $U_r = 6.15$: (a) plain-cylinder case, (b) three-rib case at $\alpha = 60^\circ$ and (c) four-rib case at $\alpha = 0^\circ$92

Figure 5.4 Comparison of root-mean-square values of the vibration amplitude y_{rms} (a & b), lift fluctuation coefficient $C_{l,rms}$ (c & d), and mean drag coefficient $\overline{C_d}$ (e & f) of the three-rib, four-rib and plain cylinders versus U_r95

Figure 5.5 The dimensionless frequency f^* of the oscillation and phase angle φ between the lift force and the transverse displacement: (a&c) three-rib cases and (b&d) four-rib cases.....97

Figure 5.6 (a&c) lift coefficient in phase with body acceleration and (b&d) energy transferred from flow to structure during one vibration cycle for the three-rib and four-rib cases, respectively.....98

Figure 5.7 Instantaneous vortex patterns of selected cases at $U_r = 6.15$: (a) the plain-cylinder case; (b) the three-rib cylinder at $\alpha = 0^\circ$; (c) the three-rib cylinder at $\alpha = 60^\circ$. $t = 0, 2T/8$ and $4T/8$ correspond to the instants when the cylinders are at the lowest location, passing the equilibrium location, and at the highest location, respectively.....100

Figure 5.8 The instantaneous vortex patterns of four-rib cases at $U_r = 6.15$: (a) $\alpha = 0^\circ$; (b) $\alpha = 45^\circ$102

Figure 5.9 The instantaneous vortex patterns of four-rib cases at $U_r = 6.15$ and $\alpha = 0^\circ$: four-rib case with its trailing edge rib length equals (a) 1/2 of other ribs and (b) 3/2 of other ribs.....104

Figure 5.10 The instantaneous pressure field of typical cases at $U_r = 6.15$: (a) plain-cylinder case; (b) three-rib case at $\alpha = 0^\circ$; (c) three-rib case at $\alpha = 60^\circ$; (d) four-rib case at $\alpha = 0^\circ$; (e) four-rib case at $\alpha = 45^\circ$. The corresponding streamlines are represented by the black line and arrows... ..105

Figure 6.1 Schematics of the experimental setup and water tunnel; (b) cross-sections of the experiment model with and without latex membrane wrapped around it as viewed from the top and (c) side-view of the steel cylindrical skeleton with (left) and without (right) ribs.....112

Figure 6.2 Averaged deformation of oscillatory morphing surfaces at different excitation frequencies: (a) oscillatory morphing surface (OMS) cylinder at $f_{osc}^* = 1$; (b) OMS cylinder at $f_{osc}^* = 2$; (c) OMS cylinder at $f_{osc}^* = 4$; (d) OMS cylinder at $f_{osc}^* = 8$. Snapshots of oscillatory morphing surfaces at different instants (t_1 to t_5) over half an excitation cycle for OMS cylinder at $f_{osc}^* = 2$ are given at the bottom position.....114

Figure 6.3 Instantaneous spanwise vorticity ω_z^* for the (a) RC cylinder, (b) SS cylinder, (c) OMS cylinder at $f_{osc}^* = 1$, (d) OMS cylinder at $f_{osc}^* = 2$, (e) OMS cylinder at $f_{osc}^* = 4$ and (f) OMS cylinder at $f_{osc}^* = 8$, where (i) $t = 0$, (ii) $t = T/6$, (iii) $t = T/3$, (iv) $t = T/2$, (v) $2T/3$ and (vi) $5T/6$ are the different periods in one vortex shedding cycle.....117

Figure 6.3 (continued).....118

Figure 6.4 Schematics of the vortex street for the (a) RC cylinder, (b) SS cylinder, (c) OMS cylinder at $f_{osc}^* = 2$ and (d) OMS cylinder at $f_{osc}^* = 8$. The red arrow denotes the oscillating of the morphing surface.....120

Figure 6.5 Power-spectral-density (PSD) analysis for the cross-stream velocities v at point A ($x^* = 1.0, y^* = 0.5$) and point B ($x^* = 1.5, y^* = 0.5$): (a) RC cylinder; (b) SS cylinder; (c) OMS cylinder at $f_{osc}^* = 1$; (d) OMS cylinder at $f_{osc}^* = 2$; (e) OMS cylinder at $f_{osc}^* = 4$; (f) OMS cylinder at $f_{osc}^* = 8$122

Figure 6.6 Variations of mean velocity fields in streamwise direction (\bar{u}/U_∞) and cross-stream direction (\bar{v}/U_∞) around the cylinders with different perturbations: (a1 & a2) RC cylinder; (b1 & b2) SS cylinder; (c1 & c2) OMS cylinder at $f_{osc}^* = 1$; (d1 & d2) OMS cylinder at $f_{osc}^* = 2$; (e1 & e2) OMS cylinder at $f_{osc}^* = 4$; (f1 & f2) OMS cylinder at $f_{osc}^* = 8$124

Figure 6.7 Distribution of mean vorticity $\overline{\omega_z^*}$ in the near wake of cylinders with different perturbations: (a) RC cylinder; (b) SS cylinder; (c) OMS cylinder at $f_{osc}^* = 1$; (d) OMS cylinder at $f_{osc}^* = 2$; (e) OMS cylinder at $f_{osc}^* = 4$; (f) OMS cylinder at $f_{osc}^* = 8$. The local maximum vorticity of the cylinders with different frequency excitations are compared in (g).....125

Figure 6.8 Distributions of (a) time-averaged streamwise velocities \bar{u}/U_∞ ; (b) streamwise fluctuating velocity u_{rms}/U_∞ , and (c) cross-stream fluctuating velocity v_{rms}/U_∞ in the centerline of cylinders ($y^* = 0$).127

Figure 6.9 Distributions of (a) streamwise fluctuating velocity u_{rms}/U_∞ and (b) cross-stream fluctuating velocity v_{rms}/U_∞ along the lines of $x^* = 1, 2, 3$ and 4. The comparison is between the RC cylinder and OMS cylinder at $f^*_{osc} = 2$127

Figure 6.10 Distributions of Reynolds shear stress R_{uv} in the near wake of the (a) RC cylinder, and (b) OMS cylinder at $f^*_{osc} = 2$. The local maximum value of R_{uv} is marked in the figure.....128

Figure 6.11 (a) coefficient correlations for RC cylinder; (b) POD eigenvalue spectrums for the RC cylinder, SS cylinder, and OMS cylinder at $f^*_{osc} = 2$; (c) mode 1 and (d) mode 2 distributions for the RC cylinder.....130

Figure 6.12 The ω_z^* contours and velocity vectors of POD modes 1-4 for the selected cases: (a) RC cylinder; (b) SS cylinder; (c) OMS cylinder at $f^*_{osc} = 2$. The range of ω_z^* for modes 1-2 is -0.4 to 0.4, and the range of ω_z^* for modes 3-4 is -0.1 to 0.1. To better show the vortex structures, the vector scale used in modes 3-4 is different from that used in modes 1-2.....131

Figure 6.13 Phase-averaged results for the (a) RC cylinder, (b) SS cylinder and (c) OMS cylinder at $f^*_{osc} = 2$, where (i) $t = 0$, (ii) $t = \pi/3$, (iii) $t = 2\pi/3$, (iv) $t = \pi$, (v) $t = 4\pi/3$, and (vi) $t = 5\pi/3$ are the different phases of the wake behavior.....133

Figure 6.14 Numerical framework setting adopted in Rabault et al.^[182] and Ren et al.^[19]'s study: (a) boundary conditions and DRL sensors location; (b) the arrangement of the pair of anti-phase jets. Note that, the oncoming flow conditions are in a parabolic distribution in the channel flow, while the jet distribution is in a sinusoidal profile.....137

Figure 6.15 Numerical framework and calculation mesh: (a) computational domain and boundary conditions; (b) the setting of a oscillating surface and a pair of anti-phase jets; (c) the

computation mesh and (d) its local details around a circular cylinder its local details around a circular cylinder for both the oscillating surface and a pair of anti-phase jets setting..... 139

Figure 6.16 Calculation mesh and time-step independent validation: (a)&(b) comparison of time-history drag coefficient C_d and lift coefficient C_l at three different densities of meshes; (c)&(d) comparison of time-history drag coefficient C_d and lift coefficient C_l at three different time-steps based on the medium mesh..... 140

Figure 6.17 Time-history curve for the drag and lift coefficients obtained from several vortex shedding cycles when the calculation reaches their steady state: (a)&(b) C_d & C_l for the uncontrolled case; (c)&(d) C_d & C_l for the pair of anti-phase jets control case, where $v^* = 2$, and $f_e^* = 0.93$; (e)&(f) C_d & C_l for the oscillating surface control case, where the maximum displacement of the oscillating surface in the cavity is $0.21D$ and its perturbation frequency f_e^* is 0.93 143

Figure 6.18 The normalized vertical velocity v^* monitored at point P caused by the oscillating surface. The location of point P is the blue point in Figure 6.15(b)..... 144

Figure 6.19 Instantaneous vortex patterns around the cylinder for (a) the uncontrolled case, (b) the anti-phase jets control case, where $v^* = 2$, and $f_e^* = 0.93$, and (c) the oscillating surface control case, where the maximum displacement of the oscillating surface in the cavity is $0.21D$ and its perturbation frequency f_e^* is 0.93 . $0T/8$, $2T/8$, and $4T/8$ represent the instants when C_l at the largest positive value, zero, and the largest negative value, respectively..... 145

Figure 6.20 Instantaneous pressure field for (a) the uncontrolled case, (b) the anti-phase jets control case, where $v^* = 2$, and $f_e^* = 0.93$, and (c) the oscillating surface control case, where

the maximum displacement of the oscillating surface in the cavity is $0.21D$ and its perturbation frequency f_e^* is 0.93.....146

Figure 6.21 Instantaneous vortex patterns around the cylinder at $Re = 100$ for the uncontrolled case (a), and the anti-phase jets control cases: (b) $v^* = 0.1, f_e^* = 0.961$; (c) $v^* = 2, f_e^* = 0.95$; (d) $v^* = 2, f_e^* = 0.93$150

Figure 6.22 Instantaneous pressure field around the cylinder at $Re = 100$ for the uncontrolled case (a), and the anti-phase jets control cases: (b) $v^* = 0.1, f_e^* = 0.961$; (c) $v^* = 2, f_e^* = 0.95$; (d) $v^* = 2, f_e^* = 0.93$151

Figure 6.23 Instantaneous vortex patterns around the cylinder at $Re = 400$ for the uncontrolled case (a), and the anti-phase jets control cases: (b) $v^* = 0.1, f_e^* = 0.961$; (c) $v^* = 2, f_e^* = 0.95$; (d) $v^* = 2, f_e^* = 0.93$152

Figure 6.24 Instantaneous pressure field around the cylinder at $Re = 400$ for the uncontrolled case (a), and the anti-phase jets control cases: (b) $v^* = 0.1, f_e^* = 0.961$; (c) $v^* = 2, f_e^* = 0.95$; (d) $v^* = 2, f_e^* = 0.93$153

Figure 6.25 Instantaneous vortex patterns around the cylinder at $Re = 1,000$ for the anti-phase jets control cases: (a) $v^* = 0.1, f_e^* = 0.961$; (b) $v^* = 2, f_e^* = 0.95$154

Figure 6.26 Instantaneous pressure field around the cylinder at $Re = 1,000$ for the anti-phase jets control cases: (a) $v^* = 0.1, f_e^* = 0.961$; (b) $v^* = 2, f_e^* = 0.95$155

Figure 6.27 Three-dimensional numerical simulation model (a) and calculation mesh (b).....156

Figure 6.28 Time-history curve for the drag and lift coefficients: (a)&(b) C_d & C_l for the uncontrolled case; (c)&(d) C_d & C_l for the pair of anti-phase jets control case, where $v^* = 2$, and $f_e^* = 1.24$. Here, only several vortex-shedding cycles are presented for the controlled case due to its good periodical performance.....158

Figure 6.29 Instantaneous vortex patterns at the mid-span of the cylinder when $Re = 1,000$: (a) uncontrolled case and (b) controlled case.....160

Figure 6.30 Instantaneous pressure field at the mid-span of the cylinder when $Re = 1,000$: (a) uncontrolled case and (b) controlled case.....161

Figure 6.31 Iso-surface of the instantaneous normalized Q^* ($= 2$) of the (a) uncontrolled case and (b) controlled case.....162

List of Tables

Table 2.1 Summary of a FIV circular cylinder with solid splitters.	22
Table 3.1 Comparison of the current simulation results with references at $Re = 100$	39
Table 3.2 Comparison of the responses for a FIV cylinder based on three meshes at $Re = 2,200$	40
Table 3.3 Time step independence validation results based on Mesh_2.....	40
Table 3.4 Displacement comparison between experiment and numerical results in typical cases.....	42
Table 4.1 Summary of test cases.....	70
Table 4.2 Simulated results of a circular cylinder with three different densities of meshes.....	72
Table 4.3 Time step independence validation results based on Mesh 2.....	72
Table 4.4 Displacement comparison between experimental and numerical results at typical cases.....	72
Table 5.1 Experimental cases.....	89
Table 5.2 Simulated results of a circular cylinder with four different densities of meshes.....	91
Table 5.3 Time step independence validation results based on Mesh 3.....	91

Table 5.4 Displacement comparison between experimental and numerical results at typical cases.....92

Table 5.5 The ratio of mean displacement \bar{y} and lift coefficient \bar{C}_l over its corresponding RMS value.....105

Table 6.1 Comparison of the numerical results with and without control at $Re = 3,200$..135

Table 6.2 Comparison of the present numerical results with Ren et al.^[19]'s data.....141

Table 6.3 Summary of test cases for three different Re148

List of Symbols

α	angle of attack
AR	aspect ratio
C_A	potential flow added-mass coefficient
C_d	drag coefficient
C_{EA}	effective added mass coefficient
$\overline{C_d}$	mean drag coefficient
$C_{d,rms}$	root-mean-square of drag coefficient
C_{DcM}	distortion effects
$\overline{C_{dc}}$	corrected drag coefficient
C_l	lift coefficient
$\overline{C_l}$	mean lift coefficient
$C_{l,rms}$	root-mean-square of lift coefficient
$C_{l,sp}$	lift coefficient on the splitter
C_P	pressure coefficient
C_{pb}	base pressure coefficient

$C_l(t)$	instantaneous lift coefficient
C_{total}	total lift force
C_{vortex}	vortex force
d	rod diameter
D	diameter of the cylinder
E	energy transmitted from fluid to a vibrating system
f^*	dimensionless frequency
f_e^*	dimensionless perturbation frequency
f_{osc}^*	dimensionless oscillating surface frequency
f_n	structure's natural frequency
f_v	vortex shedding frequency
F_x	forces acting in the x directions
F_y	forces acting in the y directions
H	span of the cylinder
k	elastic coefficient of the system
K_s	height of the cactus rib
l_c	depth of the cavity
l_{jet}	length of the jet

L	splitter/fin length
L_f	vortex formation length
m	mass
m^*	mass ratio
n	number of ribs
N	numerical mesh count
P_{avg}	mean output power
P_d	output power density
R	load resistance
Re	Reynolds number
Sc	Scruton number
St	Strouhal number
t	time
T	vortex shedding cycle
U_g	critical speed for galloping
u_{rms}	fluctuating velocity in streamwise direction
\bar{u}	time-averaged streamwise velocity
U_r	reduced velocity

U_∞	oncoming flow speed
U_y	velocity in y direction
U_a	vector sum of U_∞ and U_y
\bar{v}	time-averaged cross-stream velocity
v_{jet}	the maximum velocity of jet
v^*	normalized jet strength
V_P	volume of the piezoelectric sheets
V_{rms}	rms value of output voltage
W	width of the splitter
y	oscillation amplitude
\dot{y}_t	velocity of the system at time t
\ddot{y}_t	acceleration of the system at time t
\bar{y}	mean oscillation amplitude
y_{rms}	root-mean-square of the oscillation displacement
y^+	grid dimensionless distance from the cylinder
ζ	damping parameter
ζ_s	damping in water
θ	circumferential angle

ρ	fluid density
ν	viscosity of the water
ω_z^*	spanwise vorticity
$\overline{\omega_z^*}$	mean spanwise vorticity
φ	phase difference
φ_{total}	total phase difference
φ_{vortex}	vortex phase difference
Δt	time step
λ_1, λ_2	eigenvalues for the 1st and 2nd order modes
ε_M	empirical blockage factor
ΔC_{DM}	additive correction to drag
β	line slope

Chapter 1 Introduction

1.1 Background

A bluff body is a solid object, often with a broad, flat front, that obstructs the flow of a fluid, such as air or water, causing the fluid to separate and form a wake behind the object. Bluff bodies, such as buildings, bridges, and marine constructions, are frequently encountered in our daily lives. Normally, flow pass these bluff bodies may lead to multiple flow phenomena, such as vortex shedding, flow separation, and flow-induced vibration (FIV)^[1-7]. These complicated flow phenomena may cause structure fatigue or even damage broken. The reason is that when the vortex shedding frequency approaches the structure's natural frequency, resonance will occur and may harm the stability and safety of the structures. Famous examples include the broken Tacoma Narrows Bridge in the US in 1940, and the cooling towers at Ferrybridge Power Station in the UK collapsed in 1966. More recently, the apparent vibration of the Humen Bridge in Guangzhou and the SEG Building in Shenzhen has captured much attention, suggesting the importance of understanding these phenomena and their controls. Those typical fluid-structure interactions (FSI) problems remind us of the importance of controlling the flow, aerodynamics, or FIV of the bluff bodies. As such, those bluff bodies can perform stably and reliably under extreme conditions, which will help save the costs and protect the safety of people's lives and property.

Owing to its importance in protecting the safety of structures and saving the costs, various technologies have been applied to control the flow of the bluff bodies^[1, 8, 9]. Those technologies can be mainly divided into passive control (a method of controlling a system using only the

energy available in the system itself, without the need for external power sources), including surface modifications by a spiral wire, splitter plate, and attached fins et al., and active control (a method involves the utilize of external energy sources to influence the behavior of the system), including blowing/suction, oscillatory morphing surface, and synthetic jets et al. Surface modification is one of the widely used measures to control the aerodynamic force and FIV of the bluff bodies. It has been successfully used for numerous engineering applications due to its comparative efficiency and ease of implementation. In comparison, the active control method needs external energy input, but it has advantages over passive control in controllability and adaptivity to adjust its behavior during dynamic loads^[10]. In feedback control systems, active control schemes are categorized into active open control and active closed control, as illustrated in Figure 1.1. Additionally, flow control can be segmented into two-dimensional (2D) and three-dimensional (3D) forcing control. In 3D forcing, the force exerted on the bluff body can vary along the spanwise direction. Another method of classification is boundary-layer control versus direct-wake control. Boundary-layer control influences flow characteristics within the boundary layer, while direct-wake control targets flow characteristics directly in the wake region (see Figure 1.1).

Passive control technologies have been extensively applied to control the flow and forces of a bluff body due to their easy implementation, stable performance, and not need extra energy input^[9], including surface modifications, splitter plate, attached fins, biomimetic surface features treatment, superhydrophobic coating, small secondary control cylinder, etc. In comparison, active control requires additional energy input but offers advantages such as real-time adjustments to flow conditions and precise manipulation targeting specific flow regions^[11].

Commonly used active control methods include synthetic jets, plasma actuators, oscillating walls, vortex generators, etc.

Another perspective of flow control on a bluff body is to enhance its aerodynamic performance for energy harvesting applications^[12]. Three types of FIV are usually utilized for flow-energy harvesting, including vortex-induced vibration (VIV), galloping, and flutter. To improve the performance of FIV based flow-energy harvesters, many effective methods have been applied, such as fin attachment, wave surface treatment, bio-inspired designs, harmonic excitation, etc^[13].

Although many scholars are dedicated to investigating the flow control of bluff bodies, some unsolved issues still need to be addressed. For example, passive control of FIV of bluff bodies with high mass ratios has seldom been studied. In addition, many thought-provoking shape optimizations are inspired by biological areas, including sharks, seashells, and cacti. The implementation of nature-inspired shapes like cactus structures can be a novel approach for the control. Besides, the active control of a nature-inspired cacti cylinder with oscillatory morphing surfaces and the effect of excitation frequency has not been studied. The effectiveness of the oscillatory morphing surface on drag reduction is unknown. On the other hand, with the rapid depletion of fossil fuel resources and increasing carbon emissions, there is a pressing need for clean, sustainable energy to address these issues. Energy harvesting based on those types of modified bluff bodies is also a critical issue to address. These research gaps motivated us to conduct the present research. Note that, a two-dimensional (2D) circular or square cylinder is the most typical case of the bluff body. Therefore, the flow control methodology in this thesis is mainly demonstrated based on a 2D circular cylinder. Detailed motivation and background information can be found in Chapter 2.

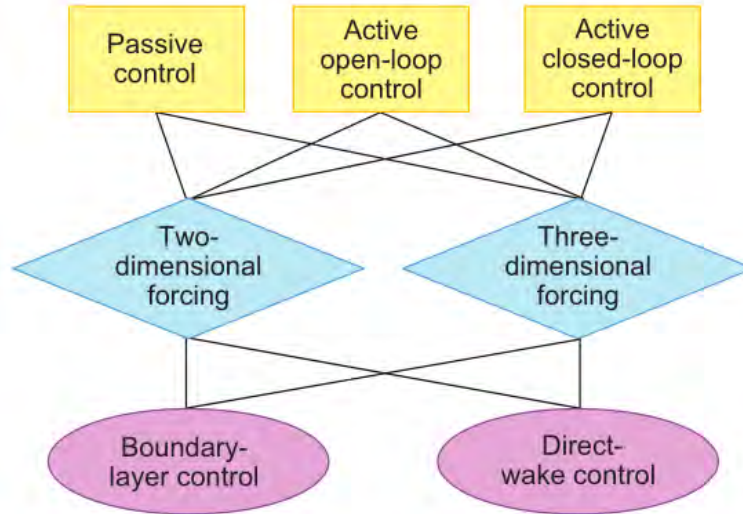


Figure 1.1 Summary of flow control techniques for a bluff body^[1].

1.2 Research aim and objectives

This PhD research aims to explore important issues for passive and active flow control of bluff bodies, including trailing edge splitter plate, attached fins, biomimetic surface features treatment, and active control with the oscillatory morphing surface and its variants (i.e., oscillating surface and anti-phase jets), the corresponding control methods are shown in the Figure 1.2. More specifically, the following objectives will be achieved:

- a. For FIV control using a trailing edge splitter plate, we plan to design an appropriate experimental setup to conduct tests. This setup will simultaneously measure the model's oscillation displacement, hydrodynamic forces (including lift, drag, and torque), and the corresponding flow field information. The relationship between cylinder's vibration displacement, length of the splitter plates, and oncoming flow speed will be systematically investigated. Different vibration modes, hydrodynamic performance, and the interactions between the cylinder and splitter plate will be

thoroughly explored. Due to challenges associated with measuring the flow field for a vibrating cylinder at high Re using PIV, we will build a numerical simulation framework. This will provide additional insights into the experimental observations, particularly in terms of providing the pressure fields and high-resolution vortex evolution process in the near wake of bluff bodies.

- b. For FIV control using attached fins treatment, a circular cylinder attached by rigid fins will be investigated to study its effects on the resulting FIV. Necessary modifications will be made to the experimental setup to measure the energy harvesting performance. The effect of fins' length, flow speed, and angles of attack on the four-fin case will be studied in detail. The energy harvesting performance of the proposed configurations will be compared, and ultimately, we will propose a new concept of a flow energy harvester that can harvest energy from opposite directions and is robust to flow disturbance.
- c. Motivated by the succulents of *Euphorbia Trigona* and *Euphorbia Abyssinica*, we will examine the FIV control effect by adopting biomimetic surface features to assess the feasibility and effectiveness of a succulent-inspired cylinder with three or four ribs. The effect of angles of attack on its FIV and hydrodynamic performance will also be checked. CFD simulations will be used to reveal the underlying physics. Then, based on the experiment results, provide new guidelines for passive FIV control.
- d. Inspired by the cacti structures, a cylinder covered by a flexible latex membrane will be tested to investigate the effects of cylindrical surface oscillations on wake flow based on a 12 V-shaped cacti cylinder. We will build a suitable experimental setup for conducting the active flow control experimental setup and measuring the flow field.

The effects of excitation frequency of the morphing surface will also be investigated to test its control effect. More importantly, the underlying physics will be uncovered, and some interesting models will be given.

- e. To further explore the feasibility of using morphing surface for drag reduction, oscillating surface and anti-phase jets, serving as the variants of the oscillatory morphing surface, will be used to control the flow and hydrodynamic performance of a two-dimensional and three-dimensional cylinder. The effects of Re , control strategies, and dimensions will be investigated in detail to reveal the underlying control mechanisms.

This study aims to address several important issues in passive and active flow control of bluff bodies. These issues are related to the use of trailing-edge splitter plate, attached fins, biomimetic surface, and oscillatory morphing surface and its variants. Both experimental and computational methods were adopted. The experiments were mainly conducted in a water tunnel, with kinematics measurements using high-speed cameras, hydrodynamic force measurements using load cells, and flow field measurements using a time-resolved particle image velocimetry (TR-PIV) system. The computations were conducted using CFD simulations to provide more detailed information supplementing the experimental measurements and also to explore the flow control performance in a much larger parameter space.

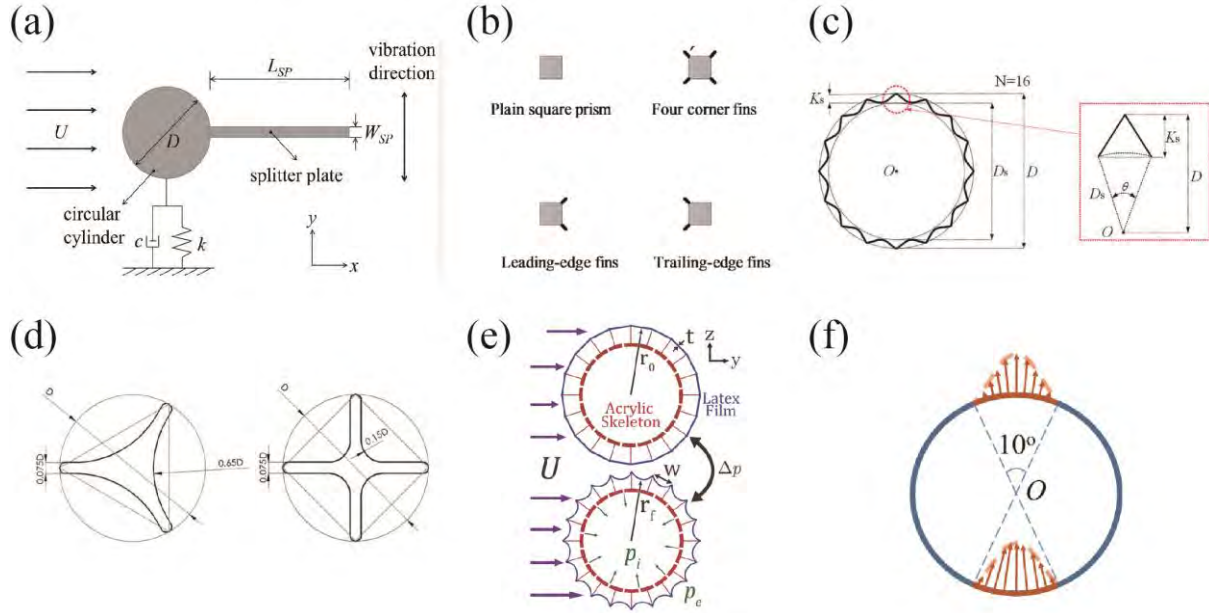


Figure 1.2 Summary of flow control techniques used in the present report: (a) trailing edge splitter plate^[14], (b) attached fins^[15], (c)&(d) biomimetic surface features treatment^[16, 17], (e) oscillatory morphing surface^[18], (f) anti-phase jets^[19].

1.3 Organization of the thesis

There are seven Chapters in this thesis.

A detailed literature review will be given in Chapter 2, including FIV of bluff bodies, and passive and active flow control schemes. Note that, different technologies applied in this thesis will be introduced separately for ease of introduction, and then the research status, research gaps, and novelty of each part of the studies will be presented.

In Chapter 3, we will discuss the FIV control of a cylinder with a trailing edge splitter plate. The effects of the length of splitters and oncoming flow speed on cylinder's oscillation displacement, hydrodynamic performance, and flow structure behavior are examined. Some CFD results are also given to reveal the underlying physics.

The FIV control of a cylinder attached by fins will be addressed in Chapter 4. The effect of fins' length, flow speed, and angles of attack of the four-fin case on the resulting FIV behavior and energy harvesting capability are investigated. The associated rich physics and FIV control mechanisms will be revealed. Besides, a new concept of flow energy harvesting from opposite directions will be proposed.

In Chapter 5, we will investigate the FIV control of bluff bodies with biomimetic surface features, i.e., a nature-inspired cylinder with three or four ribs. The effects of angles of attack and flow speed on the vibration behavior, hydrodynamic performance, and the associated flow structures are compared. The control mechanisms will be revealed based on CFD results and the potential application will be discussed.

In Chapter 6, the active flow control of a cactus-based cylinder covered with a flexible latex membrane will be addressed. The effects of excitation frequency on the cylindrical surface oscillations will be checked. The impacts of cylindrical surface oscillations on the flow fields, wake structures and vortex shedding behavior will be discussed in detail. To further explore the feasibility of using morphing surface for drag reduction, we will discuss the control effects of the variants of the morphing surface, that is, oscillating surface and anti-phase jets on a two-dimensional and three-dimensional cylinder. The control effects achieved by the oscillating surface and anti-phase jets will be compared in detail. The effects of the Reynolds number will also be discussed based on the two-dimensional simulations. Furthermore, a three-dimensional simulation will be implemented to ascertain the effectiveness of the morphing surface drag reduction control at high Re , particularly when the three-dimensional flow effect emerges.

A brief summary of conclusions and future work will be presented in Chapter 7.

Chapter 2 Literature review

This chapter introduces a detailed literature review of the FIV of bluff bodies and the associated passive and active flow control technologies. Some underlying physics related to the controls revealed/discussed in literature are also simply introduced. Specifically, the classical and state-of-the-art technologies utilized in the present thesis, including trailing edge splitter plate, fins-attached treatment, biomimetic surface modifications, oscillatory morphing surface and its variants, will be introduced to reveal their research gaps.

2.1 FIV of bluff body

The phenomenon of fluid flow over a bluff body is usually encountered, which is related to the process in which fluid flows over an obstacle, either natural or man-made^[1]. This complex flow behavior has drawn significant attention from researchers due to its theoretical importance in fluid mechanics and practical applications in engineering. The fluid-structure interaction (FSI) of a bluff body exposed to a cross-flow has become a focal point of study, as it involves the interaction between the motion of the fluid and the structure of the body and dramatically impacts the system's performance and stability.

A two-dimensional circular cylinder is the simplest and one of most representative bluff bodies. Two types of FIV for a circular cylinder are usually encountered, i.e., vortex-induced vibration (VIV) and galloping. VIV usually presents noticeable oscillation displacement primarily in the resonance region, coupled with a lock-in phenomenon where the vortex-shedding frequency (f_v) approximates the structure's natural frequency (f_n)^[2, 20-23], as shown in Figure 2.1. Clearly, the performance of a cylinder under VIV is shown to be intricately

dependent on the value of the mass-damping parameter $m^*\zeta$, which is composed of two factors, the ratio of structural mass to displaced fluid mass ($m^* = 4m/\pi\rho D^2L$, where ρ , D and L are the fluid density, diameter and length of the cylinder) and the structural damping (ζ).

For the high $m^*\zeta$ type, it is apparent that there are two vibration branches, that is, the “initial” and “lower” branches (see Figure 2.1a). The criterion to distinguish the “initial” and “lower” branches is determined by the total phase difference (φ_{total}) between the total lift force (C_{total}) and the oscillation amplitude (y) and vortex phase difference (φ_{vortex}) between the vortex force (C_{vortex}) and y . For example, a transition of the “initial” to “lower” branches is marked by φ_{vortex} and φ_{total} simultaneously presents a large jump^[2], as shown in Figure 2.2(a). Different from the high $m^*\zeta$ type, the low $m^*\zeta$ type is characterized by an additional “upper” branch exhibiting a higher-amplitude response, which occurs between the “initial” and “lower” components (see Figure 2.1b). Furthermore, the transition of the “initial” to “upper” branches is accompanied by the phase shift of φ_{vortex} , while the change from the “upper” to “lower” branches is related to the phase shift of φ_{total} , as shown in Figure 2.2(b). Similar observations are also reported by ^[24-26].

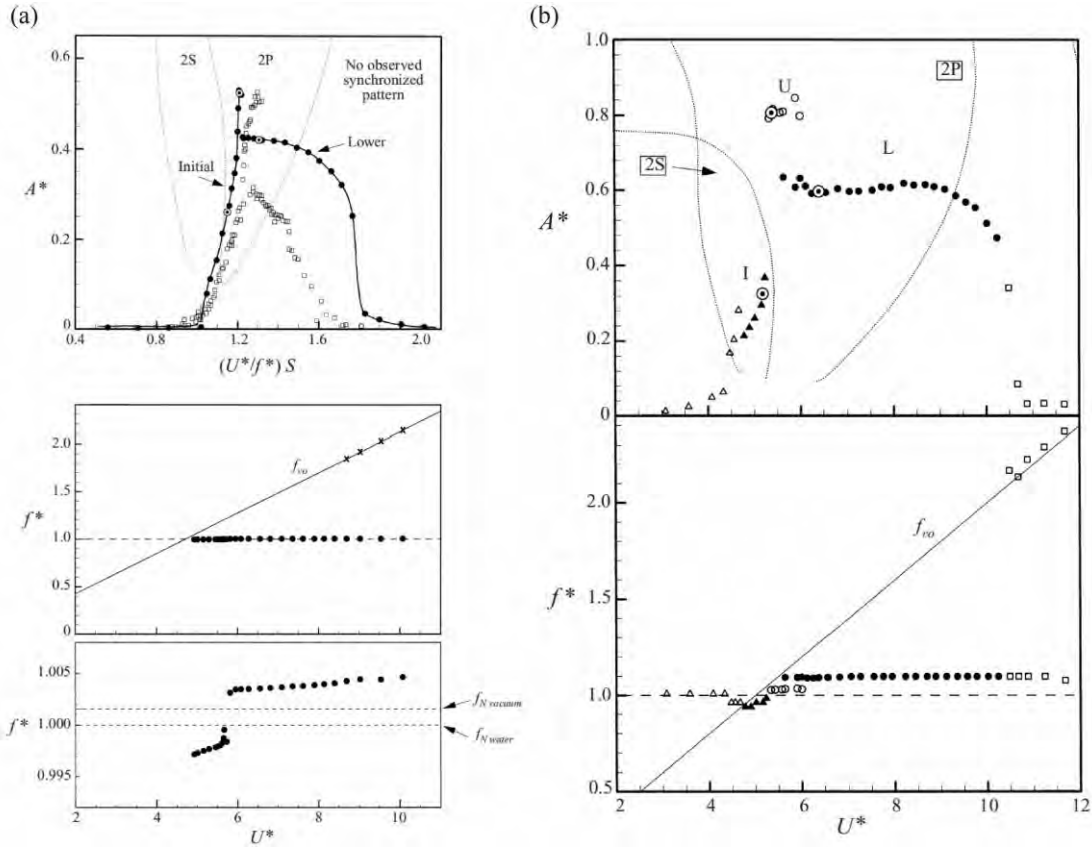


Figure 2.1 Amplitude ($A^* = \frac{1}{4\pi^3} \frac{C_y \sin \varphi}{(m^* + C_A)\zeta} \left(\frac{U^*}{f^*}\right)^2 f^*$) and frequency response ($f^* = \sqrt{\frac{m^* + C_A}{m^* + C_{EA}}}$) versus

reduced velocity U^* (a) at high $m^*\zeta$ ($m^*=320$, $(m^* + C_A)\zeta = 0.251$) and (b) at low $m^*\zeta$ ($m^*= 8.63$, $\zeta = 0.00151$); ● data from [2], □ data from [3], and ···wake mode map from [27]. C_A denotes the potential flow added-mass coefficient, and $C_A = 1.0$ for a circular cylinder. C_{EA} is the effective added mass coefficient, and

$$C_{EA} = \frac{1}{2\pi^3 A^*} \left(\frac{U^*}{f^*}\right) C_y \cos \varphi.$$

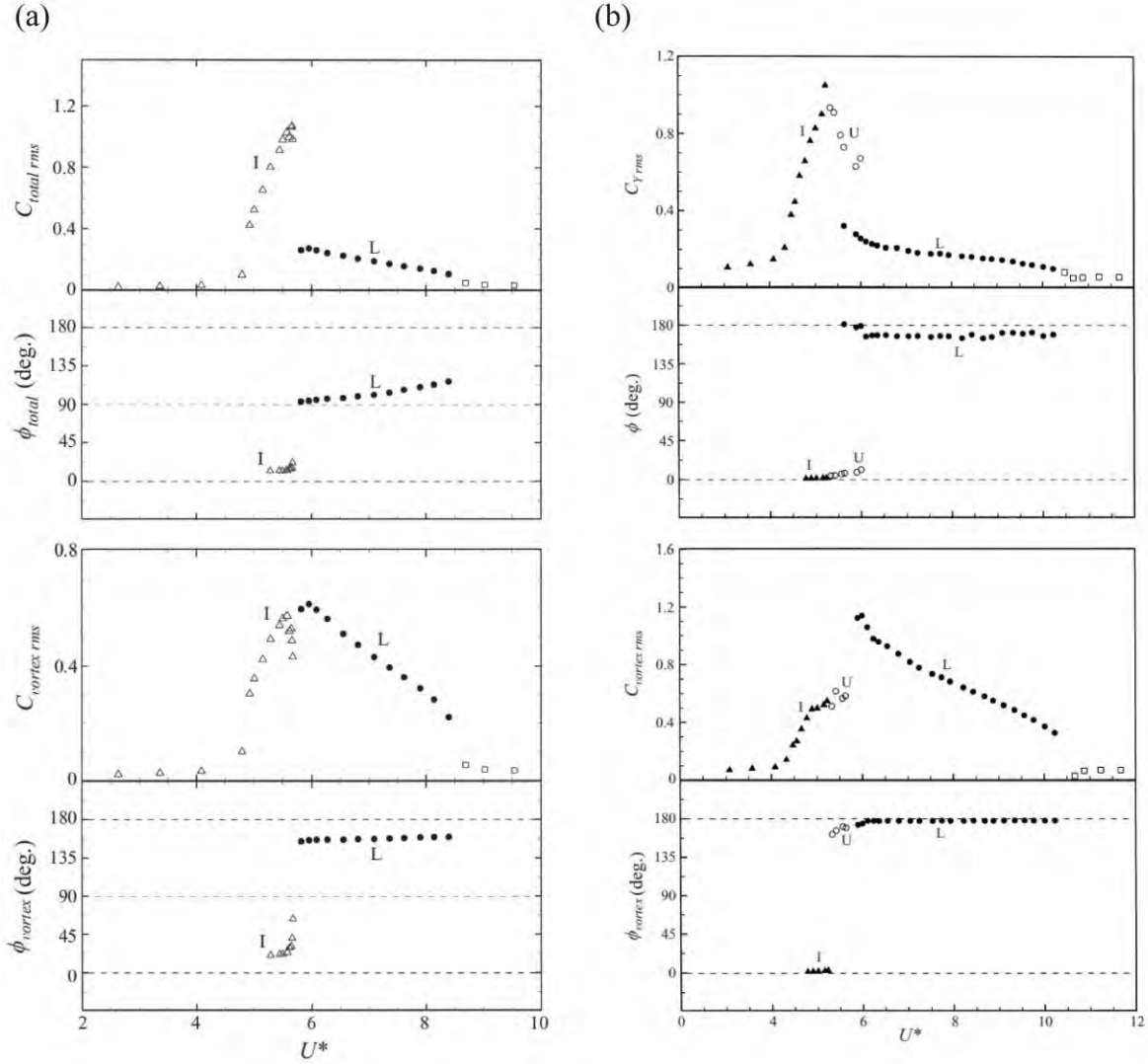


Figure 2.2 Force and phase difference versus reduced velocity (a) at high $m^*\zeta$ ($m^*=320$, $(m^*+C_A)\zeta=0.251$) and (b) at low $m^*\zeta$ ($m^*=8.63$, $\zeta=0.00151$)^[2].

In contrast, galloping sustains significant vibration amplitude once the wind speed surpasses a specific threshold, and the amplitude continues to increase with the increase in wind speed (see Figure 2.3). Besides, the occurrence of galloping is usually linked to the absence of a sharp phase difference ϕ jump or a shift in the phase angle from around 180° to around 0° ; meanwhile, the corresponding vibration frequencies are smaller than the structure's natural frequency^[4, 23, 28-30], as shown in Figure 2.3(b).

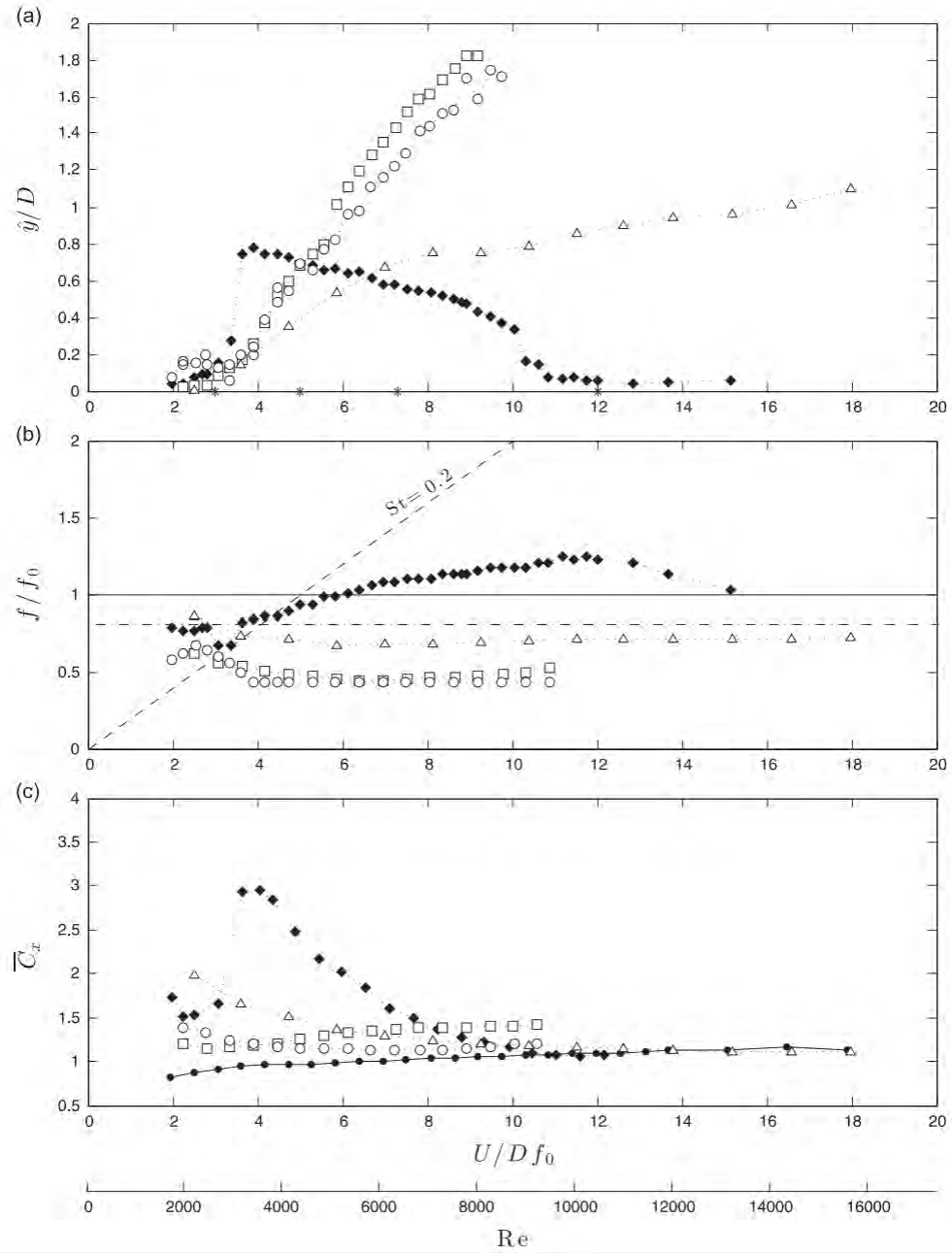


Figure 2.3 Galloping response of cylinder attached with splitter^[20]: (a) vibration amplitude, (b) frequency, and (c) mean drag coefficient vs. U . \diamond normal cylinder, \circ solid plate with $L/D = 1$, \triangle slotted plate with

$$L/D = 1.$$

It is possible to differentiate VIV and galloping by observing the changes in amplitude, frequency, and phase angle. More intrinsically, we can follow the Glauert-Den Hartog criterion

to distinguish the VIV and galloping. Readers can find more detailed information from Den Hartog^[31], Van Oudheusden^[32], and Mannini et al.^[4]. The analysis of the galloping response of a one-degree-of-freedom system is typically grounded on the quasi-static dynamics^[33, 34]. The sketch drawing of force decomposition of a cylinder is demonstrated in Figure 2.4, where the forces acting in the x and y directions are denoted by F_x and F_y , respectively, and α is the real angle of attack (AOA). U_α represents the vector sum of U_∞ and U_y . Thus, the actual lift force F_T can be assessed as it is perpendicular to U_α . And the actual drag F_D is in phase or out of phase with the U_α . As such, the instantaneous AOA $\alpha(t)$ and instantaneous lift coefficient $C_T(t)$ can be calculated as follows:

$$\alpha(t) = \tan^{-1} \frac{U_y(t)}{U_\infty} \quad (2-1)$$

$$C_T(t) = \sin \alpha(t) \frac{2F_x(t)}{\rho U^2 DL} + \cos \alpha(t) \frac{2F_y(t)}{\rho U^2 DL} \quad (2-2)$$

When AOA = 0, the occurrence of the galloping can be judged by the slope (β) of $C_T(t)$ and

$$\alpha(t), \text{ i.e., } \beta = \left. \frac{\partial C_T(t)}{\partial \alpha} \right|_{\alpha=0}.$$

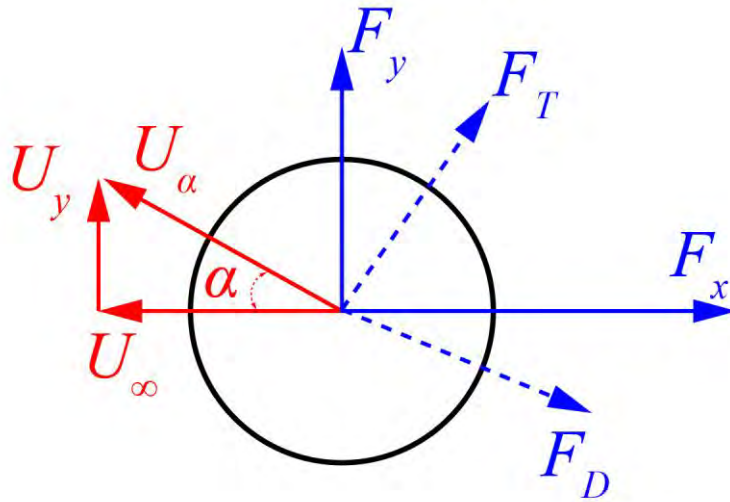


Figure 2.4 The sketch drawing of force decomposition of a cylinder.

An alternative approach to distinguish the occurrence of galloping is from an energy perspective, i.e., if the energy transmitted to a vibrating bluff body is larger than its dissipated energy, then galloping occurs^[35]. However, the happening of VIV and galloping are not always completely independent, and a hybrid type of vibration comprising both VIV and galloping has also been reported in the literature^[4, 36]. Figure 2.5 provides a schematic representation of the typical behavior of a bluff body exposed to VIV at smaller reduced velocity $U_r = U_\infty/f_n D$ (where U_∞ denotes the oncoming flow speed, while D represents the diameter of the model) and galloping at higher U_r . Here, U_g indicates the critical speed for galloping as predicted by quasi-steady theory:

$$U_g = \frac{2Sc}{a_g} f_n D \quad (2-3)$$

where Sc is the Scruton number^[37], and a_g is a parameter to describe the stability of galloping. The corresponding definitions are as follows:

$$Sc = \frac{4\pi m\zeta}{\rho D^2} \quad (2-4)$$

$$a_g = -\frac{dC_l}{d\alpha}(0) - C_d(0) \quad (2-5)$$

where C_d and C_l represent the drag and lift coefficients, and α denotes the angle of attack. The critical speed U_r for VIV is as follows:

$$U_r = \frac{f_n D}{St} \quad (2-6)$$

where $St (= f_n D/U_\infty)$ is the Strouhal number^[38]. By combination of equations (2-3) and (2-6), we can get the following equation:

$$\frac{U_g}{U_r} = \frac{2St}{a_g} Sc \quad (2-7)$$

It is clearly shown that U_g/U_r is influenced by parameters such as Sc , St and a_g , and a larger Sc will result in a higher U_g , as indicated in Figure 2.5. The co-existence of VIV and galloping can be classified as “no interaction” if these two phenomena occur independently of each other, as represented by cases a_1 and a_2 . In some cases, a “quenching” effect has been observed, such as in case b_1 , whereby the response occurs at a speed below the vortex resonance velocity^[39-42]. If galloping begins within the range of VIV, the resultant form of vibration is termed “full interaction” or “VIV-galloping instability”, as shown in cases b_2 and b_3 . In contrast, when the onset of galloping occurs between U_r (onset speed of VIV) and U_g (onset speed of galloping based on quasi-steady theory), it is known as a ‘partial interaction’ mode, as illustrated in case b_4 .

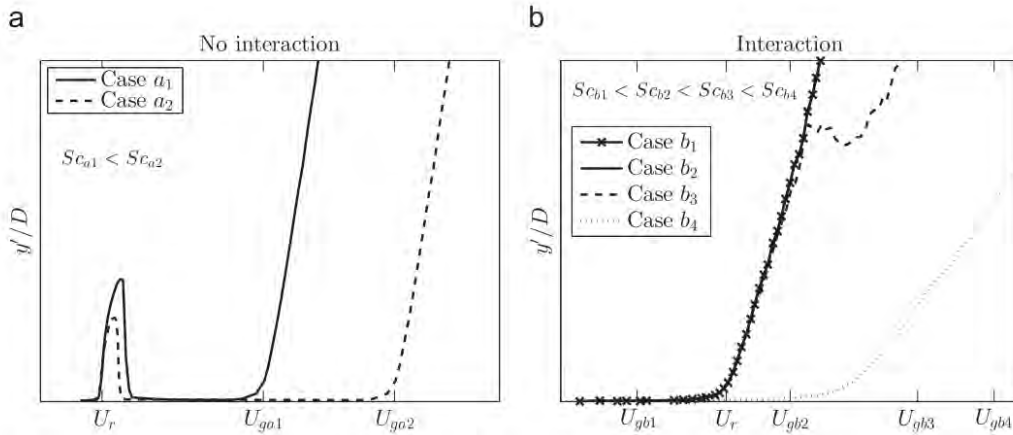


Figure 2.5 Schematic graph of the typical relationship of no-interaction and interaction between VIV and galloping^[4].

2.2 Passive control of bluff body

Bluff-body flow controls, according to Choi et al.^[1], can be divided into three groups, i.e., passive, active open-loop, and active closed-loop controls, respectively, as depicted in Figure 1.1. The difference between passive and active control is the power input. Passive controls operate without any external power input, while active controls require an additional power source. The overwhelming advantages of passive control are easy implementation, stable performance, and no need for extra energy input^[1, 8, 9, 43]. Nonetheless, the inflexibility of passive control measures can pose challenges when it comes to adapting them to different operating conditions^[44]. Active flow control measures, in contrast, present significant advantages in terms of adjustability and controllability^[11, 45]. Additionally, the feedback sensor represents the primary distinguishing feature between open-loop and closed-loop controls, with the latter incorporating the use of feedback sensors^[46, 47]. Both passive and active control technologies can be used for boundary layer and wake flow control.

Numerous passive techniques have been employed to control the aerodynamic/hydrodynamic forces and FIV of a bluff body. These techniques include surface modifications using dimple^[48, 49], roughness^[50], splitter plate^[51-56], wave surfaces^[57, 58], cactus structures^[59-61], and small secondary control cylinder^[62, 63]. Some commonly used methods are shown in Figure 2.6. Note that, we only introduce some of the techniques here, which are directly related to our work.

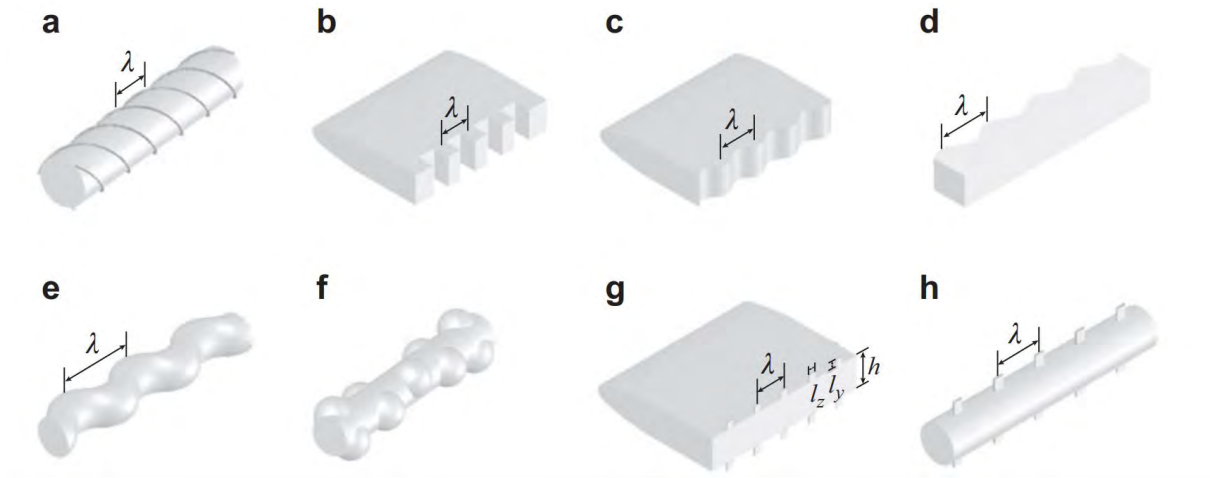


Figure 2.6 Some commonly used flow control techniques for a bluff body^[1]: (a) spiral wires, (b) segmented trailing edge, (c) wavy trailing edge, (d) wavy stagnation surface, (e) sinusoidal axis, (f) hemispherical bulge, (g,h) tiny tabs.

2.2.1 FIV control using trailing-edge splitter plate

Many investigations have been conducted on the control of the flow around a fixed circular cylinder^[1, 47, 64]. The use of splitter plates attached to cylinders has been extensively studied^[53-56, 65]. Gerrard^[56] experimentally investigated a fixed cylinder attached with splitter plates of $0 \leq L/D \leq 2$ (L represents the length of plate), focusing on the effect of Strouhal number (St) at $Re = 2 \times 10^4$. He found that St decreased first and then increased with L/D , resulting in the smallest St at $L/D = 1$. A similar observation has also been given by Apelt & West^[55], who conducted water tunnel experiment to study the effect of a stationary cylinder appended with splitter plates of $0 \leq L/D \leq 2$ at $Re = 10^4$ to 5×10^4 . They reported the mean drag coefficient $\overline{C_d}$, St and base pressure coefficient C_{pb} were suppressed by 31%, 9.6% and 50% at $L/D = 1$, respectively, accompanied by a narrower wake and a longer recirculation length. As L/D was extended to $2 \sim 7$ at the same Re range, they suggested no further changes for $\overline{C_d}$, St and C_{pb}

once the length is beyond the threshold, i.e., $L/D = 5.0$ ^[54]. This is because the flow reattaches on the plate, and the vortex shedding has been fully suppressed. Kwon & Choi^[53] numerically investigated the impact of splitter plates ($0 \leq L/D \leq 8$) connected to a cylinder at $Re = 80 \sim 160$. They found that the vortex shedding disappeared when L/D extended a critical length that was nearly proportional to Re . Moreover, they correlated the variations of St with the dimensions of the dominated vortex and length of the splitter.

Since splitter plate can successfully reduce the aerodynamic forces of a fixed cylinder, to study the control effect of a splitter plate on an oscillating cylinder, Kawai^[66] simulated a vibrating cylinder equipped with detached splitter plates of $0 \leq L/D \leq 8$. He reported that galloping occurred once the plate length and the incoming flow speed extended the threshold. He attributed the galloping to the shear layer reattachment onto the splitter, leading to negative system damping and thus synchronizing the fluctuating lift with the vibration. This observation has been further confirmed by Nakamura et al.^[67] and Assi et al.^[68]. Based on water tunnel experiments, Stappenbelt^[51] studied the transverse response of a cylinder attached to splitter plates of $0 \leq L/D \leq 4$ in a larger reduced velocity range of $3 \leq U_r \leq 60$. Three dynamic responses have been revealed, i.e., typical VIV when $L/D \leq 0.5$, galloping when $1.0 \leq L/D \leq 2.4$ and no obvious vibration when $2.8 \leq L/D \leq 4.0$. The effect of attached splitter plates on the FIV performance of a cylinder has also been reported by Assi & Bearman^[20]. They investigated the length of splitters, i.e., $L/D = 0, 0.5$ and 1 , and the composition of splitters (solid plate and solid plate with a 30% porosity) on the transverse FIV of the cylinder at $Re = 1,500 \sim 16,000$. They suggested that the appearance of the galloping was related to the intermittent reattachment of the shear layer at the front edge of plates, which resulted in a differential pressure on the splitter

and drove the vibration. Moreover, the solid plate with a 30% porosity could cause a significant delay in the occurrence of galloping to a higher U_r .

More recently, Liang et al.^[36] experimentally studied the vibration behavior of a cylinder detached with splitters of $0.4 \leq L/D \leq 5.0$ in the range of $U_r = 2 \sim 40$. They found four different dynamic modes, i.e., typical VIV when L/D smaller than 0.5; VIV combination with galloping when L/D at 1.0 & 1.5; two separated branches when $L/D = 2.0 \sim 3.0$, where the first one was VIV and the second belonged to the hybrid mode of VIV and galloping; and two isolated regions at $L/D = 4.0$ and 4.5 , where the first one presented a larger amplitude but was limited by velocity excitation, and the second branch was galloping. Sun et al.^[29] numerically calculated the dynamic performance of a cylinder attached to splitters ($0 \leq L/D \leq 1.5$) at $Re = 100$. They also reported three different vibration stages: (1) VIV when $L/D = 0, 0.25$; (2) coupled VIV with galloping when $L/D = 0.75$; (3) separated VIV and galloping when $L/D = 1, 1.5$. Moreover, a transition from VIV to galloping resulted from the competition between the lift forces on the splitter plate and on the cylinder, which drove and suppressed galloping, respectively.

Previous studies primarily concentrated on low mass-ratio cylinder's FIV response with attached or detached splitter, including numerical studies limited at low Re ^[29, 30, 69, 70]; experimental studies have primarily concentrated on the alterations in vibration mode, often without providing comprehensive explanations of the underlying flow behavior^[36, 51, 68] or with limited length of splitters^[20]. Related investigations are summarized in Table 2.1. To our best knowledge, the characteristics and mechanism of a cylinder at a large mass ratio attached with splitter plates have not been thoroughly understood yet.

In the present report, based on experimental and numerical ways, a circular cylinder connected by different rigid splitter plates was tested to investigate the effects of splitter length on the resulting FIV. A wide range of splitter plate length was considered, i.e., $L/D = 0 \sim 3.5$, and a range of freestream velocities were applied, corresponding to a range of reduced velocity $U_r = 1 \sim 25$ and the Reynolds number ranging in $Re = 800 \sim 11,000$.

Table 2.1 Summary of a FIV circular cylinder with solid splitters.

Cases	Methodology	m^*	Re	L/D	Connection way	FIV performance
Kawai ^[66]	Num	63.7	-	2.0	detached	galloping
Nakamura et al. ^[67]	Exp	1,120.5, 2,750.2	600-42,000	4.2,10.4, 20.8, 31.3	detached	galloping
Assi et al. ^[71]	Exp	2.0	2,500-30,000	0.25-2.0	attached	galloping
Stappenbelt ^[51]	Exp	2.36	12,600- 84,000	0-4.0	attached	VIV ($L/D \leq 0.5$); galloping ($0.5 < L/D \leq 2.4$); inhibited ($L/D \geq 2.8$)
Assi & Bearman ^[20]	Exp	2.6	1,500- 16,000	0.5,1.0	attached	galloping
Liang et al. ^[36]	Exp	-	3,500-52,000	0.4-5.0	detached	VIV ($L/D \leq 0.5$); partial interaction ($L/D = 1.0, 1.5$); the quenching ($L/D = 2.0, 2.5, 3.0$); two isolated regions ($L/D = 4.0, 5.0$)
Sahu et al. ^[69]	Num	2.0-1,000	150	3.5	attached	Three dispersed regimes: VIV, steady state and galloping
Sun et al. ^[29]	Num	10.0	100	0-1.5	attached	VIV ($L/D = 0, 0.25, 0.5$); coupled VIV and galloping ($L/D = 0.75$); separated VIV & galloping ($L/D = 1.0, 1.5$)
Cui et al. ^[72]	Exp	7.38	1,680-8,720	1-2.5	attached	Galloping-like vibration ($L/D = 1.0$); combination of VIV & galloping ($L/D \geq 1.5$)
Wang et al. ^[73]	Num	10	100	0-2.0	attached	VIV ($0 \leq L/D \leq 0.5$); galloping ($0.75 \leq L/D \leq 2.0$)

2.2.2 FIV control using fins

This section further discusses FIV control using fins treatment. The fins treatment can be used for FIV mitigation and FIV augmentation. In terms of the use of fins for FIV mitigation, Sha & Wang^[74] numerically studied the FIV performance of a cylinder with different fins treatment. They reported that Quadrangular45 (i.e., four fins located at 45°, 135°, 225°, and 315°) and Triangular60 (i.e., three fins located at 0°, 120°, and 240°) fins can effectively mitigate the oscillation of the cylinder. They attributed to the delay of the flow separation points, and the reduction of instability in the flow region near the cylinder. A cylinder attached with radial and longitudinal fins was experimentally studied by Zhang et al.^[75] on its FIV performance. They suggested that dual splitter plates of considerable length can efficiently mitigate the FIVs. However, a single plate, regardless of its position upstream or downstream of the circular cylinder, is ineffective. The enhancement of FIV through the use of fins is typically linked to the optimization of energy harvesting performance. Owing to the sharp drop in fossil fuel resources and constantly growing carbon emissions, clean/blue energy is an urgent need to solve this problem^[76-78]. Among various technologies, generating electricity using FIV is a popular one, on which extensive investigations have been conducted in the last two decades^[79-87].

Three types of FIV are usually utilized for flow-energy harvesting, including VIV, galloping, and flutter. VIV exhibits large amplitudes only within a narrow flow speed range^[21-23]. Therefore, energy harvesting can only be made in this range, outside which the output is close to zero. The oscillation of flutter is chaotic and unstable, and thus the flutter-based harvesters are not good in terms of stable outperforms and harvesting efficiency. In contrast, galloping achieves large-amplitude vibrations once the flow speed surpasses a threshold, and

then the vibration displacement increases as the flow speed^[29, 88-91]. Thus, galloping based flow-energy harvesters usually exhibit better performance than VIV based and flutter-based harvesters.

To enhance the capability of FIV based flow-energy harvesters, fins attachment is one of the most effective ways, which can change the vibration response of the system from VIV to galloping^[92-95]. Based on the linear stability analysis, Abdelkefi et al.^[96] theoretically investigated the impact of cross-sectional shape on the phenomenon of galloping of bluff bodies, including square, triangle, and D-section shapes. They reported that the isosceles triangle with an apex angle of 30° and square cross-sections has the highest energy harvesting efficiency and lowest cut-in speed.

Hu et al.^[15] experimentally investigated the energy collecting performance of a square cylinder attached with fins. They compared four configurations, i.e., a plain cylinder, two fins attached at its leading or trailing edges, and four fins attached at both its leading and trailing edges. Compared to the plain cylinder, about 150% more power was generated by the cylinder with leading-edge fins. In contrast, having trailing-edge fins significantly reduced the generated power by more than 50%, and the oscillation displacement for this case was almost totally suppressed, while attaching four fins to both leading-edge and trailing edge has nearly no effect on the generated power. Subsequently, Hu et al.^[97] investigated the performance of a circular cylinder attached with two parallel cylindrical rods. The effects of rod size and circumferential angle θ on the energy harvesting performance were investigated in detail. They found that when the circumferential angle of the rod, θ , increased from 0° (the front stagnation point) to 60° , the system's oscillation mode changed from VIV to galloping. As θ further increased to 90° ; however, the oscillation was nearly inhibited. For $\theta = 60^\circ$ and rods diameter ($d/D = 2.5\%$), the

system reached the peak voltage (11V) and harvested power ($24.2\mu\text{W}$) output of approximately 2.5 and 6.25 times higher than that of the plain cylinder. Besides, the energy harvesting performance was gradually improving as the increase of rod diameters from $d/D = 2.5\%$ to 20%.

More recently, Wang et al.^[98] investigated the energy harvesting performance of a circular cylinder using two fins. They also validated that the system achieved the best capability at $\theta = 60^\circ$, and the vibration was nearly fully suppressed at $\theta = 120^\circ$. The above investigations suggested that deploying attaching appendages on the windward side, especially at $\theta = 60^\circ$, can enhance the vibration and hence the energy harvesting performance, while attaching appendages on the leeward side does the opposite. This observation indicates that the appendages only perform well in one dominant flow direction. This unidirectional issue can be addressed by adding appendages on both the windward and leeward sides, allowing bi-directional usage of the device. Unfortunately, using a square cylinder, Hu et al.^[15] reported that this configuration can only obtain similar performance as the plain cylinder. To the best of our knowledge, the characteristics and mechanism of those aerodynamic modifications are not yet thoroughly understood, especially for the FSI between flow and bluff bodies. These research gaps motivate us to do the current research work. In the present study, using a new design, we revealed that using fins on both the windward and leeward sides can realize a bi-directional flow energy harvester with a much higher energy output and a much broader operational velocity range than the plain cylinder. Additionally, this conception also seems robust to flow disturbance with regard to both the direction and speed of the flow.

2.2.3 FIV control using biomimetic surfaces

As mentioned above, surface modification is a widely used measure to control the bluff

bodies' aerodynamic/hydrodynamic force and FIV. Surface modification has shown great potential in enhancing the efficiency and ease of implementation in various engineering applications. Its ability to reduce drag and FIV of bluff bodies has been demonstrated, making it a desirable passive control technique^[1, 8, 9]. Biologically-inspired shape optimizations have been a hot topic in the field of fluid dynamics in recent years, with many researchers turning to nature for inspiration. In particular, shapes found in marine life, such as sharks and seashells, as well as desert plants like cacti, have been studied for their aerodynamic properties^[99]. The present study was motivated by the aerodynamic advantages of cacti in high winds, which have been confirmed in previous research^[59-61, 100, 101].

Talley et al.^[61] were among the first to study the aerodynamic performance and flow behavior of a cylinder with a Saguaro cactus cross-section at Re of 90,000 to 200,000. Their study revealed that the 24 V-shaped cacti cylinder effectively suppressed drag and fluctuating forces when compared to a normal cylinder. This improvement was attributed to the narrower wake and smaller velocity defect caused by the cacti structure, as well as the three-dimensional effects it produced. This observation was further confirmed by Talley & Mungal^[102], and they compared the effect of cavity depth l_c/D (where l_c denotes the depth of the cavity) on aerodynamic performance and flow wake at $Re = 20,000 \sim 200,000$. They suggested that the presence of cavities can significantly affect axial flow and the symmetry of vortex shedding, resulting in higher negative pressures on the sides of the cylinder. Besides, the increased l_c/D can result in better drag reduction while having a negligible effect on the pressure distribution behavior.

Babu & Mahesh^[103] numerically studied the flow past a 24 V succulent-shaped cylinder at low Re . Their study revealed an impressive 22% reduction in drag, as well as a significant

decrease in fluctuating forces and St . The succulent-shaped cylinder was found to initiate three-dimensional effects early on due to its unique structure, with a large recirculating flow trapped in the cavities. Moreover, the flow separation occurred early than in a plain cylinder, forming a larger recirculation region. Similar observations were further reported by Wang et al.^[104], and Liu et al.^[101], they carried out experiment measurements on the flow behind a 24 cactus-shaped cylinder at high and low Reynolds number, respectively. Except for large-scale vortices, they also observed the generation of small-scale shear layer vortices because of the existence of the cavities. This modulated the downstream flow in the same phase, leading to a remarkable reduction in fluctuating forces (up to 50%). These findings support the opinion given by Bushnell & Moore^[99] and Talley & Mungal^[102] that the cactus-shaped cylinder has the better aerodynamic performance than the normal cylinder.

As reported by Pierson & Turner^[105], the number of grooves (n) on adult cacti can vary from 10 to 30. The impact of the number of grooves on the aerodynamic benefits of a stationary cylinder was investigated by Yamagishi & Oki^[106] and Guttag & Reis^[18]. Yamagishi & Oki^[106] discovered that, as n rose from 20 to 30, the drag crisis occurred gradually early, i.e., at a lower Reynolds number. However, Guttag & Reis^[18] observed different results after conducting a wind tunnel experimental study with n values of 14, 16, 20, and 24 at Re ranging from 25,000 to 150,000. They found that the drag coefficient versus the Re was highly dependent on groove depth, where the drag crisis surfaced earlier as the depth of the groove increased.

Recently, Zhdanov & Busse^[17] and Zhdanov et al.^[107] conducted numerical and experimental investigations into the aerodynamic performance and flow structures of a stationary cylinder with three and four ribs. These designs were motivated by the geometry of the succulents, namely *Euphorbia Trigona* and *Euphorbia Abyssinica* (illustrated in Figure 2.7),

indigenous to West Central and East Africa, respectively. These succulents are often influenced by the Sahara desert's effects, where the monsoon typically dictates the wind direction^[108]. Zhdanov and his co-authors discovered that the cylinder's aerodynamic performance was highly influenced by the angle of attack (AOA). They also concluded that the three-rib and four-rib configurations were capable of suppressing their aerodynamic forces at low and high AOAs, respectively. They attributed to the delay of flow separation by the rear-side ribs and the shear layer reattachment on the rear-side ribs, forming a pretty symmetrical wake behind the cylinder and thus suppressing the vortex shedding. Similarly, Irwin & Baker^[109] observed comparable aerodynamic performance for the Burj Khalifa, the tallest building globally, which has a cross-sectional area that can be simplified as a three-rib structure. They found that the Burj Khalifa experienced higher wind impact when the wind was directed towards two of its ribs, while lower wind impact was noticed when the wind was directed towards the remaining rib. Thus, it is worth exploring whether these properties could translate to vibrating cylinders featuring a three/four-rib shape and their potential practical applications for suppressing flow-induced vibration.

Research focusing on the FIV response of succulent-inspired cylinders has been relatively limited. One such study was conducted by Law & Jaiman^[110], who did numerical investigations on a vibrating cylinder featuring grooves on its surface at $Re = 4,800$. They observed a reduction in the spanwise coherence of hydrodynamic forces and a significant augmentation of the three-dimensional effects in the proximal region of the flow's wake. These modifications resulted in a maximum amplitude reduction of 37% and a mean drag reduction of 25%. More recently, Wang et al.^[111, 112] numerically studied the vortex-induced vibration inhibition of cylinders with cactus ribs at $Re = 8,000 \sim 56,000$. They compared the effect of various cactus numbers ($n = 8$,

12, 16, 20, 24) and height ratios ($K_s/D = 0.025, 0.05, 0.075, 0.1$) in-depth. They suggested the existence of grooves on the cylinder alters boundary-layer separation and weakens the vortex located in the near wake, leading to maximal amplitude reduction of 57% and 66% in cross-flow and in-line, respectively, compared with a plain cylinder. Additionally, when n was constant at 16, both the peak of displacement and the width of the lock-in region gradually decreased with increasing K_s/D due to changes in wake modes and a decrease in vortex and potential forces. To date, no related studies have investigated on the FIV performance of a succulent-shaped cylinder with three/four ribs. This omission in research motivates us to conduct a research, focusing on FIV control, hydrodynamic performance, and fluid-structure interaction details.



Figure 2.7 Succulent plants with three and four of ribs in nature^[17]: (a) *Euphorbia Trigona* and (b) *Euphorbia Abyssinica*.

2.3 Active flow control via oscillatory morphing surface

Section 2.2 gives a detailed introduction to the passive FIV control of a bluff body, and three passive control methods used in the present thesis. Here, we further present the features of active flow control and its application in the present study. For active open-loop controls,

diverse forcing techniques have been utilized, such as oscillations of a bluff body in streamwise^[113], transverse^[114-116], and rotary way^[117-119]; inflow oscillation^[120,121], blowing/suction^[122-125], synthetic jets^[126-130], electromagnetic forcing^[131, 132], and distributed forcing^[133]. On the other hand, active closed-loop controls with optimal feedback sensors involve implementing a variety of control theories or mathematical analysis methods, such as optimal control theory aimed at reducing drag in bluff bodies exposed to strong nonlinear flow^[134-136], reduced-order models^[135, 137, 138]. Other feedback control algorithms are based on machine learning or artificial intelligence^[139-143].

Section 2.2.3 comprehensively reviews the related study about the effect of cacti-shaped cylinders on drag reduction, FIV control, and flow control. However, rare studies have investigated the effects of morphing cacti-shaped surfaces on the resulting flow behavior and aerodynamic performance. For example, based on a wind tunnel experiment, Guttag & Reis^[18] studied the drag reduction effect of a morphing cylinder with a steady pneumatic loading at $Re = 25,000$ to $150,000$. As such, pressure difference (almost linearly with the cavity depth) was generated among the interior and exterior of the morphing cylinder. Different groove numbers ($n = 14, 16, 20, 24$) have also been considered. They reported that a maximum drag reduction of about 55% could be achieved by this perturbation due to an early occurrence of the drag crisis. Besides, they proposed a model to predict the extra pneumatic loading in achieving the minimal aerodynamic drag on a given oncoming flow speed and groove depth. However, they did not consider the dynamic deformation of the latex membrane, and no detailed explanation of the control mechanism was given from the flow field perspective. Motivated by this work, some research questions rise. Firstly, what if we use a continuous oscillatory morphing surface; can this perturbation achieve wake control? Secondly, how does the frequency of the oscillatory

morphing surface affect the control results? Thirdly, can drag reduction be achieved by using the oscillatory morphing surface?

To address these research gaps, we experimentally investigate the effects of cylindrical surface oscillations on the wake flow based on a 12 V-shaped cacti cylinder. The effect of different excitation frequencies has been compared. To further explore the feasibility of using morphing surface for drag reduction, some numerical simulations are also conducted, which aim to address the wake and drag control further by utilizing the oscillating surface and anti-phase jets, serving as the variants of the morphing surface.

Chapter 3 FIV control with an attached splitter plate

In this chapter, we conduct an examination of a circular cylinder attached with a rigid splitter plate of varying lengths to investigate the impact of the splitter on the resultant FIV. A comprehensive introduction to the experimental setup and measurement techniques is provided first. The hydrodynamic performance and vibration modes are then analyzed in relation to the increasing length of the splitter. Furthermore, to gain deeper insights into the flow behaviors associated with the observed vibration modes in the experiment, numerical simulations have been carried out. The main content of this chapter has been published in *Physics of Fluids* (Vol. 35: 087104, 2023).

3.1 Experimental setup and measurements

The experimental investigation on the passive FIV control of a circular cylinder was carried out in a water channel at The Hong Kong Polytechnic University (PolyU). The water tunnel in PolyU under investigation is equipped with a transparent test section measuring $0.3 \times 0.6 \times 2.0$ m in width, height, and length dimensions, respectively. This segment is comprised of detachable acrylic plates that can be easily removed to satisfy the experimental requirements. The flow is generated by a three-phase and six-pole motor pump capable of producing up to 60 horsepower and operating on 380V AC (alternating current). The flow speed can be continuously changed within the scope from 0.05 to 4 m/s, while maintaining a turbulence intensity of less than 0.5%.

The distance between the bottom side of the cylinder and the water-channel wall was around 5 mm. An end plate was placed close to the top side of the model to minimize the three-dimensional effects as well as the free surface effects. The cylinder was elastically supported by two springs along two linear guides via air bearings, such that it could freely oscillate in the transverse direction when subjected to the water flow, as shown in Figure 3.1.

An accelerometer was attached to one of the air bearings' linear rods to monitor the tested cylinder's transversal oscillation, which was used to verify the displacement obtained by a synchronous high-speed camera (FASTCAM Mini UX100). The signal from the accelerometer was sampled at 2 kHz by an A/D converter board (NI 9220). A LabView virtual instrument (DAQ chassis, NI cDAQ 9174) was used to synchronize the force and camera. Besides, the forces were measured by a load cell with six-component (ATI Mini-40); the measurement range is 0 ~ 80 Newton with an uncertainty of ± 0.02 Newton. The load cell was vertically mounted between the tested cylinders and upper platform. The sampling frequency was 2,000 Hz, and the duration was 5 minutes (Figure 3.1). The estimated uncertainty of oscillation displacement was about 0.5%, and the uncertainty of force measurements was approximately 1.5%^[144]. In order to remove the influence of the high-frequency noises, the data acquired from the force sensor was treated via a low-pass filter with a 10 Hz cut-off frequency.

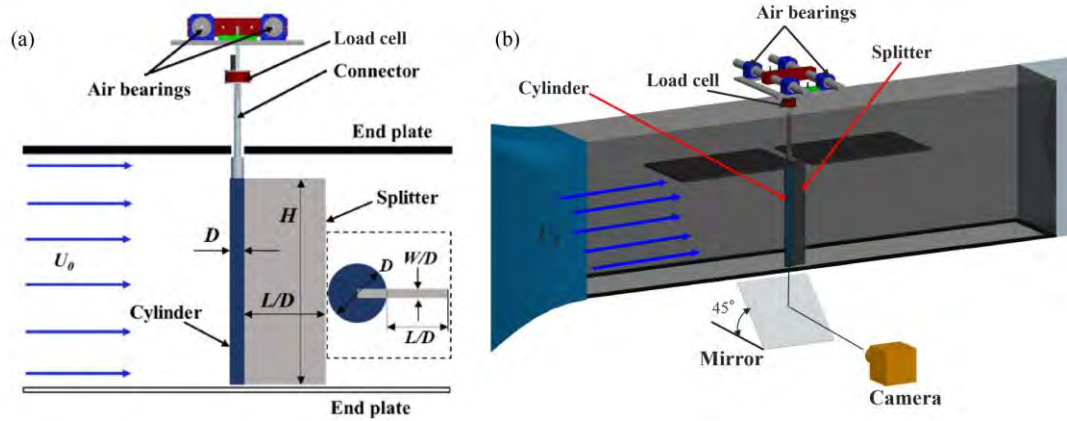


Figure 3.1 (a) Test rig installed in a closed-loop water channel; (b) schematic of the force and displacement measurements.

A cylinder model (diameter $D = 20$ mm and span $H = 430$ mm), made of aluminium, was installed in the middle of the measurement segment, causing the blockage and aspect ratio of 7.3% and 21.5, respectively (Figure 3.1a). The total mass of the cylinder and its supporting systems was around 9.0 kg, corresponding to a mass ratio $m^* \approx 50$. A splitter plate of different lengths ($L/D = 0, 0.125, 0.25, 0.5, 0.75, 1.0, 1.5, 2.0$ and 3.5), made by acrylic, was attached behind the cylinder, as shown in Figure 3.1(a). Moreover, the ratio of the width of plate to the span of the cylinder was $W/D = 0.2$. The mass of the plates could be ignored compared with the total mass of the tested system. Therefore, the mass ratio for different cases was nearly identical. Free decay tests in stationary water were conducted to estimate the system's structural damping, which was found to be $\zeta_s = 0.6\%$, resulting in $m^* \zeta_s = 0.324$, and the natural frequency to be $f_n = 1.06$ Hz.

3.2 CFD setup and validation

Due to challenges associated with measuring the flow field for a vibrating cylinder at high Re using PIV, especially the near flow field around the vibrating cylinder, ANSYS Fluent was

utilized to conduct the CFD simulations to supplement the experiments by providing detailed flow information around a FIV cylinder. The computational domain is presented in Figure 3.2. The length and width of this domain are $60D$ and $15D$, respectively. This width is set the same as that of the water channel. The cylinder is located $15D$ downstream from the inlet. A uniform velocity inlet condition is specified at the inlet boundary, while the pressure out condition is defined at its outlet side. The cylinder and splitters are no-slip walls, and the upper and lower sides of the computational domain are also set as no-slip walls.

The unsteady flow around the cylinder is assumed to be incompressible. The SST $k-\omega$ turbulence model^[145, 146] and the overset mesh have been widely adopted for analyzing bluff body FIV problems^[145, 147, 148]. This selection is based on our understanding that, for simulations with Reynolds-Averaged Navier-Stokes (RANS) equations, the SST $k-\omega$ turbulence model offers superior capabilities in capturing flow separation^[149]. Specifically, it exhibits good predictive accuracy when dealing with boundary layer flows with adverse pressure gradients, usually associated with flow separation followed by vortex formation and shedding. The diameter of the overset mesh region is set as $6.5D$, with its origin fixed at the center of the cylinder. The background and appended meshes are connected by an internal boundary of overset. The computational domain is discretized into structured tetrahedral meshes with 242,407 grid nodes. The mesh around the cylinder is a polar grid, and the minimum grid size is 1×10^{-5} m with a ratio of 1.05 (Figure 3.2 b&c). We applied the Newmark- β method^[150] to solve the vibration responses of the cylinders, which has been widely used in simulating vibration systems and evaluating the dynamic response of structure^[151, 152].

The 2-D rigid cylinder and plate system can be simplified as a typical mass-spring-damper oscillator model^[153]. The one-degree freedom motion equation is as follows:

$$m\ddot{y}_t + c\dot{y}_t + ky_t = f_y(t) \quad (3-1)$$

where m is the total mass of the cylinder and splitter plate system, c is the damping of the system, k is the system elastic coefficient, f_y is the displacement of the system in y -direction caused by the fluid force and \ddot{y}_t , \dot{y}_t and y_t represents the acceleration, velocity and lateral displacement of the system at time t , respectively.

Usually, the Newmark- β algorithm is written in C programming language and incorporated in User-Defined Functions (UDFs). Newmark- β is a method to solve forward kinematics problems, i.e., the structural displacement, velocity, and acceleration can be obtained by solving the loading force employed in the structural. The equations of Newmark- β method are as follows:

$$\dot{y}_{t+\Delta t} = \dot{y}_t + [(1-\beta)\ddot{y}_t + \beta\ddot{y}_{t+\Delta t}]\Delta t \quad (3-2)$$

$$y_{t+\Delta t} = y_t + \dot{y}_t\Delta t + [(0.5-\alpha)\ddot{y}_t + \alpha\ddot{y}_{t+\Delta t}](\Delta t)^2 \quad (3-3)$$

where Δt is the time step, α and β are parameters associated with the stability and accuracy of the integral. The reasonable values for α and β are 0.5 and 0.25, respectively^[152]. Then, we can obtain the constants by integration calculation:

$$\begin{aligned} P_1 &= \frac{1}{\alpha(\Delta t)^2}, P_2 = \frac{\beta}{\alpha\Delta t}, P_3 = \frac{1}{\alpha\Delta t}, P_4 = \frac{1}{2\alpha} - 1, \\ P_5 &= \frac{\beta}{\alpha} - 1, P_6 = \frac{\Delta t}{2} \left(\frac{\beta}{\alpha} - 2 \right), P_7 = \Delta t - \frac{\beta}{\Delta t}, P_8 = \beta\Delta t. \end{aligned} \quad (3-4)$$

By merging eqns. (3-2) -(3-4), the velocity and acceleration at $t+\Delta t$ are as follows:

$$\ddot{y}_{t+\Delta t} = P_1(y_{t+\Delta t} - y_t) - P_3\dot{y}_t - P_4\ddot{y}_t \quad (3-5)$$

$$\dot{y}_{t+\Delta t} = \dot{y}_t + (1 - \beta)\Delta t \ddot{y}_t + \beta \Delta t \ddot{y}_{t+\Delta t} \quad (3-6)$$

If we further consider the motion equation at $t+\Delta t$, we can calculate the $k_{t+\Delta t}$, $f_y(t+\Delta t)$, $\ddot{y}_{t+\Delta t}$, $\dot{y}_{t+\Delta t}$ and $y_{t+\Delta t}$ at $t+\Delta t$:

$$k_{t+\Delta t} = k_t + P_1 m + P_2 c \quad (3-7)$$

$$f_{t+\Delta t} = f_t + m(P_1 y_t + P_3 \dot{y}_t + P_4 \ddot{y}_t) + c(P_2 y_t + P_5 \dot{y}_t + P_6 \ddot{y}_t) \quad (3-8)$$

$$y_{t+\Delta t} = f_{t+\Delta t} / k_{t+\Delta t} \quad (3-9)$$

$$\ddot{y}_{t+\Delta t} = P_1 (y_{t+\Delta t} - y_t) - P_3 \dot{y}_t - P_4 \ddot{y}_t \quad (3-10)$$

$$\dot{y}_{t+\Delta t} = \dot{y}_t + P_7 \dot{y}_t + P_8 \ddot{y}_{t+\Delta t} \quad (3-11)$$

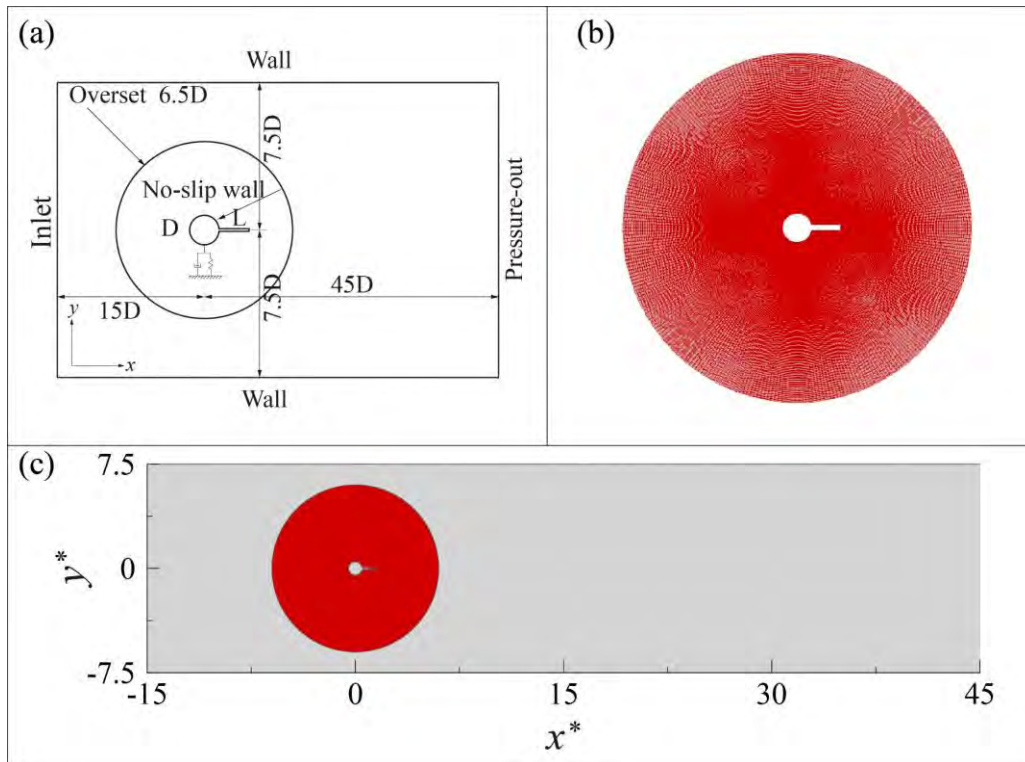


Figure 3.2 Numerical simulation model and boundary condition (a) and calculation mesh (b&c).

To validate the present numerical framework, we first calculated the case with a single fixed cylinder at $Re = 100$, as tabulated in Table 3.1. Drag and lift coefficients C_d , C_l and Strouhal number St of the calculation agree well with available literature data. The definitions of C_d , C_l and St are as follows:

$$C_d = \frac{2F_x}{\rho U_\infty^2 D} \quad (3-12)$$

$$C_l = \frac{2F_y}{\rho U_\infty^2 D} \quad (3-13)$$

$$St = \frac{f_v D}{U_\infty} \quad (3-14)$$

where F_x and F_y represent the forces acting in the x and y directions, ρ denotes the fluid density, U_∞ is the incoming flow speed, and f_v is the dominant vortex shedding frequency.

Table 3.1 Comparison of the current simulation results with references at $Re = 100$.

Data	C_d	C_l	St
Current simulation	1.356 ± 0.009	± 0.334	0.168
Norberg ^[154]	-	± 0.18 to ± 0.54	0.168
Mahír & Altaç ^[155]	1.368 ± 0.029	± 0.343	0.172
Harimi & Saghafian ^[156]	1.344 ± 0.007	± 0.306	0.165
Wang et al. ^[127]	-	± 0.337	0.169
Ren et al. ^[142]	1.375 ± 0.011	± 0.341	0.169

Then, FIV of a cylinder was calculated. The simulation parameters were set identical with the experiment, i.e., $m^* = 50$, $f_n = 1.06$ and $\zeta_s = 0.6\%$. The residual of each turbulent equation is set at 10^{-5} to guarantee convergence. Three sets of meshes and three different timesteps are adopted to examine the grid and time convergence at $U_r = 5.2$ ($Re = 2,200$), as depicted in Tables 3.2 & 3.3. For time step $\Delta t = 0.005s$, the difference of amplitude (y) between Mesh 2

and Mesh 3 is 0.7%, and the St does not change. Besides, the discrepancy of y and St between Mesh 1 and Mesh 3 is 2.86% and 1.06%, which is obviously improved. The improvement of A/D between $\Delta t = 0.005s$ and $0.0025s$ is not significant based on Mesh 2. Thus, we finally adopted Mesh 2 and $\Delta t = 0.005s$ in the present simulations.

Table 3.2 Comparison of the responses for a FIV cylinder based on three meshes at $Re = 2,200$.

Case	Grid No.	Δt	y	St	y^+
Mesh_1	152,082	0.005	0.58142(2.86%)	0.186(1.06%)	< 1
Mesh_2	242,407	0.005	0.59425(0.7%)	0.188(0%)	< 1
Mesh_3	326,150	0.005	0.59852	0.188	< 1

Table 3.3 Time step independence validation results based on Mesh_2.

Case	Δt	y	St
Mesh_2	0.01	0.57635(3.02%)	0.184(2.13%)
	0.005	0.59425(0.16%)	0.188(0%)
	0.0025	0.59521	0.188

The comparison of experimental data ($L/D = 0$) and the numerical data in the range of $2 < U_r \leq 9.6$ are shown in Figure 3.3. Although they generally agree with each other, some discrepancies are observed. The possible reasons are: First, the normal cylinder in numerical simulation is not identical to the setting of $L/D = 0$ in the experiment because the former is a completed circle, while the latter is a circle cut a small part and then filled with a short plate (Figure 3.1a). Second, the difference between the experiment and simulation values may be caused by the damping adopted. Third, the difference may be caused by the application of the turbulence model. Another possible reason may be the simplifying assumptions of numerical simulations, and the boundary conditions may not be identically the same. Although the damping adopted in the simulations is a constant, it cannot be a perfect constant in the experiments. Therefore, it is reasonable that there exists some difference in the amplitude between the experiment and numerical results, and we only apply the numerical results for additional explanations of the amplitude response observed in the experiment.

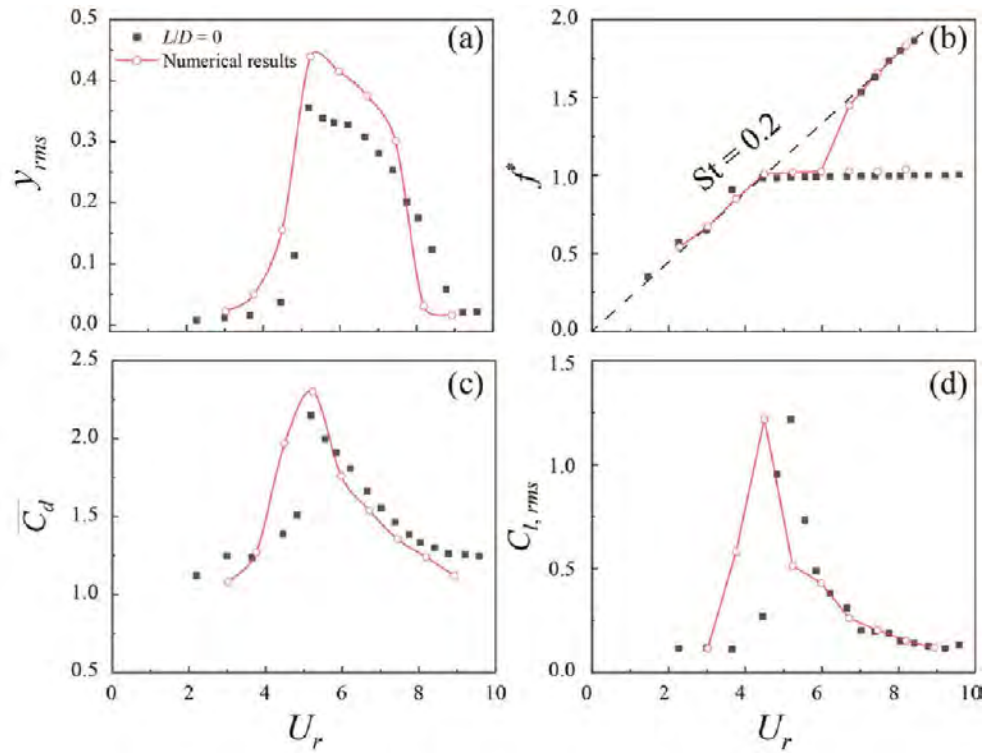


Figure 3.3 The variation of (a) rms of the oscillation displacement y_{rms} ; (b) dimensionless frequency f^* of the lift force; (c) mean drag coefficient $\overline{C_d}$, (d) rms of lift coefficient $C_{l,rms}$.

The y values obtained by CFD simulation are compared with the experimental data, as listed in Table 3.4. The amplitude response for the numerical is slightly larger, which may be caused by the fixed damping parameter in simulation. Although the maximum difference between the experimental and numerical results is about 14%, their variation trends are similar. Thus, we can use the simulation results to explain the phenomenon observed in the experiment.

Table 3.4 Displacement comparison between experiment and numerical results in typical cases.

Cases	U_r	Experimental (y)	Numerical (y)
$L/D = 0$	5.2	0.50	0.58
	10.6	0	0.03
$L/D = 0.125$	7.4	0.61	0.67
	$L/D = 0.25$	10.6	0.78
$L/D = 0.5$	16.4	0.03	0.04
	4.0	0	0.03
$L/D = 1.0$	16.4	0.75	0.87
	4.0	0.14	0.18
$L/D = 3.5$	16.4	0.18	0.22
	16.4	0.03	0.05

3.3 Hydrodynamic forces

Figure 3.4 compares the variation of y_{rms} and $C_{l,rms}$ with U_r . A typical response of VIV is presented in Figure 3.4(a), which has two distinct branches, i.e., a monotonical rise in $3.7 < U_r \leq 5.2$ followed by a decrease in $5.2 < U_r \leq 9.6$, leaving a peak y_{rms} value of $0.36D$ at $U_r = 5.2$. The range of $U_r > 9.6$ is the desynchronization zone in which y_{rms} is close to zero. These observations concur with those in earlier studies^[2,3,36,157], in which the systems have similar $m^* \zeta_s$ values. The variation of $C_{l,rms}$ with U_r is similar to y_{rms} . The maximum $C_{l,rms}$ is about 1.22 at $U_r = 5.2$, which is consistent well with that in Govardhan & Williamson^[2] at a similar $m^* \zeta_s$ value and smaller than that in Assi & Bearman^[20] at a significantly smaller $m^* \zeta_s$.

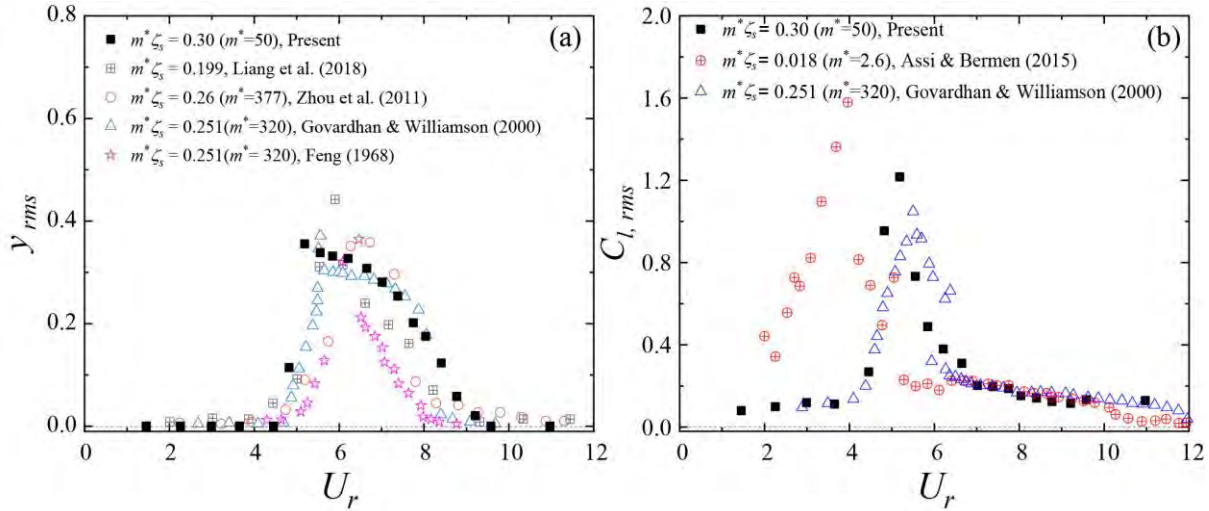


Figure 3.4 Comparison of (a) y_{rms} and (b) $C_{l,rms}$ versus U_r for the normal cylinder.

Figure 3.5 shows y_{rms} and $C_{l,rms}$ of the cylinder attached with a splitter of various lengths, i.e., $L/D = 0, 0.125, 0.25, 0.5, 0.75, 1.0, 1.5, 2.0$ and 3.5 , versus U_r . Clearly, the lock-in region is in $3.7 < U_r < 9.6$ for $L/D = 0$, and the dimensionless frequency of lift force ($f^* = f/f_n$) presents a noticeable dominant f^* locked around 1.0 (Figure 3.7). For $U_r > 9.6$ beyond the synchronization range, f^* has two dominant values, with one still being locked around 1.0 and the other returning to the line of $St = 0.2$. Similar observations can also be made at $L/D = 0.125$ and 0.25 . This is because the present test system has a higher inertia ($m^* = 50$), which means that instead of the excitation of the fluid force, its own stiffness and inertia determine the frequency. This explains the observation on the $L/D = 0.125$ and 0.25 cases due to the small length of splitter and thus a relatively lower excitation force acting on the splitter. However, the extra fluid force exerted on the splitter helps to move the peak y_{rms} value to a higher U_r , as revealed from Figure 3.5(a). Moreover, the lock-in width is significantly enlarged with the increase of L/D . This is possible because the lift force always does negative work on the normal cylinder, while the lift force may sometimes do positive work on the $L/D = 0.125$ and 0.25 cylinders, as indicated in Figures 3.14(a), 3.15(a)&(b). It seems the cylinder dominates the

vibration dynamics over the short splitters, and thus the trends of y_{rms} , $C_{l,rms}$ and f^* of the $L/D = 0.125$ and 0.25 cylinders is similar to the normal cylinder (Figures 3.5 and 3.7).

Galloping occurs at $L/D = 0.5$ and 0.75 , with the transverse amplitude gradually increasing with U_r , similar to that observed in literature^[20, 29, 30, 36]. This observation indicates that with a splitter of moderate length, the cylinder and splitter may have comparable contributions to the dynamics of the system. This is similar to the response of a galloping airfoil, where flow separation occurs at the leading edge and reattachment at the downstream surface, increasing the lift force in the vertical direction^[158, 159]. y_{rms} is then significantly suppressed when L/D approaches 1.0 and almost fully suppressed at $L/D = 1.5, 2.0$ and 3.5 (Figure 3.5a), suggesting that when the length of splitter exceeds the threshold the system behaves more like a plate. As such, the interaction of the shear layers is mitigated by the splitter, and the vortex shedding is then delayed. Note that, VIV occurs firstly for the $L/D = 1.0, 1.5$ and 2.0 cases in the range of $2.8 < U_r < 5.8$, as shown in the inset of Figure 3.5(a). These results indicate that the splitter length plays an important role in the system dynamics, which is associated with rich physics.

Figure 3.6 presents the time-history VIV amplitude curves for selected cases where the cylinder attains its maximum amplitude response. From these time-history amplitude results, we can observe that the vibrations exhibit a notably periodic behavior and are quite stable, particularly in the cases with a relatively shorter splitter plate. These observations are aligned with the findings reported in Figure 3.5(a), wherein the maximum amplitude experiences a gradual increment as the length-to-diameter ratio (L/D) varies from 0 to 0.5. However, the maximum amplitude significantly decreases when L/D approaches 1.0 and is almost zero at $L/D = 2.0$.

Following the classification of the FIV response for a cylinder attached to splitter plate^[4, 20, 36, 160], six different vibration response modes are for the first time observed at a large mass ratio ($m^* = 50$), i.e., VIV when $L/D = 0, 0.125$; coupling of VIV and galloping while dominated by VIV when $L/D = 0.25$; “full interaction” (i.e., galloping happens before the end of VIV while dominated by galloping) when $L/D = 0.5, 0.75$; “the quenching” (i.e., two isolated vibration regions with the first one happening at U_r smaller than its vortex resonance velocity) at $L/D = 1.0$; “partial suppress” at $L/D = 1.5$ and 2.0 where small VIV-like response occurs followed by total suppression; and “total suppress” at $L/D = 3.5$. For the convenience of discussion, here these modes are re-defined as five new vibration modes, i.e., VIV when $L/D = 0, 0.125$; Transition I from VIV to galloping at $L/D = 0.25$; Galloping at $L/D = 0.5$ and 0.75 ; Transition II from galloping to suppression at $L/D = 1.0$ and the Suppression when $L/D = 1.5, 2.0$ and 3.5 .

As shown in Figure 3.5(b), as $L/D \leq 0.25$, $C_{l,rms}$ increases first and then gradually decreases. Besides, the peak $C_{l,rms}$ occurs at approximately identical U_r as the peak y_{rms} . As L/D at 0.5 or 0.75 , $C_{l,rms}$ decreases almost linearly with U_r after reaching its peak, similar to that observed by Assi & Bearman^[20], and Sun et al.^[29]. Note that, when $L/D \leq 0.75$, the maximum $C_{l,rms}$ significantly shifts to higher U_r with the increase of L/D , possibly due to the increase in the effective diameter and the extra fluid force acting on the splitter. However, as $L/D = 1.0$, two peaks appear. The former may be caused by the VIV-like response, while the latter may be associated with the apparent oscillation shown in $10 < U_r < 24$. Only one $C_{l,rms}$ peak is found in the VIV-like response range for $L/D = 1.5$ and 2.0 . As the splitter length further extends to $L/D = 3.5$, $C_{l,rms}$ remains a relatively small value (Figure 3.5b).

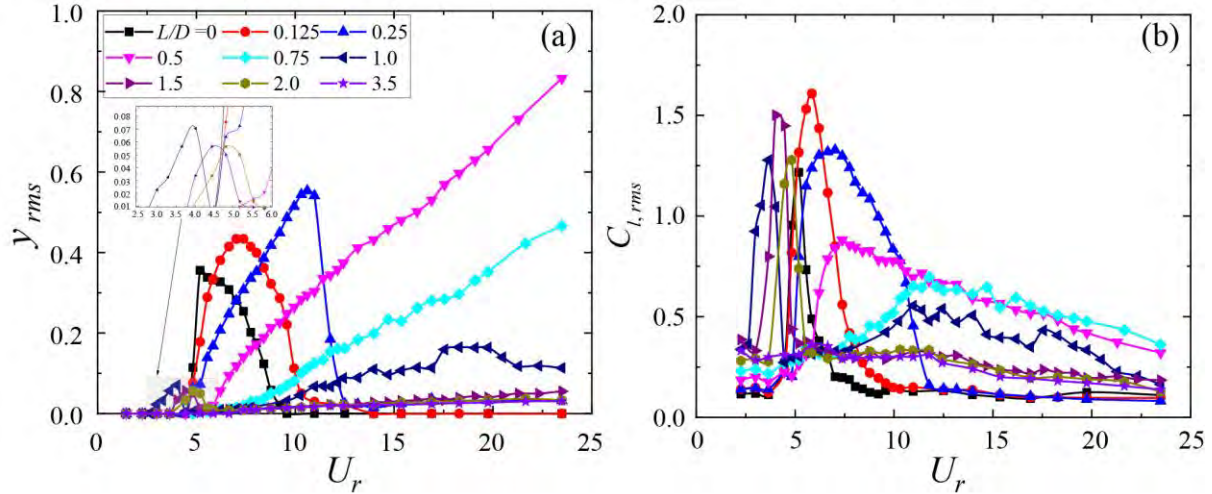


Figure 3.5 (a) y_{rms} and (b) $C_{l,rms}$ of a cylinder attached with a splitter plate vs. U_r .

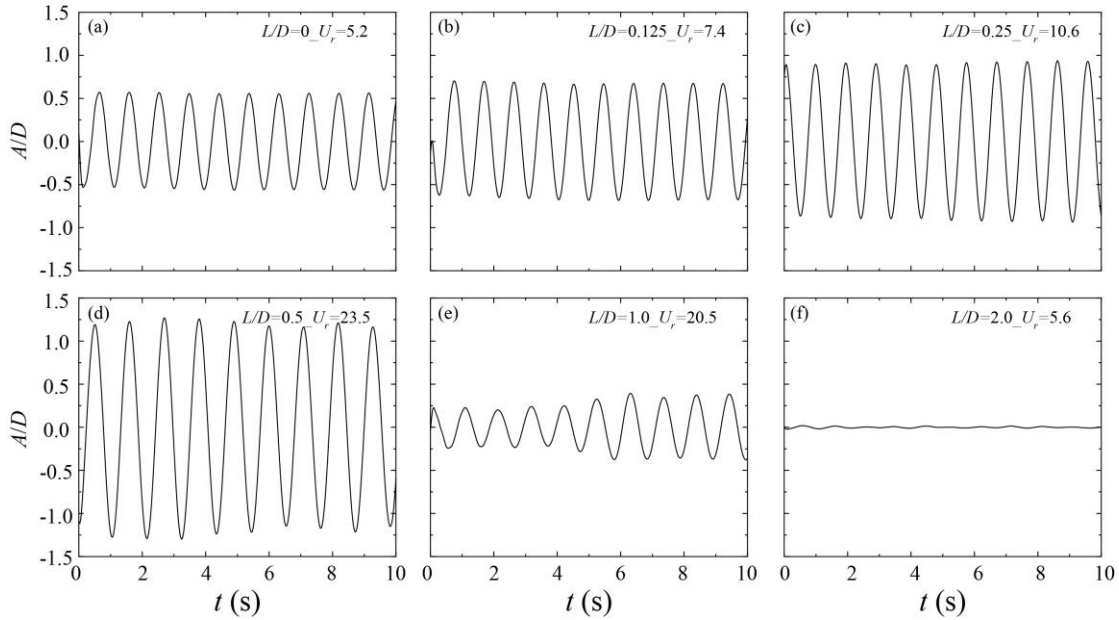


Figure 3.6 Time-history amplitude curves for selected cases: (a) $L/D = 0, U_r = 5.2$, (b) $L/D = 0.125, U_r = 7.4$, (c) $L/D = 0.25, U_r = 10.6$, (d) $L/D = 0.5, U_r = 23.5$, (e) $L/D = 1.0, U_r = 20.5$, (f) $L/D = 2.0, U_r = 5.6$.

For the $L/D = 0.5$ and 0.75 cases, just like the $L/D = 0, 0.125$ and 0.25 cases, f^* firstly linearly increases with U_r , then remains around unity for a short U_r range, as shown in Figure 3.7. These two stages may belong to VIV response because of the similar trend as in the $L/D = 0$ case. Once the vibration amplitude exceeds the threshold, i.e., $U_r = 6.2$ for $L/D = 0.5$ and U_r

$= 8.8$ for $L/D = 0.75$, f^* is no longer locked to unity, but falls to a smaller value, about 0.84 for $L/D = 0.5$ and 0.81 for $L/D = 0.75$. This observation further indicates for $L/D = 0.5$ and 0.75 , the f^* is dominated by the inertial and the excitation of the fluid force together. Subsequently, with the increase of U_r , f^* is always locked to this branch, which is a classic feature of galloping and has also been reported by Assi & Bearman^[20], Sahu et al.^[69] and Sun et al.^[29]. As mentioned before, a VIV-like region is identified for the $L/D = 1.0, 1.5$ and 2.0 cases in the range of $2.8 < U_r < 5.8$ (Figure 3.5a). The corresponding f^* is also locked in at unity when $L/D = 1.0$, as shown in Figure 3.7. Subsequently, f^* sharply decreases to around 0.25 due to the end of small-scale VIV response, and then slightly increases along a line, which is almost identical to $St = 0.2$, and finally remains stable at around 0.9 (Figure 3.7). This frequency branch is lower than that in VIV ($L/D = 0, 0.125$) but higher than that in galloping ($L/D = 0.5, 0.75$), thus defines the mode Transition II.

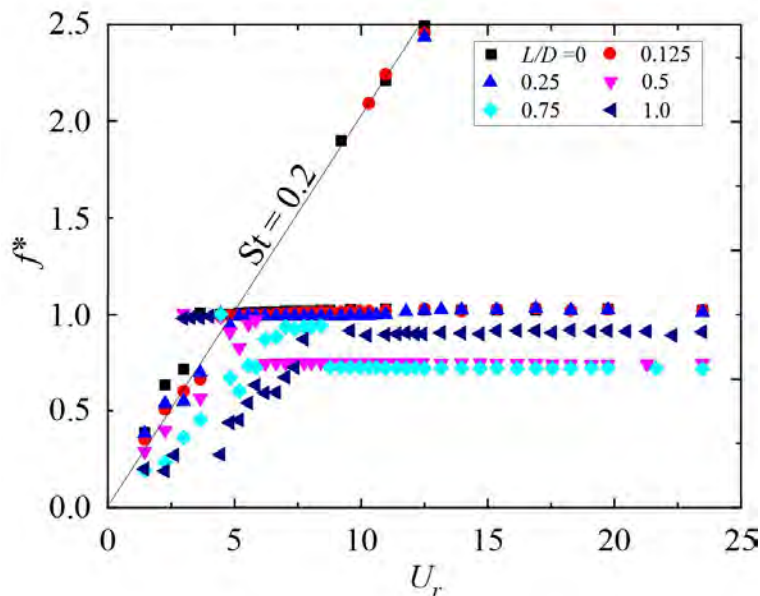


Figure 3.7 Dimensionless frequency f^* of the lift force on the cylinders versus U_r .

Figure 3.8 exhibits the $\overline{C_d}$ and $C_{d,rms}$ versus U_r of the tested cases. In $3.0 \leq U_r \leq 3.7$ and $U_r \geq 9.6$, y_{rms} is almost around zero when $L/D = 0$; thus, the cylinder performs like a stationary cylinder, and the corresponding $\overline{C_d}$ is about 1.24, according well with those reported by other studies^[22, 161-163], as shown in Figure 3.8(a). In the initial branch ($3.7 < U_r \leq 5.2$), $\overline{C_d}$ rises with U_r and reaches the maximal value of 2.15. Subsequently, $\overline{C_d}$ gradually decreases with U_r in the lower branch ($5.2 < U_r \leq 9.6$). With the increase of the splitter length from $L/D = 0$ to 0.25, the peak of $\overline{C_d}$ constantly drops with U_r , and the corresponding U_r while the peak value occurs gradually shifting to a higher value, as shown in Figure 3.8(a). Compared with $L/D = 0$, the maximum $\overline{C_d}$ reduces by about 15.8% and 25.1% for the $L/D = 0.125$ and 0.25 cases, respectively. When $L/D \geq 0.5$, the maximal $\overline{C_d}$ seems fixed around $U_r = 5.2$. Moreover, the $\overline{C_d}$ peak significantly reduces from 2.15 (plain cylinder) to 1.55 ($L/D = 0.5$), by about 27.9%, and then slowly drops as the splitter length gradually approaches $L/D = 3.5$ (Figure 3.8a). Besides, $\overline{C_d}$ gradually decreases in the range of $15.4 < U_r < 23.5$ with the elongation of the splitter plate (Figure 3.8a), indicating a vibrating cylinder attached with splitters benefits in controlling its drag forces. For the cases with y_{rms} close to zero, such as $L/D = 0.25$ and 2.0, mainly caused by the longer vortex formation length as suggested by Apelt & West^[54, 55]. For the cases where obvious oscillation happens, i.e., $L/D = 0.5, 0.75$ and 1.0, the reason may be attributed to a significantly lower pressure difference between the front and rear parts than the normal cylinder, as indicated in Figure 3.13, especially when cylinders pass their equilibrium position. The $C_{d,rms}$ curve shows a similar variation trend for all cases, i.e., $C_{d,rms}$ decreases first at $U_r < 5.0$, then rises remarkably at the onset of FIV and gradually reduces with U_r after reaching their peaks, as exhibited in Figure 3.8(b). Compared with their counterparts, $C_{d,rms}$ for $L/D = 0.5$ and 0.75

are relatively higher when $U_r > 11.5$, which is reasonably associated with the larger vibration amplitude.

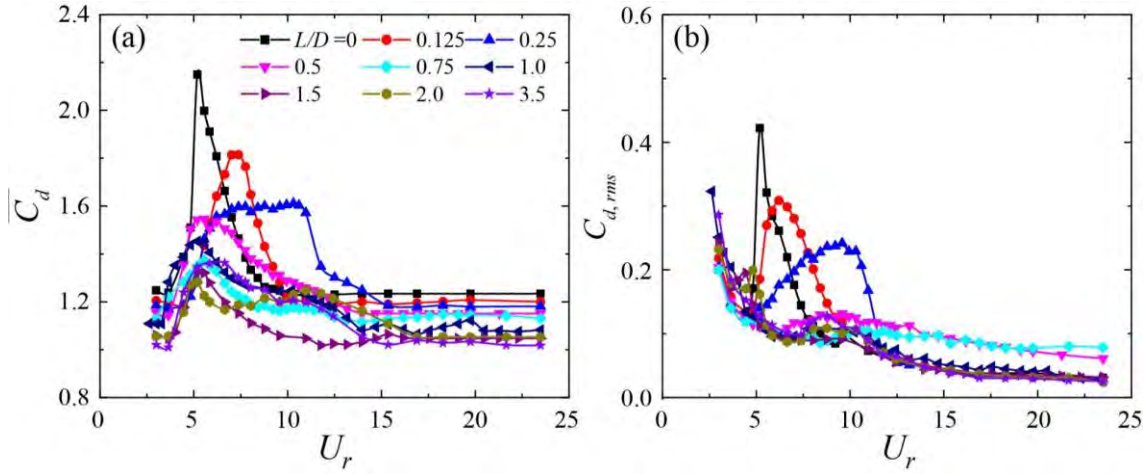


Figure 3.8 (a) mean drag coefficient $\overline{C_d}$ vs. U_r ; (b) rms drag coefficient $C_{d,rms}$ vs. U_r .

The alteration of splitter length also modifies the system's dynamics in terms of the lift force-displacement phase difference φ , as compared in Figure 3.9. Here $\varphi = \arccos R(C_l, y)$, where $R(C_l, y)$ denotes the correlation coefficient between the vibration amplitude y and lift force C_l . As $L/D = 0$, φ abruptly shifts from 0° to around 180° at the onset of VIV, which has been identified as one of the characteristics of lock-in for a normal cylinder^[2, 20, 29]. Subsequently, φ slightly decreases from 166° to around 90° with the increase of U_r . A similar phase shift phenomenon is also observed when $L/D = 0.125$ and 0.25 (Figure 3.9), suggesting the occurrence of VIV. When galloping occurs, i.e., $L/D = 0.5$ and 0.75 , φ falls back from 140° to 20° . Then, φ normally maintains at small values. φ also drops to around 20° at $L/D = 0.25$ ($U_r \approx 10$) but rapidly increases to approximately 90° ; this observation is further confirmed by CFD simulations where the lift force is almost in-phase with the oscillation at $U_r = 10.6$ (see Figure 3.15b), revealing that $L/D = 0.25$ is near the VIV-galloping boundary. As such, we classify $L/D = 0.25$ as Transition I mode. The phase jump for $L/D = 1.0, 1.5$ and 2.0 from $\varphi \approx$

0° to $\varphi \approx 180^\circ$ is advanced to a smaller U_r due to the VIV-like region, as shown in Figure 3.9. Besides, φ no longer drops back to around 0° when $L/D \geq 1.0$, indicating the vanish of the galloping. In the Suppression mode (see Figure 3.18), φ stabilizes around $120^\circ \sim 130^\circ$ with U_r (Figure 3.9).

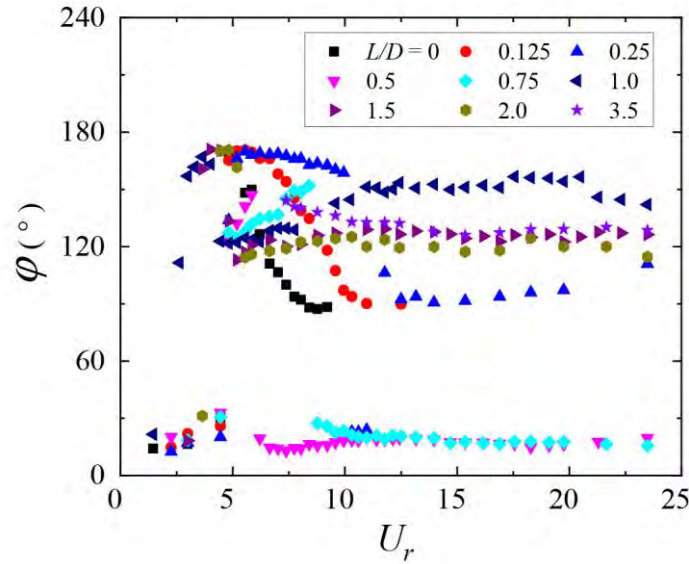


Figure 3.9 The lift-displacement phase angle φ for a circular cylinder attached with splitters vs. U_r .

Figure 3.10(a) presents $C_{l,rms} \cos\varphi$, the lift component in line with the structure acceleration, which is usually used to represent the inertia of FIV system^[22]. As $L/D = 0$ and 0.125 , $C_{l,rms} \cos\varphi$ finds its negative peak at its resonance peak, then gradually drops to zero with the increase of U_r , showing the feature of VIV. Obviously, $C_{l,rms} \cos\varphi$ shows distinguished behavior for the $L/D = 0.5$ and 0.75 cases, achieving much higher values and remaining positive once the cylinder and plate system enter the galloping stage. As such, the state of vibration mode is less likely to be changed. The variation of $C_{l,rms} \cos\varphi$ in $L/D = 0.25$ and 1.0 also indicates their vibration state may be close to the VIV-gallop boundary.

To further pin down the effect of splitter plate on the energy transferring from the flow to the FIV system, we used E to quantify the excitation, as shown in Eqn. (3-15), where $C_{l,rms} \sin\varphi$

denotes the lift component in line with the structure velocity and is thus closely related to the damping of the system.

$$E = 2\pi y_{rms} C_{l,rms} \sin\varphi \quad (3-15)$$

Clearly, the maximum hydroelastic mechanism exciting happens during synchronization when $L/D = 0, 0.125$ and 0.25 . However, as $L/D = 0.5$ and 0.75 , the energy transfer E always maintains a large value and gradually builds up with U_r in the overall trend, as shown in Figure 3.10(b). This observation indicates that under a certain length of the splitter, the cylinder and plate system constantly receive an intensive energetic mechanism for maintaining vibration, which does not belong to the VIV type. As L/D further increases, E is reduced remarkably (Figure 3.10b). As such, their oscillation will be suppressed, especially when L/D is larger than 1.0.

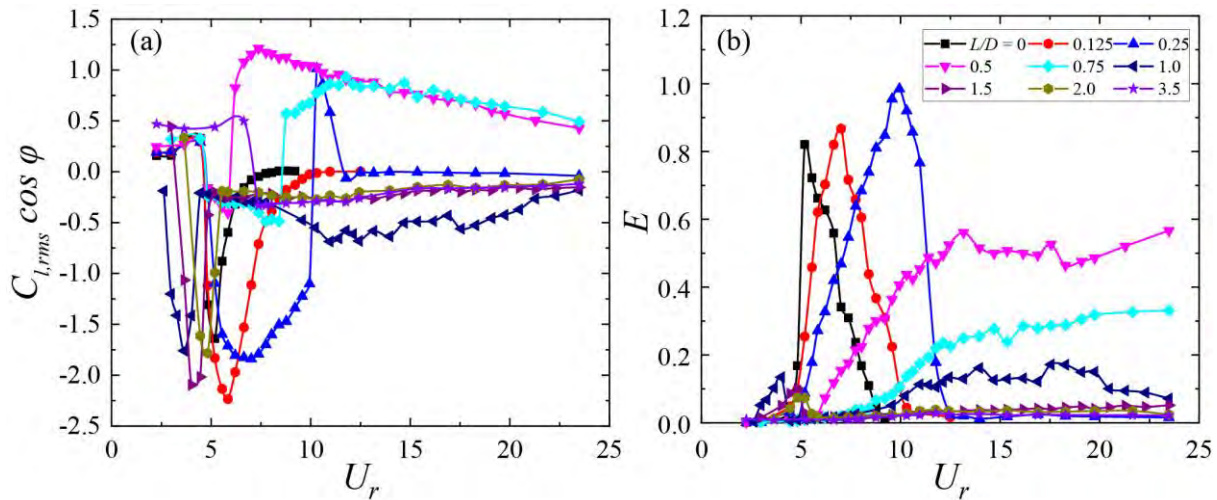


Figure 3.10 (a) lift force term synchronizes with structure's acceleration; (b) energy transmitted from fluid to the FIV system in one period.

3.4 Flow dynamics

To reveal the underlying mechanisms related to the alteration of dynamics for a FIV cylinder of a large mass ratio ($m^* = 50$) attached by different splitter plates, CFD simulations were performed to show related flow details. Figures 3.11, 3.12, and 3.13 present the numerical results of the vortex patterns, shear layers, and pressure fields within one oscillation cycle, respectively. $t = 0$ and $2T/4$ represent the moment when a cylinder is right at its lowest and highest positions, respectively, and $1T/4$ & $3T/4$ denote the moment when a cylinder passes its equilibrium position. As $L/D = 0$, alternative vortex pairs can be easily noticed at $U_r = 5.2$, thus generating the classical 2S vortex mode, as shown in Figure 3.11(a). The 2S vortex mode is still clearly noted at $U_r = 10.6$, i.e., the end of the lower branch (Figure 3.5a). However, the vortices distribute closely to the centerline of the cylinder ($y^* = 0$), and the strength is weaker (Figures 3.11b and 3.12a & b). The relationship between the calculated cylinders' amplitude and lift coefficient is presented in Figure 3.14. The amplitude response at $U_r = 5.2$ is significantly larger than that at $U_r = 10.6$, because f^* at $U_r = 5.2$ is close to system's natural frequency f_n while f^* at $U_r = 10.6$ is away from f_n (Figure 3.14c). Moreover, the spectrum peak of the fluctuating C_l at $U_r = 10.6$ is remarkably lower than at $U_r = 5.2$, reflecting the suppression of y_{rms} . For the normal cylinder, a low-pressure zone occurs as the shear layer rolls up into a vortex, and these alternately emerging low-pressure zones consistently push the cylinder back to its equilibrium position, which prevents further increase in vibration amplitude. Besides, the pressure difference between the front-rear parts of the cylinder at $U_r = 10.6$ is also obviously weaker than that at $U_r = 5.2$ (Figure 3.13a-b), resulting in a smaller $\overline{C_d}$, which is consistent with that observed in Figure 3.8(a).

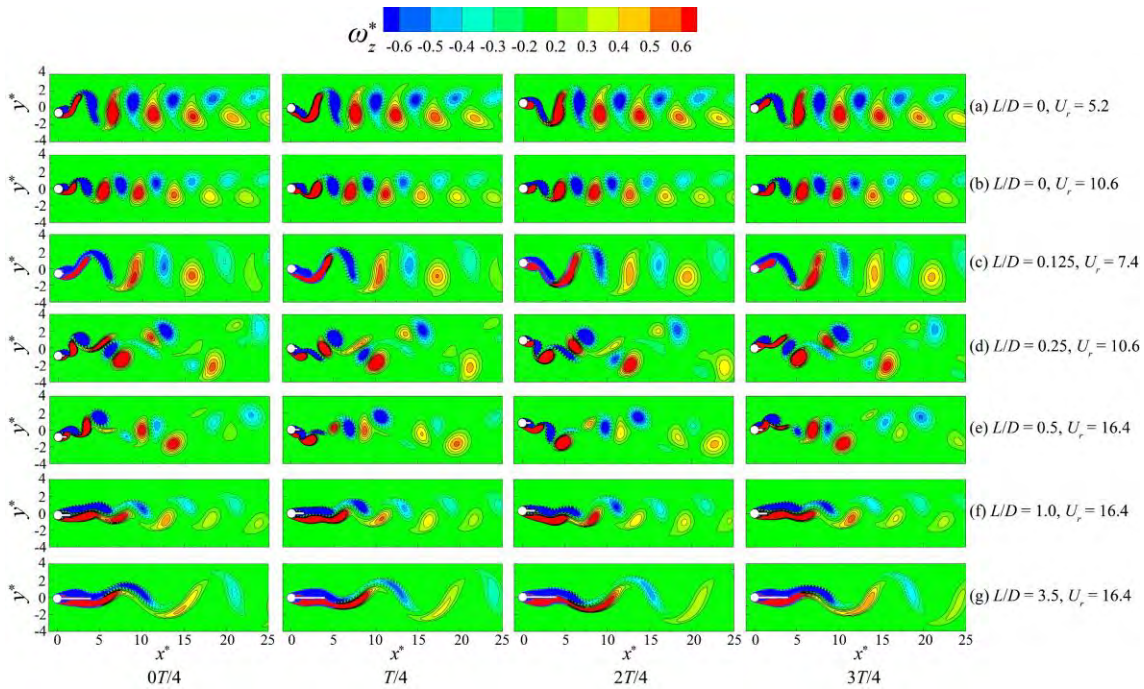


Figure 3.11 Simulated instant vortex evolution in one oscillation cycle.

As $L/D = 0.125$ and $U_r = 7.4$, although the 2S shed mode still exists, the shear layers are significantly elongated, and the associated vortex shedding is obviously delayed than the normal cylinder, as shown in Figures 3.11(c) and 3.12(c). Furthermore, small vortices are attached on both sides of the splitter. That is, negative and positive vortices are attached at the lower and upper sides of splitter when the cylinder is moving up and down, respectively. These attached vortices can change the pressure distribution on the splitter and result in extra fluid force acting on the splitter to excite the systems, thus generating larger y_{rms} than the $L/D = 0$ case (Figure 3.13c). However, the major negative pressure region in the $L/D = 0.125$ case also provides resistance force for avoiding divergent vibration of the system. Therefore, both $L/D = 0$ and 0.125 cases belong to the VIV vibration type.

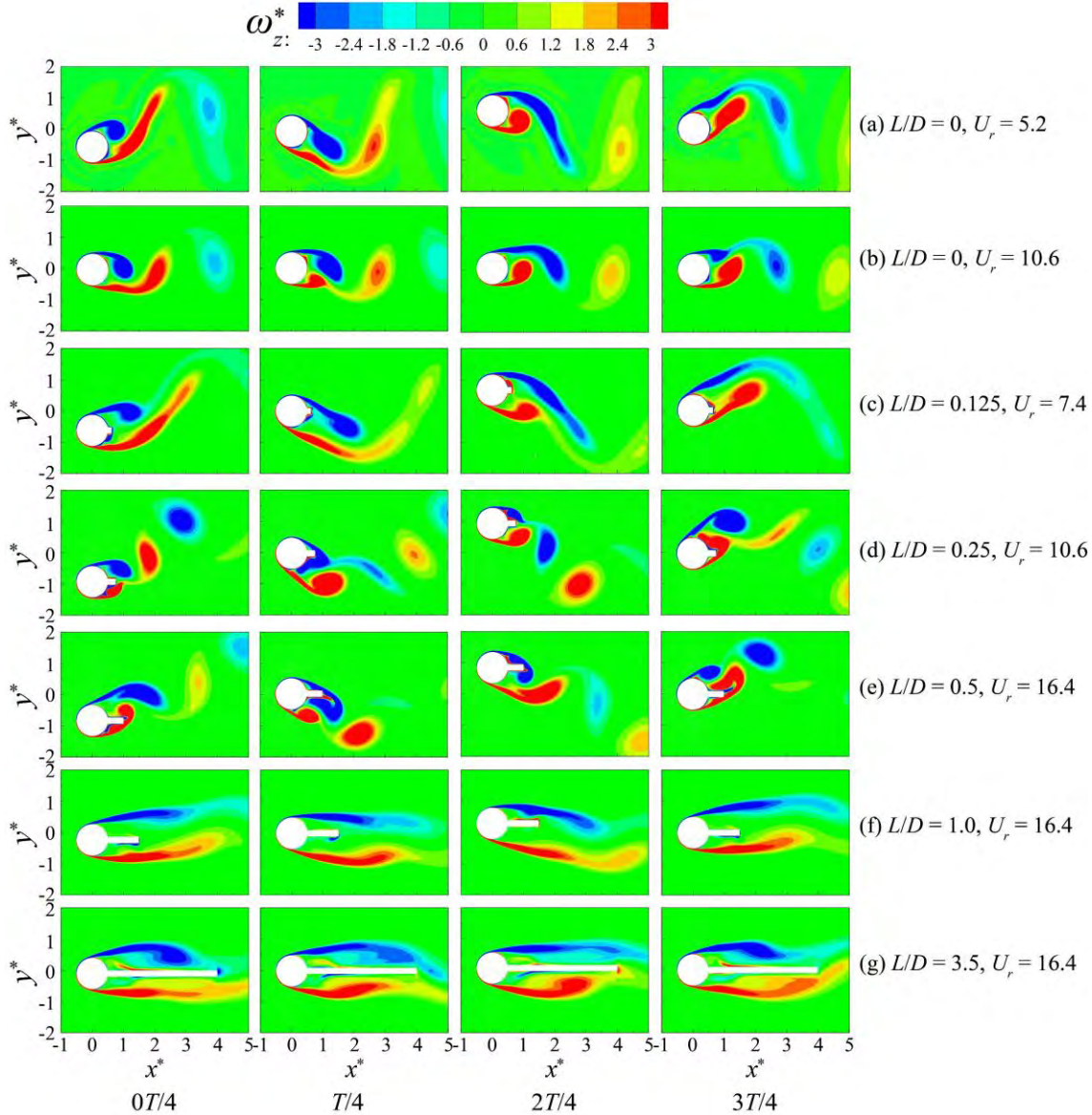


Figure 3.12 Simulated instant shear layer variation in one oscillation cycle.

As $L/D = 0.25$ and $U_r = 10.6$, the vortex pattern changes to a triplet of vortices alternatively shedding from the cylinder in one vibration period, showing the 2T shed mode as defined by Williamson & Roshko^[27], as shown in Figure 3.11(d). This is caused by the apparent interaction between the shear layers and splitters. During this process, the entire vortex will be split into two vortices by the splitter as the cylinder moves to its highest or lowest positions (Figure 3.12d). Moreover, obvious flow reattachment can be observed when the system passes the

equilibrium position, which leads to altering the differential pressure on the splitter and synchronizing with the vibration, especially when the cylinder is moving to its highest or lowest positions (Figure 3.13d). Similar observations can be made when we examine the relationships between the C_l & y , and C_{l_sp} (defined as the lift coefficient on the splitter) and system's velocity U , as displayed in Figure 3.15(b) & (c). C_l is almost in phase with y , and C_{l_sp} is always doing positive work, generating a higher excitation E and resulting in larger y_{rms} .

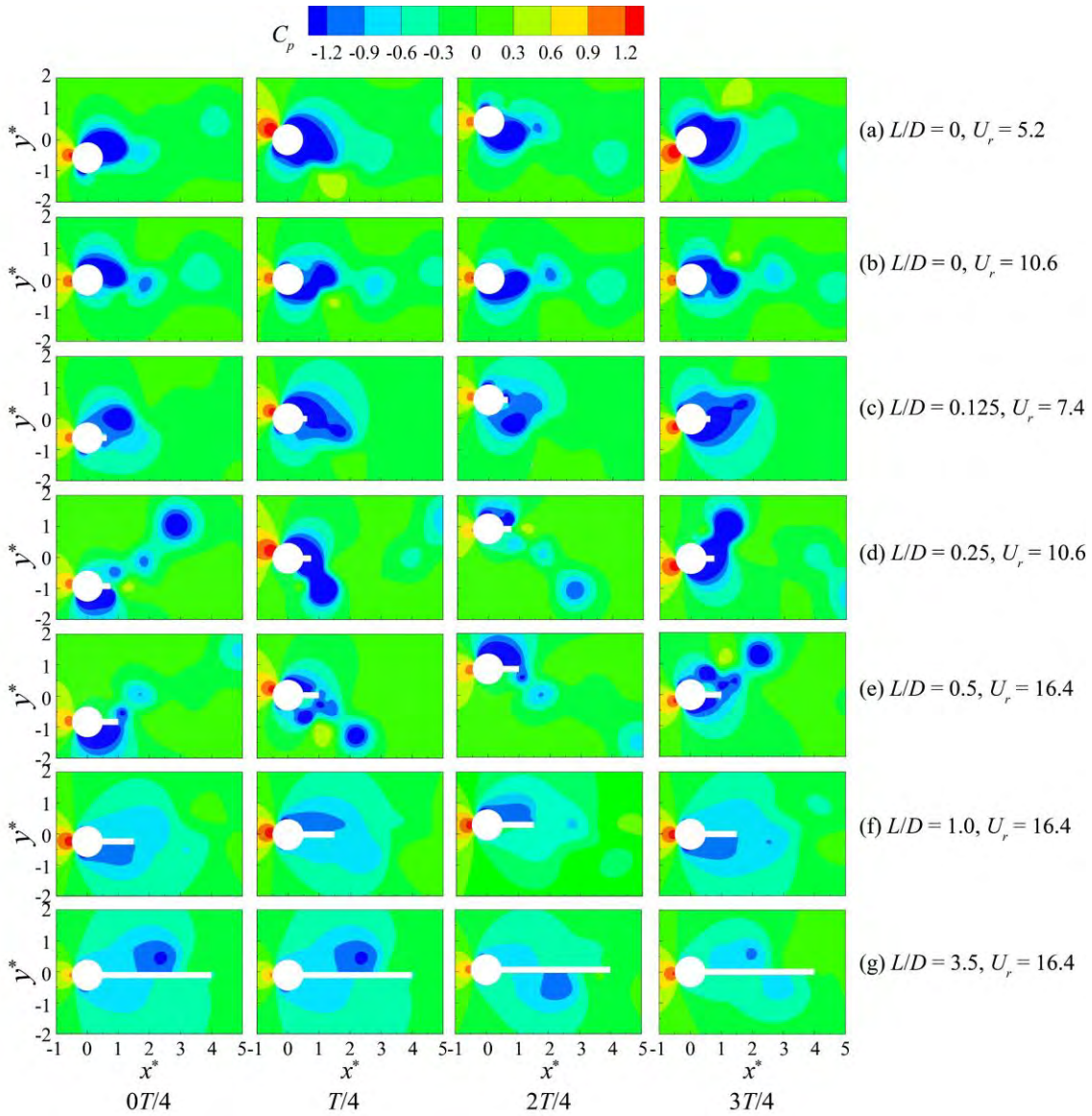


Figure 3.13 Simulated instantaneous pressure fields in one vibrating period.

Interplays between the splitter and separated shear layers are most intensive when $L/D = 0.5$ and $U_r = 16.4$, evidenced by the flow reattachment at all four selected positions, as shown in Figure 3.12(e). Similar to the $L/D = 0.25$ case, this flow reattachment can cause a pressure difference on the splitter plate, i.e., the pressure difference synchronizes with the oscillation. The difference is that the pressure difference also provides the excitation for vibration when the cylinder passes its equilibrium positions (Figure 3.13e). The associated C_{l_sp} is also significantly higher as shown in Figure 3.15(d). The lift force is almost in phase with the vibration (Figure 3.10), which means this state of pressure difference and associated stronger excitation always exist, resulting in the galloping type of response (Figure 3.5a).

As the splitter length increases to $L/D = 1.0$, y_{rms} at $U_r = 16.4$ is about 0.13 (Figure 3.5a), and the corresponding vorticity field is shown in Figure 3.11(f), which is a typical 2S shed mode. However, the distribution of vortices is almost parallel to the plate, and the interactions between positive and negative vortices become weaker owing to the more extended splitter (Figure 3.12f). As such, the roll-up of the shear layers is markedly elongated, and its related vortex shedding is then delayed to a far field, reducing the moment exchange in the near wake and the fluid excitation on the FIV system. Therefore, the corresponding vibration amplitude is suppressed. Compared to the $L/D = 0.5$ case, the asymmetry of the pressure difference on the splitter is significantly weaker, thus resulting in a smaller $C_{l,rms}$. Moreover, C_{l_sp} slightly drops at $L/D = 1.0$, and only a part of C_{l_sp} does positive work compared with a significantly smaller U than $L/D = 0.5$. As such, its y_{rms} remain at a relative higher magnitude instead of totally suppressed like $L/D = 2.0$ (Figure 3.5a).

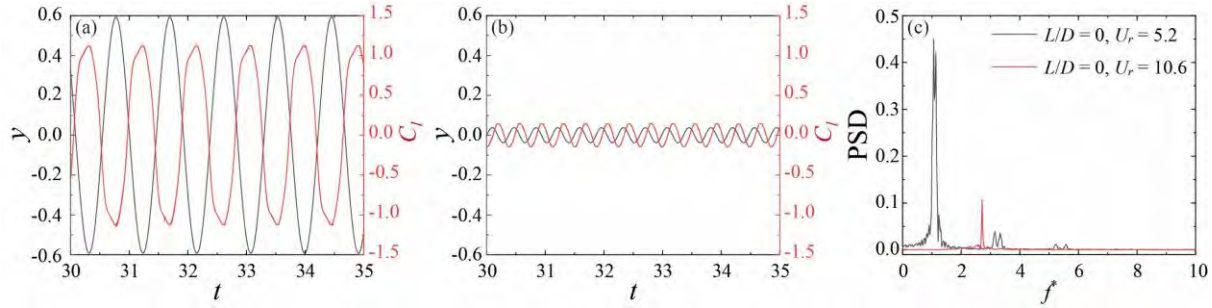


Figure 3.14 Calculated time-history of amplitude and lift coefficient for (a) $L/D = 0$, $U_r = 5.2$, (b) $L/D = 0$, $U_r = 10.6$ and (c) power spectral density (PSD) functions of C_l .

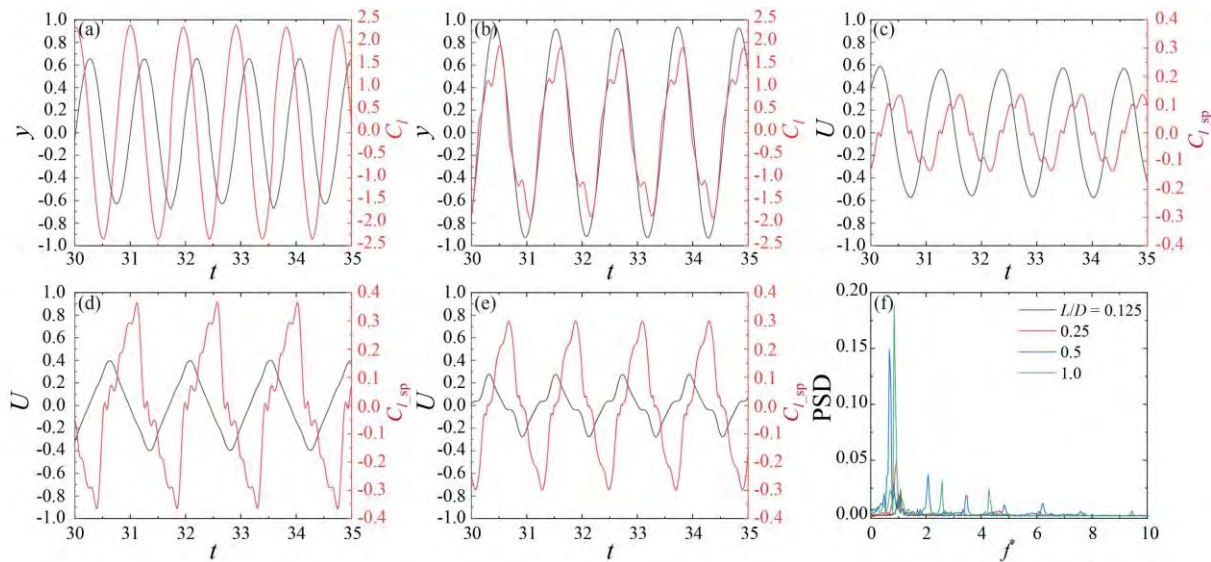


Figure 3.15 Calculated time-history of amplitude and lift coefficient for (a) $L/D = 0.125$, $U_r = 7.4$ & (b) $L/D = 0.25$, $U_r = 10.6$ and time-history of U and $C_{l,sp}$ for (c) $L/D = 0.25$, $U_r = 10.6$, (d) $L/D = 0.5$, $U_r = 16.4$, (e) $L/D = 1.0$, $U_r = 16.4$ and (f) PSD of C_l .

As $L/D = 3.5$ and $U_r = 16.4$, the shear layers are further elongated with an apparent collision on the splitter, as shown in Figures 3.11(g) & 3.12(g), which may cause the local asymmetry of pressure distribution on the splitter (Figure 3.13g). Due to the longer length of splitter, the vortex shedding in the near wake, i.e., $x^* < 7.5D$, disappears, and the associated pressure distribution on the splitter is almost symmetrical, especially near the cylinder (Figure 3.13g). This indicates that the fluctuating lift is almost fully inhibited; thus the energy input

from the fluid E and y_{rms} is nearly zero, consistent with what was observed in Figures 3.5(a) & 3.10(b). Moreover, the base pressure is significantly larger than that for the normal cylinder, leading to a lower $\overline{C_d}$ (Figure 3.8a).

Mannini et al.^[4] and McCarthy et al.^[82] have suggested the critical flutter speed for beam and critical galloping speed for bluff body, respectively, as shown in equations (3-16) and (3-17).

$$U_c = \sqrt{\frac{Yh^3}{\rho_f L^3}} \quad (3-16)$$

$$U_g = \frac{2Sc}{a_g} n_0 D, Sc = \frac{4\pi m \zeta}{\rho D^2}, a_g = -\frac{dC_l}{d\alpha}(0) - C_d(0) \quad (3-17)$$

where U_c is the critical speed for flutter, ρ_f is the density of fluid, Y , h , L is elastic modulus, thickness, and length of the beam. When Y , h and ρ_f are fixed, U_c is determined by L , i.e., one can obtain a lower U_c if the length of beam increases. Therefore, the flutter, i.e., divergent unstable vibration, is more likely to happen for a relatively long length of the splitter. As for bluff bodies, the critical galloping speed U_g is mainly determined by Sc (Scruton number), galloping stability parameter a_g (depends on C_l and C_d , which are functions of geometry and angle of attack α), natural frequency n_0 and the cross-flow side length D . In our experiment, Sc , n_0 and D are unchanged when the length of splitter increases from $L/D = 0.125$ to 0.5 . However, when we compare the C_l and C_d for these cases, it is found that a_g is larger at $L/D = 0.5$, resulting in a smaller U_g , especially when $U_r > 10$. Meanwhile, the fluid excitation injected into the FIV system for the $L/D = 0.5$ case is higher in the same U_r range (Figure 3.10b). Therefore, it is more likely that galloping happens at $L/D = 0.5$ rather than at $L/D = 0.125$. However, when L/D is larger than 1.0 , its U_g value seems smaller than that in the $L/D = 0.125$ case, owing to a

slightly larger C_l and a significantly lower C_d . Besides, the energy transmitted from fluid to the FIV system can be ignored in the entire tested U_r range. Thus, galloping type of response cannot occur in the case with a longer splitter.

The analysis of the galloping of a one-degree-of-freedom system is usually based on quasi-static dynamics^[33, 34]. The sketch drawing of force decomposition of a cylinder is given in Figure 2.4. The instantaneous angle of attack (AOA) $\alpha(t)$ and instantaneous lift coefficient $C_l(t)$ can be calculated by equations (2-1) and (2-2). When $\alpha = 0$, the occurrence of galloping can be determined by the slope (β) of $C_l(t)$ and $\alpha(t)$, i.e., $\beta = \left. \frac{\partial C_l(t)}{\partial \alpha} \right|_{\alpha=0}$, as shown in Figure 3.16. $U_r = 10.97$ is where the $L/D = 0.25$ find its maximum y_{rms} (Figure 3.5a). Clearly, for $L/D = 0.25$, $U_r = 10.97$ and $U_r = 16.89$, β is positive (Figure 3.16a&c), while for $L/D = 0.5$ at same U_r , β becomes negative (Figure 3.16b&d), indicating the happens of galloping.

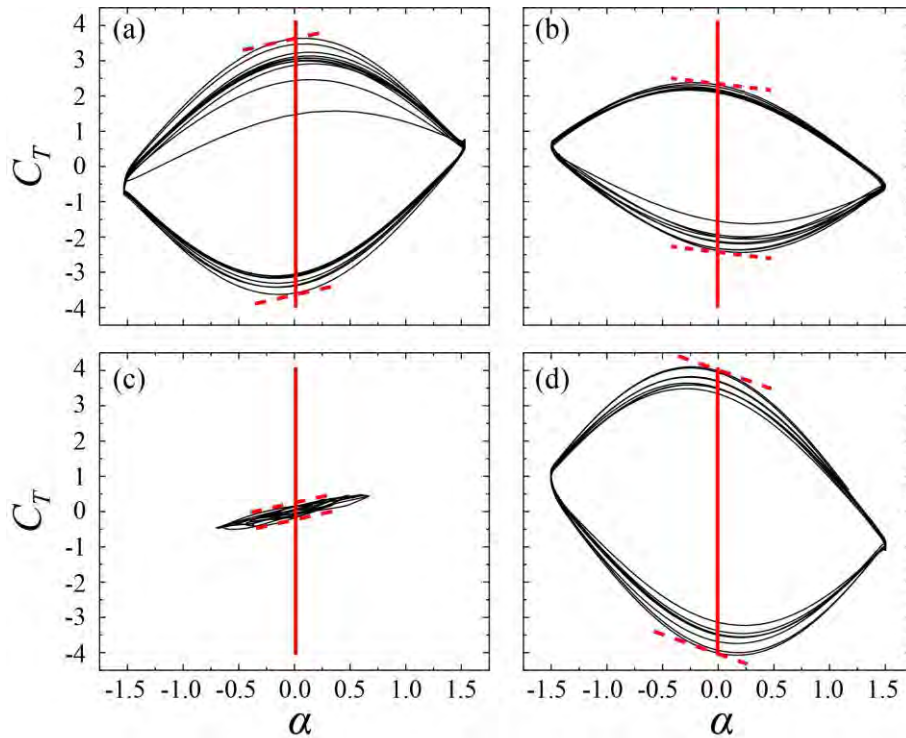


Figure 3.16 The time-history of the actual lift coefficient $C_T(t)$ vs. the actual angles of attack $\alpha(t)$: (a) $L/D = 0.25$, $U_r = 10.97$; (b) $L/D = 0.5$, $U_r = 10.97$; (c) $L/D = 0.25$, $U_r = 16.89$; (d) $L/D = 0.5$, $U_r = 16.89$. The data is coming from the experiment, and the results are presented based on several vibration periods.

To figure out why the amplitude in the $L/D = 0.25$ case cannot build up with U_r , i.e., the transition stage occurs at $L/D = 0.25$, we present the instantaneous vortex patterns and shear layers at $U_r = 16.4$ in one vibration period (Figure 3.17). The interaction between the shear layers and the splitter is negligible, and the vortex shedding changes back to the 2S mode. Besides, St is about 0.15 and the vortex shedding frequency is about 2.55 Hz, higher than the lock-in frequency. This indicates that galloping does not occur, which may be attributed to two possible reasons: the interaction between the shear layers and the splitter is too weak, and the vortex shedding frequency is far away from the lock-in frequency.

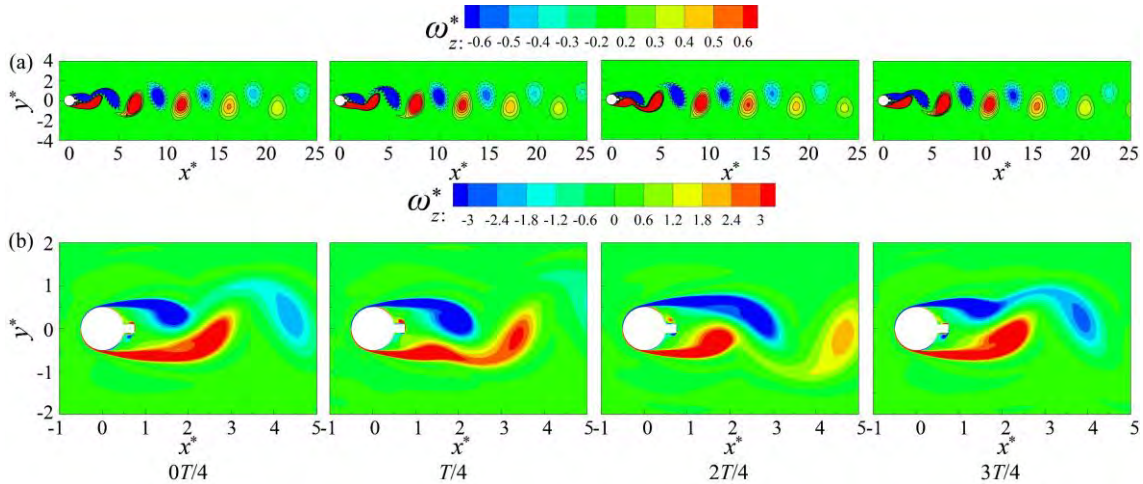


Figure 3.17 (a) Simulated instantaneous vortex patterns and (b) shear layers in an oscillating cycle for the case of $L/D = 0.25$, $U_r = 16.4$.

3.5 Vibration modes

After analyzing the hydrodynamic forces, vortex mode, shear layer, and pressure distribution, different vibration modes have been identified for an FIV cylinder of a large mass ratio ($m^* = 50$) attached by a splitter plate of length $L/D = 0 \sim 3.5$. Five vibration modes are shown in Figure 3.18, i.e., VIV, Transition I, Galloping, Transition II, and Suppression. Each dot represents a tested case, and its color indicates the y_{rms} value. The criterion to divide the regimes on the L/D versus U_r chart mainly depends on the amplitude response shown in Figure 3.5 and the lift-displacement phase angle ϕ shown in Figure 3.9.

The $L/D = 0$ and 0.125 cases are in the VIV mode. Although the y_{rms} versus U_r trend in the $L/D = 0.25$ case is similar to that in the $L/D = 0$ case, the vortex shedding mode is changed due to the interplay of the shear layers and the splitter that leads to the alteration of phase shifts from around 180° to around 25° . As such, the variation of phase difference, $C_l \cos\phi$ with U_r behaves distinctly to that in the $L/D = 0$ case. However, y_{rms} cannot constantly build up with U_r due to the disappearing of interaction and the shifting away of vortex shedding frequency from

the lock-in frequency. Thus, the $L/D = 0.25$ case is a transition mode (i.e., Transition I) between VIV and Galloping.

For the $L/D = 0.5$ and 0.75 cases, the phase angle φ changes from 140° to 20° at U_r values of 6.2 and 8.8, respectively (as observed in Figure 3.9). These specifically reduced velocities indicate the transition from VIV to galloping, despite that y_{rms} values still falling within the range of 0.1 to 0.2. When U_r is higher than its corresponding threshold, y_{rms} builds up as the increase of U_r , while the displacement-lift phase remains at a small value. Besides, flow reattachment occurs on the splitter, resulting in the pressure difference almost synchronizing with the vibration. Therefore, these two cases are in galloping mode when U_r is higher than the corresponding threshold. When U_r is lower than the corresponding threshold, they are in the VIV mode.

y_{rms} in the $L/D = 1.0$ case at $U_r \geq 15.0$ is significantly smaller than that in the $L/D = 0.75$ case, but larger than that in the $L/D = 1.5$ case. y_{rms} and E for $L/D = 1.0$ always maintain a positive value, obviously higher than the normal cylinder. As such, this case is classified as Transition II, which is a stage between galloping and suppression. At low U_r , VIV-like dynamics are observed in Figure 3.5(a) for the $L/D = 1.0, 1.5$ and 2.0 cases, which have the similar phase-shift, i.e., φ jumps from 0° to 180° , and the normalized frequency f^* lock-in around unity (Figures 3.7 and 3.9). This behavior is the major criterion for categorizing this region as VIV. As U_r increases beyond this range, the vibration amplitude undergoes significant suppression, delineating the boundary between the VIV regime and the suppression regime. Consequently, the black line segments representing these cases intersect the y_{rms} range of 0 to 0.1 for L/D values between 1.0 and 2.0.

As the splitter length further increases to $L/D = 3.5$, y_{rms} approaches zero for all tested U_r , which is classified as suppression, as shown in Figure 3.18. These observations significantly contributed to our understanding of this interesting phenomenon.

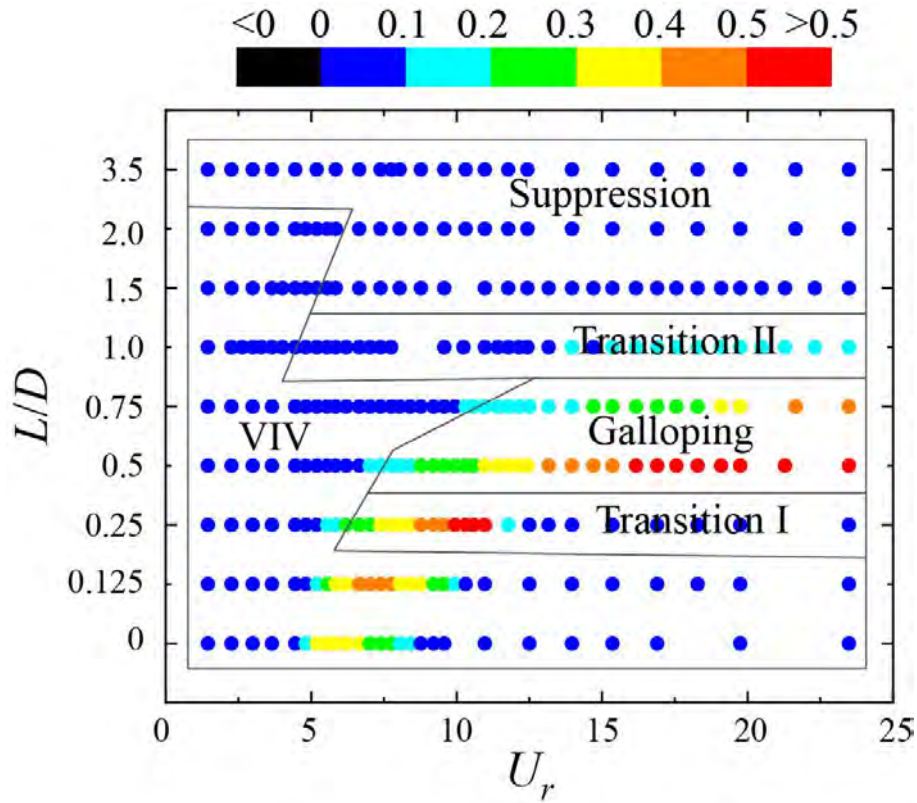


Figure 3.18 Vibration mode for a cylinder attached with splitter at $m^* = 50$. The legend bar given at the top of the figure denotes the y_{rms} values.

3.6 Remarks

A circular cylinder attached by a splitter of different length was tested to examine the effects of the splitter on the resulting FIV. The main findings of the current study are listed as follows:

- (1) As L/D increases, five different vibration modes are revealed: (a) VIV when $L/D = 0$ & 0.125, (b) Transition I from VIV to galloping at $L/D = 0.25$, (c) Galloping when $L/D = 0.5$

& 0.75 when U_r larger than the corresponding threshold, (d) Transition II from galloping to suppression region at $L/D = 1.0$ and (e) Suppression region, i.e., no significant vibration at longer splitter length, i.e., $L/D = 1.5, 2.0$ & 3.5 . Note that, the small-amplitude response for $L/D = 1.0, 1.5$ and 2.0 also belongs to VIV.

(2) With the increase of splitter length from $L/D = 0$ to 0.25 , the peak VIV amplitude gradually shifts to a higher U_r . Moreover, VIV-like response for $L/D = 1.0, 1.5$ and 2.0 at smaller U_r , the peak amplitude also slightly moves to a higher U_r with the increase of L/D .

(3) The occurrence of galloping when $L/D = 0.5$ and 0.75 is caused by the flow reattachment of the shear layers on the splitter, thus forming a pressure difference synchronizing with its vibration. Moreover, the galloping-type of response cannot occur at $L/D = 0.25$ mainly due to its vibration frequency being significantly away from its lock-in frequency. While galloping cannot maintain at $L/D = 1.0$ primarily because of the weaker shear layer interaction with the splitter and the weaker excitation obtained from the fluid.

(4) As L/D increases from 0.125 to 0.5 , the wake patterns are more and more complicated due to a gradual stronger interaction of the shear layer and splitter. That is, 2S, 2T, and four vortices shed from the cylinder and splitter per half vibration period are observed at $L/D = 0.125, 0.25$ and 0.5 , respectively. The vortex pattern changes back to 2S when L/D is larger than 1.0 , with its pressure difference slightly tending to symmetrically distribute, especially around the cylinder. As such, the oscillation displacement will be suppressed.

(5) For $L/D = 0.5$ and 0.75 , $\overline{C_d}$ keeps unchanged with U_r ($U_r > 14.0$), and its $C_{l,rms}$ nearly linearly decrease after reaching its peak with U_r . Besides, for $3.0 \leq U_r \leq 3.7$ and $15.4 < U_r < 23.5$, $\overline{C_d}$ slowly drops with the increase of L/D . In general, for low L/D ratios ranging from 0

to 0.75, the vibration tends to be amplified due to the strong interaction between the splitter plate and shear layers. Conversely, at high L/D ratios spanning from 1.0 to 3.5, the vibration is significantly suppressed, with the associated hydrodynamic forces significantly inhibited compared to the normal cylinder.

The primary impetus behind our research endeavor is to investigate the congruities and discrepancies in the control effects and flow mechanisms exhibited by a splitter-plate controlled circular cylinder with high mass ratios and low mass ratios. Our investigation can serve as a supplement for the understanding of the control of a splitter plate on a circular cylinder, especially for high mass ratio case. The present investigation revealed the VIV phenomenon similar to that observed by Stappenbelt^[51], Sun et al.^[29], and Wang et al.^[73] at lower length-to-diameter ratios (L/D), specifically $L/D = 0.125$, and the peak of vibration amplitude of vibration gradually increases as L/D extends from 0 to 0.25. Moreover, a galloping response is triggered as the length of the splitter plate is further increased, regardless of the mass ratio. It is evident that the range of L/D ratios associated with the galloping response is considerably smaller in cases of high mass ratios compared to those observed in the studies with low mass ratios. For instance, in our present study, the galloping response is observed within the L/D range of 0.5 to 0.75, whereas Wang et al.^[73] reported a range of 0.75 to 2.0, Stappenbelt^[51] observed a range of 1.0 to 2.4, Sun et al.^[29] reported a range of 0.75 to 1.5 (noting their absence of results for L/D ratios exceeding 1.5). This observation suggests the control effects of the rigid splitter plate on a circular cylinder with a high mass ratio are better in terms of the narrower range of galloping responses or regions of enhanced vibration. Moreover, analogous to findings in low mass ratio studies, the vibration is almost entirely suppressed beyond a critical splitter length, and this suppression effect remains stable even with further increases in the length of the splitter

for both high and low mass ratios. Additionally, the VIV-like regime is experimentally observed for the first time at low U_r for the cases of $L/D = 1.0$ to 2.0 at a high mass ratio, which was not shown in these low mass ratio cases.

Chapter 4 FIV control and flow energy harvesting using

fins

In this chapter, a circular cylinder attached by rigid fins is investigated to study its effects on the resulting FIV and energy harvesting performance. Four configurations are studied, i.e., a plain cylinder, a cylinder with two windward fins, a cylinder with two leeward fins, and a cylinder with four fins. The FIV performance and hydrodynamic behavior have been compared in detail. CFD simulations are then used to reveal the underlying physics. This study also looks at the effects of the angle of incidence and fin length on the performance of the four-fin case and the associated energy harvesting performance. The main content of this chapter has been published in *Applied Physics Letters* (Vol. 122: 153901, 2023).

4.1 Experimental setup and measurements

The experiments were conducted in a closed-loop water tunnel. The flow speed can be changed from 0.05 to 4 m/s, with the turbulent intensity less than 0.5%. As shown in Figure 4.1(b), a circular cylinder of diameter $D = 22$ mm and length $L = 430$ mm was vertically put at the centre of the test section, resulting in a blockage ratio of 7.3%. The total mass of the test system, including the cylinder and the supporting moving shaft, was approximately $m = 9.8$ kg, corresponding to a mass ratio $m^* = 4m/\pi\rho D^2L \approx 54$, where ρ represents the flow density. Through free decay tests, the system's structural damping was determined as $\zeta_s = 0.6\%$, such that $m^*\zeta_s = 0.324$, and the natural frequency was identified as $f_n = 0.97$ Hz.

To convert the mechanical energy of the oscillating cylinder into electricity, a tuned-mass-damper (TMD) system was installed in line with the cylinder, which consists of a mass block vertically supported by a steel beam of 320 mm long, 25 mm wide and 0.75 mm thick. A piezoelectric macro-fiber composite sheet (M8514P2) of 100 mm long, 14 mm wide and 0.35 mm thick was attached to the root of the steel beam. Therefore, electric voltage can be generated by the piezoelectric sheet through the deformation of the steel beam. In order to generate large deformation, we attached a suitable mass block (137 g) on the tip of the steel beam, such that the natural frequency of the beam is around 1.0 Hz, which is almost identical to the natural frequency of the tested cylinder system (0.97 Hz) and hence is beneficial to achieve large voltage output through resonance.

Four different configurations were considered, i.e., the plain cylinder (serving as the baseline case), the cylinder attached with two windward fins, with two leeward fins, and with four fins (i.e., two windward and two leeward), as sketched in Figure 4.1(a). The two windward fins were installed at circumferential angles $\theta = 60^\circ$, whereas the two leeward fins were installed at $\theta = 120^\circ$. According to previous results on a square cylinder, fins at $\theta = 60^\circ$ performed the best on promoting FIV, while fins at $\theta = 120^\circ$ performed the worst^[97, 98]. The test conditions for the four cylinders are listed in Table 4.1. All cases were tested in water flow of speed varying from $U_\infty = 0.066$ to 0.517 m/s, corresponding to the reduced velocity $U_r = U_\infty/f_n D \approx 2 \sim 25$ and the Reynolds number $Re = U_\infty D/\nu \approx 1,500 \sim 11,400$, where ν is the viscosity of the water. The incident angle was set as $\alpha = 0^\circ$, and the fin length was set as $L = 0.25D$. As the proposed concept, the four-fin cylinder was also tested with three more different incident angles, i.e., $\alpha = 2.5^\circ$, 5° and 8° , and one more fin length, i.e., $L = 0.5D$.

A circuit with one end connecting to the piezoelectric sheet and the other end connecting to an electrical load was used for voltage measurement on the electrical load. To supplement the experimental data and provide detailed flow information, computational-fluid-dynamics (CFD) calculations were also performed by ANSYS Fluent, which are well described and validated in Section 4.2.

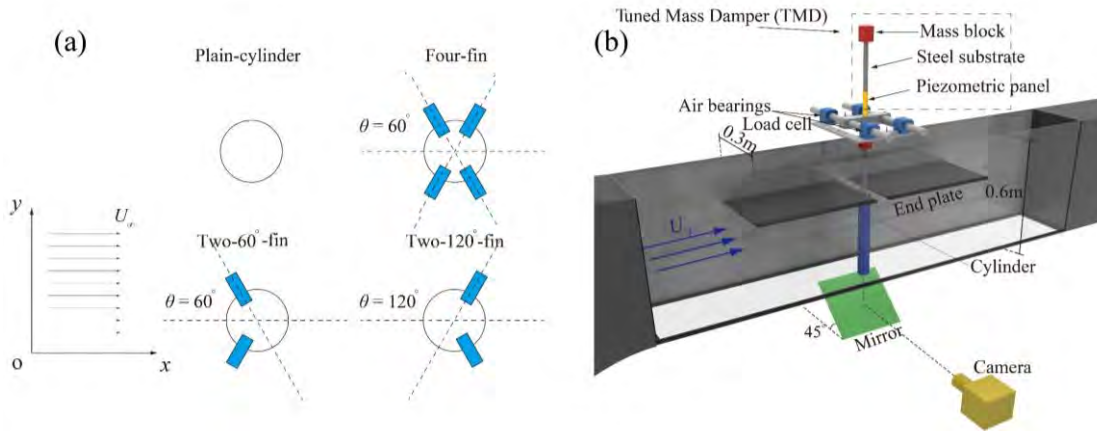


Figure 4.1 Sketches of (a) the four cylinders used in the experiments and (b) the test rig. Where the displacement was recorded by a high-speed camera, and the force was measured by a load cell.

Table 4.1 Summary of test cases.

Cases	Reduced velocity (U_r)	Incident angle (α)	Length of fin (L/D)
Plain-cylinder	2 ~ 25	-	0
Four-fin	2 ~ 25	0°, 2.5°, 5°, 8°	0.25, 0.5
Two-leeward-fin	2 ~ 25	0°	0.25
Two-windward-fin	2 ~ 25	0°	0.25

4.2 CFD setup and validation

ANSYS Fluent was utilized to conduct the CFD simulations. The computational domain is presented in Figure 4.2(a). The length and width of this domain are $40D$ and $13.6D$,

respectively. This width is set the same as that of the water channel. The cylinder is located $13.6D$ downstream from the inlet. A uniform velocity inlet condition is defined at its inlet boundary, while the pressure out condition is specified at its outlet boundary. The cylinder and fins are no-slip walls, and the upper and lower sides of the computational domain are also set as no-slip walls. The diameter of the dynamic mesh region is set as $5D$, with its origin fastened at the centre of the cylinder. The computational domain is discretized into structured tetrahedral meshes in the dynamic mesh region and triangular meshes outside, with 20,766 grid nodes. The mesh around the cylinder is a polar grid, and the minimum grid size is 1×10^{-5} m with a ratio of 1.05 (Figure 4.2 b&c).

The simulation parameters are identical with those in the experiment (without TMD system), i.e., $m^* = 54$, $f_n = 0.97$ and $\zeta_s = 0.6\%$. Three sets of meshes and three different timesteps are adopted to examine the grid and time convergence, as depicted in Tables 4.2 & 4.3. All three sets of meshes meet the $y^+ < 1$ condition on the cylinder surface. For time step $\Delta t = 0.002$ s, the difference of y_{rms} between Mesh 2 and Mesh 3 is 0.24%, and the Strouhal number St does not change. Besides, the discrepancy of y_{rms} and St between Mesh 1 and Mesh 3 is 2.38% and 1.07%, which is obviously improved. The improvement of y_{rms} between $\Delta t = 0.002$ s and 0.001s is not significant based on Mesh 2. Thus, we finally adopted Mesh 2 and $\Delta t = 0.002$ s in the present calculations.

The y_{rms} values obtained by CFD simulation are compared with the experimental data, as listed in Table 4.4. For the plain-cylinder case, y_{rms} are consistent with each other quite well, i.e., $0.43D$ in the experiment and $0.42D$ in the simulation. The simulated y_{rms} generally follows the trend of y_{rms} obtained in the experiments, i.e., the FIV system gets the largest y_{rms} in the two-windward-fin case and the smallest in two-leeward-fin case. The difference in y_{rms} between

the experiment and simulation values may be caused by the damping adopted: although the damping adopted in the simulations is a constant, it cannot be a perfect constant in the experiments.

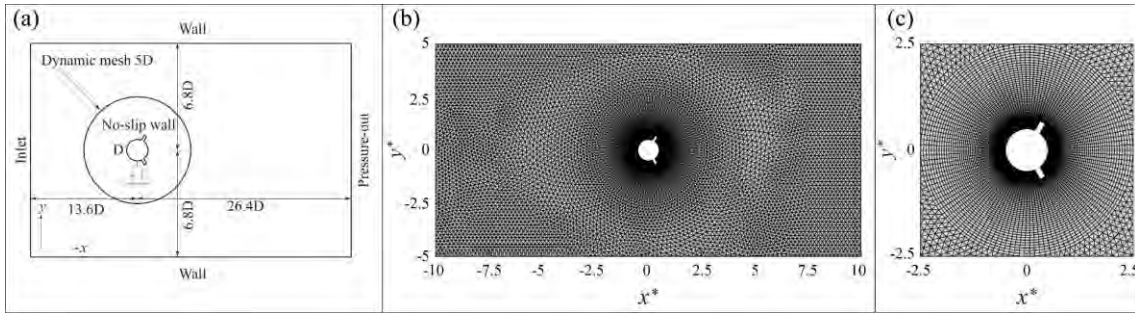


Figure 4.2 Numerical simulation model and calculation mesh.

Table 4.2 Simulated results of a circular cylinder with three different densities of meshes.

Cases	Grid No.	Δt	y_{rms}	St	y^+
Mesh 1	13,844	0.002s	0.411 (2.38%)	0.185 (1.07%)	< 1
Mesh 2	20,766	0.002s	0.420 (0.24%)	0.187 (0%)	< 1
Mesh 3	31,149	0.002s	0.421	0.187	< 1

Table 4.3 Time step independence validation results based on Mesh 2.

Case	Δt	y_{rms}	St
Mesh 2	0.004s	0.417 (1.18%)	0.187 (0%)
	0.002s	0.420 (0.47%)	0.187 (0%)
	0.001s	0.422	0.187

Table 4.4 Displacement comparison between experimental and numerical results at typical cases.

Cases	U_r	Experiments (y_{rms})	CFD (y_{rms})
Plain-cylinder	5.3	0.43D	0.42D
Four-fin	10.0	0.57D	0.63D
Two-windward-fin	10.0	1.31D	1.36D
Two-leeward-fin	10.0	0.012D	0.019D

4.3 System dynamics

Figure 4.3(a) presents the root-mean-square values of the dimensionless vibration displacement, y_{rms} , against the reduced velocity, U_r , for the four cylinders. As introduced in Chapter 3, a typical VIV response can be observed for the plain cylinder case. The dynamics of the cylinder was drastically changed when fins were deployed. When two fins were deployed at the windward side, y_{rms} sharply increases once U_r exceeds a threshold of 5.35 and does not seem to reach its level off in the current U_r range, revealing great energy harvesting potentials, as shown in Figure 4.3(a). This is a typical galloping response, as has been reported in the previous literature^[20, 29, 30, 36]. However, when the two fins were deployed at the leeward side, i.e., in the two-120°-fin case, the cylinder's oscillation is almost fully suppressed. The huge difference between these two two-fin cases suggests that, although very promising, the energy harvesting system with two fins attached at the windward side is only unidirectional. As a trade-off between these two extreme cases, the four-fin case experienced intermediate oscillations in a broad U_r range, showing a mild galloping response. This observation is similar to that reported by Hu et al.^[15] and Wang et al.^[98]. Due to the symmetric arrangement of the four fins, it is very suitable to extract energy from tidal flows or onshore/offshore winds where the flow direction usually switches between two opposite directions.

For the four-fin cylinder, Figure 4.3(b) further shows the effects of α , the incident angle, and L/D , the fin length, on y_{rms} . It is seen that when α is relatively small, i.e., $\alpha = 0^\circ$ and 2.5° , the system exhibits gallop-type dynamics, while when α is relatively large, i.e., $\alpha = 8^\circ$, the system exhibits VIV-type dynamics. At the intermediate $\alpha = 5^\circ$, the VIV-gallop hybrid dynamics appears. That is, y_{rms} gradually drops after reaching its peak, and increases again at large U_r . In general, y_{rms} reduces with α , especially at large U_r . These observations suggest that

the current system is robust in flow energy harvesting when the incoming flow deviates from the designed direction within $\pm 5^\circ$, but its performance deteriorates at larger incident angles.

It is also seen from Figure 4.3(b) that the increase of L/D from 0.25 to 0.5 can generally increase y_{rms} , especially when α is relatively small. This is consistent with what has been reported by Hu et al.^[97], where this increasing trend was observed in a smaller fin length range, i.e., from 0.025 to 0.2, at $\alpha = 0^\circ$. At the larger incident angle, i.e., $\alpha = 8^\circ$, the $y_{rms}-U_r$ responses become the VIV type. In this scenario, the increase of L/D not only enhances the y_{rms} peak, but also pushes the onset of the y_{rms} peak to larger U_r values, which is not surprising since the attachment of the four fins increases the effective diameter of the cylinder.

The change of the incident angle and fin length also changes the system's other dynamic characteristics, such as the vibration frequency and the force-displacement phase angle. As shown in Figure 4.3(c), the plain cylinder's vibration frequency $f^* = f/f_n$, where f is the cylinder's dominant oscillation frequency, is locked around unity regardless of U_r . This is attributed to the large inertia ($m^* = 54$) adopted in the current system, such that the system's frequency is dominated by its own inertia and stiffness, rather than the excitation of the fluid force. When the four fins are attached with zero incident angle, the dominant vibration frequency reduces to $f^* \approx 0.90$ for the $L/D = 0.25$ case and $f^* \approx 0.85$ for the $L/D = 0.5$ case, regardless of U_r . This is probably caused by the increased added mass brought by the fins. As α increases, the vibration frequency gradually increases towards unity, reflecting the reduction of added mass when the deviation of incident angle breaks the symmetry of the fins on the cylinder.

The variations of force-displacement phase angle φ are compared in Figure 4.3(d). Here φ is evaluated as $\varphi = \arccos R(C_y, y)$, where $R(C_y, y)$ is the correlation coefficient between the transverse hydrodynamic force C_y and the oscillation displacement y . For the plain cylinder, φ

suddenly jumps from around 0° to about 180° at the onset of VIV ($U_r \approx 5.1$), reflecting the occurrence of lock-in phenomena. After the lower branch ($5.3 < U_r \leq 10.1$), φ gradually decreases to around 90° . Similar trends are also observed for the $\alpha = 8^\circ$ case, regardless of the fin length. For the $\alpha = 0^\circ$ and 2.5° cases where galloping occurs, φ generally remains at low values, revealing the dominant fluid-to-structure energy flow in this type of FIV phenomenon. For the $\alpha = 5^\circ$ cases, it is interesting to see φ jumps and then remains at unity in the $L/D = 0.25$ case, whereas φ remains at very low values in the $L/D = 0.5$ case. This observation confirms the $\alpha = 5^\circ$ configuration is near the VIV-gallop boundary.

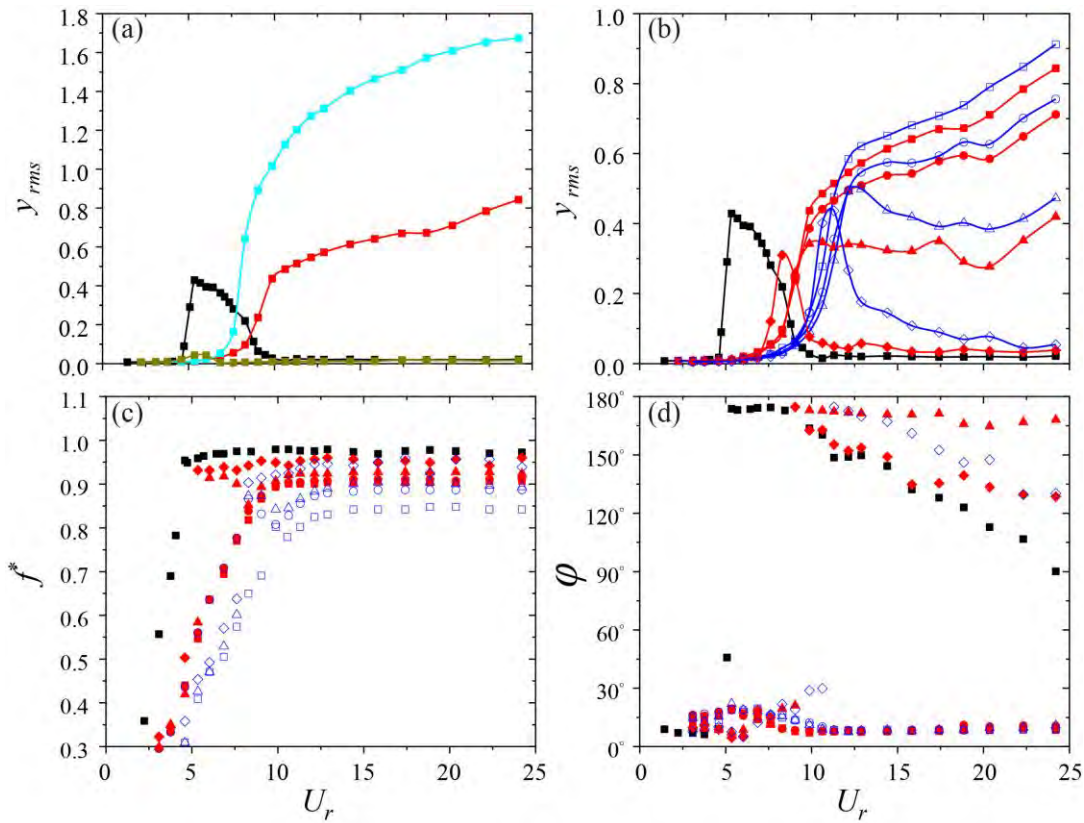


Figure 4.3 Dynamic response comparison: (a) y_{rms} of the four typical cases, \blacksquare plain-cylinder case, \blacksquare four-fin case, \blacksquare two-windward-fin case, \blacksquare two-leeward-fin case; (b), (c) & (d) y_{rms} , dimensionless frequency f^* and phase angle φ of the four-fin case with different α and L/D , \blacksquare 0° -0.25, \blacksquare 2.5° -0.25, \blacktriangle 5° -0.25, \blacklozenge 8° -0.25, \square 0° -0.5, \square 2.5° -0.5, \triangle 5° -0.5, \lozenge 8° -0.5.

To unveil the underlying physics associated with the change of dynamics for cylinders with different fin settings, CFD simulations were conducted to show more details. The vortex structures and pressure fields around the four cylinders at selected instants in a half vibration period, from the top extreme to the bottom extreme, are presented in Figures 4.4 and 4.5, respectively. For the plain cylinder oscillating with its maximum amplitude at $U_r = 5.3$, shear layers are alternatively formed and shed from the top and bottom sides of the vibrating cylinder, generating a pair of vortices in one vibration period, and forming the classical 2S vortex mode (Figure 4.4a). A corresponding low-pressure region emerges when the shear layer rolls up into a vortex, which is initiated from the top/bottom side of the cylinder and then gradually develops to the rear side, as shown in Figure 4.5(a). These alternatively appearing low-pressure regions always force the cylinder to return to its equilibrium position (i.e., $y^* = 0$). That is, they accelerate the cylinder when it is moving towards the equilibrium position, and decelerate the cylinder when it is moving away. As such, two-way energy transfer occurs between the flow and the cylinder system.

For the cylinder attached with two leeward fins operating at $U_r = 10.0$, the room left for the development of shear layers is limited by the fins. Instead of separating from the cylinder surface, these shear layers are firstly pushed away by the two fins and then forced to separate at the fin tips, forming larger and stronger vortex pairs in the wake (see Figure 4.4b). The associated low-pressure regions, although very strong, are then mainly formed after the two fins, more on the back side of the cylinder (Figure 4.5b). As such, the cylinder experiences much less net vertical force compared to the plain cylinder. This explains why the two-leeward-fin cylinder exhibits the least vibration among all four cases. Besides, the 2S vortex shed mode does not change compared with the plain cylinder case.

When the two fins are installed on the windward side, flow separation is early promoted at the fin tips. The separated shear layer on the bottom side quickly re-attaches on the cylinder's downstream convex surface, and are further elongated and bent by the cylinder's downward motion, as revealed at instant $2T/8$ in Figure 4.4(c). The bent of the shear layer generates a very strong low-pressure region right on the cylinder's bottom side, as shown in Figure 4.5(c), producing a very large net vertical force. This net vertical force seems nearly in phase with the cylinder's displacement (consistent with the observation in Figure 4.3d), and hence results in a much larger vibration amplitude, as shown in Figure 4.2(a). That is, the cylinder is undergoing galloping. Furthermore, the interaction of the shear layers in the near wake of the two-windward-fin case is significantly stronger than the plain-cylinder and the two-leeward-fin cases. And a complicated flow field is formed, i.e., four vortices shed from the cylinder per half circle (Figure 4.4c).

As for the four-fin cylinder, the two windward fins promote flow separation at the fin tips, while the two leeward fins force the re-attached shear layer, if any, to separate again, as shown in Figure 4.4(d). Similar to the two-windward-fin cylinder case, a strong low-pressure region around the bottom side of the cylinder is formed due to the lower-side separated shear layer reattaching to the cylinder as it moves downward, as revealed at instant $2T/8$ in Figure 4.5(d). The lower leeward fin disrupts this reattachment and mitigates further bending of the shear layer along the cylinder surface. As such, the low-pressure region is mainly confined between the windward and leeward fins, and hence becomes smaller and weaker than in the two-windward-fin cylinder case. This generates reduced pressure imbalance in the vertical direction, resulting in mild y_{rms} (Figure 4.2a).

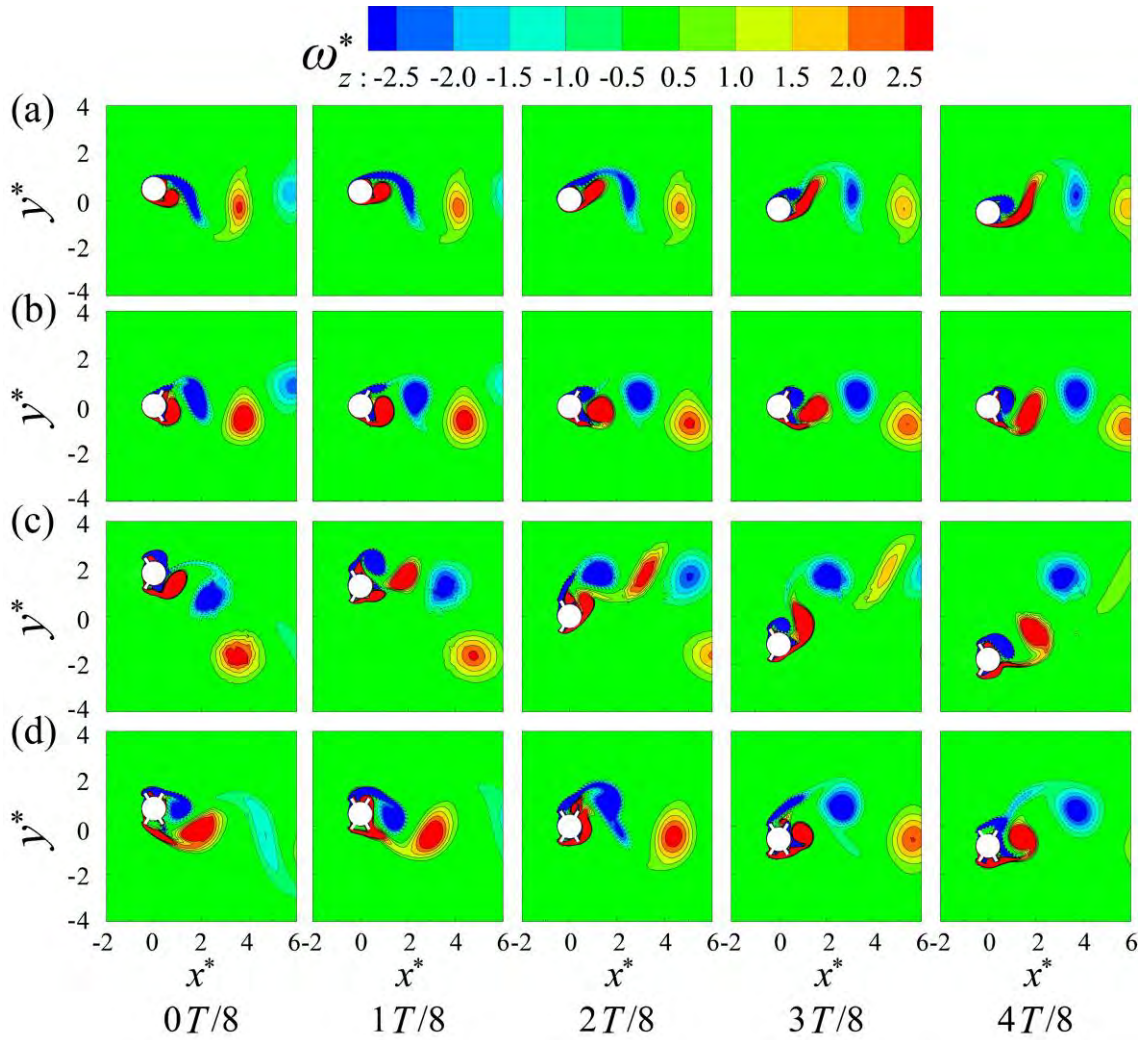


Figure 4.4 Instantaneous vortex patterns around (a) plain cylinder, $U_r = 5.3$; (b) two-windward-fin cylinder, $U_r = 10.0$; (c) two-leeward-fin cylinder, $U_r = 10.0$; (d) four-fin cylinder, $U_r = 10.0$. $0T/8$, $2T/8$ and $4T/8$ represent the instants when the cylinder is at the highest position, moving downward through the equilibrium position, and at the lowest position, respectively. ω_z^* is the spanwise vorticity normalized by D and U_∞ .

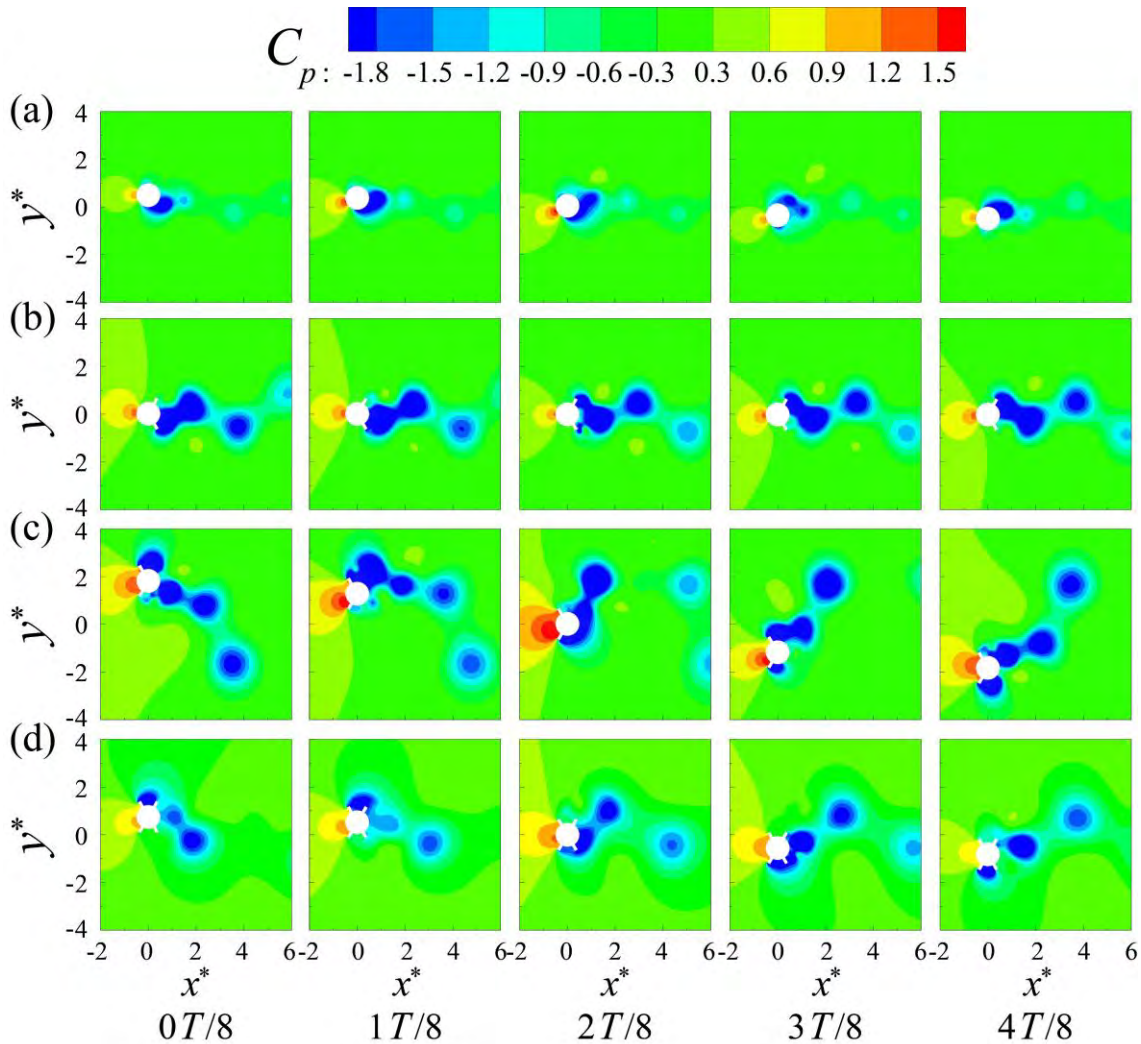


Figure 4.5 The instantaneous pressure field at typical cases: (a) plain-cylinder case, $U_r = 5.3$; (b) two-windward-fin case, $U_r = 10.0$; (c) two-leeward-fin case, $U_r = 10.0$; (d) four-fin case, $U_r = 10.0$.

As depicted in Figure 4.1(b), the springs were suspended using air bearings, while the coupling system comprising the cylinder and fin was interconnected via the load cell, which was positioned below the air bearings. In our experimental setup, we modulated the angle of attack (AOA) by means of cylinder rotation. However, we seek to examine the implications of rotating the entire system, a scenario that aligns more closely with practical engineering applications but poses challenges in terms of angle control. Hence, we compared the outcomes obtained from rotating the cylinder to those derived from rotating the air bearings, as illustrated

in Figure 4.6, where the case of $L/D = 0.5$ at $\alpha = 0^\circ$ served as baseline cases. Notably, regardless of whether the cylinder or the entire system was subjected to a rotational displacement of 2.5° , the amplitude response consistently exhibited a slight reduction compared to the $\alpha = 0^\circ$ condition. Besides, the results of these two different rotation ways accord reasonably with each other. Thus, it is reasonable for us to rotate the cylinder when we change the AOAs.

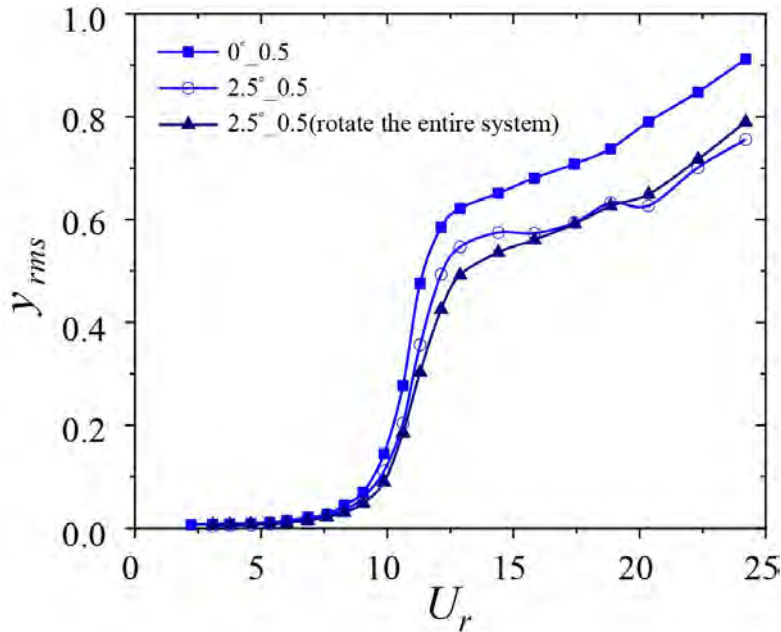


Figure 4.6 Comparison of the y_{rms} of four-fin case at $L/D = 0.5$: \circ rotate the cylinder by 2.5° and \blacktriangle rotate the air-bearing systems by 2.5° . Where \blacksquare denotes the y_{rms} of four-fin case at $\alpha = 0^\circ$.

4.4 Power extraction performance

The output voltage depends on the load resistance deployed in the piezoelectric circuit. Figure 4.7(a) presents the variation of the rms value of output voltage V_{rms} from the four-fin cylinder against the load resistance R at a selected wind speed ($U_r = 14.5$). It is seen that V_{rms} first increases and then decreases with R . The output voltage reaches its maximum value 5.85

V when $R = 30 \text{ M}\Omega$. Therefore, we chose $R = 30 \text{ M}\Omega$ as the load resistance to compare the energy harvesting performance of the four-fin cylinder cases.

Figure 4.7(b) presents the generated voltage V_{rms} with different fin length L/D and incident angle α . The maximum V_{rms} value (7.37 V) appears in the $\alpha = 0^\circ$ and $L/D = 0.25$ case, which is about 2.7 times the peak voltage in the plain cylinder case. The voltage trends seem similar to the y_{rms} trends shown in Figure 4.3(b). That is, the $\alpha = 0^\circ$ and 2.5° cases show monotonically increasing V_{rms} against U_r , whereas the $\alpha = 8^\circ$ and $L/D = 0.25$ case shows a similar variation trend as that for the plain cylinder. Differences are also observed. First, the $L/D = 0.5$ cases may not always perform better than the $L/D = 0.25$ cases, e.g., the two $\alpha = 0^\circ$ cases. Second, the $\alpha = 5^\circ$ and $L/D = 0.25$ case exhibits the VIV type response, instead of the VIV-gallop hybrid response in its vibration amplitude. Third, the $\alpha = 8^\circ$ and $L/D = 0.5$ case exhibits the VIV-gallop hybrid response instead of the VIV type response in its vibration amplitude. All these changes can be attributed to the attachment of the TMD system to the cylinder, which, although less dominant, makes dynamics of the integrated system slightly different from the dynamics of pure cylinder system.

Figure 4.7(c) further compares the mean power (defined as $P_{avg} = V_{rms}^2 / R$) among the four-fin cases. The overall trends for P_{avg} are similar to those for V_{rms} . Compared with the plain cylinder case, the maximum P_{avg} appearing in the $\alpha = 0^\circ$ and $L/D = 0.25$ case at $U_r = 24.2$ is about $1.81 \mu\text{W}$, about 7.2 times the peak power in the plain cylinder case. The output power density is defined as $P_d = P_{avg} / V_P$, and V_P is the volume of the piezoelectric sheets^[164]. P_d for our plain-cylinder case is about 0.51 mW/cm^3 (at $U = 0.11 \text{ m/s}$), smaller than that reported by Sun et al.^[165] ($P_d = 1.949 \text{ mW/cm}^3$ at $U = 0.48 \text{ m/s}$), Wang et al.^[98] ($P_d = 4.76 \text{ mW/cm}^3$ at $U = 1.5 \text{ m/s}$), and Hu et al.^[97] ($P_d = 7.89 \text{ mW/cm}^3$ at $U = 2.1 \text{ m/s}$). This suggests that our setup is not

optimized and has a large room for improvement. It is not surprising because in our case the piezoelectric sheet was attached only at one end of the vibration, while in their cases it was attached at both ends. Besides, this study is not focusing on optimizing the performance of the harvesters; we aim to conceptualize the higher performance of this bi-directional flow-energy harvester compared to the plain-cylinder case.

The ratio of improvement goes to 624% for four-fin case at $U_r = 24.2$ (Figure 4.7d). Where the ratio of improvement P_V is defined as follows:

$$P_V = \frac{P_{avg} \text{ of cases with fins} - \text{peak of } P_{avg} \text{ for the plain cylinder}}{\text{peak of } P_{avg} \text{ for the plain cylinder}} \quad (4-1)$$

As shown in Figure 4.7(d), the performance enhancement zone for $L/D = 0.25$ and 0.5 at $\alpha = 0^\circ$ starts from U_r great than 9.0 and 10.6 , respectively, indicating that all four-fin cases subjected to $\alpha = 0^\circ$ are beneficial for harvesting energy compared with VIV based energy harvester (plain-cylinder case). The maximal P_V for $L/D = 0.5$ at $\alpha = 0^\circ, 2.5^\circ$ and 5° is about 591% , 440% and 18% , which indicates its potential in extracting energy from air/water flows from two opposite directions and robust of flow directions.

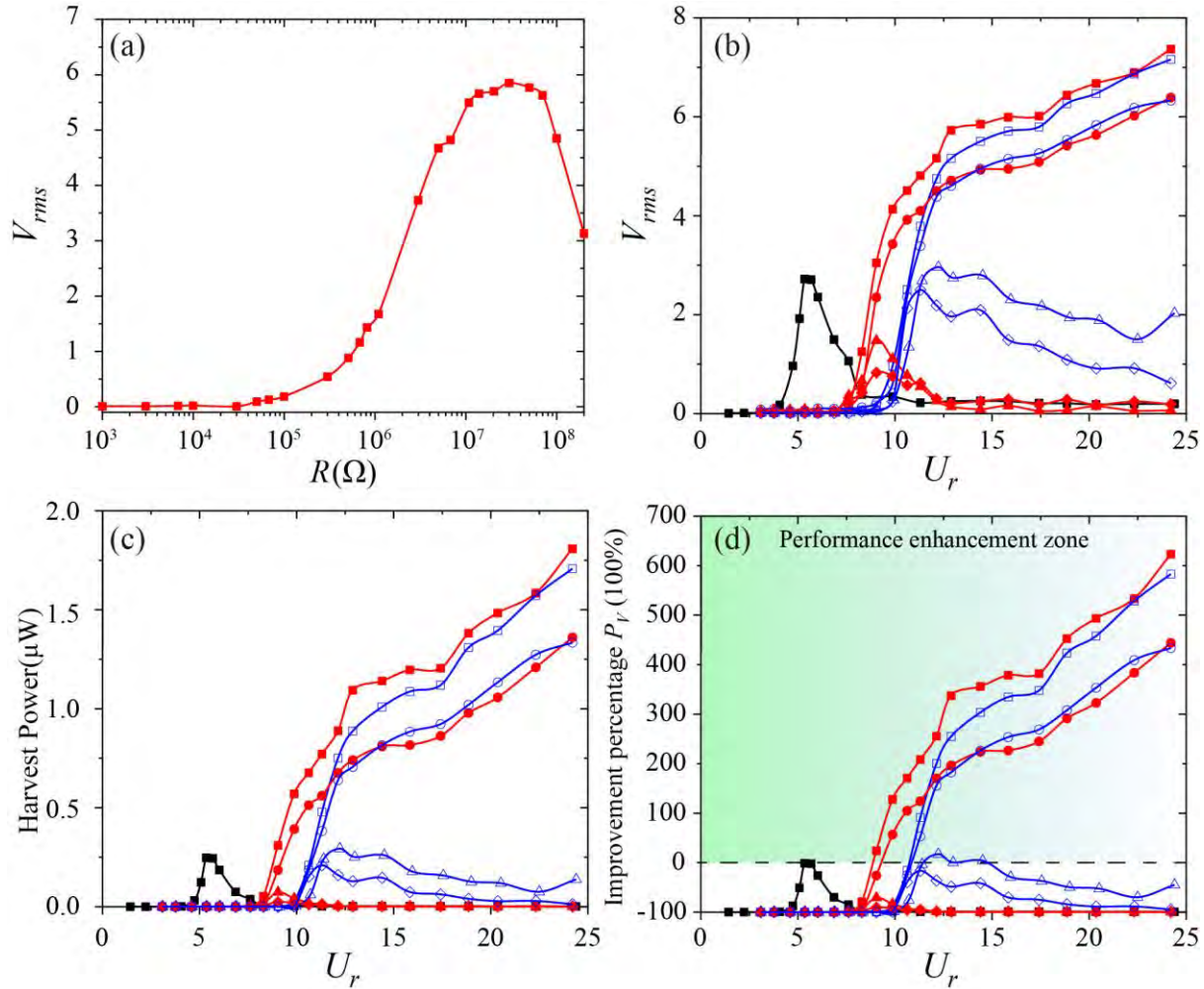


Figure 4.7 (a) variation of the rms voltage output V_{rms} of four-fin case with load resistance R ; (b), (c) & (d) variation of V_{rms} , P_{avg} , and the performance enhancement percentages of P_V for the four-fin case with different α and L/D . The symbols are identical to Figure 4.3.

4.5 Remarks

We proposed a new flow-energy harvester by attaching four small fins on a circular cylinder, two on the windward side and two on the leeward side, which is able to collect energy from ambient air/water flows from two opposite directions. A prototype has been developed and its FSI dynamics and energy harvesting performance were studied in a water channel. CFD

simulations were also conducted to reveal the underlying physics. Major findings are summarized as follows:

- (1) The four-fin cylinder combines the features of both the two-windward-fin and the two-leeward-fin cylinder designs. The two windward fins are able to promote vibration by converting the dynamics of the cylinder from VIV to galloping, while the two leeward fins only suppress the vibration. The combination of these four fins renders the cylinder with the capability of harvesting flow energy in a broad velocity range from two opposite directions. This great feature makes this concept suitable to operate at sites where the flow periodically switches between two opposite directions, such as in tidal flows.
- (2) Compared to the plain cylinder, the four-fin cylinder is able to harvest much more flow energy in a much broader velocity range by promoting instead of suppressing galloping, although it requires a larger cut-in speed to operate. Within the current flow speed range, the maximum voltage and power outputs are about 7.37 V and 1.81 μW , respectively, about 2.7 and 7.2 times the peak values for the plain cylinder. Since the maximum tested speed in the present experiment is only about 0.5 m/s, the energy harvesting performance can be further improved at higher flow speeds.
- (3) This concept is robust to flow disturbance in terms of both the speed and direction of flows. On the one hand, with a broad operational velocity range, it can sustain flows with speed fluctuations. On the other hand, it works well in flows whose direction slightly deviates from the prevailing direction (within $\pm 5^\circ$).

- (4) The fin length also affects the performance of the four-fin cylinder. The increase of the fin length generally promotes the vibration, but pushes the cut-in speed for galloping to larger values.

Although only demonstrated in laboratory settings, the concept can be easily scaled up to operate in actual river and ocean flows. Besides, the concept can be arrayed in different configurations to form a farm, which will be investigated in our future studies.

Chapter 5 FIV of a cactus-shaped cylinder

Inspired by the natural succulents of *Euphorbia Trigona* and *Euphorbia Abyssinica*, this chapter investigates the FIV performance of a nature-inspired cylinder equipped with three and four ribs, using both experimental and numerical means. This study also examines the impact of varying AOAs on the FIV and hydrodynamic performance of the cylinder, with a plain cylinder serving as the benchmark. The primary objective of this study is to offer valuable insights into the FIV behavior of cylinders featuring nature-inspired rib structures and the corresponding flow dynamics under different AOAs.

5.1 Experimental setup and measurements

A series of experiments were conducted, in which a circular cylinder with a diameter (D) of 44 mm and length (H) of 440 mm was vertically placed at the center of the test section of a water tunnel (refer to Figure 5.1b). Since the blockage ratio (BR) of 14.6% is not small, to correct the lift and drag coefficients, we applied extensions of the Maskell's theory^[166, 167]. Taking the drag correction as an example, the empirical blockage factor ε_M is calculated in eqn. (5-1).

$$\varepsilon_M = 0.96 + 1.94 \exp[-0.06(AR)] \quad (5-1)$$

where $AR (=H/D)$ is the aspect ratio. The additive correction to drag ΔC_{DM} is calculated as follows:

$$\Delta C_{DM} = \overline{C_d} \left[\frac{1}{1+x} + \frac{1}{2x} (1 - \sqrt{1+4x}) \right] \quad (5-2)$$

where $x = \varepsilon_M * BR * \overline{C_d}$. The distortion effects C_{DcM} can be calculated as:

$$C_{DcM} = \frac{\overline{C_d}}{1 + \varepsilon_M * BR * \overline{C_d}} \quad (5-3)$$

As such, the corrected $\overline{C_{dc}}$ can be obtained by:

$$\overline{C_{dc}} = \frac{\overline{C_d}}{1 + \varepsilon_M * BR * (C_{DcM} - \Delta C_{DM})} + \Delta C_{DM} \quad (5-4)$$

Free decay tests conducted in stationary water revealed that the system's structural damping is $\zeta_s = 0.6\%$, yielding a mass-damping product of $m^* \zeta_s = 0.282$. The system's natural frequency in stationary water was determined to be $f_n = 1.025$ Hz.

Three types of cylinders were tested, i.e., a three-rib cylinder, a four-rib cylinder and a plain cylinder, as exhibited in Figure 5.1(a). The AOA $\alpha = 0^\circ$ is defined in such a way that one of the ribs points upstream. The rib width is $0.075D$, and the radius of the chamfer between adjacent ribs is $0.65D$ and $0.15D$ for the three-rib and four-rib cylinders, respectively. The shapes of the three/four-rib cylinders are identical to those used by Zhdanov & Busse^[17], and Zhdanov et al.^[107].

Note that, the three- and four-rib cylinders have 3- and 4-fold rotational symmetry, respectively. As such, the range of AOAs to be tested can only be from 0° to 60° for the three-rib cylinder and from 0° to 45° for the four-rib cylinder, as illustrated in Table 5.1. All cases were tested in water flows of speeds ranging from $U_\infty = 0.066$ to 0.517 m/s, corresponding to the reduced velocity $U_r = U_\infty / f_n D \approx 2 \sim 12$ and the Reynolds number $Re = U_\infty D / \nu \approx 2,900 \sim$

24,500. The force and oscillation displacement measurement methods were identical to that in Section 3.1.

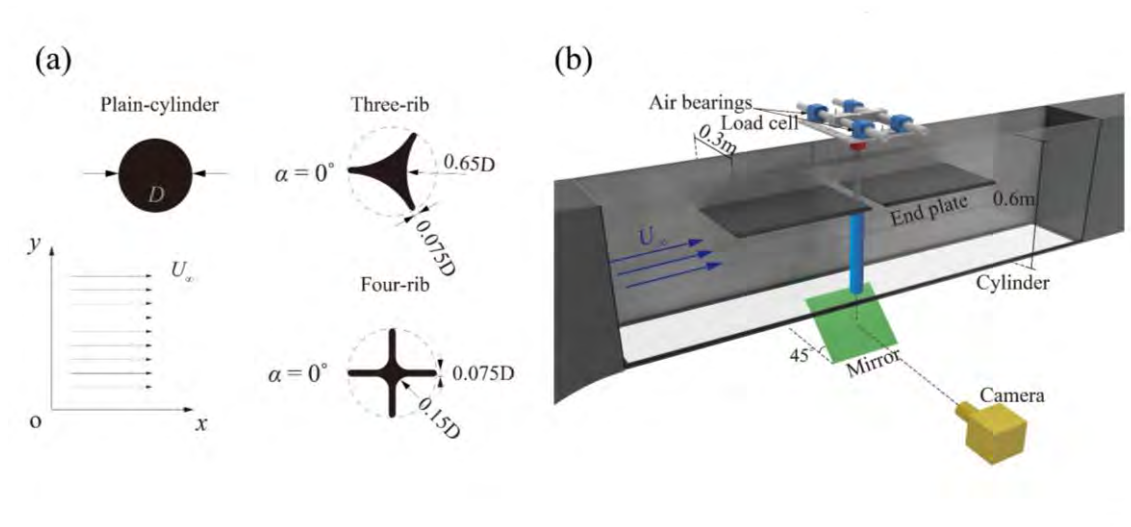


Figure 5.1 (a) the sketch of the typical tested cases; (b) test rig installed in a closed-loop water channel.

Table 5.1 Experimental cases.

Cases	U_r	AOA (α)
Plain-cylinder	2 ~ 12	0°
Three-rib	2 ~ 12	0°, 15°, 30°, 45°, 52.5°, 60°
Four-rib	2 ~ 12	0°, 7.5°, 15°, 30°, 45°

5.2 CFD setup and validation

To obtain detailed flow information around a FIV cylinder for supporting experimental observations, CFD simulations were conducted using ANSYS Fluent commercial software. Similar to that reported in Section 3.2, the present simulation was based on SST $k-\omega$ model and overset mesh. The computational domain and boundary conditions are sketched in Figure 5.2. The length and width of the domain are $35D$ and $6.8D$, respectively. The cylinder is located $10D$ downstream from the inlet boundary, which is set as a uniform flow velocity U_∞ , and its

right boundary is defined as pressure-out. The boundaries of the cylinder, bottom and top sides, are set as no-slip walls. Thus, this domain reproduces the experimental conditions of the water tunnel. The overset mesh (rectangle zone in Figure 5.2a&c) is applied near a cylinder, which moves with the cylinder and interacts with the stationary background mesh to exchange flow information. The total numerical mesh count (N) is 107,222, and the mesh around the cylinder was refined to guarantee $y^+ < 1$ (see Figure 5.2b). The Newmark- β method was used to resolve the dynamics of the cylinder when subjected to hydrodynamic forces.

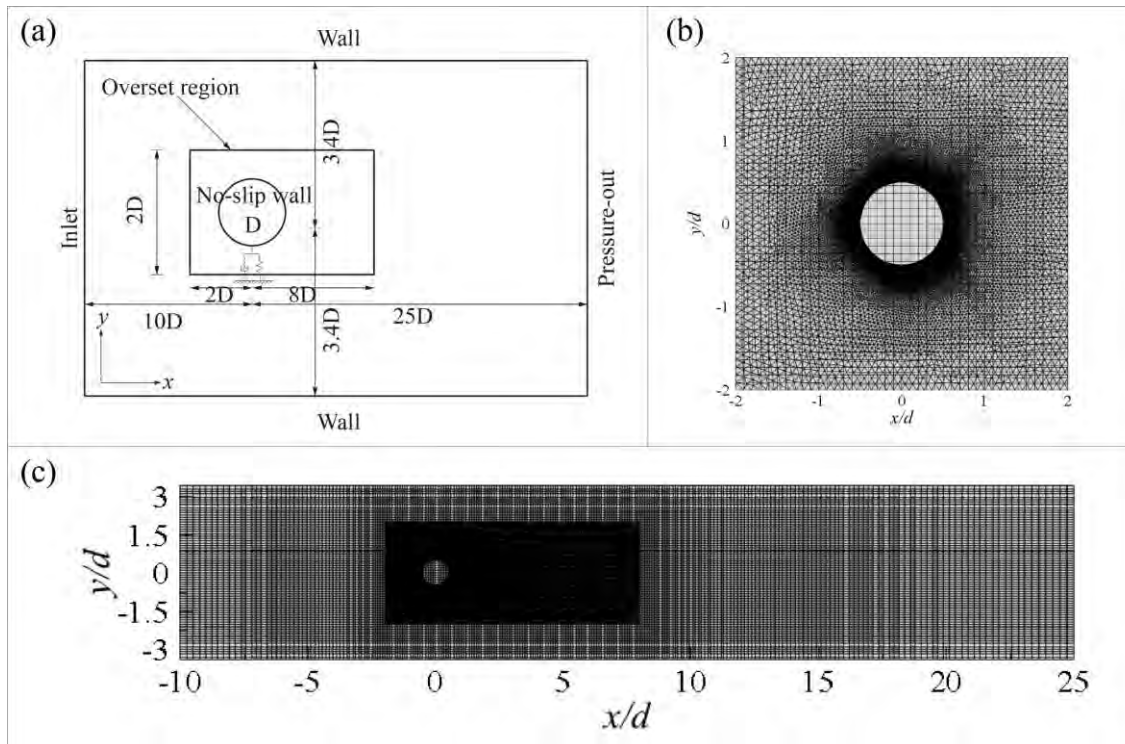


Figure 5.2 Numerical simulation model and calculation mesh.

The effects of mesh refinement and time step size on the simulation results are thoroughly investigated. Four different meshes and three time steps are employed, and the results are presented in Tables 5.2 and 5.3. It is observed that when the time step size is fixed at 0.005s, the difference in the root-mean-square displacement in the transverse direction (v_{rms}) between Mesh 3 and Mesh 4 is approximately 0.49%, and the Strouhal number (St) remains unchanged.

Furthermore, the refinement of y_{rms} between time steps of 0.0025s and 0.005s is not significant based on Mesh 3. These findings suggest that Mesh 3 and a time step size of 0.005s are adequate for accurately simulating an FIV cylinder.

The displacement obtained from numerical simulation is evaluated by comparing it with experimental data in Table 5.4. The slight deviation in y_{rms} between the experiment and simulation outcomes may be attributed to the damping effect. This is attributed to the reality that the actual damping in the experiment may vary, while the damping for simulation is typically presumed to be a fixed value. Figure 5.3 further presents a comparison of the time-history displacement between the experimental and numerical results for typical cases, showing a reasonable agreement in terms of amplitude and frequency. Thus, it is appropriate for us to apply the simulated flow field to explain the mechanism behind the experiment results.

Table 5.2 Simulated results of a circular cylinder with four different densities of meshes.

Cases	N	Δt	y_{rms}	St	y^+
Mesh 1	23,850	0.005s	0.368 (11.11%)	0.167 (0.60%)	< 1
Mesh 2	51,712	0.005s	0.399 (3.62%)	0.168 (0%)	< 1
Mesh 3	107,222	0.005s	0.412 (0.49%)	0.168 (0%)	< 1
Mesh 4	152,716	0.005s	0.414	0.168	< 1

Table 5.3 Time step independence validation results based on Mesh 3.

Case	Δt	y_{rms}	St
Mesh 3	0.01s	0.427 (3.89%)	0.165 (1.78%)
	0.005s	0.412 (0.24%)	0.168 (0%)
	0.0025s	0.411	0.168

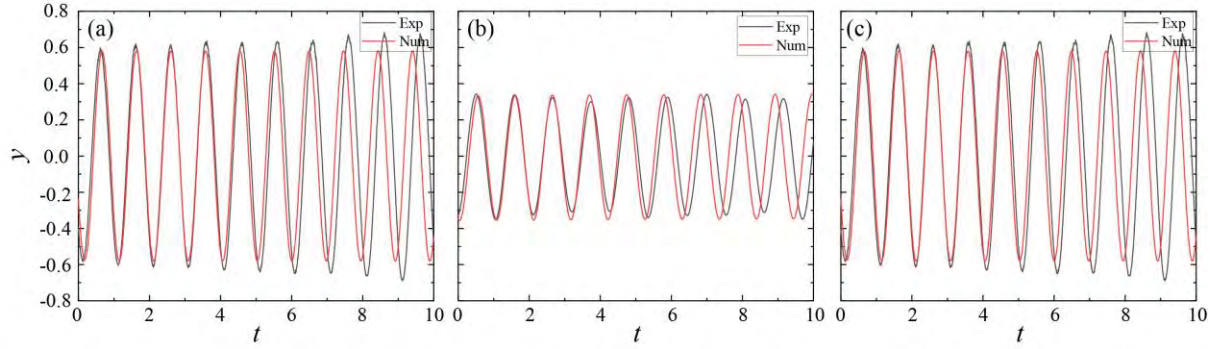


Figure 5.3 Comparison of the time-history displacement between experimental and numerical results at $U_r = 6.15$: (a) plain-cylinder case, (b) three-rib case at $\alpha = 60^\circ$ and (c) four-rib case at $\alpha = 0^\circ$.

Table 5.4 Displacement comparison between experimental and numerical results at typical cases.

Cases	α	U_r	Experimental (y_{rms})	Numerical (y_{rms})
Plain-cylinder	0°	6.15	$0.452D$	$0.412D$
Three-rib	0°	6.15	$0.01D$	$0.01D$
	60°	6.15	$0.206D$	$0.230D$
Four-rib	0°	6.15	$0.432D$	$0.427D$
	45°	6.15	$0.04D$	$0.07D$

5.3 Hydrodynamic performance

Figure 5.4(a) depicts a typical VIV response for a plain cylinder, which exhibits two distinct branches. The initial branch occurs in the range of $2.8 < U_r < 5.4$, during which y_{rms} experiences a sharp increase with the increase of U_r , eventually reaching a peak value of $0.518D$. The lower branch is observed for $5.4 \leq U_r \leq 11.5$, where y_{rms} gradually decreases with U_r . This observation is consistent with that reported in Section 3.3.

The dynamics of the cylinder are drastically changed when the cactus-shaped ribs are applied, as revealed in Figure 5.4. At lower AOAs, i.e., $0^\circ \leq \alpha \leq 30^\circ$, the three-rib cylinder's oscillation is almost entirely suppressed (see Figure 5.4a). This suggests that certain organisms,

such as Euphorbia Trigona, exhibit greater resistance to strong winds originating from lower AOAs. However, when AOA increases to a value between 45° and 60° (i.e., high AOAs), y_{rms} sharply escalates once U_r exceeds a threshold value of 3.6 and does not appear to reach a plateau in the current U_r range, indicating a typical galloping response, in line with the previous studies^[28, 29, 36].

Intriguingly, the dynamics of the three-rib and four-rib cylinders is notably divergent. The effects of AOA on the four-rib cylinder are illustrated in Figure 5.4(b). A typical VIV response is observed at lower AOAs (i.e., $0^\circ \leq \alpha \leq 15^\circ$). Besides, the peak value of y_{rms} and the width of the lock-in area gradually decrease as AOA increases. In $30^\circ \leq \alpha \leq 45^\circ$, the cylinder's oscillation is nearly entirely inhibited, which contrasts with the behavior observed for the three-rib cylinder.

The measured root-mean-square lift $C_{l,rms}$ and mean drag $\overline{C_d}$ are presented in Figure 5.4(c-f). At lower AOAs for the three-rib cylinder and higher AOAs for the four-rib cylinder where the FIV is almost entirely inhibited, $C_{l,rms}$ is markedly lower than that in the plain-cylinder case. This difference is especially pronounced in the region of $4.7 < U_r < 6.9$. The results also reveal that the drag experienced by the vibrating cylinder is closely related to its oscillation amplitude. In the region where FIV is suppressed, both the three-rib and four-rib cylinders exhibit superior drag reduction. Impressively, the maximum $\overline{C_d}$ (or $C_{l,rms}$) reduction for the three-rib and four-rib cylinders can reach up to 51.5% (95.2%) and 50.8% (89.1%), respectively, if compared with the peak values of the plain cylinder (see Figure 5.4). These significant improvements in hydrodynamic performance are believed to be associated with the alteration of flow field and pressure distribution in the near wake.

For the three-rib cylinder undergoing galloping, unlike y_{rms} , $C_{l,rms}$ does not exhibit a monotonic increase with respect to U_r (Figure 5.4c). Instead, $C_{l,rms}$ attains its maximum value

first and then declines with U_r . This is consistent with the observations made by Assi & Bearman^[20], and Sun et al.^[29]. Moreover, the peak of $C_{l,rms}$ increases as AOA increases. Notably, when U_r is large, $C_{l,rms}$ and $\overline{C_d}$ are significantly higher than those for the plain cylinder (Figure 5.4c & 5.4e).

For the four-rib cylinder, its $C_{l,rms}$ variations at lower AOAs are similar to that for the plain cylinder, as illustrated in Figure 5.4(d). However, the peak values are generally smaller. Thus, although not a complete suppression, the four-rib cylinder can still mitigate the FIV compared to the plain cylinder.

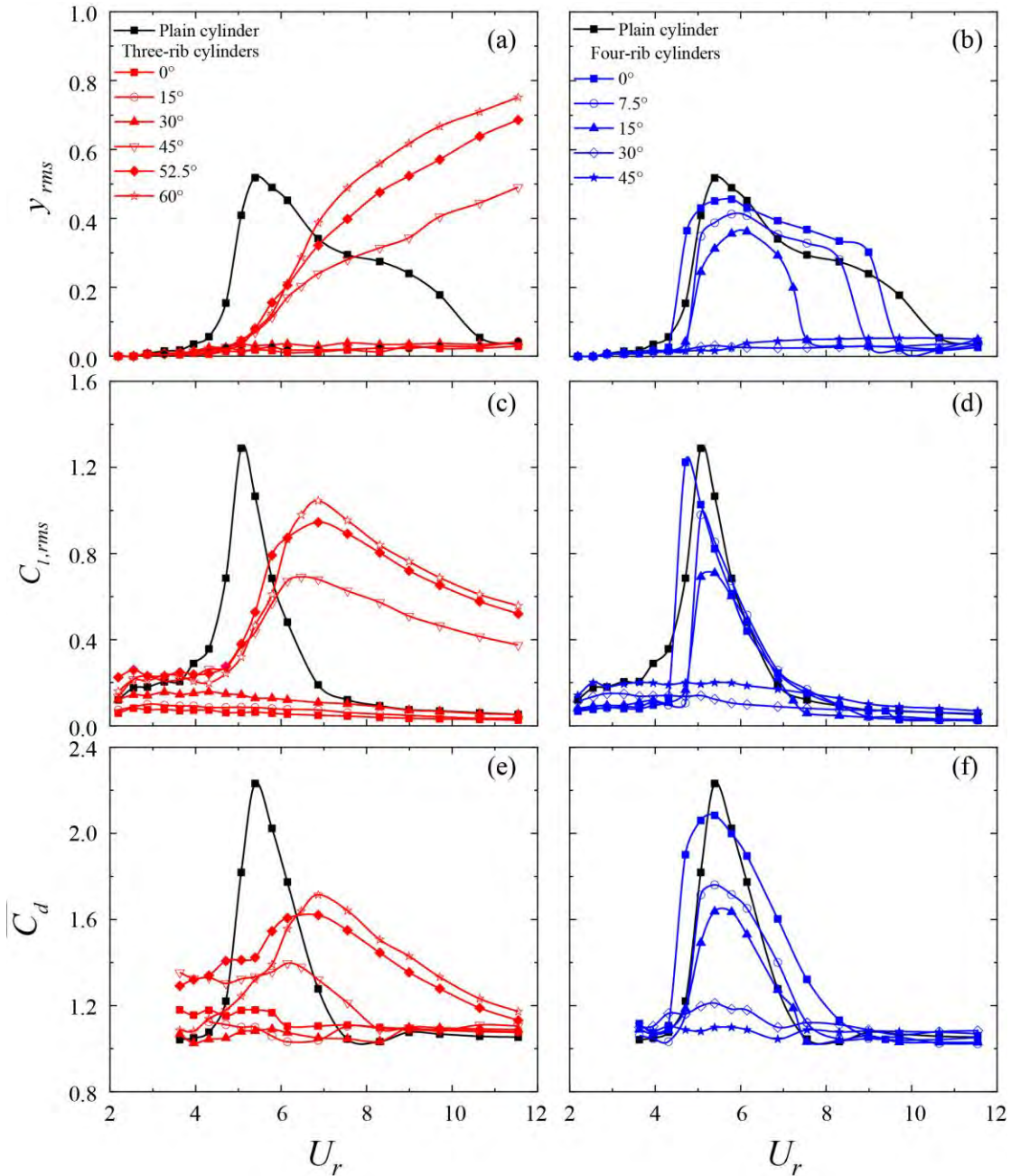


Figure 5.4 Comparison of root-mean-square values of the vibration amplitude y_{rms} (a & b), lift fluctuation coefficient $C_{l,rms}$ (c & d), and mean drag coefficient $\overline{C_d}$ (e & f) of the three-rib, four-rib and plain cylinders versus U_r .

Figure 5.5 presents the dominant frequency of response f^* and phase difference ϕ between the lift force and transverse movement. Note that, f^* and ϕ information for three-rib cases or

four-rib cases where y_{rms} are always close to zero are not shown here for brevity. Similar to our previous results, f^* locks around unity within the tested U_r range for the plain-cylinder case. Once the galloping happens for the three-rib cases at lower AOAs, its dominant f^* no longer locks to the unity but drops to a relatively smaller frequency branch and keeps nearly stable with U_r , as shown in Figure 5.5(a). To explain this behavior, we can compare $C_{l,rms} \cos\varphi$. $C_{l,rms} \cos\varphi$ for the three-rib cases at higher AOAs is remarkably greater than the plain cylinder (Figure 5.6a), corresponding to a smaller f^* .

Upon the occurrence of galloping in the three-rib cases at higher AOAs, the phase jump disappears, and φ stabilizes around 15° with the increase of U_r (as depicted in Figure 5.5c). This observation indicates that the lift force is nearly synchronizing with the oscillation, providing a substantial excitation to the system, resulting in a larger vibration that may lead to negative damping. In comparison, the four-rib cases at lower AOAs exhibit similar behavior in terms of f^* and φ to the plain cylinder case. Therefore, the four-rib cases at lower AOAs are classified as a typical VIV response.

The energy transfer from flow to structure E of the tested cases is compared in Figure 5.6(c)&(d). As expected, the E values for the three-rib cases at lower AOAs and four-rib cases at higher AOAs, where the cylinder's oscillation almost disappeared, are close to zero (see Figure 5.6c&d). As revealed in Figure 5.6(c), E for the plain cylinder reaches its highest point at the resonance region and gradually decreases to a small value near zero. In contrast, for the three-rib cases with galloping response, E maintains a relatively larger value (Figure 5.6c), constantly providing greater excitation to the FIV system, resulting in larger y_{rms} (Figure 5.4a). However, for the four-rib cases at lower AOAs, E is slightly smaller than that of the normal cylinder, consistent with the observation of y_{rms} values.

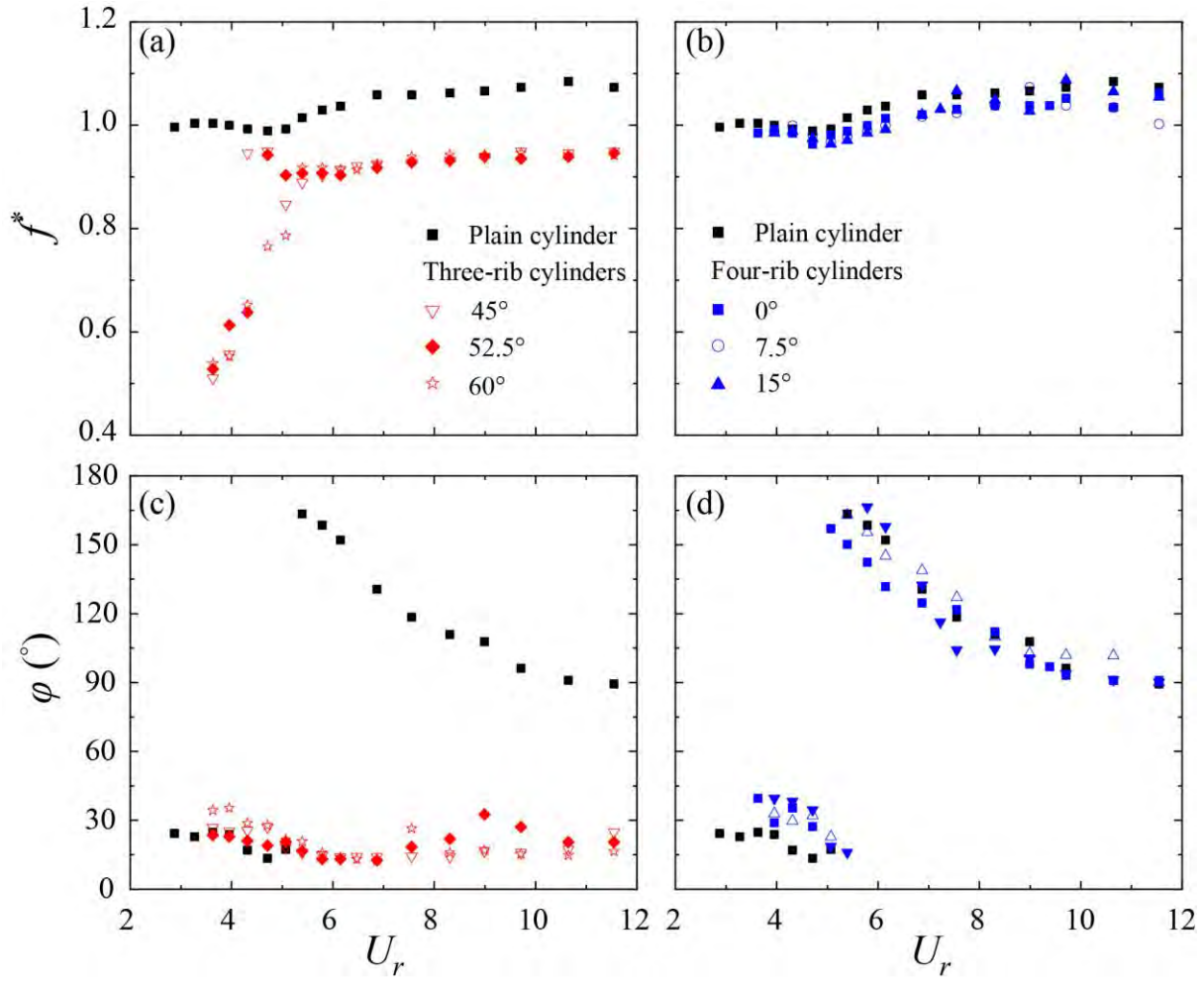


Figure 5.5 The dimensionless frequency f^* of the oscillation and phase angle φ between the lift force and the transverse displacement: (a&c) three-rib cylinders and (b&d) four-rib cylinders.

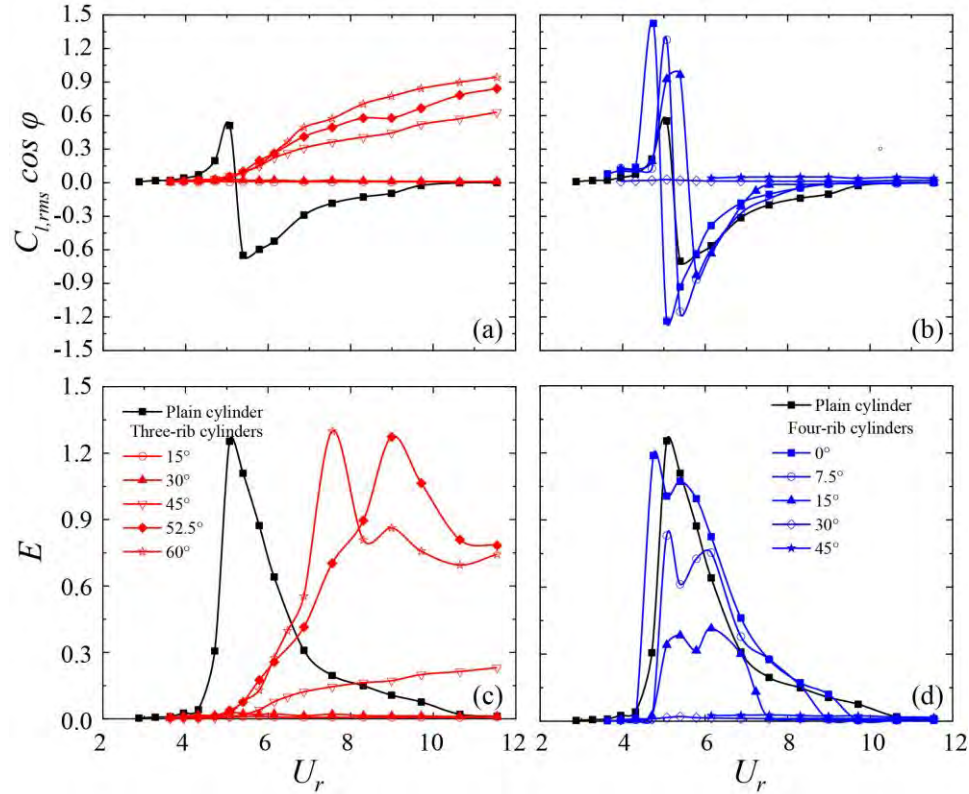


Figure 5.6 (a&c) lift coefficient in phase with body acceleration and (b&d) energy injected into the structure from the flow in one vibration cycle for the three-rib and four-rib cases, respectively.

5.4 Flow dynamics

As shown in Figures 5.7 & 5.8, we compare the normalized vorticity $\omega_z^* = \omega D/U_\infty$ in one cycle of vortex shedding for selected cases at $U_r = 6.15$, where the plain and four-rib cylinders can show apparent VIV dynamics while the three-rib cylinder can exhibit obvious galloping. For the plain cylinder, a pair of positive (green) and negative (red) vortices alternatively shed from the upper and lower sides of the cylinder during one oscillation cycle, forming the classical 2S vortex pattern (Figure 5.7a). The 2S vortex pattern remains for the three-rib cylinder at $\alpha = 0^\circ$, but the separation points are remarkably moved downstream due to the two ribs at the cylinder's leeward side. Besides, the trajectories of positive and negative vortices are

almost parallel (Figure 5.7b), suggesting that the interaction of the separated shear layers is remarkably weakened compared with the plain cylinder case. The corresponding pressure field is also presented in Figure 5.10. It is seen from Figure 5.10(b) that, unlike in the plain cylinder case, the low pressure is mainly distributed in the back of the cylinder. All these explain the much smaller lift force and close-to-zero oscillation displacement observed in Figure 5.4(c).

If rotating the three-rib cylinder by 60° , two ribs will intrude towards upstream. As such, the separation points are significantly advanced. The shear layers generated from the two windward ribs will encounter the leeward rib, leading to stronger vortex-rib interactions, as evidenced in Figure 5.7(c). Due to this interaction, the rolling-up vortex, no matter positive or negative, will be cut into two separate pieces before pinching off from the cylinder, forming a 2P vortex pattern in the wake. Note that, flow reattachment happens as the oscillating cylinder passes through its equilibrium position (see Figure 5.7c). As such, the pressure difference synchronizes with the oscillation (Figure 5.10c), leading to a greater excitation to the system compared to the plain cylinder and hence the occurrence of galloping.

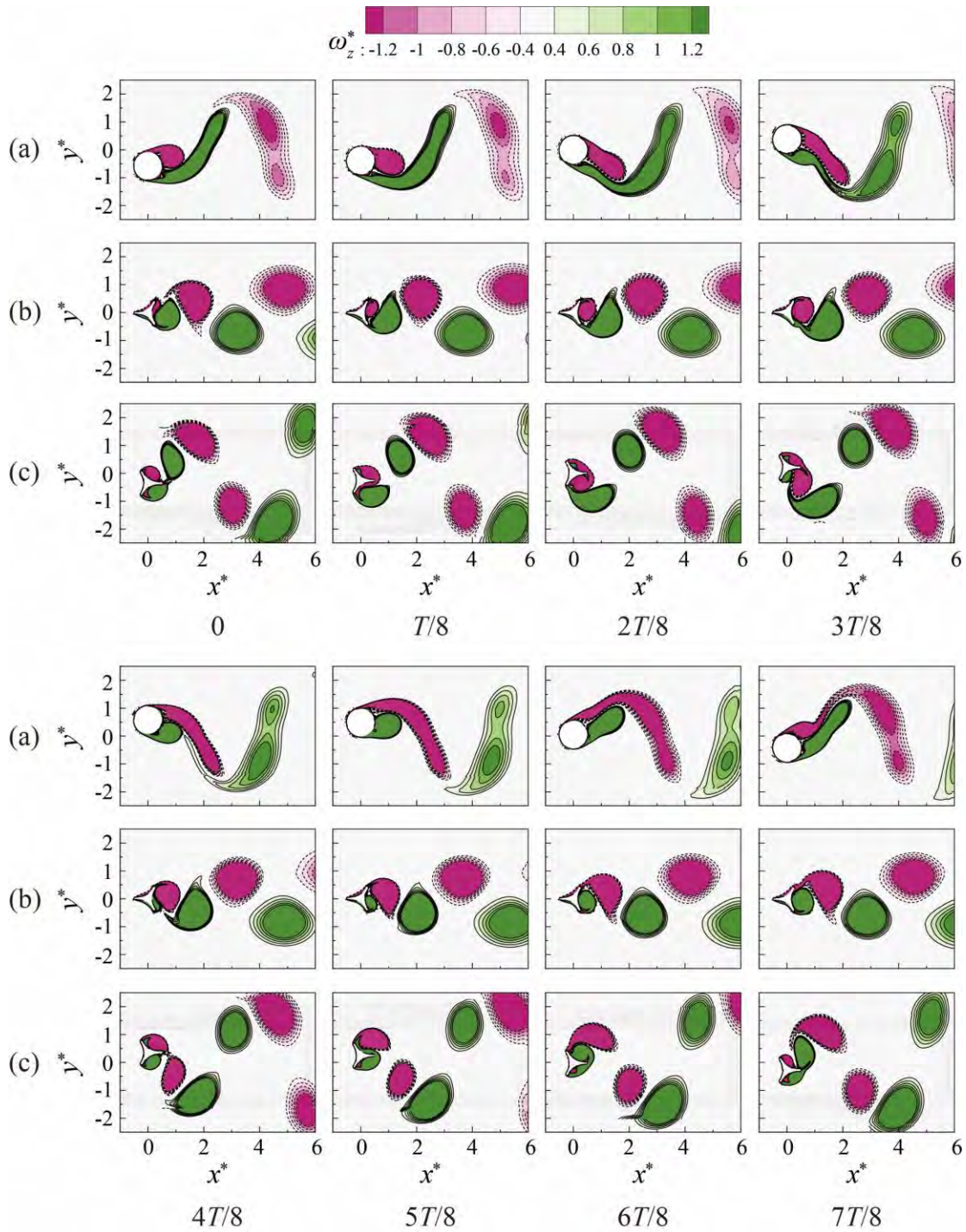


Figure 5.7 Instantaneous vortex patterns of selected cases at $U_r = 6.15$: (a) the plain-cylinder case; (b) the three-rib cylinder at $\alpha = 0^\circ$; (c) the three-rib cylinder at $\alpha = 60^\circ$. $t = 0, 2T/8$ and $4T/8$ correspond to the instants when the cylinders are at the lowest location, passing the equilibrium location, and at the highest

location, respectively.

The instantaneous vortex patterns of the four-rib cylinder cases at $U_r = 6.15$ are presented in Figure 5.8. At $\alpha = 0^\circ$, the separation points are fixed at 90° , i.e., the tips of the upper and lower side ribs, close to those in the plain-cylinder case. The interaction between the shear layers and the leeward rib can be clearly observed in Figure 5.8(a). As the cylinder moves down from $5T/8$ to $7T/8$, the rolling-up negative vortex splits the positive vortex into two pieces. However, the expected event where the positive vortex splits the negative vortex as the cylinder moves up does not occur, as revealed in Figure 5.8(a) from 0 to $2T/8$. This asymmetry results in the formation of a P+S vortex pattern. Similar phenomena are also observed for the case at $\alpha = 45^\circ$, as shown in Figure 5.8(b). These results suggest that symmetry breaking occurs in the wake of geometrically symmetric structure, i.e., the four-rib cylinder at $\alpha = 0^\circ$ or 45° . This symmetry breaking is also confirmed by obviously biased mean displacement \bar{y} and mean lift coefficient \bar{C}_l . As listed in Table 5.5, the four-rib cylinder exhibits significantly larger \bar{y}/y_{rms} and $\bar{C}_l/C_{l,rms}$ than the plain and three-rib cylinders.

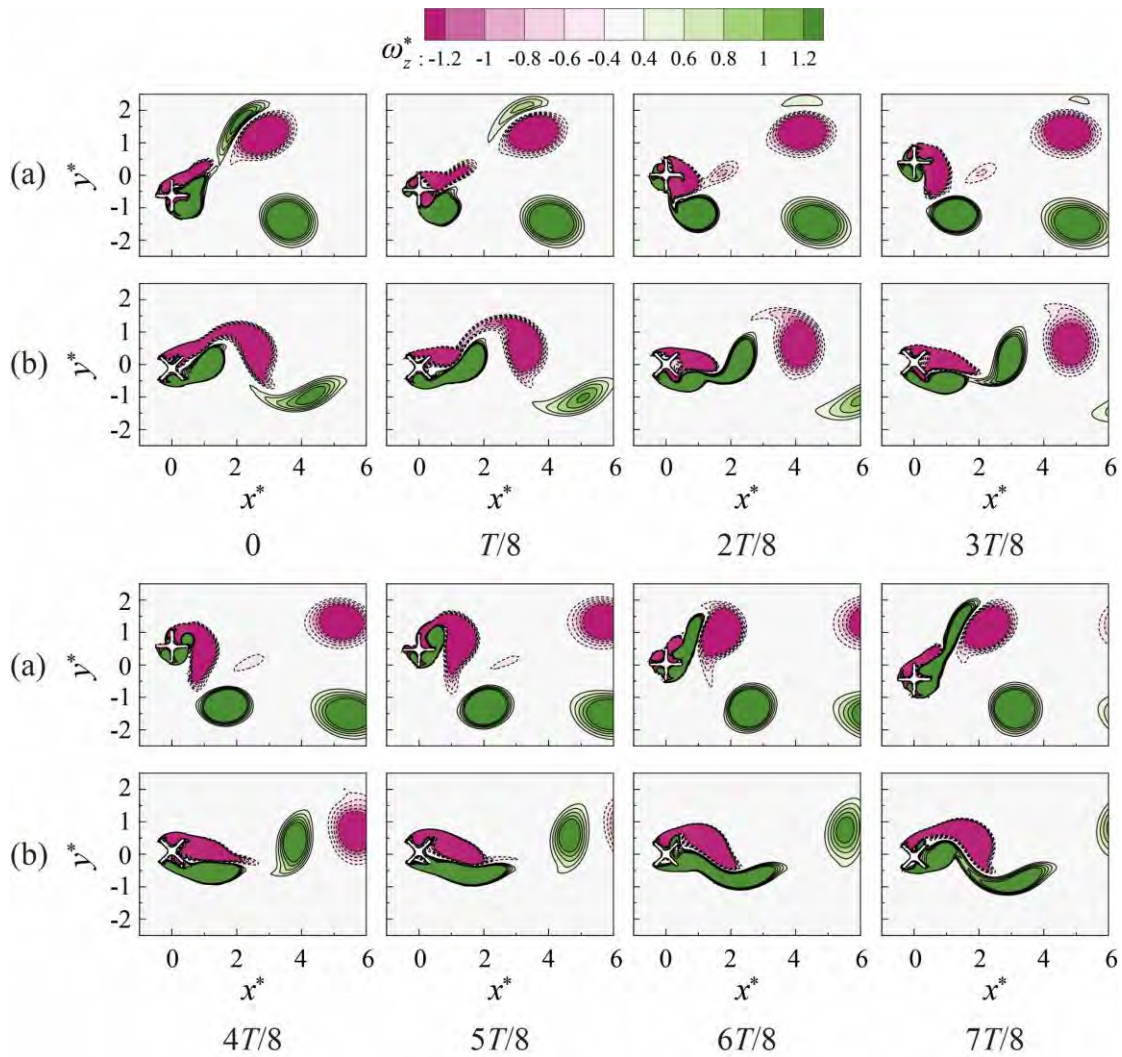


Figure 5.8 The instantaneous vortex patterns of four-rib cylinders at $U_r = 6.15$: (a) $\alpha = 0^\circ$; (b) $\alpha = 45^\circ$.

To investigate the cause of the observed symmetry breaking, two more four-rib cylinder cases were studied at $\alpha = 0^\circ$, in which the length of the trailing rib was altered, with one reduced by 50% (denoted as the 1/2-rib cylinder) and the other increased by 50% (denoted as the 3/2-rib cylinder). The simulation results are presented in Figure 5.9. Compared to the case with the trailing rib of regular length, the 1/2-rib cylinder has a slightly increased oscillation amplitude (about 3.7%), while the 3/2-rib cylinder has a prominent decreased amplitude. Interestingly, the symmetry-breaking phenomenon does not occur in both cases, indicating that the phenomenon

is sensitive to the length of the trailing rib. In engineering applications, special attention should be paid to this phenomenon, which can lead to biased lift force.

The wake asymmetry can also be reflected in the pressure field presented in Figure 5.10(c) & (d). As shown in Figure 5.10(d), for the four-rib cylinder at $\alpha = 0^\circ$, the net pressure at the windward rib is almost anti-phase with the oscillation, indicating that the pressure difference always acts as resistance to the vibrating system. This is also observed in the plain-cylinder case (Figure 5.10a). As such, y_{rms} for the four-rib cylinders cannot always increase as the three-rib cylinder at high AOAs. Another notable observation from Figure 5.10(e) is that the pressure distribution between the top and bottom sides of the cylinder is quite symmetrical, which means the excitation net force in the y direction is quite weak. Therefore, y_{rms} for the four-rib cylinder at $\alpha = 45^\circ$ are almost completely suppressed.

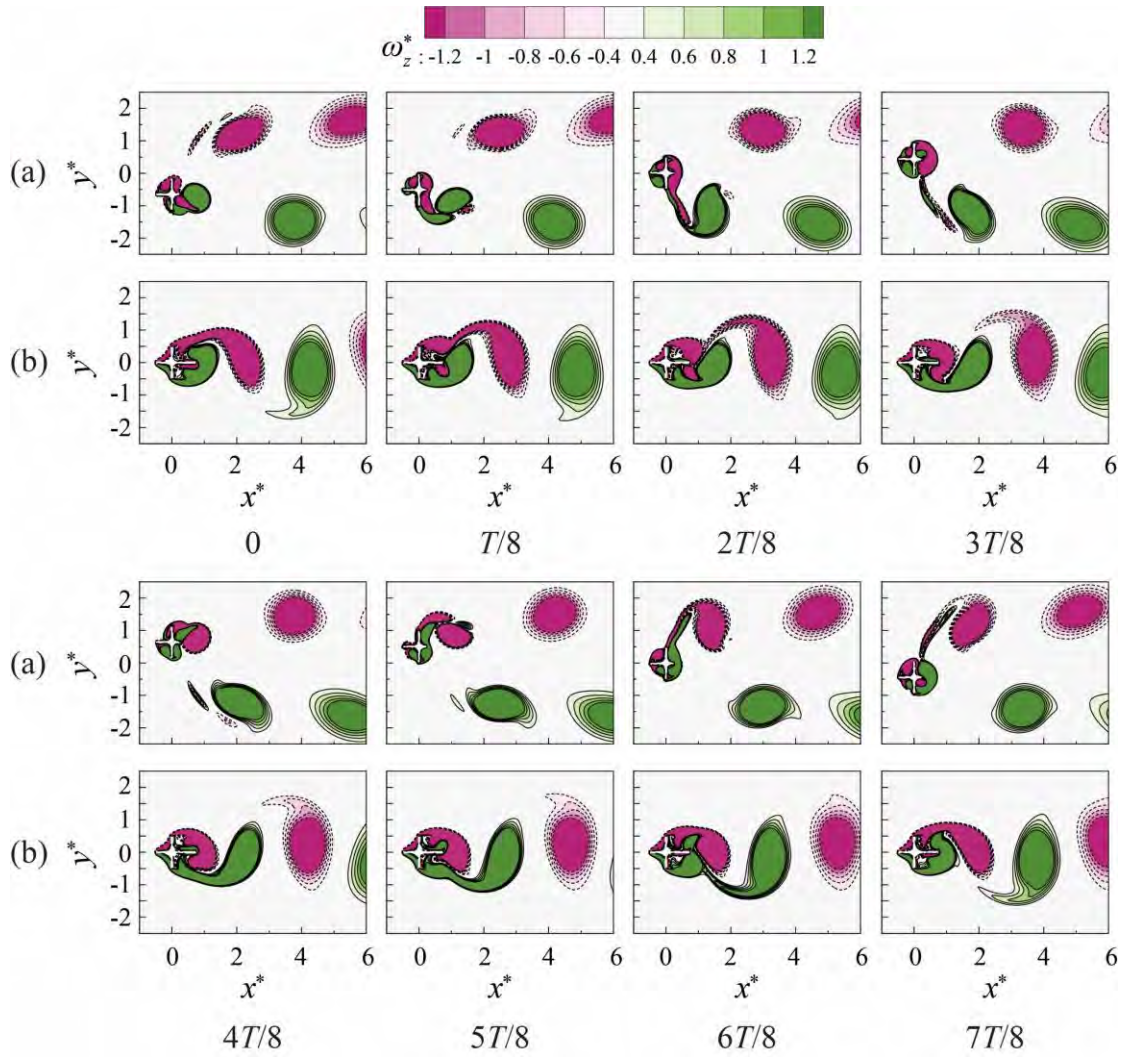


Figure 5.9 The instantaneous vortex patterns of four-rib cylinders at $U_r = 6.15$ and $\alpha = 0^\circ$: four-rib case with its trailing edge rib length equals (a) $1/2$ of other ribs and (b) $3/2$ of other ribs.

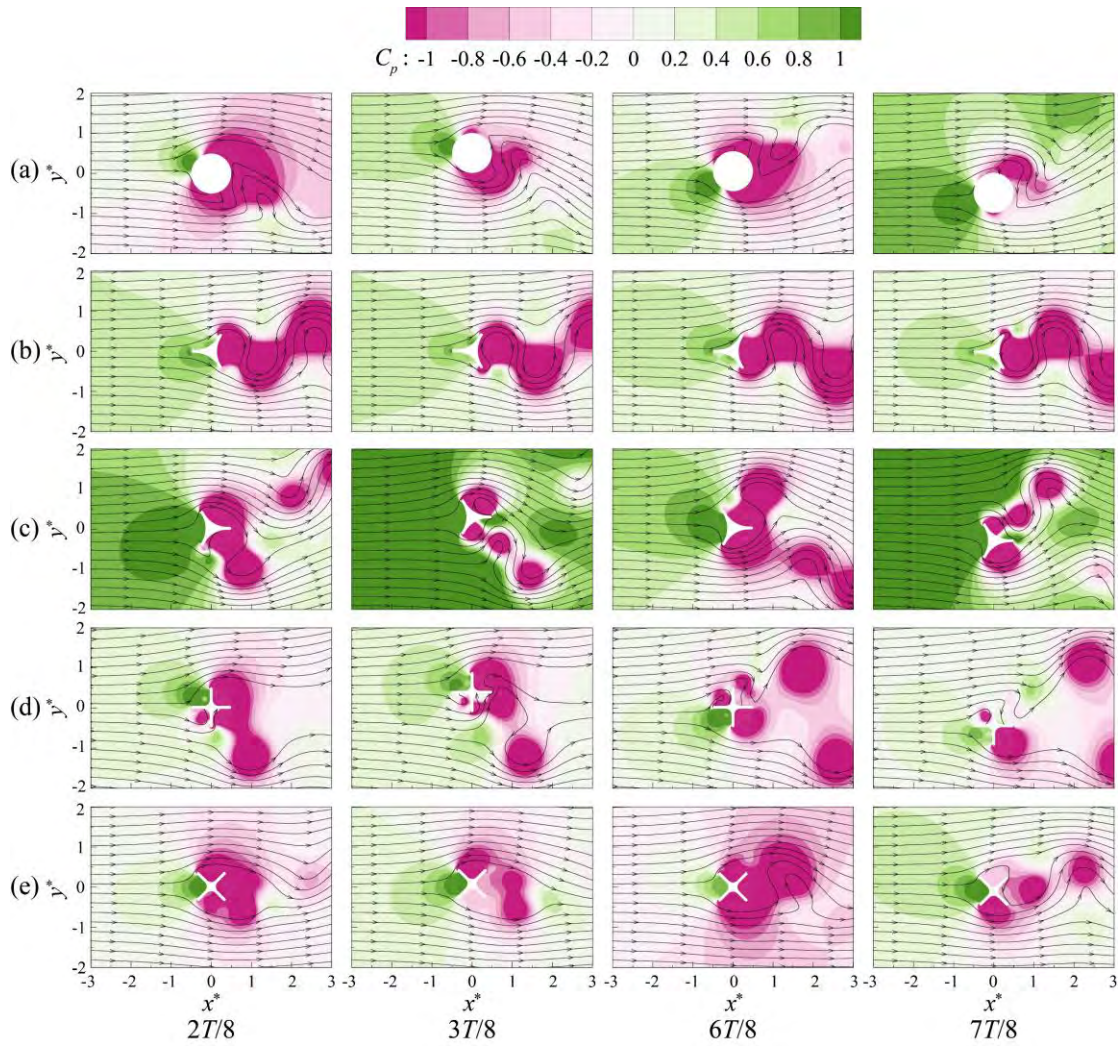


Figure 5.10 The instantaneous pressure field of selected cases at $U_r = 6.15$: (a) plain-cylinder; (b) three-rib cylinder at $\alpha = 0^\circ$; (c) three-rib cylinder at $\alpha = 60^\circ$; (d) four-rib cylinder at $\alpha = 0^\circ$; (e) four-rib cylinder at $\alpha = 45^\circ$. The corresponding streamlines are represented by the black line and arrows.

Table 5.5 The ratio of mean displacement \bar{y} and lift coefficient \bar{C}_l over its corresponding RMS value.

Cases	α	U_r	Exp (\bar{y}/y_{rms})	Num (\bar{y}/y_{rms})	Exp ($\bar{C}_l/C_{l,rms}$)	Num ($\bar{C}_l/C_{l,rms}$)
Plain-cylinder	0°	6.15	0.61%	0.21%	0.47%	0.30%
Three-rib	0°	6.15	0.71%	0.58%	0.64%	0.57%
	60°	6.15	0.88%	0.91%	0.72%	0.59%
Four-rib	0°	6.15	7.95%	10.78%	12.09%	18.25%
	45°	6.15	1.56%	1.70%	1.46%	1.86%

5.5 Remarks

The current study investigated the impacts of the angles of attack on the FIV performance of a nature-inspired cylinder with three or four ribs, using experimental measurements and CFD simulations. Major findings are summarized as follows:

(1) The three-rib cylinder and the four-rib cylinder show quite different dynamics. Compared to the plain cylinder, the three-rib cylinder suppresses the FIV at low AOAs ($0^\circ \leq \alpha \leq 30^\circ$) while promoting galloping at high AOAs ($45^\circ \leq \alpha \leq 60^\circ$). However, the four-rib cylinder experiences VIV at low AOAs ($0^\circ \leq \alpha \leq 15^\circ$), while exhibiting almost no oscillation at high AOAs ($30^\circ \leq \alpha \leq 45^\circ$).

(2) The separation points for the three-rib cylinder at high AOAs are significantly advanced, generating shear layers with a larger curvature that re-attach to the leeward rib. As such, the pressure difference synchronizes with the oscillation and enhances the energy transformed from flow to the system, leading to the occurrence of galloping. However, the flow separation is obviously delayed, and the pressure distribution in the near wake is quite symmetrical for the three-rib cylinder at low AOAs and the four-rib cylinder at high AOAs. Therefore, the corresponding oscillation is almost entirely suppressed.

(3) At $U_r = 6.15$, the classical 2S vortex mode is observed behind the plain cylinder and the three-rib cylinder at $\alpha = 0^\circ$. In contrast, the 2P and P+S vortex mode occurs behind the three-rib cylinder at $\alpha = 60^\circ$ and the four-rib cylinder at $\alpha = 0^\circ$ & 45° , respectively. Interestingly, symmetry breaking occurs in the four-rib cylinder cases, which is related to the incoming flow speed and the length of the trailing rib. However, decreasing or increasing the length of the trailing rib by 50% makes the symmetry breaking disappear.

The present study provides valuable insights into the FIV behavior of cylinders with nature-inspired rib structures, which are useful for designing similar cylindrical structures in relevant engineering applications. Actually, the findings can be used to explain the strategies adopted in some existing engineering applications. For example, the Burj Khalifa in Dubai, which can be conceptually simplified as a three-rib cylinder, primarily experiences wind from the northwest, with secondary wind sources from the south and east. Its architectural design makes one rib oriented in the southeast direction, corresponding to $AOA = 0^\circ$ as defined in our study. According to our findings, this design can enhance the building's stability and security.

Chapter 6 Wake and force control with oscillatory

morphing surface

In this chapter, the wake of a cylinder is actively controlled by the cylinder's oscillatory morphing surface. We begin by detailing the experimental setup and measurements, followed by the presentation and discussion of results to elucidate the control mechanisms of the oscillatory morphing surface under varying perturbation frequencies. Several intriguing models have been proposed based on the experimental findings. However, due to the constraints of the experimental setup, force measurements are not conducted. To further explore the feasibility of using oscillatory morphing surface for drag reduction, numerical simulation has been conducted based on its variants, i.e., oscillating surface and anti-phase jets. The effects of Re are also included. Both two-dimensional and three-dimensional calculations are considered.

6.1 Experimental setup and measurements

The experiments were conducted in a closed-loop water channel at Nanyang Technological University with a test section of 0.45m (W) \times 0.6m (H) \times 1.1m (L). The freestream velocity can be varied between 0.04 and 0.18 m/s, with a turbulence intensity level of less than 1%. For more details, readers can refer to Wen et al.^[126] and Wei et al.^[168].

A rigid circular (denoted as baseline) cylinder of diameter $D = 36$ mm and length $H = 420$ mm was positioned vertically at the center of the test section as illustrated in Figure 6.1(a), which resulted in a small blockage ratio of 8%. Two flat plates with round leading edges and similar lateral dimensions as the test section were mounted horizontally at the cylinder's two

ends to fix the cylinder and to minimize boundary-layer effects. This led to an effective cylinder length of $10D$. A membrane-covered cylinder was also manufactured, which consisted of a steel skeleton and longitudinally attached ribs. The ribs were used to support a latex membrane of 0.5 mm thickness, as shown in Figure 6.1(b). Its working diameter remained at 36 mm. The height of the rib and the length of the membrane between two adjacent ribs were $0.15D$ and $0.27D$, respectively. A few holes were also drilled through the skeleton along the cylinder (see Figure 6.1c) to unifying the pressure inside the cylinder. An external oscillating piston was used to push/pull water from the steel skeleton, which leads to the deformation of the membrane. The water circulation is facilitated through holes drilled in a spanwise spiral direction (refer to Figure 6.1c). Water was enclosed in a circuit consisting of a pipe, a crank slider, and a membrane cylinder. A bottom cover is utilized to ensure the water remains sealed within the model. Hose clips were used in the connection points to avoid water and air leakages, as depicted in Figure 6.1(a).

The freestream velocity was set at $U_\infty = 0.09$ m/s with a resulting Reynolds number of $Re = U_\infty D / \nu = 3240$, where ν is the kinematic viscosity of water. With the Strouhal number of the baseline cylinder being about $St = fD/U_\infty = 0.2$ ^[56, 169], the natural frequency of its vortex shedding was about $f_{\text{vor}} = 0.5$ Hz. To study the effects of surface oscillations, the membrane surface was driven at four different harmonics of the baseline wake frequency, i.e., $f_{\text{osc}} = 0.5, 1, 2$ and 4 Hz. For convenience, we define a dimensionless oscillatory frequency $f_{\text{osc}}^* = f_{\text{osc}} / f_{\text{vor}}$ to describe these oscillations for the cylinder with oscillatory morphing surface, i.e., $f_{\text{osc}}^* = 1, 2, 4$ and 8 . For comparison purposes, a rigid circular cylinder and a cylinder covered with non-oscillating membrane are served as the benchmark cases.

A time-resolved particle image velocimetry (TR-PIV) system was used to measure the flow in the near wake of the cylinders. In this system, a 2W, 532nm wavelength, continuous-wave laser was used to provide a laser beam. Beam-steering mirrors were used to redirect the laser beam to a plano-concave cylindrical lens that expands the laser beam into a thin laser sheet of approximately 1.5 mm thick, as depicted in Figure 6.1(a). 20 μm tracer particles were used to seed the water flow. A high-speed CCD camera (IDT NX8-S1) was used to capture raw particle images with a resolution of $1600 \times 1200 \text{ pixel}^2$. The sampling framerate was 200 frames-per-second (FPS). A total of 25,000 images (about 62.5 natural vortex-shedding cycles) were recorded to ensure statistical convergence. The exposure time was kept at about 2.5 ms to minimize streaking of the particles. PIV measurements were conducted in two different measurement windows, with window sizes of $5D$ and $2D$, corresponding to spatial resolutions of 0.1125 and 0.045 mm/pixel, respectively. The larger measurement window was selected for Proper Orthogonal Decomposition (POD) analysis, while the smaller measurement window enabled detailed observations of shear-layer developments.

PIVlab software was used within MATLABTM to analyze the raw particle images. The post-processed procedures were similar to those used by New et al.^[57, 170] and New & Zang^[171]. Readers may refer to those papers for the data-processing and uncertainty analysis details. To acquire the velocity maps, three interrogation windows and two sets of multi-grid cross correlations were used on the sequential particle images. The initial and final interrogation windows were 128×128 and $32 \times 32 \text{ pixel}^2$, respectively, with 50% overlap in both directions. The experimental uncertainty for the present velocity map (99×74 vectors) was estimated to be less than 2%.

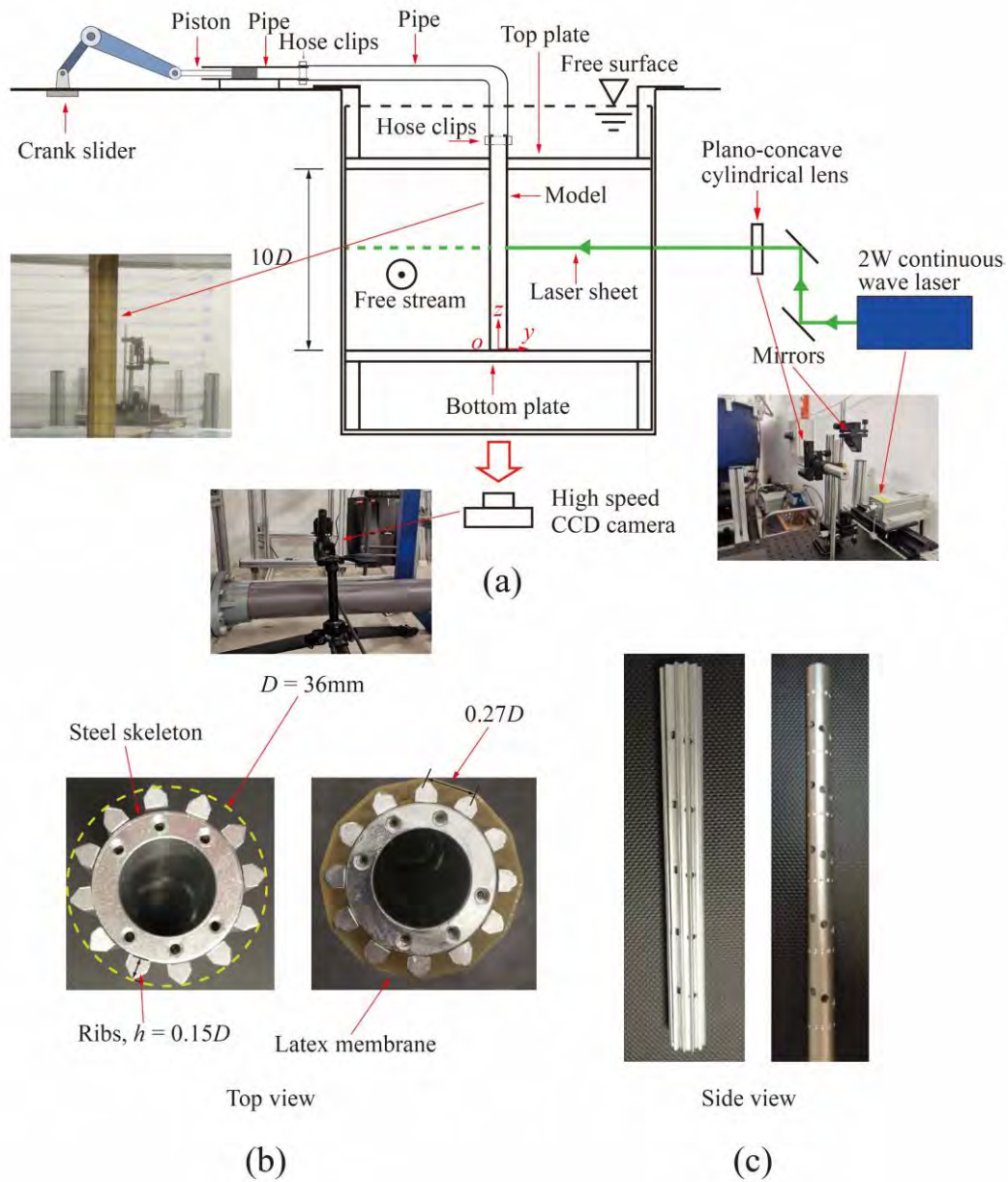


Figure 6.1 (a) Schematics of the experimental setup and water tunnel; (b) cross-sections of the experiment model with and without latex membrane wrapped around it as viewed from the top and (c) side-view of the steel cylindrical skeleton with (left) and without (right) ribs.

POD is a mathematical technique used for data analysis and signal processing. It is a method for decomposing a signal or data set into a set of orthogonal basis functions, which are ranked according to their contribution towards the total variance in the data. This allows for a simplified representation of complex data sets, where only the most significant basis functions are retained. Based on the snapshot POD technique^[57, 126, 172-175], dominant flow structures can be differentiated by decomposing the velocity fields into individual modes, which would help to better understand the underlying flow physics under different surface oscillations. To do that, the TR-PIV measured velocities are firstly decomposed into the mean and fluctuating velocity components, with the latter being further decomposed into various POD modes. The POD modes are then ranked according to their energy contributions. Motivated by New et al.^[57, 173], phase-averaged results were also reconstructed by averaging the PIV data in $\pi/3$ intervals with a $\pm \pi/72$ phase bin size. This is possible due to the highly cyclical nature of the vortex shedding behavior observed for the present test cylinders.

6.2 Evolution of oscillatory morphing surface

The deformation of the membrane was measured using a thin laser sheet by tracing the membrane outline and imaged using a high-speed camera. The oscillatory displacement y^* ($= y/D$) was obtained at the midpoint of the membrane section between two neighboring ribs and averaged over four such membrane sections. In this chapter, normalization by D and/or U_∞ is denoted with a superscript '*'. As revealed in Figure 6.2, the variation of y^* under excitation of all four frequencies is highly periodic. For all tested cases, their oscillation amplitude is approximately $0.0065D$ (0.234mm). The ratio of this amplitude to the length of membrane

section is about 2.4%. Besides, the peak displacements under oscillations of different frequencies are close as the stroke length of the crank slider is identical.

As an example, snapshots of oscillatory morphing surfaces at selected instants (t_1 to t_5) over half an excitation cycle for the morphing-surface cylinder oscillating at $f_{osc}^* = 2$ are given at the bottom of Figure 6.2. The shrinking and expanding membrane interacts with the incoming flow that may affect the flow separation and the stability of the generated shear layers.

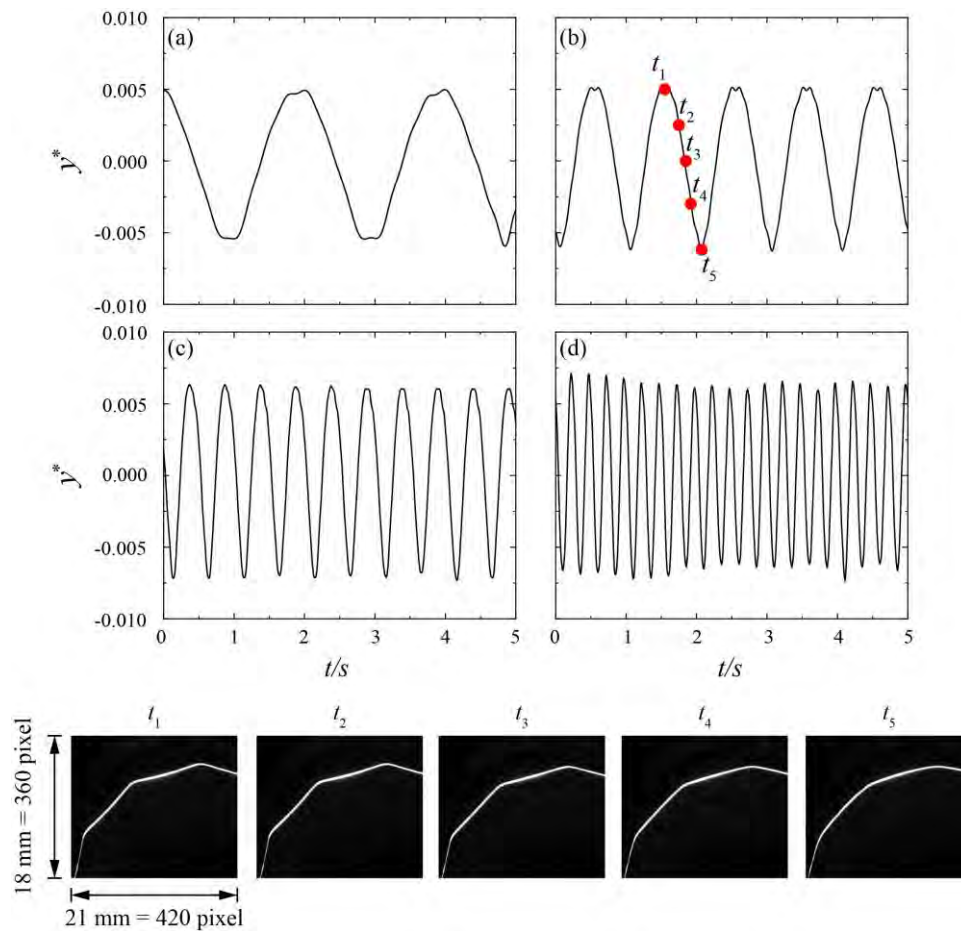


Figure 6.2 Averaged deformation of oscillatory morphing surfaces at different excitation frequencies: (a) oscillatory morphing surface (OMS) cylinder at $f_{osc}^* = 1$; (b) OMS cylinder at $f_{osc}^* = 2$; (c) OMS cylinder at $f_{osc}^* = 4$; (d) OMS cylinder at $f_{osc}^* = 8$. Snapshots of oscillatory morphing surfaces at different instants (t_1 to t_5) over half an excitation cycle for OMS cylinder at $f_{osc}^* = 2$ are given at the bottom position.

6.3 Effects on vortex shedding

Figure 6.3 compares the vortex shedding processes behind the rigid circular (RC) cylinder, the grooved, static surface (SS) cylinder, and the grooved, oscillatory morphing surface (OMS) cylinder driven at $f_{\text{osc}}^* = 1, 2, 4, 8$. For the RC and SS cylinders, the elongated shear layers can be clearly seen (compared with the OMS cylinders driven at $f_{\text{osc}}^* = 2, 4$ and 8), which roll up into large vortices as shown in Figures 6.3(a) & 6.3(b), resembling the observation reported by El-Makdah & Oweis^[60]. The small vortices shown in the instantaneous flow fields may be caused by turbulence related to the subcritical flow at the present Reynolds number. The rolling-up of the shear layers from the SS cylinder is slightly later than that from the RC cylinder, possibly due to early flow separation caused by the ribs of the SS cylinder, as sketched in Figure 6.4(b). For the OMS cylinder at $f_{\text{osc}}^* = 1$, its shear layers roll up slightly early and thus may exhibit a shorter vortex formation length (Figure 6.3c).

As the excitation frequency increases, i.e., the OMS cylinder at $f_{\text{osc}}^* = 2$ and 4, the interaction between the membranes and shear layers becomes stronger, thus breaking the integrity and continuity of the shear layers, as shown in Figures 6.3(d) & 6.3(e). As such, the rolling-up of the shear layers occur significantly earlier, leading to a significantly shorter vortex formation length as will be revealed in Figure 6.8 later.

Interestingly, at the highest driving frequency $f_{\text{osc}}^* = 8$, the broken-up shear layers grow into many small vortices that still follow the trace of the primary shear layers, as shown in Figure 6.3(f). This wake pattern is quite similar to that obtained by Wang et al.^[127] and Ma & Feng^[176] using synthetic jets operating at high perturbation frequencies. These small vortices then roll up like the primary shear layers to form the von Karman vortex street. As such, both

the dominant vortex shedding frequency ($f^* = f/f_{\text{vor}} = 0.9$) and the excitation frequency ($f^* = 7.2$) are prominent in the spectra presented in Figure 6.5(f). The well-organized small vortices along the trace of the primary shear layers are almost parallel, reflecting significantly weaker interactions between the opposite-signed vortices as compared to the RC and SS cases. These observations also indicate that an excitation frequency close to the natural vortex-shedding frequency may not significantly change its vortex-shedding behavior.

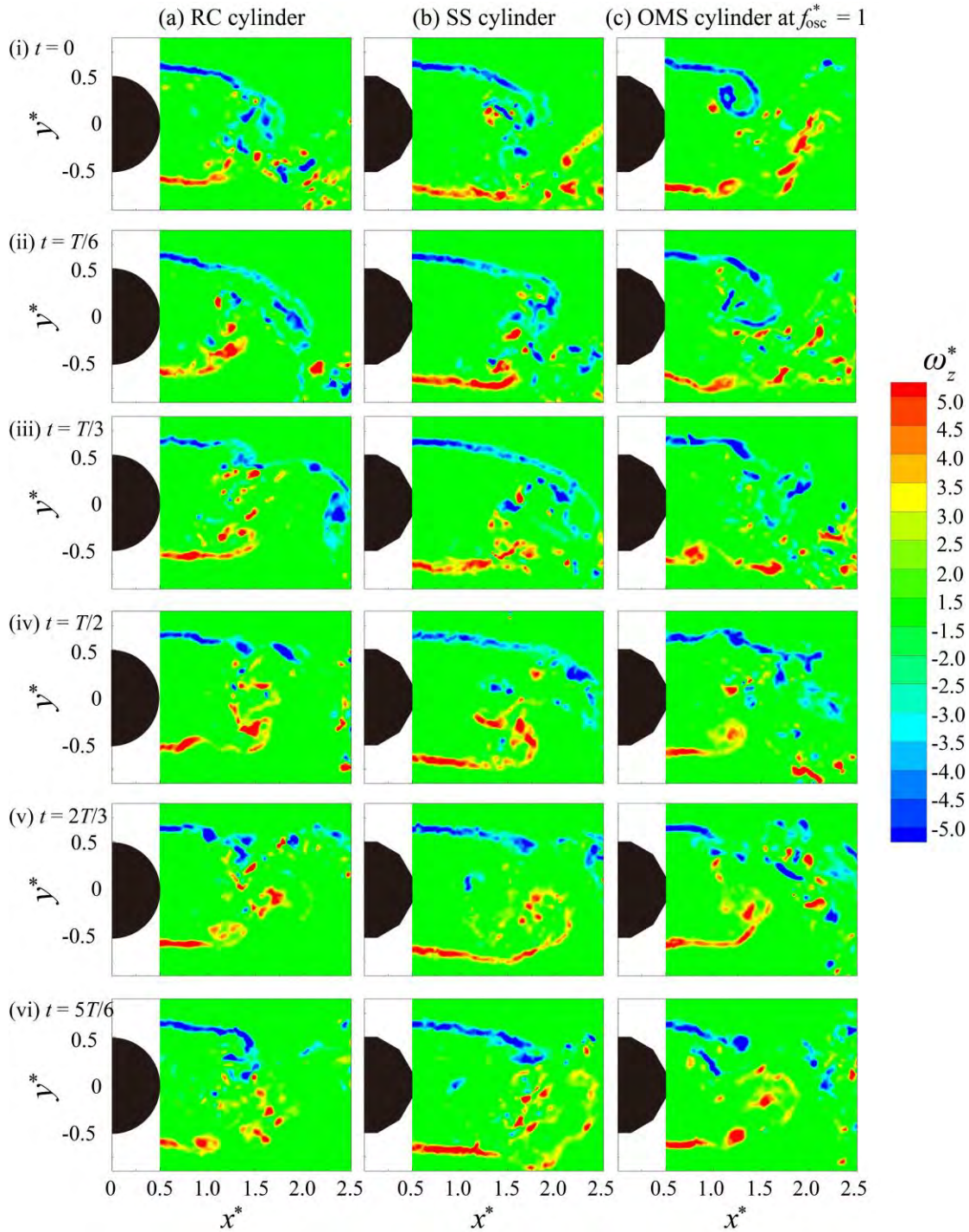


Figure 6.3 Instantaneous spanwise vorticity ω_z^* for the (a) RC cylinder, (b) SS cylinder, (c) OMS cylinder at $f_{\text{osc}}^* = 1$, (d) OMS cylinder at $f_{\text{osc}}^* = 2$, (e) OMS cylinder at $f_{\text{osc}}^* = 4$ and (f) OMS cylinder at $f_{\text{osc}}^* = 8$, where (i) $t = 0$, (ii) $t = T/6$, (iii) $t = T/3$, (iv) $t = T/2$, (v) $2T/3$ and (vi) $5T/6$ are the different periods in one vortex shedding cycle.

To summarize our observations, we sketch in Figure 6.4 different vortex patterns for the RC and SS cylinders, as well as the OMS cylinder at $f_{\text{osc}}^* = 2$ and 8. For the RC cylinder, flow separation occurs at a location slightly larger than 90° (0° is defined as the upstream stagnation point) due to turbulence associated with the subcritical flow^[177], and a classical von Karman vortex street forms in the wake (Figure 6.4a). In contrast, the SS cylinder shows early separation caused by the rib right before 90° , leading to the formation of a wider and longer wake, as sketched in Figure 6.4(b). Note that, the separation points indicated on the cylinder surface are determined based on our estimation derived from observing the flow behavior depicted in Figure 6.3. It is evident that at $f_{\text{osc}}^* = 2$, smaller vortices are present for the OMS cylinder, which roll up closer to the cylinder compared to the RC cylinder. Additionally, the wake width of the OMS cylinder at $f_{\text{osc}}^* = 2$ is noticeably narrower than that of the RC cylinder. Therefore, it is more probable that the separation points for the OMS cylinder at $f_{\text{osc}}^* = 2$ would occur further downstream, as illustrated in Figure 6.4(c).

For the OMS cylinder, the oscillatory morphing surface delays the occurrence of flow separation, and meanwhile increases the instability of the separated shear layers, leading to an early rolling-up. As such, a shorter and narrower wake will form (Figure 6.4c). Moreover, when the excitation frequency is as high as $f_{\text{osc}}^* = 8$, small vortices are induced along the trace of the primary shear layers. Although disturbed by the small vortices, the primary shear layers can still roll up into large vortices, forming a unique flow pattern as sketched in Figure 6.4(d).

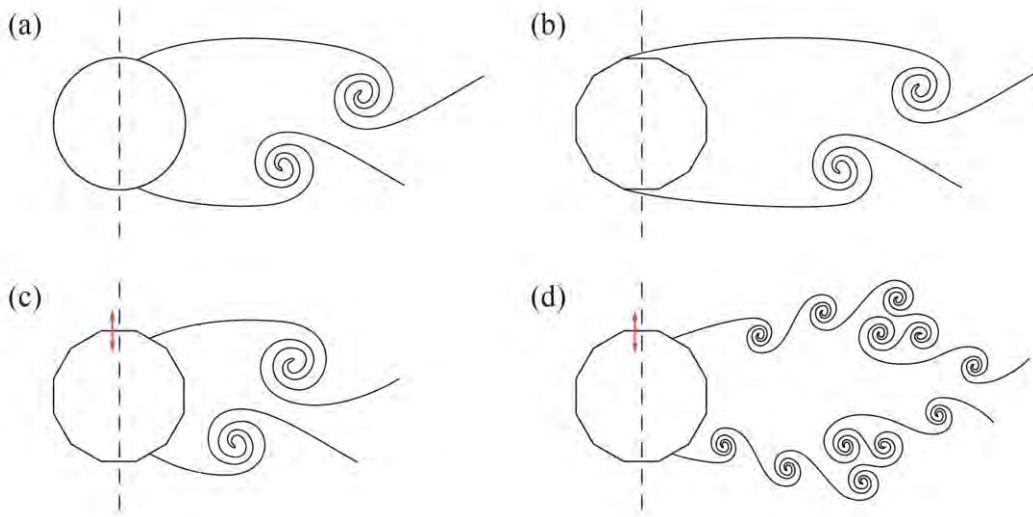


Figure 6.4 Schematics of the vortex street for the (a) RC cylinder, (b) SS cylinder, (c) OMS cylinder at $f_{\text{osc}}^* = 2$ and (d) OMS cylinder at $f_{\text{osc}}^* = 8$. The red arrow denotes the oscillating of the morphing surface.

Power-spectral-density (PSD) analysis is also conducted for the wakes, as presented in Figure 6.5, on the cross-stream velocities at two selected locations, i.e., point A: $x^* = 1.0$, $y^* = 0.5$, and point B: $x^* = 1.5$, $y^* = 0.5$ (denoted in Figure 6.5a), with all 25,000 velocity maps. These two probe locations are selected to detect the evolution of shear layers and the resulting vortex-shedding behavior. The PSD was determined using the MATLAB *pwelch* function with a segment length of 5,000 and a Hamming window with 50% overlap. As revealed in Figures 6.5(a) & 6.5(b), no evident dominant frequency is detected at point A for the RC and SS cylinders, indicating that the rolling-up of the shear layers does not occur at this location. This is not surprising because the RC and SS cylinders have a longer vortex formation length, and the probe location is within the recirculation region. This observation is consistent with the instantaneous flow structures shown in Figures 6.3(a) & 6.3(b). In contrast, a dominant peak appears at $f_{\text{osc}}^* = 0.9$ for the OMS cylinder driven at $f_{\text{osc}}^* = 2$ and $f_{\text{osc}}^* = 4$, as shown in Figures 6.5(d) & 6.5(e), corresponding to the vortex shedding frequency. Note that, the detected vortex

shedding frequency is $f^* = 0.9$, corresponding to 0.45 Hz that is slightly less than the estimated 0.5 Hz. Since these two frequencies are still very close, lock-in phenomena occur as confirmed in Figure 6.5. Hence, the oscillation frequencies we applied can promote or mitigate the fundamental wake shedding frequency and its harmonics. The oscillation frequency of the morphing surface also appears in these two cases, with a weaker PSD magnitude though. This indicates that the vortex shedding occurs closer to the cylinder, which agrees well with that observed in Figure 6.3. Besides, the vortex shedding frequency is not attracted to the excitation frequencies that are the former's even multiples, implying that the lock-on phenomenon as reported by Wang et al.^[178] does not occur here. The reason is probably that the membrane oscillations are still not strong enough to induce the attraction. At the other two excitation frequencies, i.e., the lowest one $f_{osc}^* = 1$ and the highest one $f_{osc}^* = 8$, only a weak peak is observed at the excitation frequency, as shown in Figures 6.5(c) & 6.5(f), suggesting that the roll-up of shear layers is almost not affected by the weak excitation.

As the probe moves downstream to point B, the dominant vortex shedding frequency can be well captured for the RC and SS cylinders (Figures 6.5a & 6.5b). The peak for the SS cylinder (0.0039) is also slightly higher than that for the RC cylinder (0.0034), indicating that the SS cylinder generates stronger vortex shedding. This is consistent with the vorticity information revealed in Figure 6.7. After applying the excitation, the energy at the dominant vortex shedding frequency is significantly enhanced in the $f_{osc}^* = 1, 2$ and 4 cases. Additionally, the peaks at the excitation frequency in the $f_{osc}^* = 2$ and 4 cases are lower than their counterparts at point A, showing the decaying feature of the excitation influence.

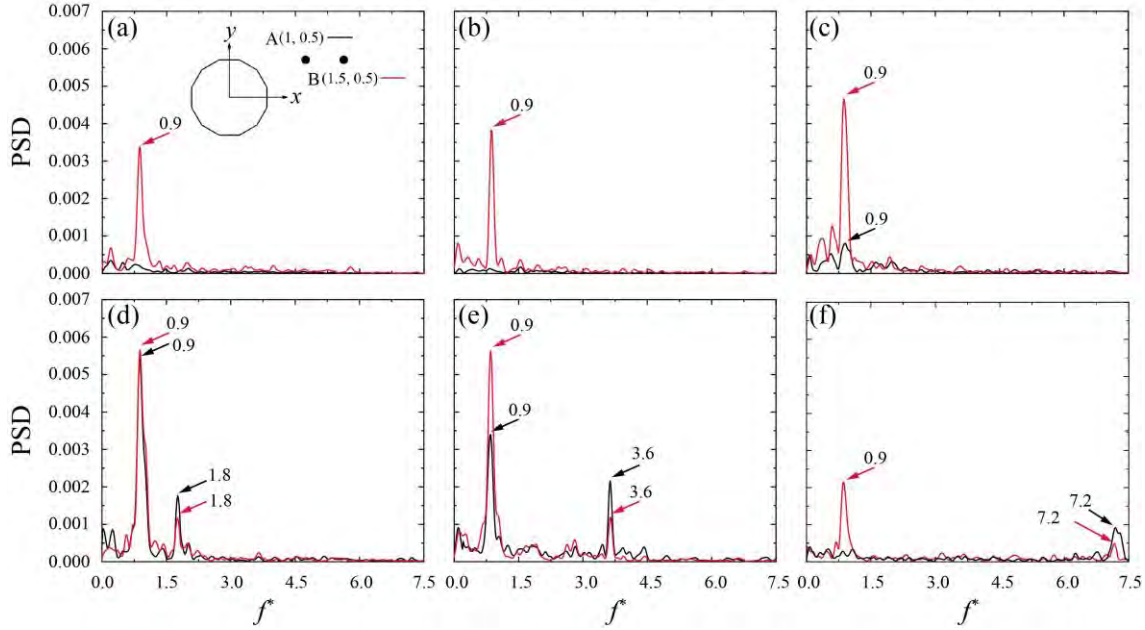


Figure 6.5 Power-spectral-density (PSD) analysis for the cross-stream velocities v at point A ($x^* = 1.0, y^* = 0.5$) and point B ($x^* = 1.5, y^* = 0.5$): (a) RC cylinder; (b) SS cylinder; (c) OMS cylinder at $f_{\text{osc}}^* = 1$; (d) OMS cylinder at $f_{\text{osc}}^* = 2$; (e) OMS cylinder at $f_{\text{osc}}^* = 4$; (f) OMS cylinder at $f_{\text{osc}}^* = 8$.

6.4 Effects on mean flow field

Figure 6.6 shows the influence of oscillatory morphing surface on the time-averaged flow fields, including the streamwise (\bar{u}/U_∞) and cross-stream (\bar{v}/U_∞) velocities. Compared with the RC and SS cylinders, a narrower wake with a shorter and weaker reversed flow is formed behind the OMS cylinder at $f_{\text{osc}}^* = 2$ and 4 (see Figures 6.6c1 and 6.6d1), reflecting the delayed flow separation, which further results in the vortex patterns presented in Figure 6.3(a) and 6.3(b) and sketched in Figure 6.4(c). This observation is consistent with the cross-stream velocity contours, in which the peaks for the OMS cylinder at $f_{\text{osc}}^* = 2$ and 4 remarkably shift towards the upstream, i.e., closer to the cylinder (Figure 6.6d2 & e2), suggesting an early roll-up of the shear layers. However, this effect seems to be weakened at the higher frequency, i.e., $f_{\text{osc}}^* = 8$

(Figure 6.6f1 & f2). In this case, the shear layer is broken up by the high-frequency force into a train of small vortices. Although following the trace of the shear layer to roll up (see Figure 4d), the generation of these small vortices attenuates the strength of the shear layer and hence delays the roll-up process.

The contours of time-averaged vorticity shown in Figure 6.7(a-f) and the peak vorticity values compared in Figure 6.7(g) further revealed that, the surface oscillation not only promotes the roll-up of the shear layer, but also suppresses its strength, especially for the OMS cylinder at $f_{osc}^* = 2$ and 4. However, without the dynamic oscillation, the strength of the shear layer is enhanced, which can be read by comparing vorticities between the SS cylinder case and the RC cylinder case.

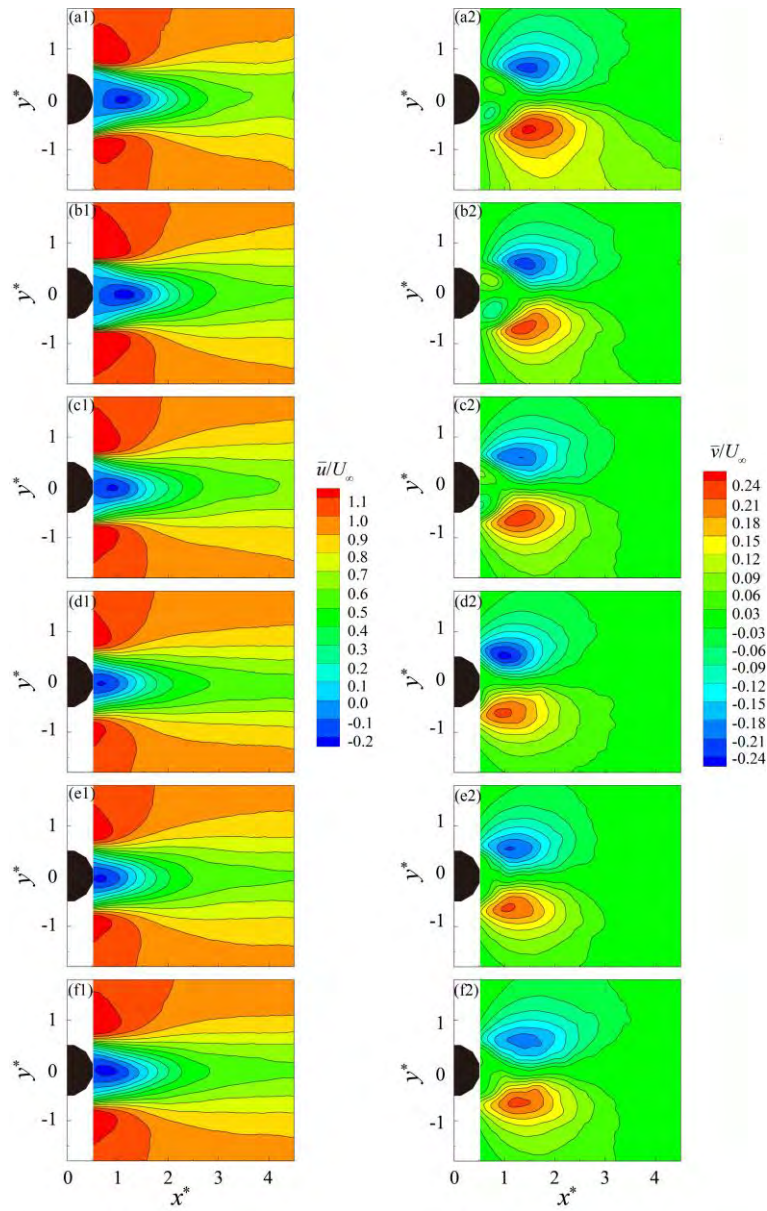


Figure 6.6 Variations of mean velocity fields in streamwise direction (\bar{u}/U_∞) and cross-stream direction (\bar{v}/U_∞) around the cylinders with different perturbations: (a1 & a2) RC cylinder; (b1 & b2) SS cylinder; (c1 & c2) OMS cylinder at $f_{\text{osc}}^* = 1$; (d1 & d2) OMS cylinder at $f_{\text{osc}}^* = 2$; (e1 & e2) OMS cylinder at $f_{\text{osc}}^* = 4$; (f1 & f2) OMS cylinder at $f_{\text{osc}}^* = 8$.

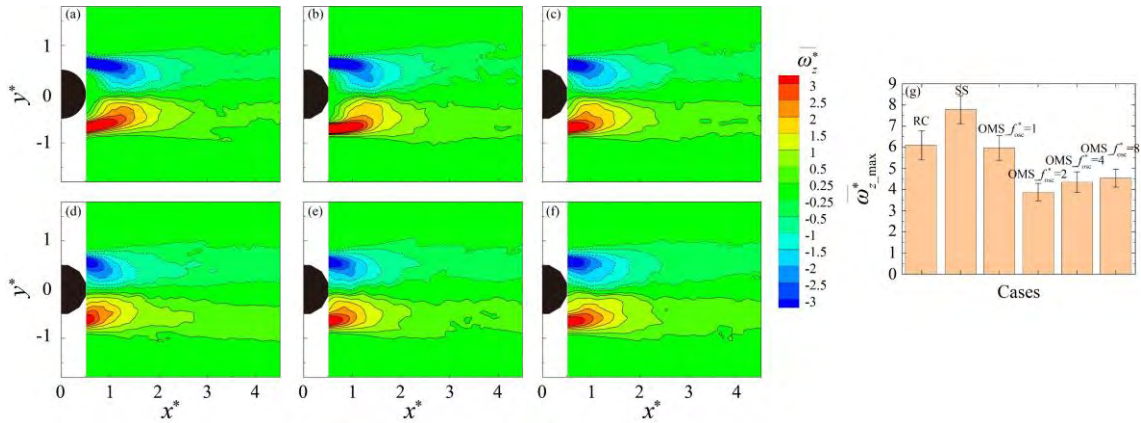


Figure 6.7 Distribution of mean vorticity $\overline{\omega_z^*}$ in the near wake of cylinders with different perturbations: (a) RC cylinder; (b) SS cylinder; (c) OMS cylinder at $f_{osc}^* = 1$; (d) OMS cylinder at $f_{osc}^* = 2$; (e) OMS cylinder at $f_{osc}^* = 4$; (f) OMS cylinder at $f_{osc}^* = 8$. The local maximum vorticity of the cylinders with different frequency excitations are compared in (g).

Vortex formation length, defined as the distance between the center of the cylinder and the location of zero mean streamwise velocity in the cylinder's centerline, is a key indicator to evaluate the flow behavior (i.e., vortex development and shedding) and aero/hydrodynamic performance (such as base pressure and mean drag) of bluff bodies [56, 57, 173, 179]. The variations of mean streamwise velocities \bar{u}/U_∞ along the centerline (i.e., $y^* = 0$) are compared in Figure 6.8(a). It is seen that the vortex formation length for the SS cylinder ($1.68D$) is only slightly longer than that for the RC cylinder ($1.63D$), suggesting that these two cases share similar flow behavior in the near wake, as confirmed by the contours in Figure 6.6(a1-b2). This observation aligns with the findings reported by El-Makdah & Oweis^[60], who reported that both circular and cactus-like cylinders exhibit similar characteristics in terms of the magnitudes and spatial extent of the mean streamwise velocity contours at $Re = 50,000$.

Compared to the RC cylinder, the OMS cylinder results in a smaller vortex formation length especially at intermediate frequencies of $f_{\text{osc}}^* = 2$ and 4. The maximum reduction in vortex formation length of about 25.2% is achieved at $f_{\text{osc}}^* = 2$. This observation implies that in these two cases the rolling-up of shear layers happens closer to the cylinder, consistent with the observations in Figure 6.3. With perturbations of lower ($f_{\text{osc}}^* = 1$) or higher ($f_{\text{osc}}^* = 8$) frequencies, however, the vortex formation length turns to increase towards the value of the non-morphing cases, as displayed in Figure 6.8(a) as well as in Figure 6.6. According to the vortex formation length, it is estimated that the drag experienced by the cylinder is either increased or almost unchanged. The reason for not achieving drag reduction is probably due to the relatively weak oscillatory forcing we applied in the experiments, which is limited by the present experimental setup.

Figure 6.8(b-c) shows the centerline distribution of the streamwise velocity fluctuation (u_{rms}/U_∞), and cross-stream fluctuation (v_{rms}/U_∞). Compared with the RC cylinder, the streamwise velocity fluctuation for the SS cylinder is slightly stronger in the very near wake, i.e., $x^* < 1$, but becomes obviously weaker downstream. This is not surprising because the rib-supported leading edges of the top and bottom pieces of membranes for the SS cylinder promote earlier flow separation. As such, the shear layers start earlier and also roll up a bit earlier, resulting in nearer occurrence of strong streamwise velocity fluctuations. It is also seen that the v_{rms}/U_∞ magnitude for the SS cylinder is slightly larger than the RC cylinder (Figure 6.8b).

For the OMS cylinder at $f_{\text{osc}}^* = 2$, its velocity fluctuation is significantly stronger with a most upstream peak, indicating that the oscillation of the morphing surface at this frequency promotes earlier roll-up of the shear layers and induces stronger turbulence, as shown in Figure 8(b-c) This also leads to a shorter vortex formation length as revealed in Figure 6.8(a).

Figure 6.9 compares u_{rms}/U_∞ and v_{rms}/U_∞ along the $x^* = 1, 2, 3,$ and 4 lines between the RC and OMS cylinders at $f_{osc}^* = 2$. The OMS cylinder at $f_{osc}^* = 2$ exhibits a significantly greater velocity fluctuation than the RC cylinder at $x^* = 1$, particularly in v_{rms}/U_∞ . However, further downstream, the peaks of the u_{rms}/U_∞ and v_{rms}/U_∞ for the RC cylinder are slightly higher than those of the OMS cylinder. It is also observed that the OMS cylinder displays higher velocity fluctuations at locations away from the central line ($y^* = 0$). These findings suggest that the oscillation of the morphing surface enhances the turbulence in the near wake, particularly at $x^* \leq 1$.

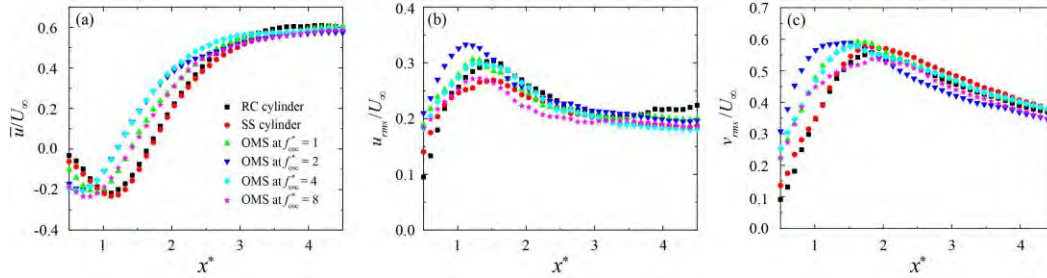


Figure 6.8 Distributions of (a) time-averaged streamwise velocities \bar{u}/U_∞ ; (b) streamwise fluctuating velocity u_{rms}/U_∞ , and (c) cross-stream fluctuating velocity v_{rms}/U_∞ in the centerline of cylinders ($y^* = 0$).

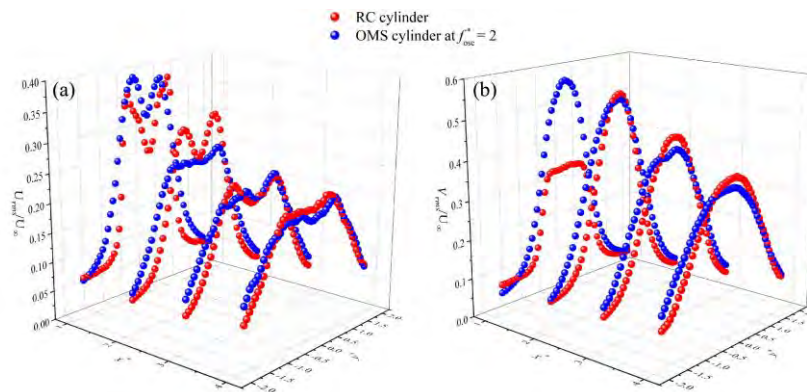


Figure 6.9 Distributions of (a) streamwise fluctuating velocity u_{rms}/U_∞ and (b) cross-stream fluctuating velocity v_{rms}/U_∞ along the lines of $x^* = 1, 2, 3$ and 4 . The comparison is between the RC cylinder and OMS cylinder at $f_{osc}^* = 2$.

To further compare the turbulence effect caused by the OMS cylinder, a comparison has been made on the Reynolds shear stress R_{uv} ($= \overline{u'v'}$) between the RC cylinder and the OMS cylinder driven at $f_{\text{osc}}^* = 2$, as shown in Figure 6.10, where u' and v' denotes the fluctuation component of u and v . The figures presented are derived from the analysis of all 25,000 images. Two observations can be noticed: first, the peak of R_{uv} occurs closer to the cylinder for the OMS cylinder at $f_{\text{osc}}^* = 2$; second, the absolute maximal value of R_{uv} , which indicates the intensity of interaction between positive and negative vortices, is significantly higher for the OMS cylinder at $f_{\text{osc}}^* = 2$ than the RC cylinder. As such, the turbulence intensity near the cylinder is enhanced due to the interaction between the oscillating membranes and shear layers, which in return alters the near-wake flow structures.

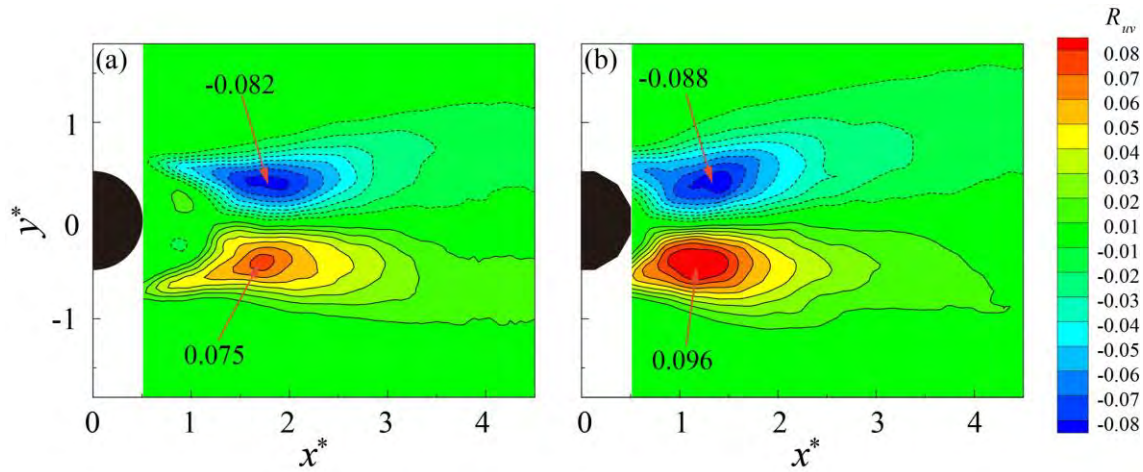


Figure 6.10 Distributions of Reynolds shear stress R_{uv} in the near wake of the (a) RC cylinder, and (b) OMS cylinder at $f_{\text{osc}}^* = 2$. The local maximum value of R_{uv} is marked in the figure.

6.5 POD analysis

From the previous sections, we have presented and discussed the difference in the mean and instantaneous wakes under different perturbation conditions, which can be attributed to the

change of shear layer behavior due to the dynamic morphing. To reveal more physical insights, POD analyses are conducted to extract energy-carrying coherent structures from phase-averaged wakes. Readers can refer to related references for details about the classical Snapshot POD algorithm^[175, 180].

Since all the dynamic morphing cases exhibit similar results, for the sake of simplicity, only the RC cylinder, the SS cylinder, and the OMS cylinder at $f_{\text{osc}}^* = 2$ are presented and discussed here. Figure 6.11(a) presents a phase diagram spanned by the coefficients of the first two POD modes, i.e., a_1 and a_2 , of the wake of the RC cylinder. It is seen that the (a_1, a_2) point travels in circles, with each circle representing a vortex-shedding cycle. This reflects good periodicity of the vortex-shedding process and is well suited for phase-averaging analysis^[57, 181]. Figure 6.11(b) shows the fractional contributions of the first ten POD modes to the total fluctuation kinetic energy, where λ_n is the eigenvalue of the n th mode. It is seen that the first two modes contribute the most as compared with the other modes for all selected cylinders. This implies that the wake dynamics has not been substantially changed by the dynamic morphing. The energy contribution from the first two modes of the static membrane is higher than the baseline cylinder, which is aligned with the findings of Wang et al.^[104] on a grooved cylinder.

The u/U_∞ and v/U_∞ contours in the first two POD modes of the RC cylinder are depicted in Figure 6.11 (c) & (d). The u/U_∞ and v/U_∞ data reveal that the vortex-shedding behavior for the captured cases exhibited a high degree of symmetry and repeatability. Modes 1 and 2 exhibit a strong correlation, with about 1/4 cycle streamwise dislocation between them. This correlation is distinctly represented by the positions of the peak u/U_∞ and v/U_∞ in Figure 6.11(c) & (d). This observation corresponds to the first two POD modes, which are similar and

characterized by alternately arranged vortices (Figure 6.12 a) with about 1/4 shedding cycle shifted in the streamwise direction. These observations collectively depict the streamwise evolution of Karman vortex shedding through these two modes.

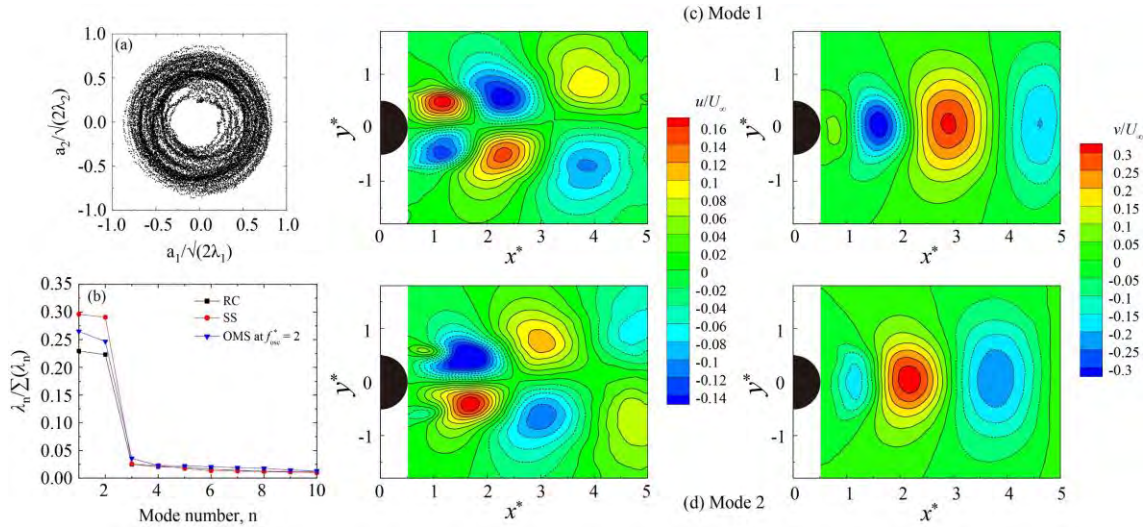


Figure 6.11 (a) coefficient correlations for RC cylinder; (b) POD eigenvalue spectrums for the RC cylinder, SS cylinder, and OMS cylinder at $f_{osc}^* = 2$; (c) mode 1 and (d) mode 2 distributions for the RC cylinder.

To provide a deeper understanding of the flow behavior associated with the oscillatory morphing surface, Figure 6.12 presents the flow fields of POD modes 1-4. These are depicted through velocity vectors and vorticity contours. For the RC cylinder, owing to the dominance of energy contribution by the first two modes, the strength of their vortices is significantly stronger than modes 3 and 4. The vorticity contours in modes 1 and 2, characterized by opposite signs, are arranged alternately in the streamwise direction, reflecting the convection of the vortices. Similar observations can also be made on the SS cylinder and the OMS cylinder at $f_{osc}^* = 2$. The vorticity distribution in mode 3 (RC cylinder) is symmetrical about the centerline ($y^* = 0$) and thus reflecting the asymmetrical vortex shedding. This asymmetrical behavior is more obvious for the OMS cylinder at $f_{osc}^* = 2$ (mode 3). Besides, coherent flow structures can

be found in the wake of the RC cylinder for the first three POD modes, while only the first two POD modes show apparent coherent flow structures for the SS cylinder and the OMS cylinder at $f_{osc}^* = 2$. The incoherent flow behavior is more obvious for the OMS cylinder at $f_{osc}^* = 2$ in modes 3 and 4, which means the oscillatory morphing surface may reduce the flow coherence. Another observation is that the occurrence of vorticity peaks is shifted upstream for the OMS cylinder at $f_{osc}^* = 2$, aligning with the shorter vortex formation length.

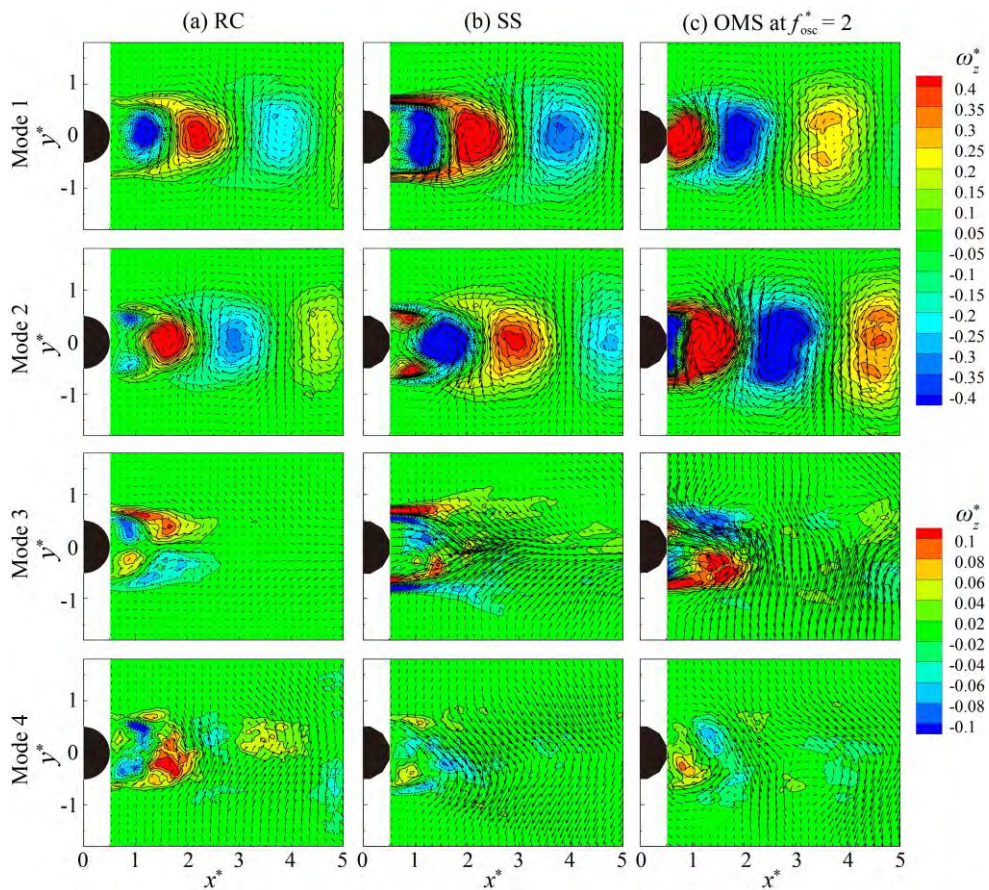


Figure 6.12 The ω_z^* contours and velocity vectors of POD modes 1-4 for the selected cases: (a) RC cylinder; (b) SS cylinder; (c) OMS cylinder at $f_{osc}^* = 2$. The range of ω_z^* for modes 1-2 is -0.4 to 0.4, and the range of ω_z^* for modes 3-4 is -0.1 to 0.1. To better show the vortex structures, the vector scale used in modes 3-4 is different from that used in modes 1-2.

Figure 6.13 compares the phase-averaged wakes at six phases, i.e., $t = 0$ to $5\pi/3$ with a $\pi/3$ interval, which are determined through the POD analysis. About 350 images (corresponding to $\pm \pi/72$ phase bin size) are used to calculate the mean results at each phase. For the RC cylinder, positive- and negative-signed vortices are alternatively shed from the cylinder, forming a classical von Karman vortex street (see Figure 6.13a). The wakes of the SS and RC cases are also similar. However, unlike the apparent rolling-up of the shear layers observed in the RC case, the shear layers behind the SS cylinder are almost parallel at the beginning, then gradually roll up in the far wake, as shown in Figure 6.13(b). This is because the flow separation occurs early for the special geometric characteristics of the SS cylinder.

For the dynamic morphing cases, the oscillation of the morphing surface affects the instability of the shear layers and thus changes the subsequent vortex-shedding behavior. For the OMS cylinder at $f_{\text{osc}}^* = 2$, the shear layers roll up early due to the increased instability, as shown in Figure 6.13(c). As such, a shorter recirculation region forms. This observation is consistent with the instantaneous flow structures presented in Figure 6.3. Differently, phase-averaged results help to focus on the dominant flow structure and show that the von Karman vortex shedding has not been changed for the OMS cylinder at $f_{\text{osc}}^* = 2$, confirming the results found in Figure 6.5. More importantly, the location of the first two positive and negative vortices in this case is closer to cylinder, and the distance between these vortices is smaller than the RC and SS cylinders, leading to the higher turbulence intensity in the near wake of the cylinder (Figure 6.13c). This explains the results found in Figures 6.9 and 6.10. Moreover, the strength of the vortices in this case is relatively weaker than the RC and SS cylinders, consistent with that revealed in Figure 6.7.

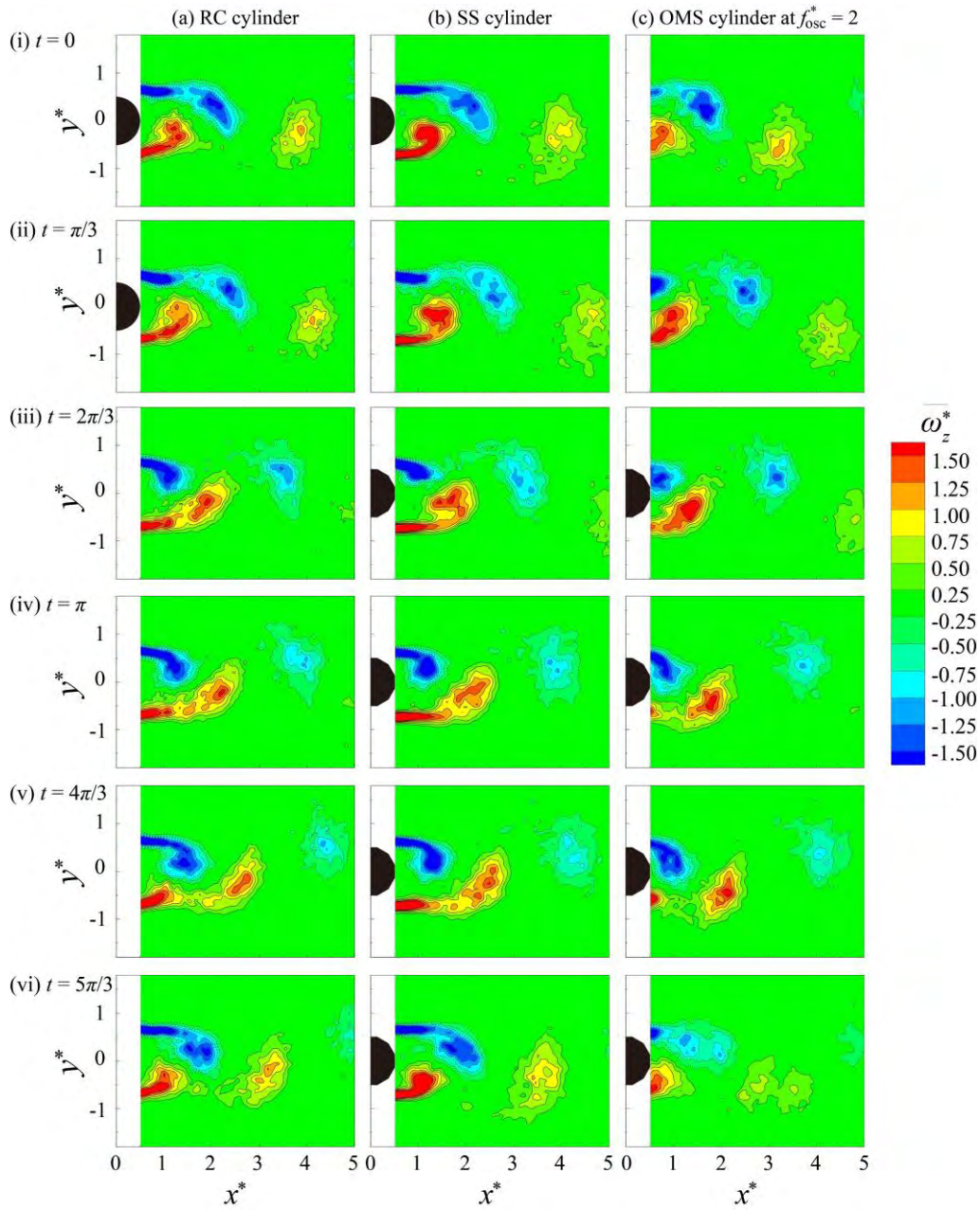


Figure 6.13 Phase-averaged results for the (a) RC cylinder, (b) SS cylinder and (c) OMS cylinder at $f_{\text{osc}}^* = 2$, where (i) $t = 0$, (ii) $t = \pi/3$, (iii) $t = 2\pi/3$, (iv) $t = \pi$, (v) $t = 4\pi/3$, and (vi) $t = 5\pi/3$ are the different phases of the wake behavior.

6.6 Wake and force control using oscillating surface/anti-phase jets

Due to the constraints of the experimental setup, it is necessary to connect pipes to the cylinder model to allow water to flow in and out, thereby driving the deformation of the membrane. Consequently, we are unable to install a load cell to measure the force (refer to Figure 6.1). Additionally, the maximum deformation of the membrane is relatively minimal, approximately $0.0065D$ (see Figure 6.2). To investigate the potential of using a morphing surface for drag reduction, we conducted CFD simulations based on ANSYS Fluent. Consequently, we are able to explore the flow control performance in a much larger parameter space.

To begin with, we adopt the same model as our experiment model and try to examine its hydrodynamic performance under a larger oscillation displacement. Unfortunately, the results turn out to be a drag and fluctuating lift force increase (as shown in Table 6.1) by the oscillatory morphing surface. Note that, the results given in Table 6.1 are based on a two-dimensional simulation and thus may exist disparity with those reported in the literature. Here, f_e is the perturbation frequency, and we use $f_e^* = (f_e/f_n)$, f_n is the natural frequency of the uncontrolled case) to normalize the perturbation frequency. f_{dis} is the normalized displacement of the oscillating surface compared to the cylinder's diameter D . This is not what we expected. But actually, we have tested different oscillation displacements and perturbation frequencies, the number of ribs, angles of attack, and Reynolds number effects (such as $Re = 100, 400, 1,000,$ and $3,200$), and the forces still increase when we used the oscillatory morphing surface control. The reasons are possible as follows: Firstly, the flow separation points are relatively unchanged

although we apply the control, i.e., located at the ribs between two membrane surfaces, and thus, the separation points are generally fixed. Secondly, based on our later results, that is, utilizing an oscillating surface in a cavity, the deformation of the morphing surface should be close to the order of the diameter D , which is unphysical and cannot be reached. This indicates that the excitation forces caused by the morphing surface are not high enough to achieve lock-on, thus not achieving the drag reduction outcome.

Table 6.1 Comparison of the numerical results with and without control at $Re = 3,200$.

Cases	$\overline{C_d}$	$C_{l,rms}$
Uncontrolled	1.45	0.83
$f_e = 2, f_{dis} = 0.05$	1.50	0.88
$f_e = 2, f_{dis} = 0.1$	1.53	0.88
$f_e = 2, f_{dis} = 0.2$	1.62	1.0
$f_e = 4, f_{dis} = 0.05$	1.51	0.88
$f_e = 8, f_{dis} = 0.05$	1.50	0.87
$f_e = 8, f_{dis} = 0.2$	1.63	1.05
$f_e = 16, f_{dis} = 0.05$	1.50	0.88

6.6.1 CFD setup and validation

Generally, the oscillatory morphing surface works like a zero-net-flux mass jet. Inspired by Rabault et al.^[182] and Ren et al.^[19], they successfully achieve a maximum drag reduction of about 8% at $Re = 100$ and around 30.7% at $Re = 1,000$, respectively, based on a deep reinforcement learning (DRL) technique and a pair of anti-phase jets, as shown in Figure 6.14. The jets are arranged at the cylinder's top and bottom parts with a range of 10° . Thus, a zero-net-flux mass can be achieved. The purpose of this setting is that it will not cause extra force in the horizontal direction, which means it will not directly influence the drag force. More

importantly, from their prior investigation, we can refer that the perturbation frequency of the jets is suggested to choose a value close to the cylinder's natural frequency to achieve lock-on. For example, the effective control frequency utilized in Rabault et al.^[182]'s results are about 3.5% lower than its natural frequency when $Re = 100$. Their work motivates us to further examine the control effects of the variants of oscillatory morphing surface, namely, the oscillating surface and anti-phase jets.

To test the effect of an oscillating surface (resembling a pair of anti-phase synthetic jets or dual synthetic jets) as a variant of the previous morphing surface, we adopted an oscillating surface located in a cavity, as shown in Figure 6.15(b). This is because it can significantly enlarge the jet speed through a small orifice by mildly oscillating the bottom surface. As we discussed before, this is a possible reason why we cannot achieve the drag reduction on a morphing surface identical to our experimental model. Besides, this kind of oscillating surface setting is essentially resembling a synthetic jet pair. After confirming that the control effect achieved by the oscillating surface is similar to that of the anti-phase jets, as illustrated in Figures 6.17 and 6.19, we decide to utilize the anti-phase jets setting for a broader investigation of control parameters. This choice is influenced by the limitations of the oscillating surface, especially the oscillation's amplitude.

It's important to note that the current configuration of the jets differs from those used in the studies of Rabault et al.^[182] and Ren et al.^[19]. In the current configuration, the jets on the upper and lower sections within a 10° range are applied on a horizontal segment (refer to Figure 6.15b), and the velocity profile of the jets is parabolic. The jet profile is given in equation (6-1), where v_{jet} is the maximum jet speed, and later, we use $v^* = (v_{jet}/U_\infty)$ to normalize the jet

strength; x is the coordinate in Cartesian coordinate system, and l_{jet} denote the length of the jet applied section; t is the time.

$$v_{jet} = v_{jet} \left(1 - \left(\frac{2x}{l_{jet}}\right)^2\right) \sin(2\pi f_e t) \quad (6-1)$$

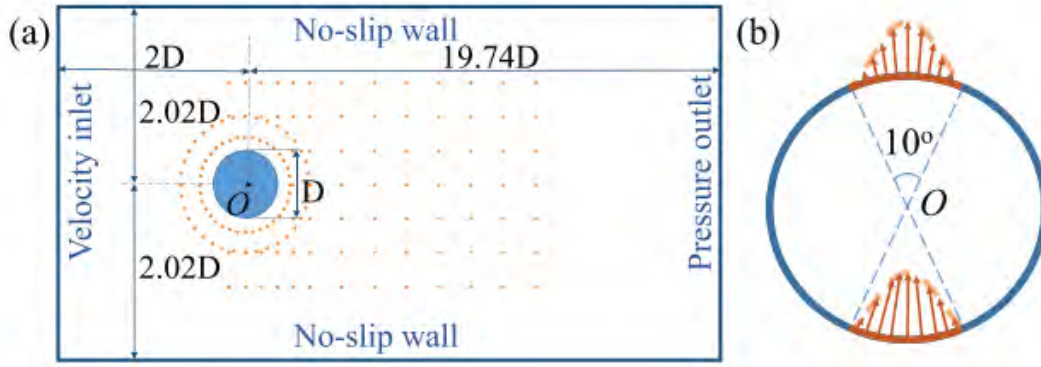


Figure 6.14 Numerical framework setting adopted in Rabault et al.^[182] and Ren et al.^[19]'s study: (a) boundary conditions and DRL sensors location; (b) the arrangement of the pair of anti-phase jets. Note that, the oncoming flow conditions are in a parabolic distribution in the channel flow, while the jet distribution is in a sinusoidal profile.

The computational domain and boundary conditions are displayed in Figure 6.15(a). The diameter of the cylinder is D and is located at $10D$ from the inlet and $30D$ from the outlet. The distance from the center of the cylinder to each side of the domain is $10D$. A uniform velocity inlet condition is established at its inlet boundary, while the pressure out condition is specified at its outlet boundary. The cylinder is no-slip wall, and the upper and lower sides of the computational domain are set as symmetry. For the oscillating surface case, the moving surface is defined as a no-slip wall with a prescribed moving displacement, which is the integral of eqn. (6-1). For the case of the anti-phase jet, the upper and lower sides of the cylinder are defined as velocity inlets, with the corresponding velocity profile given in eqn. (6-1). The diameter of

the mesh refinement area is approximately $5D$, with its origin fastened at the center of the cylinder. The computational domain is discretized into triangular meshes within the refinement area and quadrilateral meshes outside, with 73,681 grid elements, as presented in Figure 6.15(c)&(d). The smallest grid size is about 8×10^{-5} m around the cylinder to ensure the y^+ on the cylinder surface is smaller than 1.

The unsteady flow around the cylinder is assumed to be incompressible. We utilize Large Eddy Simulation (LES) to capture the flow details, choosing the WALE sub-grid model due to its extensive applicability. The convection and diffusion terms are discretized using a second-order upwind scheme. A second-order accurate implicit scheme is employed to resolve the time term.

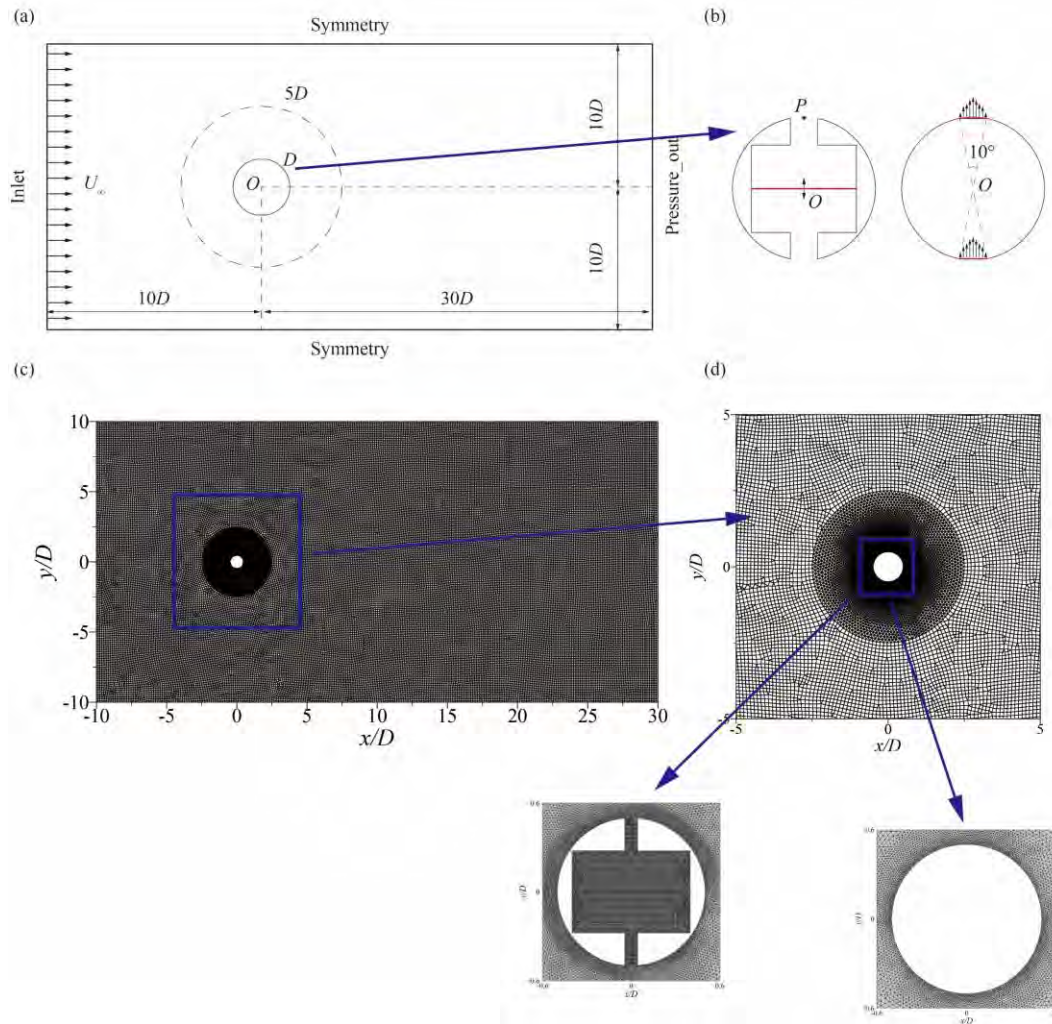


Figure 6.15 Numerical framework and calculation mesh: (a) computational domain and boundary conditions; (b) the setting of an oscillating surface and a pair of anti-phase jets; (c) the computation mesh and (d) its local details around a circular cylinder for both the oscillating surface and a pair of anti-phase jets setting.

The calculation mesh and time-step independence are checked at $Re = 1,000$, as shown in Figure 6.16. The results of time-history drag coefficient C_d and lift coefficient C_l have been compared among three different densities of meshes and time-steps. The total grid elements for the coarse, medium, and fine mesh are 49,217, 73,681, and 102,990, respectively. Clearly, the time-history variations of C_d and C_l are almost identical between the medium and fine meshes,

while a significant discrepancy between the coarse and medium meshes on the resolution of C_l can be noticed, as shown in Figure 6.16(a)&(b). Additionally, the results of C_d and C_l calculated by different time steps are nearly identical. As such, the following calculations are based on the medium mesh and time-step equals to 0.001 s.

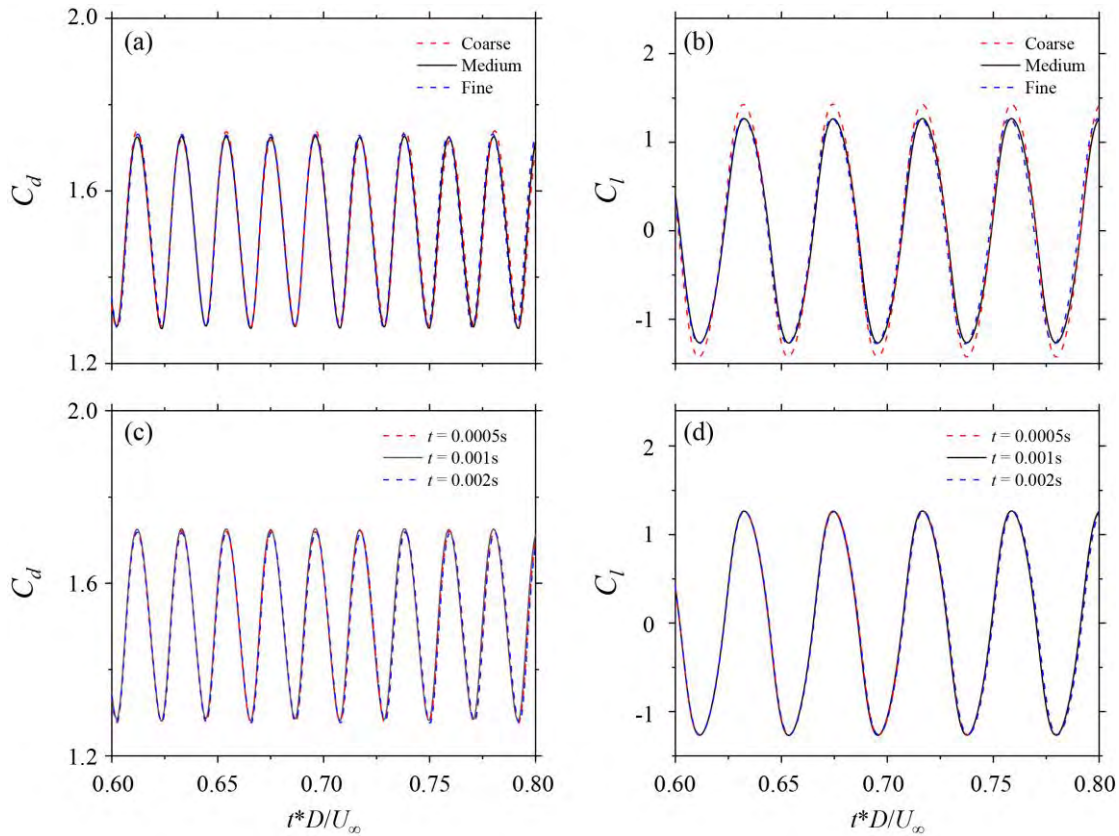


Figure 6.16 Calculation mesh and time-step independent validation: (a)&(b) comparison of time-history drag coefficient C_d and lift coefficient C_l at three different densities of meshes; (c)&(d) comparison of time-history drag coefficient C_d and lift coefficient C_l at three different time-steps based on the medium mesh.

In the validation part, we also conduct a simulation based on the identical parameters used in Ren et al.^[19]'s study (see Figure 6.14). As shown in Table 6.2, the $\overline{C_d}$, $C_{l,rms}$ and St for a normal cylinder in the present study is 3.36, 2.53 and 0.358, which is about 2.03%, 8.17% and

2.29% differ from that reported by Ren et al.^[19] based on their in-house code simulation. The optimal control effect achieved in their study is about 30.7% reduction in $\overline{C_d}$ and 55.2% suppression in $C_{l,rms}$. In our open-loop control cases, we can achieve approximately 14.3% reduction in $\overline{C_d}$ and 66.1% suppression in $C_{l,rms}$. The drag reduction effect, which is lower than their results, is well understood because they can almost reach the optimal control effect by DRL, and the jet variations in their study are highly irregular and asymmetrical. However, in our control cases, the jet changes are periodic and symmetrical. Overall, we can obtain similar results with Ren et al.^[19] for both the uncontrolled and controlled cases, thus validating our present simulation framework.

Table 6.2 Comparison of the present numerical results with Ren et al.^[19]'s data.

Cases	Present			Ren et al. ^[19]		
	$\overline{C_d}$	$C_{l,rms}$	St	$\overline{C_d}$	$C_{l,rms}$	St
Uncontrolled	3.36	2.53	0.358	3.293	2.339	0.35
Controlled	2.28	0.857		2.28	1.048	

6.6.2 Oscillating surface vs. anti-phase jets

To compare the control effect of the oscillating surface and anti-phase jets, we first give the comparison of time-history drag (C_d) and lift (C_l) coefficients between the uncontrolled and controlled cases when $Re = 1,000$, as displayed in Figure 6.17. Here, we offer the results based on several vortex-shedding cycles when the calculation reaches its steady state. It's worth noting that the control strategies were implemented on the cylinder only after its surrounding flow had reached a dynamic steady state for a considerable duration.

As depicted in Figure 6.17, the C_d & C_l curves for both the uncontrolled and controlled scenarios are notably periodic and stable. This indicates a consistent periodic characteristic of

the flow wake across various vortex-shedding cycles. As a result, we can focus on the instantaneous vortex patterns and pressure field within a selected vortex-shedding cycle to further clarify the control mechanism of the oscillating surface and anti-phase jets, as presented in Figures 6.19 and 6.20. The time-averaged mean drag coefficient $\overline{C_d}$ and rms lift coefficient $C_{l,rms}$ for the uncontrolled case are about 1.512 and 0.682, respectively. By applying the oscillating surface or anti-phase jets with appropriate strategy, $\overline{C_d}$ and $C_{l,rms}$ can be significantly reduced. For example, when $v^* = 2$, and $f_e^* = 0.93$, anti-phase jets control can achieve approximately 16.6% drag reduction and 24.5% rms lift suppression, as shown in Figure 6.17(c)&(d). In contrast, a 14.3% reduction in $\overline{C_d}$ and 9.3% reduction in $C_{l,rms}$ can be accomplished by the oscillating surface at the same excitation frequency as the anti-phase jets, i.e., $f_e^* = 0.93$ (see Figure 6.17e&f). The oscillating surface's maximum amplitude is $0.21D$, which is nearly the highest we can attain due to the area restriction in the cavity and the challenges in smoothly and successfully updating the dynamic mesh. Additionally, it's beneficial to note that the perturbation frequency at which the control works (i.e., lock-on occurs) is the same for both the oscillating surface and the anti-phase jets. The inherent relationship between the oscillating surface and the dual synthetic jets can be validated by the observed variations in vertical velocity v^* at point P , as shown in Figure 6.18. These observations suggest that the oscillating surface (dual synthetic jets) can effectively reduce the drag. Anti-phase jets can also achieve similar control performance, which indicates that the anti-phase jets are a good compromise for representation of the oscillating surface. These two variants show the possibility of drag reduction by utilizing an oscillatory morphing surface, which is worth investigating in our future study.

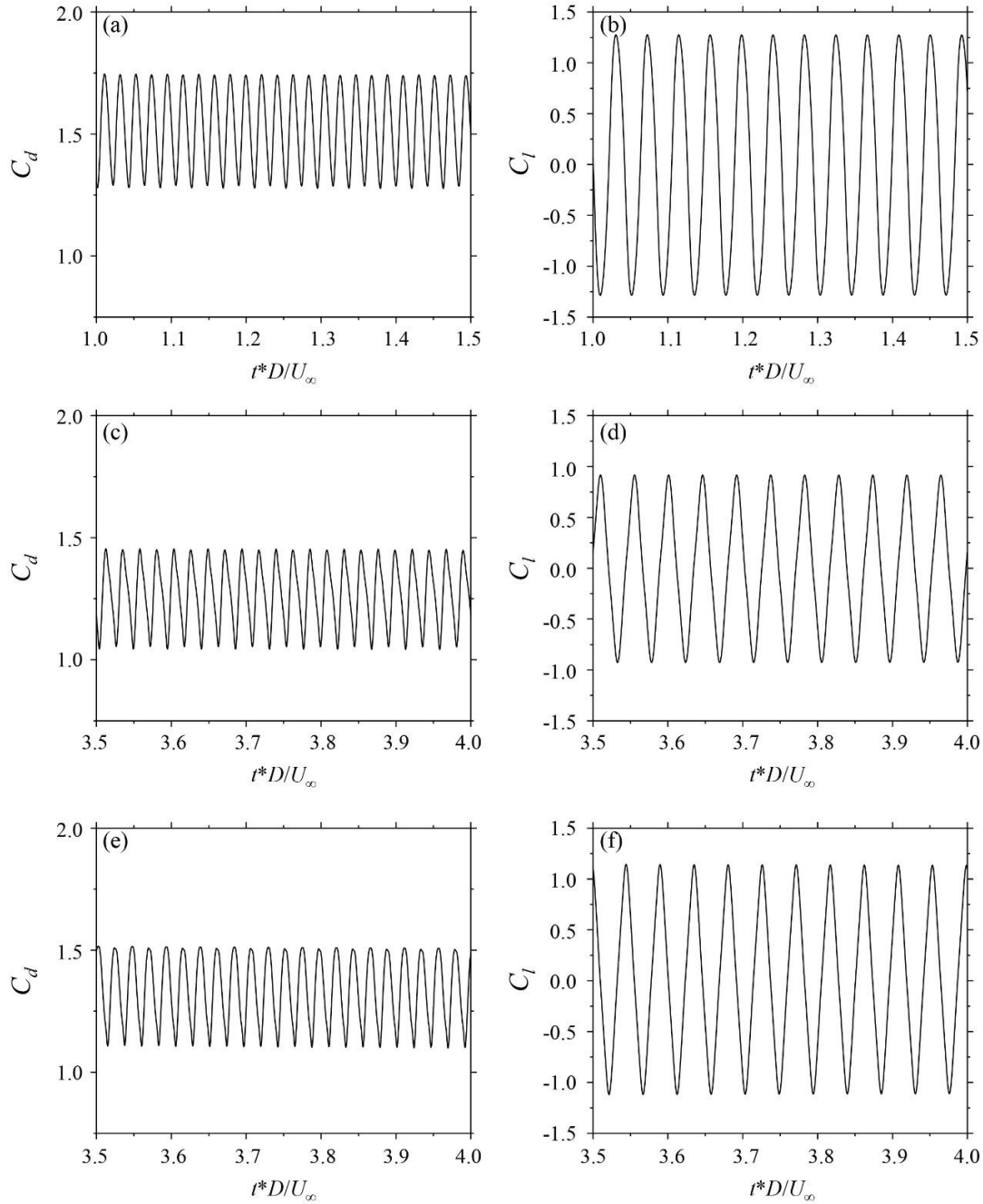


Figure 6.17 Time-history curve for the drag and lift coefficients obtained from several vortex shedding cycles when the calculation reaches their steady state: (a)&(b) C_d & C_l for the uncontrolled case; (c)&(d) C_d & C_l for the pair of anti-phase jets control case, where $v^* = 2$, and $f_e^* = 0.93$; (e)&(f) C_d & C_l for the oscillating surface control case, where the maximum displacement of the oscillating surface in the cavity is $0.21D$ and its perturbation frequency f_e^* is 0.93 .

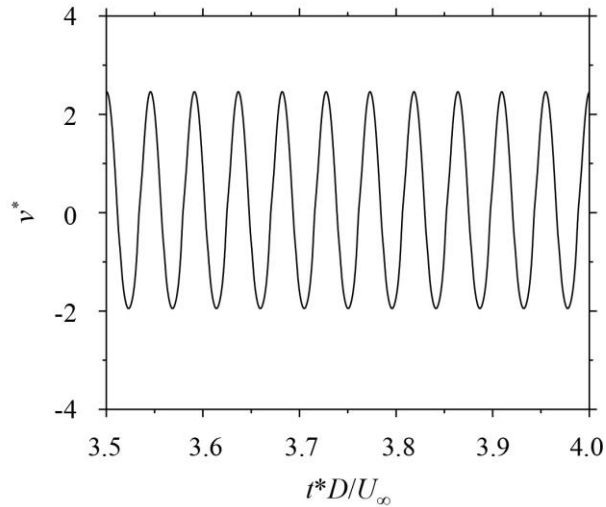


Figure 6.18 The normalized vertical velocity v^* monitored at point P caused by the oscillating surface.

The location of point P is the blue point in Figure 6.15(b).

For the uncontrolled case, positive and negative vortices are alternatively shed from the cylinder, thus generating a classical 2S pattern in the flow wake, as clearly shown in Figure 6.19(a). A corresponding low-pressure region emerges as the shear layer rolls up into a vortex, especially close to the rear part of the cylinder, as revealed in Figure 6.20(a). Compared to the uncontrolled case, through lock-on, the anti-phase jets can break the shear layers and suppress an early roll-up of the shear layers, leading to a parallel distribution of vortices in the near wake, as shown in Figure 6.19(b). As such, the interaction of the vortices in the near wake of the controlled case will be remarkably reduced, thus leading to a lower $C_{l,rms}$. A similar control effect of the flow wake can be achieved by applying oscillating surface technology (see Figure 6.19c). Because of the significant suppression of the roll-up of the shear layers in the near wake, the corresponding negative pressure behind the cylinder will rapidly move away and will not wrap around to the vicinity of the cylinder's rear side, resulting in a significant reduction of drag force, as shown in Figure 6.20(b)&(c).

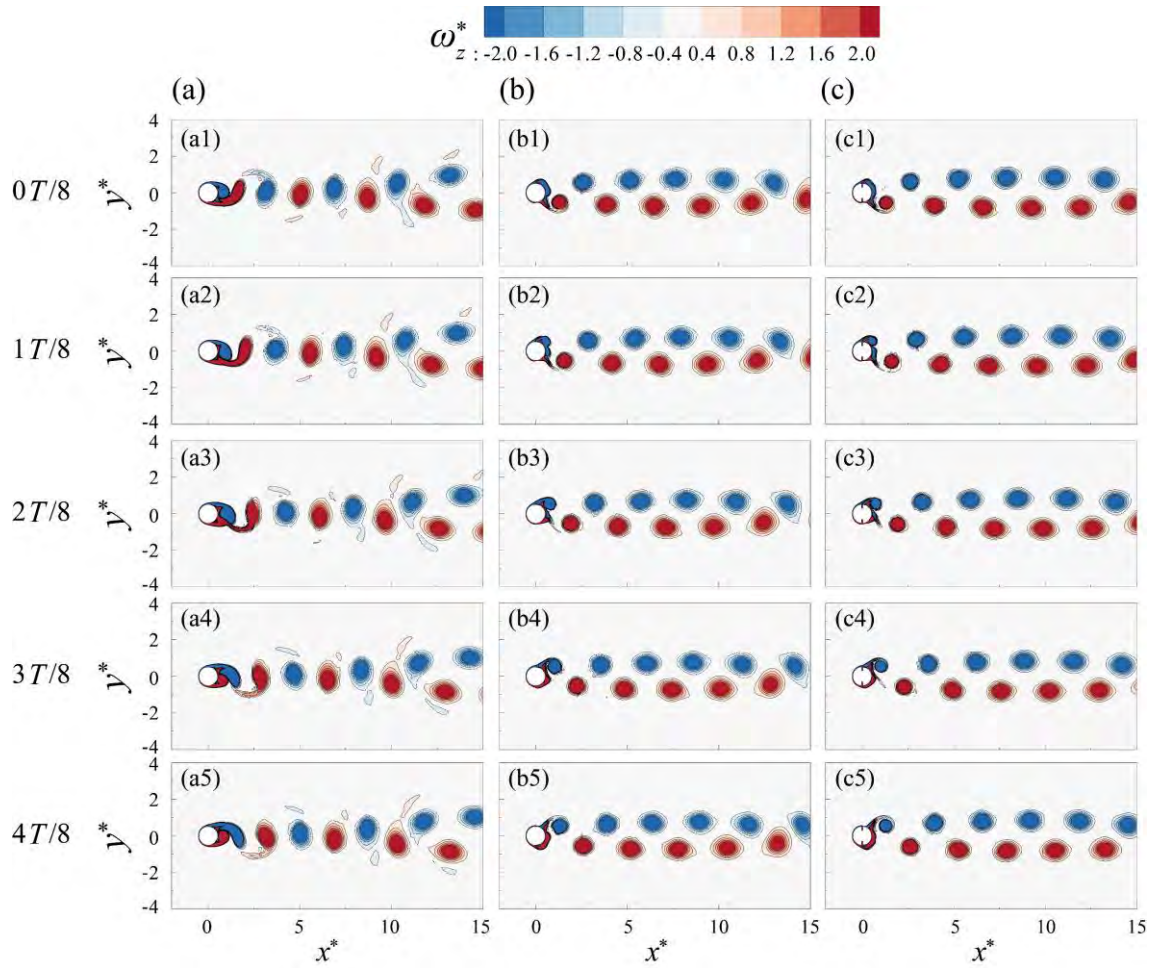


Figure 6.19 Instantaneous vortex patterns around the cylinder for (a) the uncontrolled case, (b) the anti-phase jets control case, where $\nu^* = 2$, and $f_e^* = 0.93$, and (c) the oscillating surface control case, where the maximum displacement of the oscillating surface in the cavity is $0.21D$ and its perturbation frequency f_e^* is 0.93 . $0T/8$, $2T/8$, and $4T/8$ represent the instants when C_l at the largest positive value, zero, and the largest negative value, respectively.

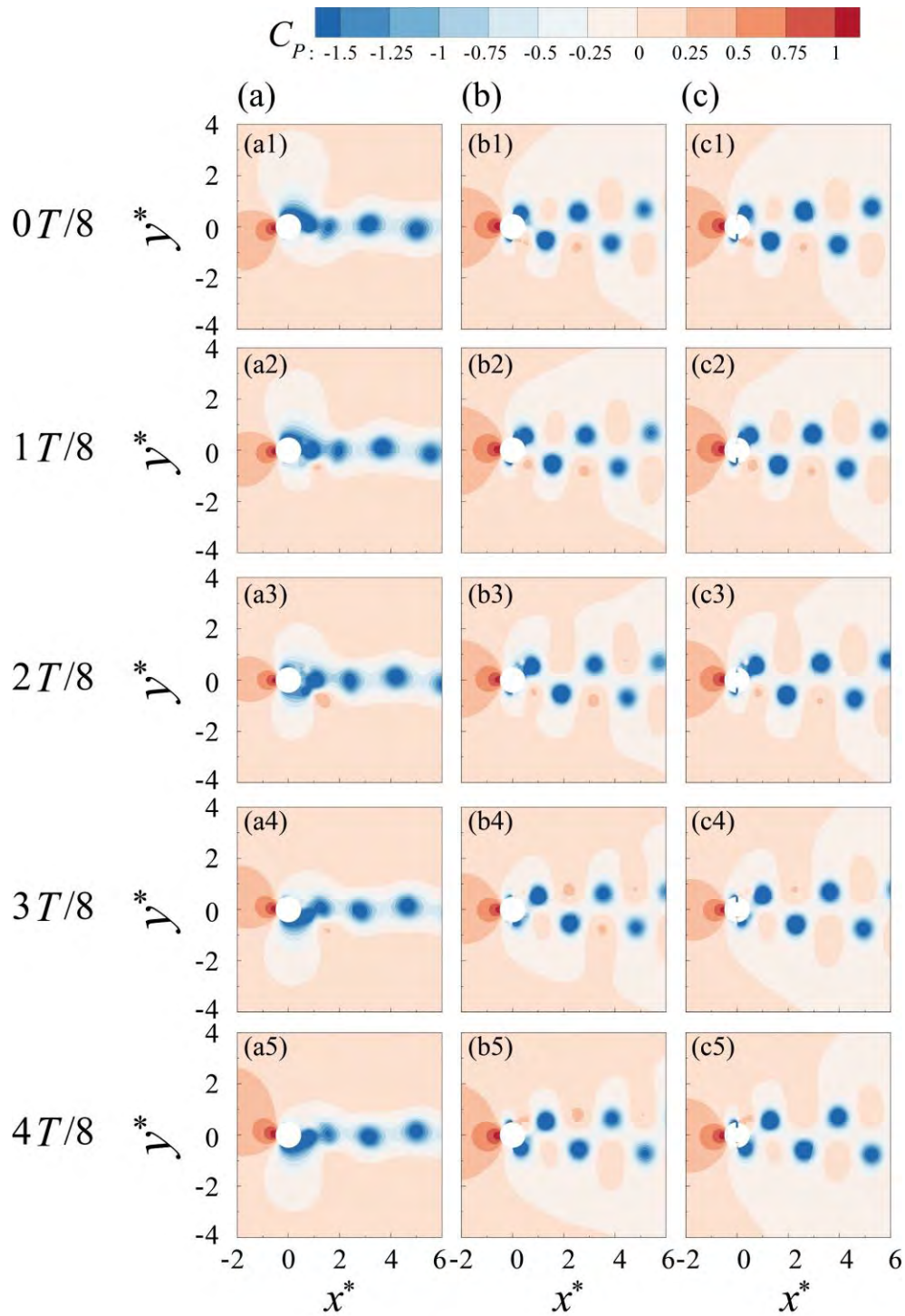


Figure 6.20 Instantaneous pressure field for (a) the uncontrolled case, (b) the anti-phase jets control case, where $v^* = 2$, and $f_e^* = 0.93$, and (c) the oscillating surface control case, where the maximum displacement of the moving wall in the cavity is $0.21D$ and its perturbation frequency f_e^* is 0.93 .

6.6.3 Effects of Reynolds number

In this section, we provide an in-depth discussion on the effects of Re on the control of hydrodynamic forces and flow wake of the cylinder, based on the anti-phase jets. We have considered three different Re values, namely 100, 400, and 1,000, to represent the conditions of laminar flow and weakly turbulent flow. Here, by utilizing the open-loop control method, our objective is not to showcase the optimal control effect. Rather, our focus is to emphasize instances where control has been effectively implemented at different Re values, and to concentrate on comprehending the underlying physics.

The effectively controlled parameters of the anti-phase jets and their corresponding obtained $\overline{C_d}$ and $C_{l,rms}$ are listed in Table 6.3. Note that, the normalized perturbation frequency f_e^* is determined based on their natural vortex shedding frequency at different Re . For example, when the jet strength is set as 0.1 of the oncoming flow speed, and the perturbation frequency is about 0.961 of cylinder's natural frequency at $Re=100$, a reduction of 2.73% in $\overline{C_d}$ and 14.4% reduction in $C_{l,rms}$ can be achieved when compared to the baseline case at $Re = 100$. The operational jet strength and perturbation frequency are nearly aligned with the values used in Rabault et al.^[182] and Ren et al.^[19]'s study. However, the drag reduction ratio is less than those reported in their research, where they achieved a maximum of approximately 8% drag reduction effect based on DRL. The potential reasons could be attributed to the jet forcing being entirely or significantly skewed in their cases. That is, one side of the jet pair consistently blows while the other side continuously suctions. Another possible reason is that a channel flow has been considered in their works, whereas in our current simulation, the computation domain is significantly larger than their setting.

Compared to the suppression of $\overline{C_d}$ and $C_{l,rms}$ at $v^* = 0.1$ and $f_e^* = 0.961$ when $Re = 100$, this strategy is not as effective in the cases of $Re = 400$ and $1,000$, with their $\overline{C_d}$ is almost equivalent to the uncontrolled case, while $C_{l,rms}$ significantly increases, as demonstrated in Table 6.3. Similarly, control parameters that are effective in the cases of $Re = 400$ and $1,000$ may result in a significant augment in $\overline{C_d}$ and $C_{l,rms}$ when $Re = 100$. For instance, for $v^* = 2$ and $f_e^* = 0.95$, they can achieve approximately 6.9% of $\overline{C_d}$ reduction and 21.6% of $C_{l,rms}$ suppression at $Re = 400$. However, under this control approach, the $\overline{C_d}$ and $C_{l,rms}$ at $Re = 1,000$ for the controlled case are slightly lower than the uncontrolled case, and it may result in a 40.0% increase in $\overline{C_d}$ and 416.7% enhancement in $C_{l,rms}$ at $Re = 100$. Additionally, it's worth noting that the control approach ($v^* = 2$ and $f_e^* = 0.93$), which works in the case of $Re = 1,000$, also achieves a comparable effect at $Re = 400$ compared to adopting $v^* = 2$ and $f_e^* = 0.95$ (see Table 6.3). These findings indicate that a lower jet control strength is effective in low Re cases, while a higher control strength may be necessary for high Re cases. Additionally, a gradual deviation in the perturbation frequency from the corresponding natural frequency might be required to efficiently control the hydrodynamic forces as the Re increases.

Table 6.3 Summary of test cases for three different Re .

Cases	$Re = 100$		$Re = 400$		$Re = 1,000$	
	$\overline{C_d}$	$C_{l,rms}$	$\overline{C_d}$	$C_{l,rms}$	$\overline{C_d}$	$C_{l,rms}$
Baseline (Uncontrolled)	1.355	0.215	1.420	0.667	1.512	0.862
$v^* = 0.1, f_e^* = 0.961$	1.318	0.184	1.407	0.733	1.549	1.025
$v^* = 2, f_e^* = 0.95$	1.856	1.111	1.322	0.523	1.448	0.811
$v^* = 2, f_e^* = 0.93$	1.832	1.117	1.399	0.586	1.261	0.651

In order to further discover the underlying physics for the control effect at different Re , Figures 6.21-6.26 present the corresponding instantaneous vortex patterns and pressure fields around the cylinder for the selected cases. For the uncontrolled case at $Re = 100$, a classical Karmen vortex shedding street can be identified in the flow wake, as displayed in Figure 6.21(a). After applying the anti-phase jet's control with $v^* = 0.1$ and $f_e^* = 0.961$, the vortex shedding fancy has not been changed. However, the corresponding strength of the vortices and the associated negative pressure magnitude near the rear part of the cylinder is slightly weaker and higher than the baseline case, respectively, as shown in Figure 6.21(a&b) and Figure 6.22(a&b), thus resulting in a lower $\overline{C_d}$ and $C_{l,rms}$. In comparison, for the cases of $v^* = 2$, $f_e^* = 0.95$ and 0.93 at $Re = 100$, the strength of the jet forcing does obviously interfere with the separated shear layer and split the shear layer, as indicated in the instant of $3T/8$ in Figure 6.21(c4&d4). The shear layer, at the subsequent instant, recovers and sheds from the cylinder. This observation is significantly different from that observed in the cases of $Re = 400$ and $1,000$, where the separated shear layer is broken into a smaller vortex and immediately shed away from the cylinder instead of gradually rolling up like in the uncontrolled case. In addition, the strength of the vortices and associated negative pressure behind the cylinder remarkably increases and decreases than the uncontrolled case, leading to a higher $\overline{C_d}$ and $C_{l,rms}$. These observations indicate that under the same strength of jet ($v^* = 2$), controlling the flow in the laminar condition is more difficult than in a weakly turbulent condition.

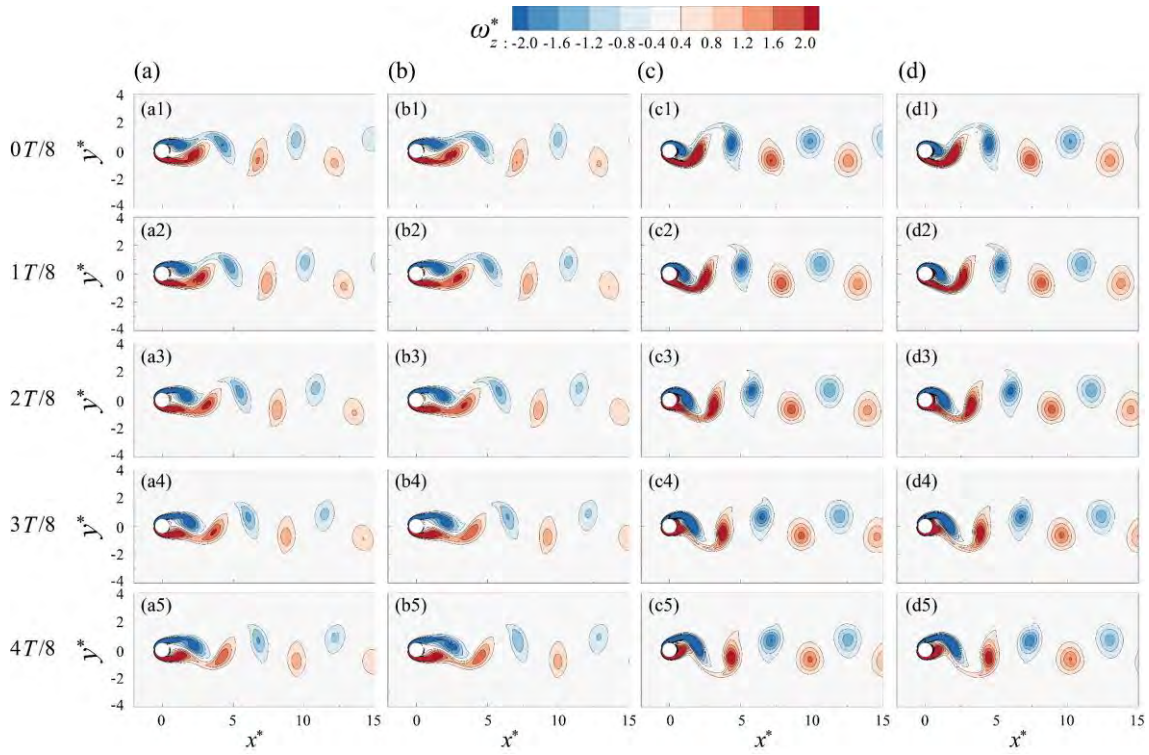


Figure 6.21 Instantaneous vortex patterns around the cylinder at $Re = 100$ for the uncontrolled case

(a), and the anti-phase jets control cases: (b) $v^* = 0.1, f_e^* = 0.961$; (c) $v^* = 2, f_e^* = 0.95$; (d) $v^* = 2, f_e^* =$

0.93.

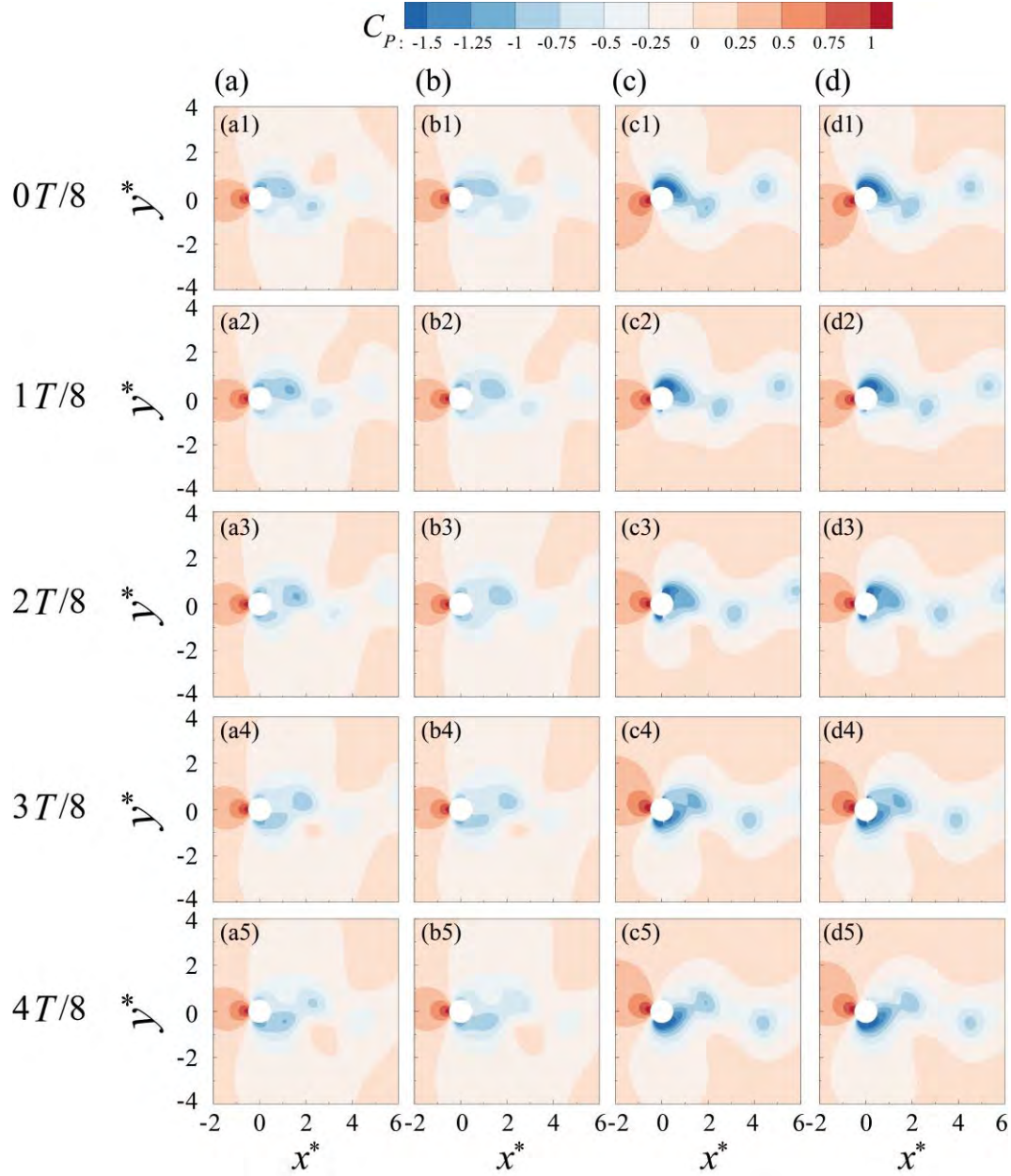


Figure 6.22 Instantaneous pressure field around the cylinder at $Re = 100$ for the uncontrolled case (a), and the anti-phase jets control cases: (b) $v^* = 0.1, f_e^* = 0.961$; (c) $v^* = 2, f_e^* = 0.95$; (d) $v^* = 2, f_e^* = 0.93$.

As for $v^* = 0.1$ and $f_e^* = 0.961$ applied to the cases of $Re = 400$ and $1,000$, the strength of the jets is too weak to alter the flow behavior, and their instantaneous vortex patterns and pressure fields around the cylinder is highly similar to the uncontrolled cases, as shown in

Figures 6.19-6.20, 6.23-6.26. Therefore, $\overline{C_d}$ between the uncontrolled and controlled cases is comparable. As demonstrated in Figures 6.23 and 6.24, the control mechanism at $Re = 400$ closely resembles that at $Re = 1,000$, characterized by a parallel arrangement of vortices in the near wake. The corresponding negative pressure region also moves directly away from the cylinder, rather than fully curling up around the rear side of the cylinder, leading to a substantial reduction in drag. For $v^* = 2$ and $f_e^* = 0.95$ when $Re = 1,000$, the control effect is not as effective as observed when $v^* = 2$ and $f_e^* = 0.93$. This is primarily due to the failure to achieve a well-stabilized parallel distribution of vortices as in the case when $v^* = 2$ and $f_e^* = 0.93$. In other words, the roll-up of the separated shear layers remains prominent in the near wake, leading to an enlargement of the negative pressure region behind the cylinder.

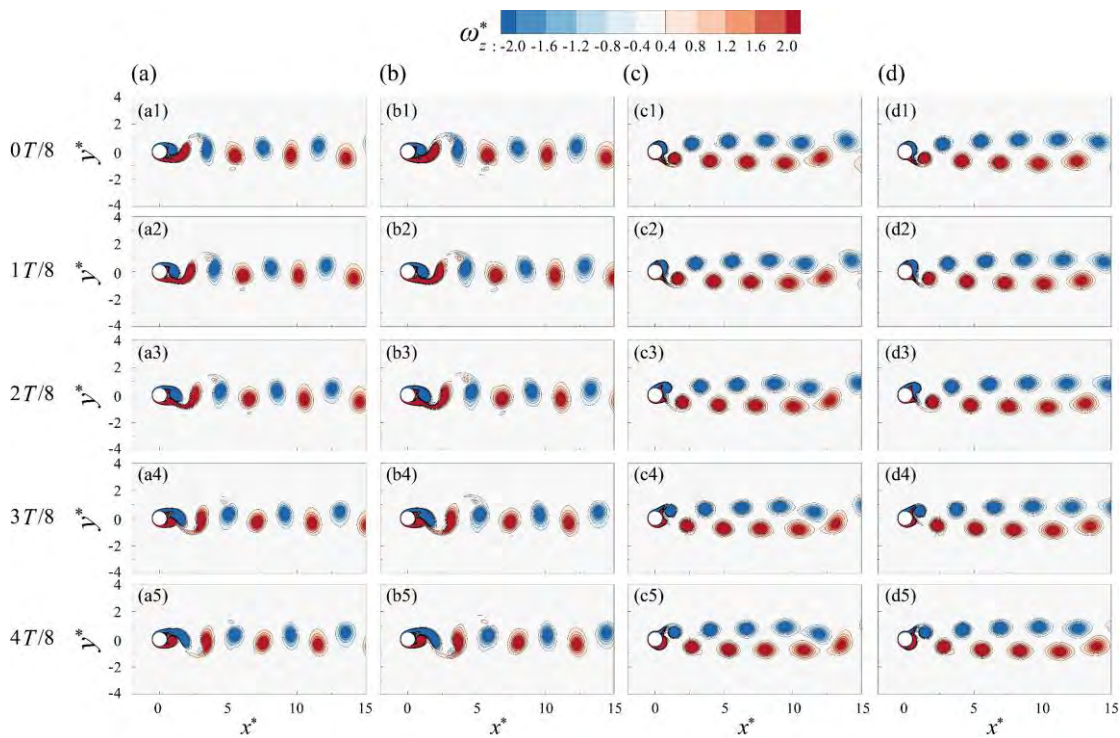


Figure 6.23 Instantaneous vortex patterns around the cylinder at $Re = 400$ for the uncontrolled case (a), and the anti-phase jets control cases: (b) $v^* = 0.1, f_e^* = 0.961$; (c) $v^* = 2, f_e^* = 0.95$; (d) $v^* = 2, f_e^* =$

0.93.

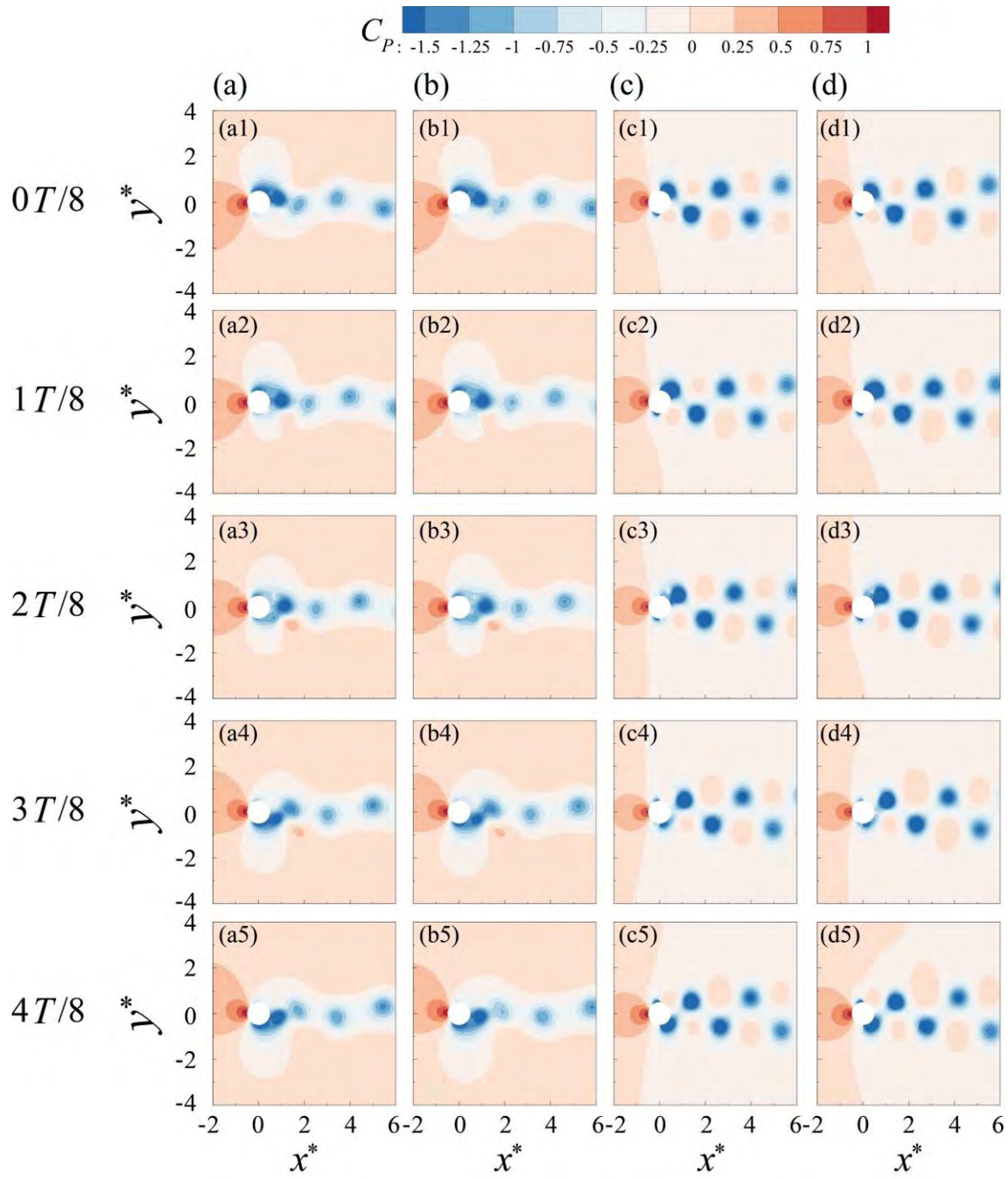


Figure 6.24 Instantaneous pressure field around the cylinder at $Re = 400$ for the uncontrolled case (a), and the anti-phase jets control cases: (b) $v^* = 0.1, f_e^* = 0.961$; (c) $v^* = 2, f_e^* = 0.95$; (d) $v^* = 2, f_e^* = 0.93$.

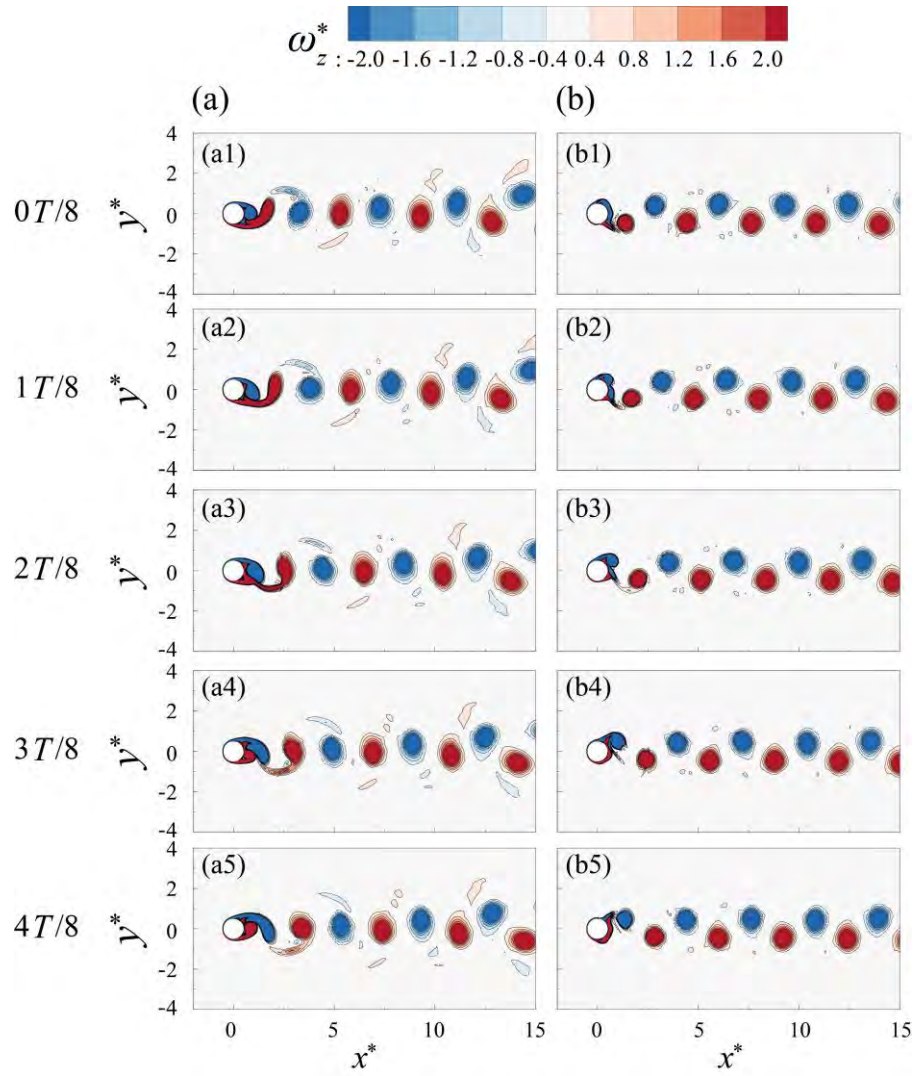


Figure 6.25 Instantaneous vortex patterns around the cylinder at $Re = 1,000$ for the anti-phase jets

control cases: (a) $v^* = 0.1, f_e^* = 0.961$; (b) $v^* = 2, f_e^* = 0.95$.

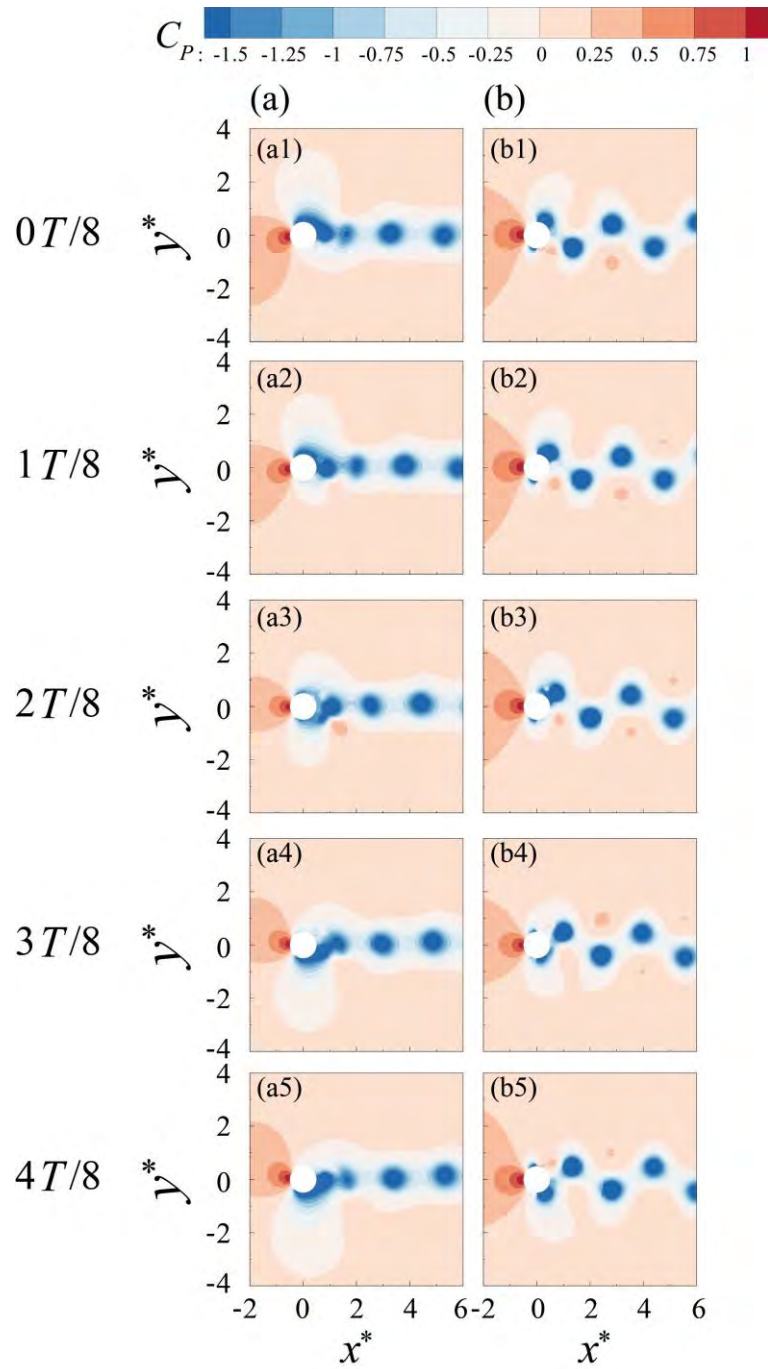


Figure 6.26 Instantaneous pressure field around the cylinder at $Re = 1,000$ for the anti-phase jets

control cases: (a) $v^* = 0.1, f_e^* = 0.961$; (b) $v^* = 2, f_e^* = 0.95$.

6.6.4 Control in three-dimensional space

To investigate whether the oscillating surface control parameters are still effective at high Re when the three-dimensional flow effect appears, we further conduct a three-dimensional (3D) simulation at $Re = 1,000$. In this section, we mainly focus on the control effect of the anti-phase jets on a three-dimensional (3D) cylinder and compare the similarities and differences with two-dimensional (2D) control outcomes. The three-dimensional numerical model and calculation mesh are shown in Figure 6.27. 3D LES has been used to conduct the present simulation, with its minimum height of mesh and calculation time-step identical to that adopted in a 2D simulation. The upper and lower sides of the domain are set as periodic, and the lateral surfaces are specified as symmetry. Following the definition of the spanwise wavelength λ_z given by Williamson et al.^[183] and Williamson^[6], λ_z for a normal cylinder can be estimated by $\lambda_z/D \sim 25 Re^{-1/2}$. λ_z is about $0.79D$ when $Re = 1,000$. Therefore, around eight wavelengths have been employed in the z direction to guarantee adequate resolution of the large-scale eddies in the flow (Lin et al.^[184]), as illustrated in Figure 6.27(a). A structured quadrilateral mesh was created on the bottom surface and then extended in the span direction, maintaining a distance of $0.05D$ in the z -direction. which is similar to that used by Lam and Lin^[185], and Lam et al.^[186], Lin et al.^[184]. A total of about 2.45 million elements have been used to conduct the present 3D simulations (see Figure 6.27b).

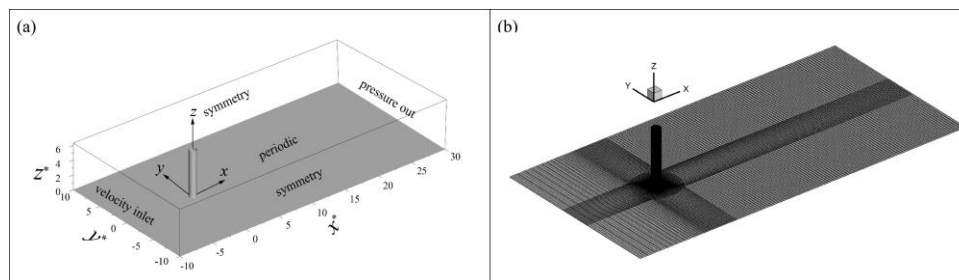


Figure 6.27 Three-dimensional numerical simulation model (a) and calculation mesh (b).

As revealed in Figure 6.28(a&b), the time-history curves of C_d & C_l for the 3D uncontrolled case are pretty chaotic, significantly different from that observed in a 2D uncontrolled case (Figure 6.17a&b). This observation is attributed to a three-dimensional flow behavior occurring for a normal cylinder when Re is larger than 180-190^[187, 188], at which the flow changes from a two-dimensional state to a three-dimensional state. The time-averaged drag coefficient $\overline{C_d}$, rms lift coefficient $C_{l,rms}$ and rms drag coefficient $C_{d,rms}$ for the uncontrolled case is about 1.340, 0.415 and 0.074, respectively. Here, the data statistics start from t^*D/U_∞ larger than 0.75 to avoid the initial largely unstable pulsations in the flow field. Interestingly, C_d & C_l reach a stable and periodic variation state for the controlled case (indicating a good modulation in the flow wake), as depicted in Figure 6.28(c&d), achieving approximately 9.18% reduction in $\overline{C_d}$, and 29.8% reduction in $C_{d,rms}$. However, this control strategy, i.e., $v^* = 2$, and $f_e^* = 1.24$, may cause a notable increase of $C_{l,rms}$ (about 67.2%). Note that, the strength of the jet adopted in a 3D control case is the same as that used in a 2D case at $Re = 1,000$. However, the perturbation frequency of the jet differs in the two cases, which is about 7% lower (2D) and 24% higher (3D) than the corresponding natural frequency of the uncontrolled case, respectively. The possible reason is that a closer excitation frequency with optimal jet forcing can effectively control the wake and drag of the cylinder when C_l curve (showing clear only one dominant peak) and flow wake for the 2D uncontrolled case are quite periodical and stable. While, for the 3D uncontrolled case, owing to the chaotic changes of C_l , multiple frequency components will occur rather than only one dominant peak. Therefore, an excitation frequency further away from the dominant peak may work in controlling cylinder's drag and flow wake. This observation is consistent with that reported by Ren et al.^[19].

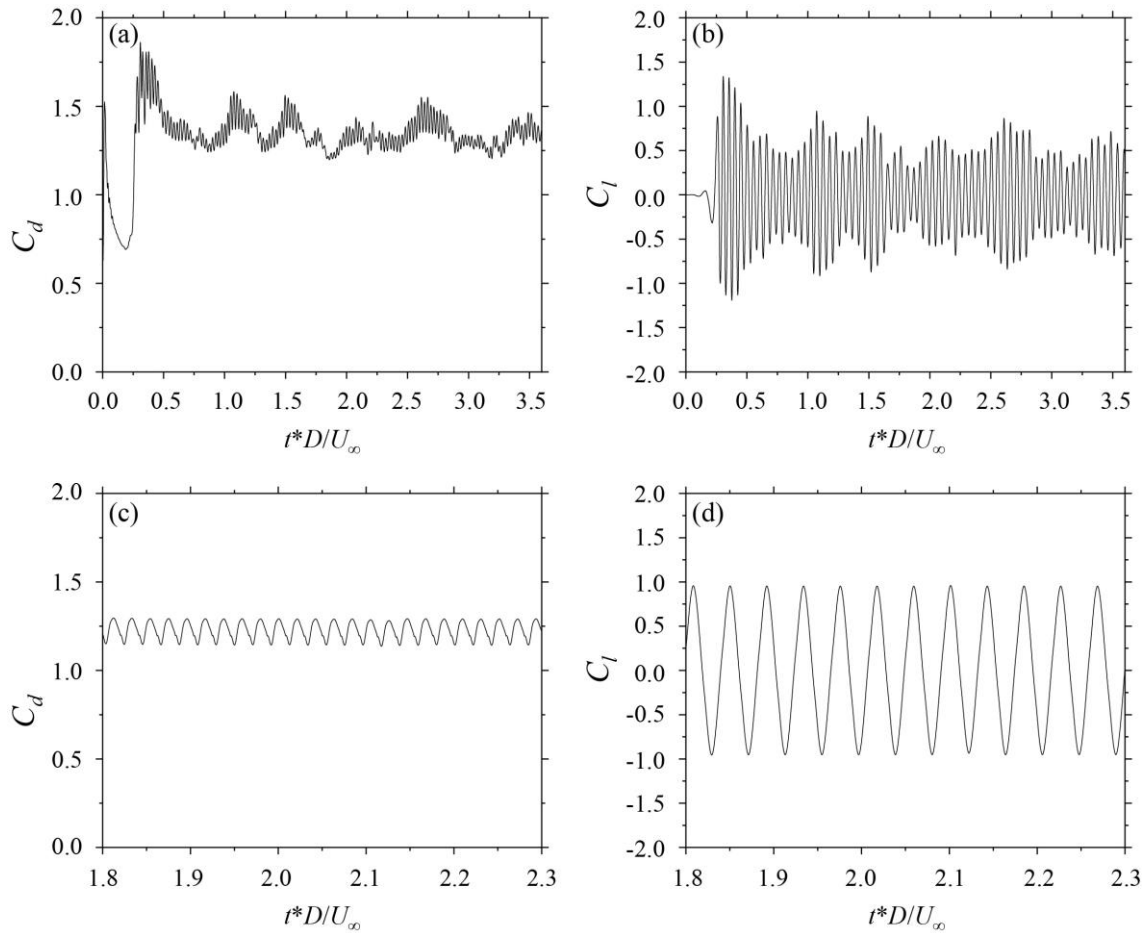


Figure 6.28 Time-history curve for the drag and lift coefficients: (a)&(b) C_d & C_l for the uncontrolled case; (c)&(d) C_d & C_l for the pair of anti-phase jets control case, where $v^* = 2$, and $f_e^* = 1.24$. Here, only several vortex-shedding cycles are presented for the controlled case due to its good periodical performance.

The instantaneous vortex structures at the mid-span of the cylinder for the uncontrolled and controlled cases are given in Figure 6.29. The start time (t^*D/U_∞) used for presenting the instantaneous vortex structures for the uncontrolled and controlled cases is about 2.32 and 2.08 when C_l reaches its minimal value, as shown in Figure 6.28(b&d). The vortex patterns for the uncontrolled case are highly irregular and turbulent, presenting a 3D flow behavior (see Figure 6.29a), which is distinct with that observed in a 2D case (Figure 6.19a). In the near wake of the cylinder, the vortex shedding, and alternative roll-up of the separated shear layers can still be

clearly noticed, thus forming a low-pressure region near the rear part of the cylinder, as illustrated in Figure 6.30(a). After applying the jet control, the 3D chaotic flow behavior develops into a more regular state, as shown in Figure 6.29(b). This flow behavior is quite similar to that observed in a 2D controlled case (see Figure 6.19b). This is possible because the control method applied to the 3D cylinder is essentially a 2D jet distribution expended in the spanwise direction. Due to the similarity of the vortex evolutions in the near wake between the 3D and 2D controlled cases, a quite similar distribution of the pressure field is formed behind the cylinder, as shown in Figure 6.30(b). Compared to the uncontrolled case, the lower pressure region has been significantly reduced, as the lower pressure region associated with the alternatively shedding vortices will quickly move away from the cylinder instead of fully rolling up to cover a larger area behind the cylinder, like the uncontrolled case. As such, $\overline{C_d}$ for the controlled case can be remarkably reduced.

Figure 6.31 further presents the 3D flow structure by exhibiting the iso-surface of the normalized Q^* for the uncontrolled and controlled cases. Readers may find the detailed calculation of Q in those references^[189, 190]. Compared to the chaotic state of the uncontrolled case, the iso-surface ($Q^* = 2$) for the controlled case consists of larger-scale stable vortices along its spanwise direction, especially near the cylinder, and thus helps to effectively stabilize the flow wake and transit the highly 3D flow state to a quite 2D flow behavior. That is, through lock-on, the jet can stabilize the spanwise flow and delay the occurrence of three-dimensional flow, forming a quasi-two-dimensional one. However, this alternation may simultaneously lead to the increase in the strength of cylinder's spanwise vortex shedding, and thus lead to the increase of $C_{l,rms}$.

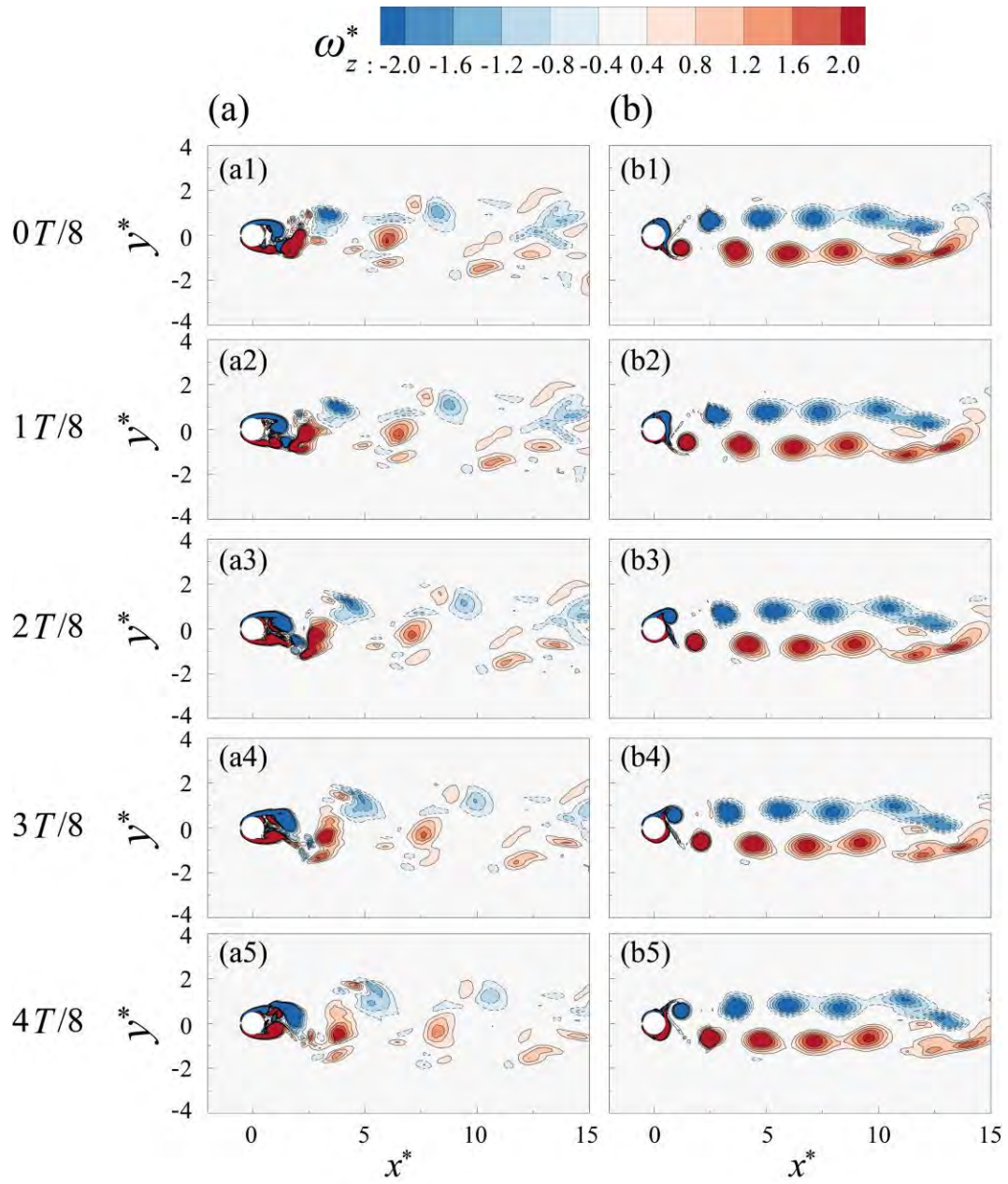


Figure 6.29 Instantaneous vortex patterns at the mid-span of the cylinder when $Re = 1,000$: (a) uncontrolled case and (b) controlled case.

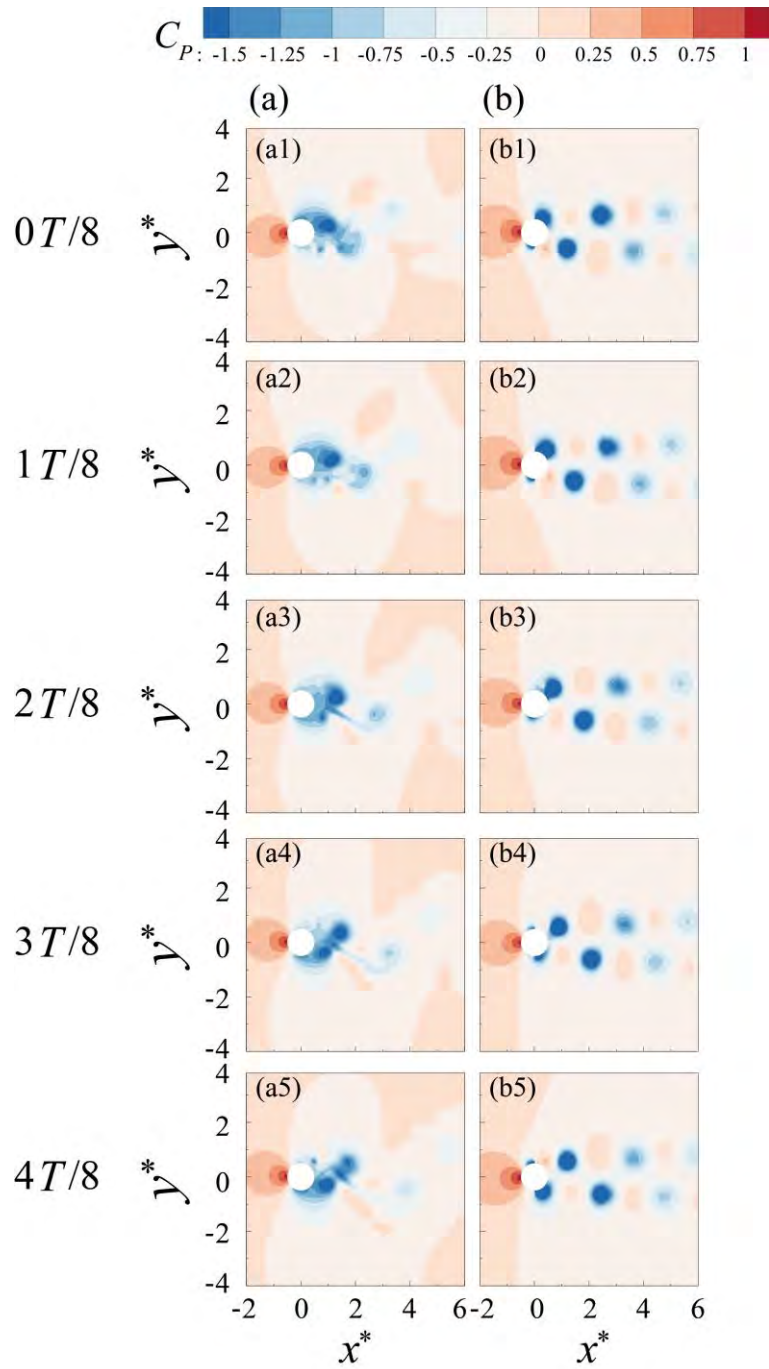


Figure 6.30 Instantaneous pressure field at the mid-span of the cylinder when $Re = 1,000$: (a) uncontrolled case and (b) controlled case.

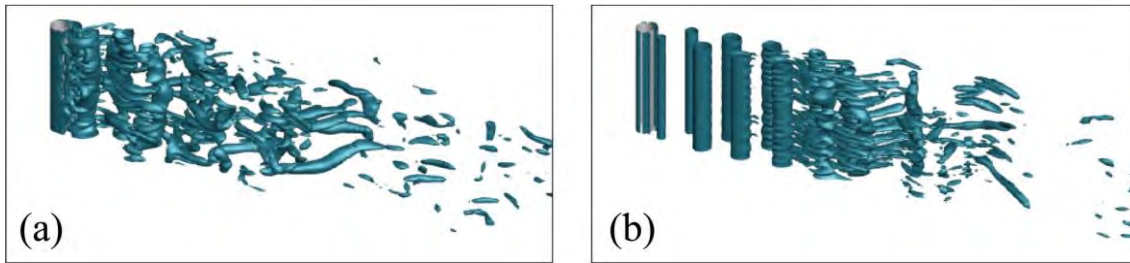


Figure 6.31 Iso-surface of the instantaneous normalized Q^* ($= 2$) of the (a) uncontrolled case and (b) controlled case.

6.7 Remarks

Based on the experimental measurements, the effects of oscillatory morphing surface on the wake flow were investigated, and the effect of the excitation frequency was discussed in great detail. Based on the 2D and 3D simulations, the effects of the oscillating surface and anti-phase jets (serving as the variants of the oscillatory morphing surface) on the control of a cylinder's hydrodynamic forces and flow wake were examined, and the effect of Re was discussed. Major findings are summarized below:

- (1) Compared with the RC and SS cylinders, the OMS cylinders are able to reduce their vortex formation length, especially for $f_{osc}^* = 2$, which can achieve a reduction of about 25.2%, with the largest u_{rms} and v_{rms} in the near wake. Besides, the OMS cylinder at $f_{osc}^* = 2$ can best suppress the strength of time-averaged vorticity and local maximum vorticity.
- (2) The oscillatory morphing surface can manipulate the wake structure. Phase-averaged and instantaneous results show that the oscillatory morphing surface can affect the instability of the shear layers. For a lower-frequency perturbation case (e.g., OMS cylinder at $f_{osc}^* = 1$), the instability of the shear layers is only slightly enhanced. And

the vortex-shedding behavior is not significantly changed when the excitation frequency is close to the natural vortex-shedding frequency.

- (3) For the OMS cylinder operating at $f_{osc}^* = 2$ and 4, an extra PSD component corresponding to the excitation frequency can be clearly detected. The flow instability is significantly increased owing to the intensive interaction of the morphing surfaces with the shear layers. As such, the shear layers will transition and roll up earlier with a shorter vortex formation length.
- (4) When the excitation frequency is remarkably higher than the dominant vortex shedding frequency, i.e., the OMS cylinder at $f_{osc}^* = 8$, the shear layers are broken up. Interestingly, a train of small vortices will form. They follow the trace of the primary shear layers and roll up into a relatively large vortex.
- (5) Using an oscillating surface can effectively manipulate the wake of the cylinder and reduce the drag. Anti-phase jets can also achieve similar control performance (drag reduction up to 16.6%), which indicates that the anti-phase jets are a good compromise for the representation of the oscillating surface.
- (6) As for a 2D simulation when $Re = 400$ and 1,000, compared to the uncontrolled case, the anti-phase jets can break the shear layers and suppress an early roll-up of the shear layers, leading to a parallel distribution of vortices in the near wake. The associated low-pressure region behind the cylinder will directly move away instead of fully curling up around the rear side of the cylinder, resulting in a significantly reduced drag.
- (7) The effective control strategies for a 2D cylinder at $Re = 100, 400,$ and 1,000 vary due to the Re effects. In general, a lower jet control strength is effective in low Re cases, while a higher control strength may be necessary for high Re cases. Additionally, a

gradual deviation in the perturbation frequency from the corresponding natural frequency might be required to efficiently control the hydrodynamic forces as the Re increases.

- (8) For a 3D cylinder, through lock-on, the jet can stabilize the spanwise flow and delay the occurrence of three-dimensional flow, forming a quasi-two-dimensional one. Besides, a drag reduction of about 9.18% can be achieved.

While we have ascertained that the oscillatory morphing surface can effectively manipulate the wake and decrease drag, the practical application of this finding still requires further consideration. Moreover, it would be beneficial to conduct an experimental study using the oscillating surface to corroborate the observations made through CFD. It would also be valuable to explore the impact of a partial oscillatory morphing surface on a cylinder, specifically in terms of force and wake control effects.

Chapter 7 Conclusions and future work

7.1 Conclusions

In this thesis, we aim to address several important issues in passive and active flow control of bluff bodies. These issues are related to the use of trailing-edge splitter plate, attached fins, biomimetic surface, and oscillatory morphing surface and its variants. The main conclusions of the present thesis are as follows:

7.1.1 FIV control with an attached splitter plate

A cylinder attached by different lengths (L) of rigid splitter plates was tested to examine its effects on the resulting FIV. The Re ranges from 800 ~ 11,000. Different vibration modes have been revealed for a FIV circular cylinder at a large mass ratio ($m^* = 50$), i.e., VIV ($L/D = 0$ to 0.125), Transition I (L/D at 0.25), Galloping ($L/D = 0.5, 0.75$), Transition II (L/D at 1.0), and Suppression region (L/D from 1.5 to 3.5). We also found that, as L increases from $L/D = 0$ to 0.25, the peak value of cylinder oscillation amplitude increases and appears at higher reduced velocities. When L continues to rise, galloping-type oscillations occur at $L/D = 0.5$ and 0.75. This is because the shear layers attach to the tip of splitter spitter, thus resulting in the occurrence of flow reattachment. As such, the pressure difference synchronizes with its vibration and leads to the happen of galloping. The transition stage has been found at $L/D = 1.0$. Oscillation is then significantly suppressed when the splitter length is larger than $L/D = 1.5$, mainly because of the significantly weaker excitation force from the flow and quite symmetrical pressure distribution in the near wake.

7.1.2 FIV control and flow energy harvesting using fins

FIV and energy harvesting performance of a cylinder attached by fins were investigated ($Re \approx 1,500 \sim 11,400$). We found that the two-windward-fin cylinder undergoes galloping, whereas the two-leeward-fin cylinder only undergoes weak vortex-induced vibrations. By attaching both two windward and two leeward fins to the cylinder, a novel bi-directional flow-energy harvester is implemented, which outperforms the plain cylinder with much larger vibration amplitudes and a much broader velocity range. More importantly, due to the geometric symmetry, it is able to harvest flow energy from two opposite directions. Within the current flow speed range, the maximal voltage and power outputs are about 7.37 V and 1.81 μW , respectively, about 2.7 and 7.2 times the plain cylinder's peak values. This new bi-directional flow-energy harvester is a suitable candidate to operate at sites where the flow periodically switches its directions, such as in tidal flows.

By further conducting numerical simulations, we found that, shear layers are alternatively formed and shed from the top and bottom sides of the vibrating plain cylinder, leading to alternatively appearing low-pressure regions that always force the cylinder to return to its equilibrium position. While for cylinder attached with two leeward fins, the associated low-pressure regions are then mainly further downstream of the two fins, more on the back side of the cylinder. As such, the cylinder experiences much less net vertical force compared to the plain cylinder. In comparison, flow separation is promoted early at the fin tips for the two-windward-fin case. The separated shear layer on the bottom side quickly re-attaches on the cylinder's downstream convex surface, thus generating a very strong low-pressure region right on the cylinder's bottom side and producing a very large net vertical force to sustain the

galloping response. As for the four-fin cylinder, a strong low-pressure region around the bottom side of the cylinder is formed due to the lower-side separated shear layer reattaching to the cylinder as it moves downward, while the lower leeward fin disrupts this reattachment and mitigates further bending of the shear layer. Therefore, this generates reduced pressure imbalance in the vertical direction, resulting in mild FIV vibration.

7.1.3 FIV of a cactus-shaped cylinder

The FIV performance of a nature-inspired cylinder equipped with three or four ribs was studied. The Re ranges from 2,900 ~ 24,500. The effect of AOAs on the FIV and hydrodynamic performance of the cylinder has been compared in detail. The results showed that the three ribs suppress the cylinder's oscillation at lower AOAs ($0^\circ \sim 30^\circ$) while promoting galloping at higher AOAs ($45^\circ \sim 60^\circ$) as compared with the plain cylinder. This is due to the earlier flow separation for three-rib cases at higher AOAs, resulting in a larger curvature of shear layers and flow reattachment. As such, the pressure difference synchronizes with the oscillation, providing a more significant excitation to the system. For the three-rib cases at lower AOAs and the four-rib cases at higher AOAs ($30^\circ \sim 45^\circ$), the cylinder's oscillation is almost entirely suppressed, leading to improved hydrodynamic performance. This improvement is primarily due to the delayed flow separation and the symmetrical distribution of pressure in the near wake. The four-rib cases at lower AOAs ($0^\circ \sim 15^\circ$) display a typical VIV response, accompanied by a symmetry break, i.e., a P+S vortex shed mode. This symmetry break is associated with the length of the trailing edge and the oncoming flow speed. These findings offer significant insights into the FIV behavior of cylinders featuring nature-inspired rib structures and the

corresponding flow dynamics under varying AOAs. Such insights could prove beneficial for design considerations and practical engineering applications.

7.1.4 Wake and force control with oscillatory morphing surface

A cylinder covered by a flexible latex membrane was tested to investigate the effects of cylindrical surface oscillations on the wake flow ($Re = 3,240$). It was found that, the oscillatory morphing surface can alter the wake structure. Compared with the baseline and static membrane cases, the perturbation cases can reduce their vortex formation length, especially for $f_{osc}^* = 2$, which can achieve a reduction of about 25.2%. For a lower-frequency perturbation case (e.g., OMS cylinder at $f_{osc}^* = 1$), the instability of the shear layers is only slightly enhanced. And the vortex-shedding behavior is not significantly changed when the excitation frequency is close to the natural vortex-shedding frequency. For optimal frequency excitations, i.e., $f_{osc}^* = 2$ and 4, the flow instability is significantly increased owing to the intensive interaction of the morphing surfaces with the shear layers. As such, the shear layers will transition and roll up earlier with a shorter vortex formation length. Interestingly, small vortices form regularly along and superimpose upon the separated shear layers at higher perturbation, i.e., $f_{osc}^* = 8$. They follow the trace of the primary shear layers and roll up into a relatively large vortex.

The oscillating surface and anti-phase jets, serving as the variants of the oscillatory morphing surface, were used to control the drag and flow wake of a cylinder. It was found that, using an oscillating surface can effectively manipulate the wake of the cylinder and reduce the drag. Anti-phase jets can also achieve similar control performance (drag reduction up to 16.6%), which indicates that the anti-phase jets are a good compromise for representation of the oscillating surface. At $Re = 400$ and 1,000, the jet can transmit the relatively large-scale vortices

into a smaller one and successfully modulate their flow patterns from an alternative Karmen vortex street into a parallel distribution of vortices in the near wake. The low-pressure region associated with the roll-up of the separated shear layers for the controlled case will quickly move away from the cylinder. The wake and hydrodynamic force of the cylinder have been successfully controlled at different Re , i.e., $Re = 100, 400$ and $1,000$, under different control parameters. A lower jet control strength is effective in low Re cases, while a higher control strength may be necessary for high Re cases. As for a 3D cylinder, through lock-on, the jet can stabilize the spanwise flow and delay the occurrence of three-dimensional flow, forming a quasi-two-dimensional one. Besides, a drag reduction of about 9.18% can be achieved.

7.2 Future work

The present thesis aims to address the research gaps identified in the introduction and literature review sections. The research findings and limitations presented in this work offer valuable insights that could inspire future studies.

1. In the research concerning the control of FIV of a circular cylinder using a trailing edge splitter plate, there has been a noticeable lack of studies focusing on the combined heaving and pitching of the splitter plate. Therefore, the influence of freedom of vibration (i.e., heaving motion only and coupled heaving and pitching motions) on the associated vibration response and physics will be compared in our further work. Furthermore, the rigidity of the trailing edge splitter plate presents another area of interest that merits further investigation.
2. In the study of FIV control and flow energy harvesting systems based on a circular cylinder equipped with fins, it is crucial to evaluate its practical application and

efficiency in a bidirectional flow. This could be done, for instance, in a towing tank/channel or through numerical simulation. Moreover, due to the turbulence of tidal and wind flows, the incoming flow cannot be perfectly uniform. Therefore, it would be intriguing to assess the performance of the proposed energy-harvesting prototype in actual turbulent flow conditions. Furthermore, this concept can be arranged in various configurations to create a farm, which will be the focus of our future research.

3. For FIV control using a cactus-shaped cylinder, stability analysis could be employed to scrutinize the symmetry breaking observed in the four-rib cases (a notably symmetrical configuration). Additionally, we plan to explore more intriguing nature-inspired shapes in our subsequent research.
4. For the wake control by a cylinder with oscillatory morphing surface, the displacement of the morphing surface in the current model during a water channel test is significantly minimal. As such, we aim to construct a wind tunnel platform to increase the model's surface morphing displacement and simultaneously measure its force performance. More complex and interesting deformation modes can be introduced instead of only using simple sinewave. Additionally, it would be valuable to compare the impact of global control, where all membrane surfaces oscillate in unison, and local control, where only a portion of the membrane pieces oscillate while the rest remain stationary.
5. Regarding the anti-phase jets control, we plan to conduct more thorough and detailed studies using a three-dimensional simulation framework. This will allow us to examine the effects of jet strength, jet perturbation frequency, jet distribution, and Reynolds number. In addition, we will conduct experiments based on our simulation of the

oscillating surface achieved in a cavity. Our aim is to investigate the effects of oscillating displacement and perturbation frequencies of the membrane on the aerodynamic behavior and flow performance of a cylinder, using a wind tunnel experiment.

References

- [1] Choi H, Jeon W, Kim J. Control of Flow Over a Bluff Body[J]. Annual Review of Fluid Mechanics, 2008,40:113-139.
- [2] Govardhan R, Williamson C H K. Modes of vortex formation and frequency response of a freely vibrating cylinder[J]. Journal of fluid mechanics, 2000,420:85-130.
- [3] Feng C C. The measurement of vortex induced effects in flow past stationary and oscillating circular and D-section cylinders[D]. University of British Columbia, 1968.
- [4] Mannini C, Marra A M, Bartoli G. VIV–galloping instability of rectangular cylinders: Review and new experiments[J]. Journal of wind engineering and industrial aerodynamics, 2014,132:109-124.
- [5] Anagnostopoulos P. Flow-induced vibrations in engineering practice[J]. Advances in Fluid Mechanics, 2002(vol. 31).
- [6] Williamson C H K. Vortex dynamics in the cylinder wake[J]. Annual Review of Fluid Mechanics, 1996,28:477-539.
- [7] Berger E, Wille R. Periodic flow phenomena[J]. Annual Review of Fluid Mechanics, 1972.
- [8] Rashidi S, Hayatdavoodi M, Esfahani J A. Vortex shedding suppression and wake control: A review[J]. Ocean Engineering, 2016,126:57-80.
- [9] Ran Y, Deng Z, Yu H, et al. Review of passive control of flow past a circular cylinder[J]. journal of visualization, 2022:1-44.
- [10] Chen W L, Huang Y, Chen C, et al. Review of active control of circular cylinder flow[J]. Ocean Engineering, 2022, 258: 111840.

References

- [11] Cattafesta III L N, Sheplak M. Actuators for active flow control[J]. *Annual Review of Fluid Mechanics*, 2011, 43: 247-272.
- [12] Ding L, Zhang L, Wu C, et al. Flow induced motion and energy harvesting of bluff bodies with different cross sections[J]. *Energy conversion and management*, 2015,91:416-426.
- [13] Truitt A, Mahmoodi S N. A review on active wind energy harvesting designs[J]. *International journal of precision engineering and manufacturing*, 2013,14(9):1667-1675.
- [14] Wu Y, Lien F, Yee E, et al. Numerical Investigation of Flow-Induced Vibration for Cylinder-Plate Assembly at low Reynolds Number[J]. *Fluids (Basel)*, 2023,8(4):118.
- [15] Hu G, Tse K T, Kwok K C S. Enhanced performance of wind energy harvester by aerodynamic treatment of a square prism[J]. *Applied Physics Letters*, 2016, 108(12).
- [16] Wang W, Song B, Mao Z, et al. Numerical investigation on VIV suppression of the cylinder with the bionic surface inspired by giant cactus[J]. *Ocean Engineering*, 2020,214:107775.
- [17] Zhdanov O, Busse A. Angle of attack dependence of flow past cactus-inspired cylinders with a low number of ribs[J]. *European Journal of Mechanics - B/Fluids*, 2019,75:244-257.
- [18] Guttag M, Reis P M. Active aerodynamic drag reduction on morphable cylinders[J]. *Physical review fluids*, 2017,2(12).
- [19] Ren F, Rabault J, Tang H. Applying deep reinforcement learning to active flow control in weakly turbulent conditions[J]. *Physics of Fluids*, 2021,33(3).
- [20] Assi G R S, Bearman P W. Transverse galloping of circular cylinders fitted with solid

References

- and slotted splitter plates[J]. *Journal of Fluids and Structures*, 2015,54:263-280.
- [21] Bearman P W. Circular cylinder wakes and vortex-induced vibrations[J]. *Journal of Fluids and Structures*, 2011,27(5-6):648-658.
- [22] Williamson C H K, Govardhan R. Vortex-induced vibrations[J]. *Annual Review of Fluid Mechanics*, 2004,36:413-455.
- [23] Bearman P W. Vortex Shedding from Oscillating Bluff Bodies[J]. *Annual review of fluid mechanics*, 1984,16(1):195-222.
- [24] Wang W, Mao Z, Song B, et al. Suppression of vortex-induced vibration of a cactus-inspired cylinder near a free surface[J]. *Physics of fluids*, 2021,33(6):67103.
- [25] Jauvtis N, Williamson C H K. Vortex-induced vibration of a cylinder with two degrees of freedom[J]. *Journal of Fluids and Structures*, 2003,17(7):1035-1042.
- [26] Pan Z Y, Cui W C, Miao Q M. Numerical simulation of vortex-induced vibration of a circular cylinder at low mass-damping using RANS code[J]. *Journal of Fluids and Structures*, 2007,23(1):23-37.
- [27] Williamson C H K, Roshko A. Vortex formation in the wake of an oscillating cylinder[J]. *Journal of fluids and structures*, 1988,4(2):355-381.
- [28] Zeng L, Zhao F, Wang H, et al. A bi-directional flow-energy harvester[J]. *Applied Physics Letters*, 2023, 122(15).
- [29] Sun X, Suh C S, Ye Z, et al. Dynamics of a circular cylinder with an attached splitter plate in laminar flow: A transition from vortex-induced vibration to galloping[J]. *Physics of fluids*, 2020,32(2):27104.
- [30] Sahu T R, Furquan M, Mittal S. Numerical study of flow-induced vibration of a circular cylinder with attached flexible splitter plate at low[J]. *Journal of fluid mechanics*,

- 2019,880:551-593.
- [31] Den Hartog J P. Transmission line vibration due to sleet[J]. Transactions of the American Institute of Electrical Engineers, 1932, 51(4): 1074-1076.
- [32] Van Oudheusden B W. On the quasi-steady analysis of one-degree-of-freedom galloping with combined translational and rotational effects[J]. Nonlinear dynamics, 1995,8(4):435-451.
- [33] Sourav K, Sen S. Determination of the transition mass ratio for onset of galloping of a square cylinder at the least permissible Reynolds number of 150[J]. Physics of fluids, 2020,32(6):63601.
- [34] Zhao J, Hourigan K, Thompson M C. Flow-induced vibration of D-section cylinders: an afterbody is not essential for vortex-induced vibration[J]. Journal of fluid mechanics, 2018,851:317-343.
- [35] Rostami A B, Armandei M. Renewable energy harvesting by vortex-induced motions: Review and benchmarking of technologies[J]. Renewable & sustainable energy reviews, 2017,70:193-214.
- [36] Liang S, Wang J, Hu Z. VIV and galloping response of a circular cylinder with rigid detached splitter plates[J]. Ocean Engineering, 2018,162:176-186.
- [37] Scruton C. The use of wind tunnels in industrial aerodynamic research[J]. 1960.
- [38] Strouhal V. Über eine besondere Art der Tonerregung[M]. Stahel, 1878.
- [39] Bearman P W, Gartshore I S, Maull D J, et al. Experiments on flow-induced vibration of a square-section cylinder[J]. Journal of Fluids and Structures, 1987,1(1):19-34.
- [40] Parkinson G V, Sullivan P P. Galloping response of towers[J]. Journal of Wind Engineering and Industrial Aerodynamics, 1979,4(3):253-260.

References

- [41] Bouclin D N. Hydroelastic oscillations of square cylinders[D]. University of British Columbia, 1979.
- [42] Santosham T V. Force measurements on bluff cylinders and aeroelastic galloping of a rectangular cylinder[D]. University of British Columbia, 1966.
- [43] Sarpkaya T. A critical review of the intrinsic nature of vortex-induced vibrations[J]. *Journal of Fluids and Structures*, 2004,19(4):389-447.
- [44] ZHOU K, LI Z, LIU Y, et al. Sweeping jet control of flow around a circular cylinder[J]. *Experimental Thermal and Fluid Science*, 2022:110785.
- [45] Jahanmiri M. Active flow control: a review[R]. 2010.
- [46] Oertel J H. Wakes behind blunt bodies[J]. *Annual Review of Fluid Mechanics*, 1990,22(1):539-562.
- [47] Zdravkovich M M. Review and classification of various aerodynamic and hydrodynamic means for suppressing vortex shedding[J]. *Journal of Wind Engineering and Industrial Aerodynamics*, 1981,7(2):145-189.
- [48] Bearman P W H J. Control of circular cylinder flow by the use of dimples[J]. *AIAA Journal*, 1993(31):1753-1756.
- [49] Choi J, Jeon W P, Choi H. Mechanism of drag reduction by dimples on a sphere[J]. *Physics of Fluids*, 2006, 18(4).
- [50] Shih W C L, Wang C, Coles D, et al. Experiments on flow past rough circular cylinders at large Reynolds numbers[J]. *Journal of Wind Engineering and Industrial Aerodynamics*, 1993,49(1):351-368.
- [51] Stappenbelt B. Splitter-plate wake stabilisation and low aspect ratio cylinder flow-induced Splitter-plate wake stabilisation and low aspect ratio cylinder flow-induced

References

- vibration mitigation[J]. International Journal of Offshore and Polar Engineering, 2010.
- [52] Anderson E A, Szewczyk A A. Effects of a splitter plate on the near wake of a circular cylinder in 2 and 3-dimensional flow configurations[J]. Experiments in fluids, 1997,23(2):161-174.
- [53] Kwon K, Choi H. Control of laminar vortex shedding behind a circular cylinder using splitter plates[J]. Physics of fluids, 1996,8(2):479-486.
- [54] Apelt C J, West G S. The effects of wake splitter plates on bluff-body flow in the range $10^4 < R < 5 \times 10^4$. Part 2[J]. Journal of Fluid Mechanics, 1975, 71(1): 145-160.
- [55] Apelt C J, West G S, Szewczyk A A. The effects of wake splitter plates on the flow past a circular cylinder in the range $10^4 < R < 5 \times 10^4$ [J]. Journal of Fluid Mechanics, 1973, 61(1): 187-198.
- [56] Gerrard J H. The mechanics of the formation region of vortices behind bluff bodies[J]. Journal of fluid mechanics, 1966,25(2):401-413.
- [57] New T H, Shi S, Liu Y. Cylinder-wall interference effects on finite-length wavy cylinders at subcritical Reynolds number flows[J]. Experiments in fluids, 2013,54(10):1-24.
- [58] Lam K, Lin Y F. Effects of wavelength and amplitude of a wavy cylinder in cross-flow at low Reynolds numbers[J]. Journal of Fluid Mechanics, 2009,620:195-220.
- [59] Wang W, Song B, Mao Z, et al. Numerical investigation on VIV suppression of the cylinder with the bionic surface inspired by giant cactus[J]. Ocean Engineering, 2020,214:107775.
- [60] El-Makdah A M, Oweis G F. The flow past a cactus-inspired grooved cylinder[J]. Experiments in fluids, 2013,54(2):1-16.

References

- [61] Talley S, Iaccarino G, Mungal G, et al. An experimental and computational investigation of flow past cacti[J]. Annual Research Briefs, Center for Turbulence Research, NASA Ames/Stanford University, 2001:51-63.
- [62] Bingham C, Raibaudo C, Morton C, et al. Suppression of fluctuating lift on a cylinder via evolutionary algorithms: Control with interfering small cylinder[J]. Physics of fluids, 2018,30(12):127104.
- [63] Zhu H, Yao J, Ma Y, et al. Simultaneous CFD evaluation of VIV suppression using smaller control cylinders[J]. Journal of Fluids and Structures, 2015,57:66-80.
- [64] Owen J C, Bearman P W, Szewczyk A A. Passive control of VIV with drag reduction[J]. Journal of Fluids and Structures, 2001, 15(3-4): 597-605.
- [65] Roshko A. On the drag and shedding frequency of two-dimensional bluff bodies[R].1954.
- [66] Kawai H. A discrete vortex analysis of flow around a vibrating cylinder with a splitter plate[J]. Journal of Wind Engineering and Industrial Aerodynamics, 1990,35:259-273.
- [67] Nakamura Y, Hirata K, Kashima K. Galloping of a Circular Cylinder in the Presence of a Splitter Plate[J]. Journal of Fluids and Structures, 1994,8(4):355-365.
- [68] Assi G R S, Bearman P W, Tognarelli M A. On the stability of a free-to-rotate short-tail fairing and a splitter plate as suppressors of vortex-induced vibration[J]. Ocean Engineering, 2014,92:234-244.
- [69] Sahu T R, Furquan M, Jaiswal Y, et al. Flow-induced vibration of a circular cylinder with rigid splitter plate[J]. Journal of Fluids and Structures, 2019,89:244-256.
- [70] Wu J, Shu C, Zhao N. Numerical investigation of vortex-induced vibration of a circular cylinder with a hinged flat plate[J]. Physics of fluids, 2014,26(6):63601.

References

- [71] Assi G R S, Bearman P W, Kitney N. Low drag solutions for suppressing vortex-induced vibration of circular cylinders[J]. *Journal of Fluids and Structures*, 2009,25(4):666-675.
- [72] Cui G, Feng L, Hu Y. Flow-induced vibration control of a circular cylinder by using flexible and rigid splitter plates[J]. *Ocean Engineering*, 2022,249:110939.
- [73] Wang E, Zhao S, Xu W, et al. Effect of splitter plate length on FIV of circular cylinder[J]. *International Journal of Mechanical Sciences*, 2023,254:108413.
- [74] Sha Y, Wang Y. Vortex induced vibrations of finned cylinders[J]. *Journal of Hydrodynamics*, 2008,20(2):195-201.
- [75] Zhang M, Øiseth O, Petersen Ø W, et al. Experimental investigation on flow-induced vibrations of a circular cylinder with radial and longitudinal fins[J]. *Journal of Wind Engineering and Industrial Aerodynamics*, 2022,223:104948.
- [76] Chen Z, Han G, Yang L, et al. Nanostructured thermoelectric materials: Current research and future challenge[J]. *Progress in Natural Science: Materials International*, 2012,22(6):535-549.
- [77] Amin S. Review on biofuel oil and gas production processes from microalgae[J]. *Energy Conversion and Management*, 2009,50(7):1834-1840.
- [78] Al-falahi M D A, Jayasinghe S D G, Enshaei H. A review on recent size optimization methodologies for standalone solar and wind hybrid renewable energy system[J]. *Energy Conversion and Management*, 2017,143:252-274.
- [79] Zhu H, Tang T, Yang H, et al. The State-of-the-Art Brief Review on Piezoelectric Energy Harvesting from Flow-Induced Vibration[J]. *Shock and vibration*, 2021,2021.
- [80] Wang J, Geng L, Ding L, et al. The state-of-the-art review on energy harvesting from

References

- flow-induced vibrations[J]. *Applied Energy*, 2020, 267: 114902.
- [81] Abdelkefi A. Aeroelastic energy harvesting: A review[J]. *International Journal of Engineering Science*, 2016,100:112-135.
- [82] McCarthy J M, Watkins S, Deivasigamani A, et al. Fluttering energy harvesters in the wind: A review[J]. *Journal of sound and vibration*, 2016,361:355-377.
- [83] Anton S R, Sodano H A. A review of power harvesting using piezoelectric materials (2003–2006)[J]. *Smart materials and structures*, 2007,16(3):R1-R21.
- [84] Saadon S, Sidek O. A review of vibration-based MEMS piezoelectric energy harvesters[J]. *Energy Conversion and Management*, 2011,52(1):500-504.
- [85] Ma X, Zhou S. A review of flow-induced vibration energy harvesters[J]. *Energy Conversion and Management*, 2022,254:115223.
- [86] Maamer B, Boughamoura A, El-Bab A M R F, et al. A review on design improvements and techniques for mechanical energy harvesting using piezoelectric and electromagnetic schemes[J]. *Energy Conversion and Management*, 2019, 199: 111973.
- [87] Shaikh F K, Zeadally S. Energy harvesting in wireless sensor networks: A comprehensive review[J]. *Renewable and Sustainable Energy Reviews*, 2016,55:1041-1054.
- [88] Yu H, Zhang M. Effects of side ratio on energy harvesting from transverse galloping of a rectangular cylinder[J]. *Energy*, 2021,226:120420.
- [89] He X, Yang X, Jiang S. Enhancement of wind energy harvesting by interaction between vortex-induced vibration and galloping[J]. *Applied physics letters*, 2018,112(3):33901.
- [90] Abdelkefi A, Scanlon J M, McDowell E, et al. Performance enhancement of piezoelectric energy harvesters from wake galloping[J]. *Applied physics letters*,

References

- 2013,103(3):33903.
- [91] Chang C C J, Kumar R A, Bernitsas M M. VIV and galloping of single circular cylinder with surface roughness at $3.0 \times 10^4 \leq Re \leq 1.2 \times 10^5$ [J]. *Ocean Engineering*, 2011, 38(16): 1713-1732.
- [92] Ding L, Mao X, Yang L, et al. Effects of installation position of fin-shaped rods on wind-induced vibration and energy harvesting of aeroelastic energy converter[J]. *Smart materials and structures*, 2021,30(2):25026.
- [93] Hu G, Wang J, Su Z, et al. Performance evaluation of twin piezoelectric wind energy harvesters under mutual interference[J]. *Applied physics letters*, 2019,115(7):73901.
- [94] Hu G, Liu F, Li L, et al. Wind energy harvesting performance of tandem circular cylinders with triangular protrusions[J]. *Journal of Fluids and Structures*, 2019,91:102780.
- [95] Abdelkefi A, Hajj M R, Nayfeh A H. Power harvesting from transverse galloping of square cylinder[J]. *Nonlinear dynamics*, 2012,70(2):1355-1363.
- [96] Abdelkefi A, Hajj M R, Nayfeh A H. Piezoelectric energy harvesting from transverse galloping of bluff bodies[J]. *Smart Materials and Structures*, 2012,22(1):15014.
- [97] Hu G, Tse K T, Kwok K C S, et al. Aerodynamic modification to a circular cylinder to enhance the piezoelectric wind energy harvesting[J]. *Applied physics letters*, 2016,109(19):193902.
- [98] Wang J, Gu S, Abdelkefi A, et al. Enhancing piezoelectric energy harvesting from the flow-induced vibration of a circular cylinder using dual splitters[J]. *Smart materials and structures*, 2021,30(5):5.
- [99] Bushnell D M, J. M K. Drag reduction in nature[J]. *Annual review of fluid mechanics*,

References

- 1991,23(1):65-79.
- [100] Jie H, Liu Y Z. Large eddy simulation of turbulent flow over a cactusanalogue grooved cylinder[J]. Journal of Visualization, 2016,19(1):61-78.
- [101] Liu Y Z, Shi L L, Yu J. TR-PIV measurement of the wake behind a grooved cylinder at low Reynolds number[J]. Journal of Fluids and Structures, 2011,27(3):394-407.
- [102] Talley S, Mungal G. Flow around cactus-shaped cylinders[J]. Center for Turbulence Research Annual Research Briefs, 2002:363.
- [103] Babu P, Mahesh K. Aerodynamic loads on cactus-shaped cylinders at low Reynolds numbers[J]. Physics of fluids, 2008,20(3):35112.
- [104] Wang S F, Liu Y Z, Zhang Q S. Measurement of flow around a cactus-analogue grooved cylinder at $Re_D = 5.4 \times 10^4$: wall-pressure fluctuations and flow pattern[J]. Journal of Fluids and Structures, 2014,50:120-136.
- [105] Pierson E A, Turner R M. An 85-year study of saguaro (*Carnegiea gigantea*) demography[J]. Ecology, 1998,79(8):2676-2693.
- [106] Yamagishi Y, Oki M. Effect of the Number of Grooves on Flow Characteristics around a Circular Cylinder with Triangular Grooves[J]. Journal of Visualization, 2005,8(1):57-64.
- [107] Zhdanov O, Green R, Busse A. Experimental investigation of the angle of attack dependence of the flow past a cactus-shaped cylinder with four ribs[J]. Journal of Wind Engineering and Industrial Aerodynamics, 2021,208:104400.
- [108] Eke P, Kumar A, Sahu K, et al. Endophytic bacteria of desert cactus (*Euphorbia trigonas* Mill) confer drought tolerance and induce growth promotion in tomato (*Solanum lycopersicum* L.)[J]. Microbiological research, 2019,228:126302.

References

- [109] Irwin P A, Baker W. The wind engineering of the Burj Dubai Tower: In: Proceedings of the Council on Tall Buildings and Urban Habitat Seventh World Congress, Renewing the Urban Landscape[C], New York, 2005.
- [110] Law Y Z, Jaiman R K. Passive control of vortex-induced vibration by spanwise grooves[J]. *Journal of Fluids and Structures*, 2018,83:1-26.
- [111] Wang W, Song B, Mao Z, et al. Numerical investigation on vortex-induced vibration of bluff bodies with different rear edges[J]. *Ocean Engineering*, 2020,197:106871.
- [112] Wang W, Mao Z, Song B, et al. Numerical investigation on vortex-induced vibration suppression of the cactus-inspired cylinder with some ribs[J]. *Physics of fluids*, 2021,33(3):37127.
- [113] Cetiner O, Rockwell D. Streamwise oscillations of a cylinder in a steady current. Part 1. Locked-on states of vortex formation and loading[J]. *Journal of fluid mechanics*, 2001,427:1-28.
- [114] Dennis S C R, Nguyen P, Kocabiyik S. The flow induced by a rotationally oscillating and translating circular cylinder[J]. *Journal of fluid mechanics*, 2000,407:123-144.
- [115] Blackburn H M, Henderson R D. A study of two-dimensional flow past an oscillating cylinder[J]. *Journal of fluid mechanics*, 1999,385:255-286.
- [116] Nakano M, Rockwell D. The wake from a cylinder subjected to amplitude-modulated excitation[J]. *Journal of fluid mechanics*, 1993,247:79-110.
- [117] Bourguet R. Flow-induced vibrations of a rotating cylinder in an arbitrary direction[J]. *Journal of fluid mechanics*, 2019,860:739-766.
- [118] Wong K W L. Experimental investigation of flow-induced vibration of a rotating circular cylinder[J]. *journal of fluid mechanics*, 2017.

References

- [119] Zhao M, Cheng L, Lu L. Vortex induced vibrations of a rotating circular cylinder at low Reynolds number[J]. *Physics of fluids*, 2014,26(7):73602.
- [120] Konstantinidis E, Balabani S, Yianneskis M. The timing of vortex shedding in a cylinder wake imposed by periodic inflow perturbations[J]. *Journal of fluid mechanics*, 2005,543(1):45-55.
- [121] Nehari D, Armenio V, Ballio F. Three-dimensional analysis of the unidirectional oscillatory flow around a circular cylinder at low Keulegan–Carpenter and numbers[J]. *Journal of fluid mechanics*, 2004,520:157-186.
- [122] Li Y, Li S, Zeng L, et al. Control of the VIV of a cantilevered square cylinder with free-end suction[J]. *Wind and Structures*, 2020,29(1):75-84.
- [123] Wang H, Zeng L, Alam M M, et al. Large eddy simulation of the flow around a finite-length square cylinder with free-end slot suction[J]. *Wind and Structures*, 2020,30(5):533-546.
- [124] Wang C, Tang H, Yu S C M, et al. Active control of vortex-induced vibrations of a circular cylinder using windward-suction- leeward-blowing actuation[J]. *Physics of fluids*, 2016,28(5):53601.
- [125] Jeon S, Choi J, Jeon W P, et al. Active control of flow over a sphere for drag reduction at a subcritical Reynolds number[J]. *Journal of fluid mechanics*, 2004,517:113-129.
- [126] Wen X, Tang H, Duan F. Interaction of in-line twin synthetic jets with a separated flow[J]. *Physics of Fluids*, 2016,28(4):43602.
- [127] Wang C, Tang H, Duan F, et al. Control of wakes and vortex-induced vibrations of a single circular cylinder using synthetic jets[J]. *Journal of Fluids and Structures*, 2016,60:160-179.

References

- [128] Tang H, Salunkhe P, Zheng Y, et al. On the use of synthetic jet actuator arrays for active flow separation control[J]. *Experimental Thermal and Fluid Science*, 2014,57:1-10.
- [129] Feng L, Wang J. Synthetic jet control of separation in the flow over a circular cylinder[J]. *Experiments in fluids*, 2012,53(2):467-480.
- [130] Tang H, Zhong S. 2D numerical study of circular synthetic jets in quiescent flows[J]. *Aeronautical journal*, 2005,109(1092):89-97.
- [131] Mutschke G, Gerbeth G, Shatrov V, et al. The scenario of three-dimensional instabilities of the cylinder wake in an external magnetic field: A linear stability analysis[J]. *Physics of fluids*, 2001,13(3):723-734.
- [132] Kim S J, Lee C M. Investigation of the flow around a circular cylinder under the influence of an electromagnetic field[J]. *Experiments in Fluids*, 2000,28:252-260.
- [133] Kim J, Choi H. Distributed forcing of flow over a circular cylinder[J]. *Physics of Fluids*, 2005,3(17):33103.
- [134] Dalla Longa L, Morgans A S, Dahan J A. Reducing the pressure drag of a D-shaped bluff body using linear feedback control[J]. *Theoretical and computational fluid dynamics*, 2017,31(5-6):567-577.
- [135] Protas B. Linear feedback stabilization of laminar vortex shedding based on a point vortex model[J]. *Physics of fluids*, 2004,16(12):4473-4488.
- [136] Li Z, Navon I M, Hussaini M Y, et al. Optimal control of cylinder wakes via suction and blowing[J]. *Computers & Fluids*, 2003,32(2):149-171.
- [137] Bergmann M, Cordier L, Brancher J P. Optimal rotary control of the cylinder wake using proper orthogonal decomposition reduced-order model[J]. *Physics of fluids*, 2005,17(9):97101.

References

- [138] Cortelezzi L. Nonlinear feedback control of the wake past a plate with a suction point on the downstream wall[J]. *Journal of fluid mechanics*, 1996,327:303-324.
- [139] Ren F, Hu H, Tang H. Active flow control using machine learning: A brief review[J]. *Journal of hydrodynamics. Series B*, 2020,32(2):247-253.
- [140] Zhou Y, Fan D, Zhang B, et al. Artificial intelligence control of a turbulent jet[J]. *Journal of Fluid Mechanics*, 2020(897):A27.
- [141] Brunton S L, Noack B R, Koumoutsakos P. Machine learning for fluid mechanics[J]. *Annual review of fluid mechanics*, 2020(52):477-508.
- [142] Ren F, Wang C, Tang H. Active control of vortex-induced vibration of a circular cylinder using machine learning[J]. *Physics of fluids*, 2019,31(9):93601.
- [143] Gautier N, Aider J L, Duriez T, et al. Closed-loop separation control using machine learning[J]. *Journal of Fluid Mechanics*, 2015(770):442-457.
- [144] Mumtaz Qadri M N, Zhao F, Tang H. Fluid-structure interaction of a fully passive flapping foil for flow energy extraction[J]. *International Journal of Mechanical Sciences*, 2020,177:105587.
- [145] Menter F R. Two-equation eddy-viscosity turbulence models for engineering applications[J]. *AIAA journal*, 1994,32(8):1598-1605.
- [146] Menter F. Zonal Two Equation kw Turbulence Models For Aerodynamic Flows 23rd Fluid Dynamics, Plasmadynamics, and Lasers Conference[J]. Reston, Virginia: American Institute of Aeronautics and Astronautics, 1993.
- [147] Chen D, Marzocca P, Xiao Q, et al. Vortex-induced vibration on a low mass ratio cylinder with a nonlinear dissipative oscillator at moderate Reynolds number[J]. *Journal of Fluids and Structures*, 2020,99:103160.

References

- [148] Rocha P A C, Rocha H H B, Carneiro F O M, et al. $k-\omega$ SST (shear stress transport) turbulence model calibration: A case study on a small scale horizontal axis wind turbine[J]. Energy, 2014,65:412-418.
- [149] Kang Z, Zhang C, Ma G, et al. A numerical investigation of two-degree-of-freedom VIV of a circular cylinder using the modified turbulence model[J]. Ocean Engineering, 2018,155:211-226.
- [150] Newmark N M. A method of computation for structural dynamics[J]. Journal of the engineering mechanics division, 1959,85(3):67-94.
- [151] Teixeira P R F, Awruch A M. Numerical simulation of fluid–structure interaction using the finite element method[J]. Computers & fluids, 2005,34(2):249-273.
- [152] Zhang B, Song B, Mao Z, et al. Numerical investigation on VIV energy harvesting of bluff bodies with different cross sections in tandem arrangement[J]. Energy, 2017,133:723-736.
- [153] Khalak A, Williamson C H K. Motions, forces and mode transitions in vortex-induced vibrations at low mass-damping[J]. Journal of fluids and Structures, 1999, 13(7-8): 813-851.
- [154] Norberg C. Fluctuating lift on a circular cylinder: review and new measurements[J]. Journal of Fluids and Structures, 2003,17(1):57-96.
- [155] Mahir N, Altaç Z. Numerical investigation of convective heat transfer in unsteady flow past two cylinders in tandem arrangements[J]. International Journal of Heat and Fluid Flow, 2008,29(5):1309-1318.
- [156] Harimi I, Saghafian M. Numerical simulation of fluid flow and forced convection heat transfer from tandem circular cylinders using overset grid method[J]. Journal of Fluids

References

- and Structures, 2012,28:309-327.
- [157] Zhou T, Razali S F M, Hao Z, et al. On the study of vortex-induced vibration of a cylinder with helical strakes[J]. Journal of Fluids and Structures, 2011,27(7):903-917.
- [158] Amitay M, Glezer A. Role of actuation frequency in controlled flow reattachment over a stalled airfoil[J]. AIAA journal, 2002,40(2):209-216.
- [159] Lee T, Gerontakos P. Investigation of flow over an oscillating airfoil[J]. Journal of Fluid Mechanics, 2004,512:313-341.
- [160] Wang J, Fan D, Lin K. A review on flow-induced vibration of offshore circular cylinders[J]. Journal of hydrodynamics. Series B, 2020,32(3):415-440.
- [161] Assi G R S, Bearman P W. Vortex-induced vibration of a wavy elliptic cylinder[J]. Journal of Fluids and Structures, 2018,80:1-21.
- [162] Zdravkovich M M. Flow around circular cylinders: Volume 2: Applications[M]. Oxford university press, 1997.
- [163] Tritton D J. Experiments on the flow past a circular cylinder at low Reynolds numbers[J]. Journal of fluid mechanics, 1959,6(4):547-567.
- [164] Dai H L, Abdelkefi A, Wang L. Theoretical modeling and nonlinear analysis of piezoelectric energy harvesting from vortex-induced vibrations[J]. Journal of intelligent material systems and structures, 2014,25(14):1861-1874.
- [165] Sun W, Zhao D, Tan T, et al. Low velocity water flow energy harvesting using vortex induced vibration and galloping[J]. Applied Energy, 2019,251:113392.
- [166] Hackett J E, Cooper K R. Extensions to Maskell's theory for blockage effects on bluff bodies in a closed wind tunnel[J]. The Aeronautical Journal, 2001,105(1050):409-418.
- [167] Maskell E. A Theory of the Blockage Effects on Bluff Bodies and Stalled Wings in a

References

- Closed Wind Tunnel[R]. Aeronautical Research Council London (United Kingdom): 1963.
- [168] Wei Z, New T H, Lian L, et al. Leading-edge tubercles delay flow separation for a tapered swept-back wing at very low Reynolds number[J]. *Ocean Engineering*, 2019,181:173-184.
- [169] Lienhard J H. Synopsis of lift, drag, and vortex frequency data for rigid circular cylinders[M]. Pullman, WA: Technical Extension Service, Washington State University, 1966.
- [170] New T H, Long J. Dynamics of laminar circular jet impingement upon convex cylinders[J]. *Physics of fluids*, 2015,27(2):24109.
- [171] New T H, Zang B. Head-on collisions of vortex rings upon round cylinders[J]. *Journal of fluid mechanics*, 2017,833:648-676.
- [172] Zhao C, Wang H, Zeng L, et al. Effects of oncoming flow turbulence on the near wake and forces of a 3D square cylinder[J]. *Journal of Wind Engineering and Industrial Aerodynamics*, 2021,214:104674.
- [173] New T H, Shi S, Liu Y. On the flow behaviour of confined finite-length wavy cylinders[J]. *Journal of Fluids and Structures*, 2015,54:281-296.
- [174] Wang H F, Cao H L, Zhou Y. POD analysis of a finite-length cylinder near wake[J]. *Experiments in Fluids*, 2014,55(8):1-15.
- [175] Meyer K E, Pedersen J M, Özcan O. A turbulent jet in crossflow analysed with proper orthogonal decomposition[J]. *Journal of Fluid Mechanics*, 2007,583:199-227.
- [176] Ma L, Feng L. Experimental investigation on control of vortex shedding mode of a circular cylinder using synthetic jets placed at stagnation points[J]. *Science China*.

References

- Technological sciences, 2013,56(1):158-170.
- [177] Kim N, Kim H, Park H. An experimental study on the effects of rough hydrophobic surfaces on the flow around a circular cylinder[J]. *Physics of fluids* (1994), 2015,27(8):85113.
- [178] Wang C, Tang H, Yu S C M, et al. Lock-on of vortex shedding to a pair of synthetic jets with phase difference[J]. *Physical review fluids*, 2017,2(10).
- [179] Norberg C. LDV-measurements in the near wake of a circular cylinder: In: Proceedings of the 1998 ASME Fluids Engineering Division Summer Meeting, FED-vol. 245, FEDSM98-5202. [C], Washington, DC, 1998.
- [180] L S. Turbulence and the dynamics of coherent structures[J]. *Quarterly of Applied Mathematics*, 1987,45:561-590.
- [181] Oudheusden B W, Scarano F, Hinsberg N P, et al. Phase-resolved characterization of vortex shedding in the near wake of a square-section cylinder at incidence[J]. *Experiments in Fluids*, 2005, 39: 86-98.
- [182] Rabault J, Kuchta M, Jensen A, et al. Artificial neural networks trained through deep reinforcement learning discover control strategies for active flow control[J]. *Journal of fluid mechanics*, 2019,865:281-302.
- [183] Williamson C H K, Wu J, Sheridan J. Scaling of streamwise vortices in wakes[J]. *Physics of fluids*, 1995,7(10):2307-2309.
- [184] Lin Y F, Bai H L, Alam M M, et al. Effects of large spanwise wavelength on the wake of a sinusoidal wavy cylinder[J]. *Journal of Fluids and Structures*, 2016,61:392-409.
- [185] Lam K, Lin Y F. Large eddy simulation of flow around wavy cylinders at a subcritical Reynolds number[J]. *International Journal of Heat and Fluid Flow*, 2008,29(4):1071-

- 1088.
- [186] Lam K, Lin Y F, Zou L, et al. Investigation of turbulent flow past a yawed wavy cylinder[J]. *Journal of Fluids and Structures*, 2010,26(7):1078-1097.
- [187] Jiang H, Cheng L, Draper S, et al. Three-dimensional direct numerical simulation of wake transitions of a circular cylinder[J]. *Journal of fluid mechanics*, 2016,801:353-391.
- [188] Williamson C H K. The existence of two stages in the transition to three-dimensionality of a cylinder wake[J]. *The Physics of fluids*, 1988,31(11):3165-3168.
- [189] Green M A, Rowley C W, Haller G. Detection of Lagrangian coherent structures in three-dimensional turbulence[J]. *Journal of Fluid Mechanics*, 2007, 572: 111-120.
- [190] Haller G. An objective definition of a vortex[J]. *Journal of fluid mechanics*, 2005,525:1-26.